Probing Hydrodynamic Transport in Graphene Heterostructures

Andrew David Niblett

This thesis is submitted for the degree of

Doctor of Philosophy

April 2026

Supervised by Dr. Leonid A. Ponomarenko

Department of Physics

Declaration

I declare that this thesis is, to the best of my knowledge and belief, original and my own work. No portion of the work referred to in this thesis has been submitted in support of an application for another degree at any other institution.

Where part of this research has been carried out in collaboration, Chapter 2, the specific contributions have been acknowledged in the relevant sections. All other experimental work, data analysis, modelling, and writing are my own.

This thesis does not exceed the maximum permitted word length, excluding preliminary text, references and appendices.

Acknowledgements

I would first like to express my deepest gratitude to my supervisor, Dr. Leonid Ponomarenko, whose patience and teaching ability have been invaluable throughout this work. You are precise and forward, qualities I admire. Over the time we have worked together I am grateful for the grace and understanding you showed me during difficult periods. I can only hope I have offered you the same in return.

I am also indebted to my deputy supervisor, Prof. Oleg Kolosov, who not only opened his laboratory, where much of this research was made possible, but also generously shared his expertise and guidance. Your excitement for this work was always contagious, and I know that, with this thesis complete, we can do more together.

I gratefully acknowledge the Royal Society for funding this research, without whom the Encyclopaedia of Physics would today be a few pages shorter.

I am also indebted to the National Graphene Institute, whose ability to produce devices and researchers is unmatched.

Massive thanks to all those within the department who encouraged me to persevere. Their support gave me the strength to continue when stopping due to poor health was a real possibility. Therefore, I also extend my thanks to the University for its understanding and grace in allowing intercalation, which was much needed, and as a result, I have come back much stronger.

To my friends, both those still with me and those no longer here, thank you. In many different ways, you carried me through, and this thesis carries a part of you with it.

Finally, to my mum, dad, and sister, for their constant encouragement and love; to my Nana, for her kind and uplifting messages; and to my extended family in Yorkshire.

Your support has meant more than I ever say.

For from him and through him and to him are all things.
To him be the glory forever. Amen.

Probing Hydrodynamic Transport in Graphene Heterostructures

Andrew David Niblett, MPhys (Hons)

Abstract

This thesis addresses two outstanding gaps in the study of electronic transport in graphene.

The first concerns the inadequacy of conventional Drude models to describe charge transport near the neutrality point (NP). Using transport measurements on high-mobility hBN-encapsulated graphene devices, we show that electron-hole interactions near the NP produce apparent negative mobilities that were previously unexplained. In collaborative work, a drag-modified Drude model was developed that accurately reproduces measured longitudinal and Hall resistivities. This demonstrated that the negative mobility was due to significant electron-hole drag (majority-carriers drag the minority-carriers). The model provides a predictive, compact description of graphene transport over a wide range of carrier densities and a practical method for extracting microscopic scattering times from macroscopic resistivity data.

The second advance is the introduction of a systematic method to analyse scanning gate microscopy (SGM) data in transport experiments. While SGM had been previously applied to probe transport in 2D materials, no experimental work, until now, had been demonstrated on spatially probing hydrodynamic transport in graphene-based devices. Further, no solid framework appears for interpreting such spatial resistance maps. Here, we establish such a framework by combining SGM measurements with analytical solutions, in simplified geometries, and in finite-element simulations. We reveal unexpected crescent-shaped response patterns in four-probe non-local configurations, characteristic of diffusive flow. Likewise, unique patterns were observed at lower temperatures, 160 K, consistent with hydrodynamic flow. Further, the numerical analysis enabled the extraction of the electronic fluid's kinematic viscosity from spatial SGM maps.

Together, these studies demonstrate the significance of carrier-carrier interactions that produce measurable phenomena. Our models and insight provide a better understanding of interacting electronic fluids. The methodologies developed here supply models and experimental tools that may extend beyond graphene, offering a foundation for future studies of intrinsic transport in two-dimensional materials.

Contents

Declaration ii

Acknowledgements iii

Abstract iv

1 Background Understanding 1

1.1 Electronic Properties of Graphene-based Devices 2

1.1.1 Graphene Origins: The Hybridisation of Carbon Allotropes . . 2

1.1.2 Monolayer Graphene Band Structure 4

1.1.3 Excitation of Phonon Quasiparticles 12

1.2 Transport Regimes in Graphene 15

1.2.1 Transport of Quasiparticles in the Diffusive Limit 15

1.2.2 Quantum Transport of Quasiparticles in the Ballistic Limit . . 24

1.2.3 Electronic Transport in the Hydrodynamic Window 26

1.2.4 Potential Applications for Hydrodynamic Electronic Devices . 28

1.2.5 Coulomb Drag and Charge Puddles 30

1.2.6 Quantum Hall Effect, Landau Levels, and SdH Onset 30

1.3 Fabricating High-Quality Graphene Heterostructures 32

1.3.1 Using Hexagonal Boron Nitride For Graphene-Based Heterostructures 32

1.3.2 Graphene Heterostructure Fabrication Process 33

1.4 Experimental Considerations for Characterisation Measurements . . . 34

1.4.1 Device Geometry and Measurement Configuration 34

1.4.2 Experimental Setup for Transport Measurements 38

1.5 Scanning Gate Microscopy of Nanoscale Devices 47

1.5.1 Basic Principles of Atomic Force Microscopy 48

1.5.2 Probing Quantum Carrier Transport Inside Graphene Using Scanning Gate Microscopy 50

2 Electron-Hole Drag and Negative Mobility in Graphene's Dirac Plasma 51

2.1 Experimental System and Methods 52

2.1.1 Device Fabrication and Structure 53
2.1.2 Measurement Techniques and Protocols 54
2.1.3 Device Quality and Characterisation 62
2.2 Transport Phenomena Near Neutrality Point 65
2.2.1 Universal Scaling with Temperature 65
2.2.2 Hall Resistivity & Predictions of the Drude Model 68
2.2.3 Drude Model with Unequal and Negative Mobilities 71
2.3 Boltzmann Transport Model and Microscopic Theory 76
2.3.1 Kinetic Equation for Coupled Electron-Hole System 77
2.3.2 Analytical Modified Drude Equations for Interacting Two-Carrier System 77
2.3.3 Mobility and Hall Response from the Drag-Modified Drude model 82
2.3.4 Fitting Drag-Modified Drude Model to Experimental Data . . 94
2.4 Charge Inhomogeneity: Electron-Hole Puddles 99
2.4.1 Model for Inhomogeneous Conductivity 100
2.5 Final Remarks on Drag-Modified Transport in Graphene 104

3 Probing Electronic Transport via Scanning Gate Microscopy 105
3.1 Scanning Gate Microscopy Methodology 106
3.1.1 SGM Experimental Setup 106
3.1.2 Preliminary Experiment on Scanning Gate Microscopy 114
3.1.3 Probing 4-Probe Non-local Resistance Using Scanning Gate Microscopy 117
3.2 Model Solution to Probing Diffusive Transport via SGM 130
3.2.1 Influence of the SGM probe on a 2DEG 131
3.2.2 Current Density in Infinite Strip With Point-like Current Injector 138
3.2.3 Impact of a Local Dipole on 4-Probe Resistance 141
3.3 Numerical Simulation of SGM on Hydrodynamic Transport 149
3.3.1 Linearised Navier-Stokes for Density-Modulated Hydrodynamic Electron Transport 150
3.3.2 Finite Element Method Implementation 153
3.3.3 Results of Numerical Simulations 158

3.3.4 Extracting 4-Probe Resistance Maps from the Numerical Solution . . . 161
3.4 Probing Transport via SGM: Conclusions and Future Work . . . 165

4 Last Words **168**

A Solving Hydrodynamics Using The Finite Element Method **169**

B Mathematica Code for SGM Models **171**
B.1 Analytical Model Code . . . 171
B.2 Numerical Finite Element Method Code . . . 173

Bibliography **177**

CHAPTER 1

Background Understanding

I have split this thesis into three chapters; the first, which we are reading now, starts with a brief overview of some complex areas of research, on which people have and still do write whole theses. The intention of this chapter is to provide all the necessary context and background understanding we need as we enter into the novel research conducted in Chapters 2 and 3.

In Chapter 1 we cover a basic overview of what graphene is (see Section 1.1.1), followed by the origins of key electrical phenomena: band structure (Section 1.1.2); phonons (Section 1.1.3); as well as the resulting different transport regimes (Section 1.2). We will discuss each major electronic transport regime, looking into specific detail on diffusive and hydrodynamic transport (see Sections 1.2.1 and 1.2.3 respectively). We will also briefly consider other regimes, such as ballistic and quantised transport, with the hope of avoiding those regimes in our experiments.

With the more theoretical background covered, we will move on to the experimental methods used to probe these phenomena. The fabrication of the types of devices used in this work is briefly covered in Section 1.3. We will look at measurement techniques used in our research to get precise and accurate data (Section 1.4.1) at low temperatures and in small magnetic fields (see Section 1.4.2).

Finally in this chapter, we will cover the scanning gate microscopy technique (Section 1.5) that is a crucial tool used in Chapter 3 of this thesis.

With all the necessary background covered, we will jump into the two main sections of study in this thesis. In Chapter 2, we observe the effects of electron-hole drag in high-quality monolayer graphene. In collaboration with theorists, a model is developed to explain the observed phenomena, and, as a result, two microscopic parameters are identified that accurately reproduce the observations over a wide range of conditions.

In Chapter 3, we aim to directly probe intrinsic transport flow in diffusive and hydrodynamic regimes using scanning gate microscopy. The results show distinct differences in measured maps between the two regimes and are supported by analytical and numerical models.

But first, we begin with Chapter 1 - Section 1.1, what is graphene?

1.1 Electronic Properties of Graphene-based Devices

The electronic behaviour of graphene-based devices originates from the unique structure of graphene at the atomic scale. The arrangement of carbon atoms in a two-dimensional honeycomb lattice leads to unusual electronic properties that differ significantly from those of conventional semiconductors.

In this section we introduce the fundamental concepts required to understand graphene transport, beginning with the atomic origins of graphene through carbon hybridisation, followed by its electronic band structure and the role of phonons in charge-carrier scattering.

1.1.1 Graphene Origins: The Hybridisation of Carbon Allotropes

Explaining the differing nature of separate forms of the same element intrigued scientists as early as the mid-1800s. In fact, it was German scientist Moritz Frankenheim who proposed the new term 'allotrope' in 1841. The word comes from the Greek words *'allos'*, meaning 'other', and *'tropos'*, meaning 'to turn'. And so, 'allotrope' means 'other turn' or, more figuratively, *'other behaviour'*. [1]

The most well-known allotropes in the study of allotropy are those of the element carbon, specifically diamond and graphite. Two structures, naturally formed of pure carbon, with wildly different structural, electronic, optical, and thermal behaviours. The versatile nature of carbon is a result of the many types of bonds it may form, due to 'hybridisation'.

To understand hybridisation, let's consider the ground-state electronic configuration of carbon, $1s^2\,2s^2\,2p^2$. [2, p. 1] The ground state has four valence electrons, of which two are paired up in the $2s$ orbital, which results in carbon atoms only being able to form two bonds in their ground state. However, it is more energetically favourable to start in an excited state, $1s^2\,2s^1\,2p^3$, and have four unpaired electrons available for bonding.

There are two relevant chemical bonds, σ and π, forming when atomic orbitals overlap. Strong σ bonds form when an end-to-end overlapping of hybrid orbitals occurs. Weaker π bonds occur when orbitals are parallel. [3, p. 232]

Note that in this overview, the details of atomic orbitals, bonding, and their mathematical expressions are not the focus.

From an excited state, the carbon atom orbitals can combine (hybridise), creating

a new orbital, *sp*. *sp* orbitals form stronger σ bonds; this becomes relevant as strong and rigid bonds will play a key part in electron-phonon interactions that influence transport. There are three ways for carbon to hybridise from the first excited state:

1. **sp³ hybridisation:** The $2s$ combines with all three $2p$ orbitals, giving rise to a new configuration $1s^2\,2sp^3$. The resulting hybrid orbitals, $2sp^3$, have four electrons, and they will optimise their position in space by forming a tetrahedral geometry. The strong covalent σ bonds form at angles of 109.5°, of length 1.54 Å producing a rigid 3D structure. This material is exceptionally strong, exhibiting very high hardness, unusually high thermal conductivity, optical transparency, and electrical insulation (band gap: 5.5 eV), and is known as diamond [4, pp. 5,210] (from ancient Greek *adámas*, meaning 'the unbreakable one').

2. **sp² hybridisation:** The $2s$ orbital hybridises with only two $2p$ orbitals. The new electronic configuration, $1s^2\,2sp^2\,2p$, has three hybrid orbitals, and they will optimise their position in space by forming a trigonal planar geometry. The three hybrid orbital electrons will form σ bonds at angles 120° with a length of 1.42 Å. The remaining p-orbital electron will form a weaker π bond that is positioned perpendicular to the plane of σ bonds. In the plane of the strong σ bonds, the resulting structure is a strong hexagonal lattice (often called a honeycomb) and honeycomb cardboard springs to mind as an analogy of in-plane strength, while still being flexible out-of-plane. This 2D structure was coined graphene (from English *graphite*, derived from the ancient Greek *gráphein*, meaning 'to write').

   Electronically, monolayer graphene (or single-layer graphene, SLG), unlike diamond, is not a conventional semiconductor, but is known as a zero-band-gap semiconductor. This means that the conduction and valence bands touch at specific points in momentum space. In principle, in perfect undoped SLG, the chemical potential sits exactly at these touching points where the number of available states is zero and no conduction is possible. However, in practice, due to disorder and finite temperature, there is typically a finite conductivity. Importantly, the carrier density and the position of the chemical potential in graphene are readily tunable by electrostatic gating, allowing continuous control between electron and hole-dominated transport regimes.

   Multiple layers of graphene can be stacked, and the resulting structures are commonly referred to according to the number of atomic layers, such as bilayer graphene (BLG), trilayer graphene (TLG), or multilayer graphene (MLG). In few-layer graphene ($\approx 2-5$ layers), the electronic structure varies markedly with thickness and remains strongly tunable by an external gate. However,

once the thickness exceeds approximately $8-10$ layers, additional layers lead to only minor changes in in-plane electronic transport. In this regime, electrostatic screening becomes efficient, substantially reducing gate-voltage tunability, and the system exhibits converging transport properties approaching bulk graphite.

Finally, due to the weak out-of-plane π bonds, atomic layers are mechanically held weakly together, particularly susceptible to shear loads, allowing for the good application in pencils (hence the graphite name) and dry lubrication. [5]

3. **sp hybridisation:** The final hybridisation of carbon is the combination of the $2s$ orbital with just one $2p$ orbital, $1s^2\,2sp\,2p^2$. With two electrons in the hybrid orbital, it can be expected that the angle of separation of the bonds shall be 180°, creating one-dimensional chains called carbyne. The isolation of such chains proves to be a greater challenge than any other carbon allotrope described here due to the instability of the 1D structure. [6]

Under normal conditions (1 atm and room temperature), carbon will hybridise into the second state, sp^2, forming nanostructures based on the trigonal base shape. These nanostructures include three-dimensional structures [2] like the buckyball and carbon nanotubes; one-dimensional structures like graphene ribbons; and many more polymorphisms that will not be covered here, including nanotoroids, nanofoams, pentaheptite/Haeckelites, etc.

However, from this point on, we will be focusing on just one structure in the sp^2 allotrope, the two-dimensional sheet, graphene. Graphene comes in multiple forms with drastically different electronic structures and properties; the focus here is mainly going to be on monolayer graphene and not bilayer or many-layer graphene.

1.1.2 Monolayer Graphene Band Structure

The descriptions of the monolayer graphene lattice and the tight-binding model are straightforward, but they have non-trivial features. The first description of the graphene band structure comes from P.R. Wallace in 1947, [7] where he investigates the single hexagonal layer of graphite in order to build up his model for bulk graphite. As seen in Section 1.1.1, the hybridisation of carbon will lead to a trigonal plane with three strong σ bonds per atom. This results in a hexagonal lattice structure where the remaining $2p$ orbitals do not contribute significantly to the bonding in graphene; however, they are instrumental for determining the electronic properties.

We can simplify the periodic structure of the hexagonal lattice by looking at its unit cell of two atoms, $A\,\&\,B$. The unit cell is the smallest repeating unit that,

through translation, recreates the entire periodic lattice structure. The primitive lattice vectors, the smallest vectors that through linear combinations generate all lattice points, are given as $\mathbf{a_1}$ and $\mathbf{a_2}$:

$$\mathbf{a_1} = \frac{a}{2}\left(\sqrt{3}, 1\right), \quad \mathbf{a_2} = \frac{a}{2}\left(\sqrt{3}, -1\right)$$

where, in graphene, $a = 2.46\,\text{Å}$. The magnitude of the basis displacement between the two atoms A and B is simply the carbon-carbon bond length, $a_{cc} = \frac{a}{\sqrt{3}} \approx 1.42\,\text{Å}$.

Then by using the condition $\mathbf{a_i} \cdot \mathbf{b_j} = 2\pi\delta_{ij}$, the reciprocal lattice vectors, $\mathbf{b_1}$ and $\mathbf{b_2}$, are likewise determined:

$$\mathbf{b_1} = \frac{2\pi}{\sqrt{3}a}\left(1, \sqrt{3}\right), \quad \mathbf{b_2} = \frac{2\pi}{\sqrt{3}a}\left(1, -\sqrt{3}\right).$$

The reciprocal lattice vectors define the periodic structure in momentum space, ensuring that Bloch waves, solutions to Schrödinger's equation, correctly maintain periodicity across the real-space lattice.

The resulting triangular reciprocal Bravais lattice has a first Brillouin zone defined by the Wigner-Seitz cell, the smallest volume that contains all points closer to a given lattice point than any other and, therefore, all unique wavevectors. In SLG, this is a hexagonal cell whose corners are defined by six $\mathbf{K}$ points. The points may be split into two unique sets of points where each set of three $\mathbf{K}$ points can be described by linear combinations of the reciprocal lattice vectors, $\mathbf{b_1}$ and $\mathbf{b_2}$, and likewise with the remaining three. This result yields two inequivalent $\mathbf{K}$ points in the first Brillouin zone; we label them $\mathbf{K}_+$ and $\mathbf{K}_-$:

$$\mathbf{K}_\pm = \pm\left(0, \frac{4\pi}{3a}\right) \tag{1.1}$$

To determine the electronic behaviour throughout the Brillouin zone, we now introduce the tight-binding model for the honeycomb lattice, from which the significance of the $\mathbf{K}_\pm$ points emerges naturally.

1.1.2.1 The Tight-Binding Description of Graphene

The tight-binding model [7, 8] is used as a method for calculating the electronic band structure of a periodic lattice. Electrons are described as tightly-bound to their own atom, so the Hamiltonian, which represents the total energy of the electrons, includes both their on-site energies and hopping interactions between nearest-neighbour atomic orbitals. 'Hopping' is the movement of an electron between neighbouring atomic orbitals, which ultimately leads to the formation of electronic band

structure, where discrete atomic energies have broadened into continuous energy bands.

The first step of the tight-binding model is to approximate the wavefunction, Ψ, of the system, such that the energy eigenvalues, E, may be obtained from the Schrödinger equation, $\hat{H}\Psi_{\mathbf{k}}(\mathbf{r}) = E\Psi_{\mathbf{k}}(\mathbf{r})$. The wavefunction can be constructed by exploiting the periodicity of the lattice. By Bloch's theorem, the crystal wavefunction acquires a phase factor $e^{i\mathbf{k}\cdot\mathbf{R}}$ under translations by a lattice vector $\mathbf{R}$. This result falls out of the Bloch description of periodic lattices.

The total wavefunction then is a linear combination of each orbital wavefunction over all the unit cells:

$$\Psi_{\mathbf{k}}(\mathbf{r}) = \frac{1}{\sqrt{N}} \sum_{i=A,B} \sum_{\mathbf{R}_i} c_i(\mathbf{k})\, e^{i\mathbf{k}\cdot\mathbf{R}_i}\, \phi_i(\mathbf{r} - \mathbf{R}_i)\,,$$

where $\mathbf{R}_i$ denotes the position of an atomic site on sublattice $i \in \{A, B\}$, the summation runs over all N unit cells of the crystal, $\phi_i(\mathbf{r})$ represents the localised atomic p_z orbital on sublattice i, and $c_i(\mathbf{k})$ are $\mathbf{k}$-dependent coefficients specifying the relative weight of each sublattice in the Bloch wavefunction.

Assuming that overlap integrals between atomic orbitals on different sites may be neglected then we can project the full Hamiltonian, $\hat{H}$, into a 2×2 matrix, $\tilde{H}$, such that $\tilde{H}(\mathbf{k})c(\mathbf{k}) = \varepsilon(\mathbf{k})c(\mathbf{k})$ where,

$$\tilde{H} = \begin{pmatrix} \tilde{H}_{AA} & \tilde{H}_{AB} \\ \tilde{H}_{BA} & \tilde{H}_{BB} \end{pmatrix},$$

$$\tilde{H}_{ij} = \frac{1}{N} \sum_{\mathbf{R}_i} \sum_{\mathbf{R}_j} e^{i\mathbf{k}\cdot(\mathbf{R}_j - \mathbf{R}_i)} \langle \phi_i(\mathbf{r} - \mathbf{R}_i)|\hat{H}|\phi_j(\mathbf{r} - \mathbf{R}_j)\rangle, \tag{1.2}$$

where $\tilde{H}_{ij}$ is the Hamiltonian element.

With Eq. (1.2), the Hamiltonian elements can be evaluated. The Hamiltonian $\tilde{H}_{AA}$ will be mostly dominated by the same evaluation site and therefore simplifies to $\tilde{H}_{AA} \approx \langle \phi_A(\mathbf{r} - \mathbf{R}_A)|\hat{H}|\phi_A(\mathbf{r} - \mathbf{R}_A)\rangle$, which is the energy of the $2p$ orbital, ε_{2p}. As the carbon atoms are chemically identical between the two sublattices, then the Hamiltonians are equal, $\tilde{H}_{AA} = \tilde{H}_{BB} \approx \varepsilon_{2p}$.

To calculate the off-diagonal Hamiltonians, the vectors between the nearest-neighbours of an atom site must be calculated. The displacement vectors δ_i (for $i = 1, 2, 3$) connect a carbon atom in sublattice A to its three nearest neighbors in sublattice B:

$$\delta_1 = \left(\frac{a}{\sqrt{3}}, 0\right) \quad \delta_2 = \left(-\frac{a}{2\sqrt{3}}, \frac{a}{2}\right) \quad \delta_3 = \left(-\frac{a}{2\sqrt{3}}, -\frac{a}{2}\right).$$

Due to the symmetry of the system, it can also be determined that the act of swapping index of Eq. (1.2) is identical to that of the complex conjugate, therefore $\tilde{H}_{BA} = \tilde{H}^*_{AB}$. By substitution, the final Hamiltonian is determined:

$$\tilde{H} = \begin{pmatrix} \varepsilon_{2p} & -\gamma_0 f(\mathbf{k}) \\ -\gamma_0 f^*(\mathbf{k}) & \varepsilon_{2p} \end{pmatrix},$$

$$f(\mathbf{k}) = \exp\left(i\frac{ak_x}{\sqrt{3}}\right) + 2\exp\left(-i\frac{ak_x}{2\sqrt{3}}\right)\cos\left(\frac{ak_y}{2}\right)$$

where $\tilde{H}$ is an approximated Hamiltonian matrix capturing the energy of electrons, focusing on the on-site energy, ε_{2p}, and hopping interactions between nearest-neighbor atoms. The hopping interactions are a function of the wavevector, $\mathbf{k}$, whose structure is given by $f(\mathbf{k})$. The parameter γ_0 is the hopping energy defining those interactions. For graphene, the value of γ_0, the hopping parameter, has been determined experimentally to be approximately 2.7 eV. [9]

Given that the energy eigenvalues are given by $\det[\tilde{H} - I\varepsilon] = 0$, the final energy bands are determined, as a function of wavevector, $\mathbf{k}$, and hopping parameter, γ_0:

$$\begin{aligned} \varepsilon(\mathbf{k}) &= \varepsilon_{2p} \pm \gamma_0 |f(\mathbf{k})|, \\ \varepsilon(k_x, k_y) &= \pm\gamma_0 \sqrt{1 + 4\cos^2\left(\frac{ak_y}{2}\right) + 4\cos\left(\frac{ak_y}{2}\right)\cos\left(\frac{a\sqrt{3}k_x}{2}\right)} \end{aligned} \tag{1.3}$$

where ε_{2p} can be defined as zero for convenience in choosing the reference energy with no effect on the electronic band structure. The wavevector, $\mathbf{k} = (k_x, k_y)$, is well-defined. $\varepsilon(\mathbf{k})$ is a dispersion relation, relating the energy of an electron to its momentum.

Immediately, one of the key properties of graphene, the electron-hole symmetry, is clear. For electrically neutral graphene, the negative energy band (valence band) will be fully occupied, and the positive energy band (conduction band) will be empty. Therefore, as the bands touch, at the $K_\pm$ points in the reciprocal space, the Fermi surface is comprised of these two discrete points. This can be confirmed by substitution of Eq. (1.1) in Eq. (1.3), to find the energy at the $K_\pm$ points is zero. Because the Fermi surface of graphene reduces to discrete points (zero-dimensional) at the Brillouin zone corners, graphene is classed as a zero-gap semiconductor (or semimetal). The other interesting relation to pop out of this description of graphene is a linear dispersion relation. By expanding Eq. (1.3) around the $K_\pm$ points, or Dirac points, it is seen that for small changes in crystal momentum, $\mathbf{k}$, around the Dirac

points, a linear dispersion is generated:

$$\varepsilon(\mathbf{k}) = \pm\hbar v_F|\mathbf{k} - \mathbf{K}_{\pm}|, \tag{1.4}$$

where terms can be consolidated into $v_F = \frac{\sqrt{3}\gamma_0 a}{2\hbar}$, the Fermi velocity, which has been experimentally measured, $v_F \approx (1.0 - 1.1) \times 10^6\,\mathrm{m\,s^{-1}}$. [10–12]

The dispersion relation (see Eq. (1.4)) implies a massless result that is analogous to the energy-momentum relation of photons or other massless particles in relativity, $E = pc$. This arises because the low-energy Hamiltonian around $K_{\pm}$ is mathematically equivalent to the 2D massless Dirac Hamiltonian. The linear dispersion gives an equivalence between the phase velocity and group velocity, and therefore, allows for the study of relativistic transport [13] of Dirac fermions in the vicinity of the Dirac points. However, electrons do have an effective mass that can be derived in different contexts. In condensed-matter systems, the concept of mass emerges from how carriers respond to external perturbations such as electric or magnetic fields. Consequently, different experimental contexts give rise to different definitions of an effective mass, each capturing a distinct physical aspect of carrier dynamics. In graphene transport theory, the most commonly used definition is the cyclotron mass.

1.1.2.2 Cyclotron Mass

In the presence of a magnetic field free electrons can be described classically, moving in cyclotron motion. The cyclotron angular frequency, ω_c, for a charge, q, with mass, m, moving in magnetic field, B, is given by $\omega_c = qB/m$. By relating the orbital period to the geometric properties of the band structure, the cyclotron effective mass is defined as [14, pp. 229–233]:

$$m_c(\varepsilon, k) = \frac{\hbar^2}{2\pi}\frac{\partial A(\varepsilon, k)}{\partial \varepsilon} \tag{1.5}$$

where A represents the area in reciprocal (momentum) space enclosed by the constant energy contour in the Brillouin zone, where $A = \pi k^2$ for graphene. Experimental observations have been in good accordance with the cyclotron mass. [10]

Rearrangement of Eq. (1.5) gives an equivalent form for the cyclotron mass in terms of the wavevector, k [15]:

$$m_c(\varepsilon, k) = \hbar^2 k \left(\frac{\partial \varepsilon}{\partial k}\right)^{-1} = \frac{p}{v_g} \tag{1.6}$$

which is simply the ratio of the crystal momentum, $p = \hbar k$, to the group velocity, $v_g = \frac{1}{\hbar}\frac{\partial \varepsilon}{\partial k}$.

By substitution of Eq. (1.4) in Eq. (1.6):

$$m_c(\varepsilon, k) = \frac{\hbar k_F}{v_F} = \frac{\varepsilon_F}{v_F^2}, \tag{1.7}$$

where, m_c is the cyclotron mass. ε_F, k_F, and v_F are the Fermi energy, Fermi wavevector, and Fermi velocity, respectively.

This is analogous to how an effective/relativistic mass of the photon may be defined when describing its momentum transfer in situations such as radiation pressure and also gravitational interactions. [16, p. 110]

1.1.2.3 Uniqueness of the Linear Dispersion vs Classical Parabolic Dispersion

Most semiconductors (including bilayer graphene), have approximately parabolic electronic band structures close to maxima and minima points. Parabolic band extrema are typically the rule, and monolayer graphene, due to its two equivalent sublattice symmetry, is an exception.

Near the band extrema, an effective mass approximation (derived from applying Newton's second law with the free electron model [4, pp. 218–219]) can be used describing charge carriers as simple free particles with effective mass, m^*, determined by the local curvature of the band structure:

$$m^* = \hbar^2 \left(\frac{\partial^2 \varepsilon}{\partial k^2} \right)^{-1}.$$

Note that such a definition of effective mass leads to an infinite effective mass for linear dispersion relations. That is to say, a force parallel to the velocity of a carrier does not change the carrier speed; the group velocity is fixed. This is why monolayer graphene carriers are often described as relativistic.

Applying the effective mass approximation leads to a Schrödinger-like equation incorporating the influence of the periodic lattice through m^*: [17, pp. 30–31]

$$\left[E_c + \frac{(i\hbar\nabla + e\mathbf{A})^2}{2m^*} + U(\mathbf{r}) \right] \psi(\mathbf{k}, \mathbf{r}) = E(\mathbf{k})\psi(\mathbf{k}, \mathbf{r}),$$
$$E(\mathbf{k}) = E_0 + \frac{\hbar^2 \mathbf{k}^2}{2m^*},$$

where, $E(\mathbf{k})$ is the energy of the band carrier at wavevector $\mathbf{k}$, E_c is the energy of the conduction band edge, $\psi(\mathbf{k}, \mathbf{r})$ is the wavefunction of the band carrier, e is the elementary charge, $\mathbf{A}$ is the vector potential, m^* is the effective mass of the band carrier, and $U(\mathbf{r})$ is the potential energy of the system.

The result is a parabolic dispersion relation, $E(\mathbf{k})$, for most semiconductor band structures, approximated at band extrema. In comparison, graphene's linear dispersion relation (see Eq. (1.4)) leads to a number of unique properties absent in materials with parabolic band structures.

1.1.2.4 Density of States and Fermi-Dirac Statistics in Graphene

To understand the distinct electronic properties of graphene, it is important to understand the distribution of electrons in the energy bands. Fermi-Dirac statistics [18, 19] describe the probability of occupancy of an energy state by an electron at a given temperature, T, and chemical potential, μ.

Graphene Density of States

The density of states (DOS), $g(\varepsilon)d\varepsilon$, defines the number of states per unit area in an energy window, $d\varepsilon$. [9, 20] It is a crucial concept in understanding the electronic properties of materials, as it determines how many electrons can become available for conduction within a given energy range.

Given the periodic lattice described in Section 1.1.2.1, the Bloch theorem requires:

$$\phi(x + L_x, y) = \phi(x, y), \quad \phi(x, y + L_y) = \phi(x, y),$$

where $\phi(x, y)$ is the Bloch wavefunction of an electron in graphene, depending on real-space coordinates x and y, defined over a two-dimensional sample of graphene of dimensions (L_x, L_y).

Imposing the periodic boundary conditions on the plane-wave part of the Bloch wave, $e^{i\mathbf{k}\cdot\mathbf{R}}$:

$$e^{i[k_x(x+L_x)+k_y y]} = e^{i[k_x x+k_y(y+L_y)]} = e^{i(k_x x+k_y y)},$$

requires that $e^{ik_x L_x} = e^{ik_y L_y} = 1$.

Since $e^{i\theta} = 1$ if, and only if, $\theta = 2\pi n$ with $n \in \mathbb{Z}$, the allowed wavevectors for the plane-wave under periodic boundary conditions are:

$$k_x = \frac{2\pi\, n_x}{L_x}, \quad k_y = \frac{2\pi\, n_y}{L_y}, \qquad n_x, n_y \in \mathbb{Z},$$

which yield a uniform $\mathbf{k}$-space grid with spacings $\Delta k_x = 2\pi/L_x$ and $\Delta k_y = 2\pi/L_y$.

In momentum-space, the area around each valid wavevector point (k_x, k_y) is given by $\Delta k_x \Delta k_y = (2\pi)^2/A$, where $A = L_x L_y$.

Given the linear dispersion around the Dirac point (see Eq. (1.4)) counting the total number of states, N(k), below energy ε is trivial. The k-space area at energy ε is

given by the circumference of a circle of radius $|\mathbf{k}|$, $2\pi|\mathbf{k}|$, where $\mathbf{k}$ is the wavevector. Therefore the total area up to $\mathbf{k}$ at energy ε is $\int_0^{\mathbf{k}} 2\pi|\mathbf{k}|dk = \pi|\mathbf{k}|^2$. The number of available k-space states in this disk, N(k), is the degeneracy, g (the number of actual electron states that share the same energy/k-point), multiplied by the total area, then divided by the area per k-point:

$$N(k) = g\frac{\pi k^2}{(2\pi)^2/A} = \frac{Ak^2}{\pi} \tag{1.8}$$

where $g = g_s g_v = 4$ is the total degeneracy in graphene, arising from two spin states ($g_s = 2$) and two inequivalent Dirac valleys at $K_\pm$ ($g_v = 2$).

Therefore, the density of states per unit area, from a 2D plane wave solution with total degeneracy of 4, assuming linear dispersion near the Dirac point under weak magnetic fields (no quantisation):

$$g(k) = \frac{1}{A}\frac{dN(k)}{dk} = \frac{2k}{\pi}$$

$$g(\varepsilon) = g(k)\frac{dk}{d\varepsilon} = \frac{g_s g_v k}{2\pi}\frac{dk}{d\varepsilon} = \frac{2|\varepsilon|}{\pi\hbar^2 v_F^2} \tag{1.9}$$

which defines the number of states per unit area in any energy window, $d\varepsilon$, as $g(\varepsilon)d\varepsilon$.

Graphene Carrier Density

At any given energy, the number of states per unit area is $g(\varepsilon)d\varepsilon$. The probability of those states being filled is given by the Fermi-Dirac distribution:

$$f(\varepsilon, \mu) = \frac{1}{e^{(\varepsilon-\mu)/k_B T} + 1} \tag{1.10}$$

where, ε is the energy of the state, μ is the chemical potential, k_B is the Boltzmann constant and T is the temperature in Kelvin.

Therefore, the total number of electrons per unit area between energy ε and $\varepsilon + d\varepsilon$, is given by the product of the occupation probability, $f(\varepsilon, \mu)$, and the number of states in the energy window, $g(\varepsilon)d\varepsilon$. Taking the integral across all energies gives us our total number of carriers per unit area, our carrier density:

$$n, p = \int_0^\infty f(\varepsilon, \pm\mu)g(\varepsilon)d\varepsilon = -\frac{2}{\pi}\left(\frac{k_B T}{\hbar v_F}\right)^2 \mathrm{Li}_2\left(-e^{\pm\mu/k_B T}\right) \tag{1.11}$$

where n is the electron density, p is the hole density as a reflection about the Dirac point, Li_2 is the second-order polylogarithm function, and $g(\varepsilon)$ is given by Eq. (1.9).

At the NP, the chemical potential, μ, is zero, therefore the carrier density simpli-

fies to:

$$n_{th} = \frac{\pi}{6}\left(\frac{k_B T}{\hbar v_F}\right)^2 \tag{1.12}$$

where n_{th} is the thermal carrier density at the NP, k_B is the Boltzmann constant, T is the temperature in Kelvin and $\hbar$ is the reduced Planck's constant. The factor of $\pi/6$ comes from the evaluation of the polylogarithm function, $\mathrm{Li}_2(-1) = -\pi^2/12$. So, despite the zero chemical potential, there is still finite carrier density when there is a finite temperature that broadens the occupation distribution. Room temperature thermal carrier density in graphene is approximately $n_{th} \approx 8 \times 10^{10}\,\mathrm{cm}^{-2}$.

Using Eq. (1.8), we can also deduce a useful relation between the carrier density and the Fermi wavevector. The carrier density at zero temperature is simply the number of available states per unit area, $n = N(k_F)/A$, where k_F is the Fermi wavevector. Therefore, rearranging Eq. (1.8) gives:

$$k_F = \sqrt{\pi n} \tag{1.13}$$

This relation is often used to translate Fermi energies into carrier densities via substitution of Eq. (1.13) into Eq. (1.4)

$$\varepsilon_F = \hbar v_F \sqrt{\pi n} \tag{1.14}$$

where, ε_F is the Fermi energy, v_F is the Fermi velocity and n is the carrier density. Eq. (1.14) is applicable at low temperatures and high carrier densities, $k_B T \ll \varepsilon_F$.

1.1.3 Excitation of Phonon Quasiparticles

Phonons are quasiparticles describing collective lattice vibrations and play a central role in charge-carrier scattering in crystalline solids. Their occupation vanishes as temperature approaches zero, while at finite temperatures phonon populations follow the Bose-Einstein distribution. In lattices with more than one atom per unit cell, such as graphene, phonon modes are classified as acoustic or optical depending on whether atomic motion is in-phase or out-of-phase, respectively. [4, 14, 21]

Acoustic phonons describe coherent in-phase motion of atoms and include longitudinal (LA), transverse in-plane (TA), and out-of-plane flexural (ZA) modes, with frequencies that tend to zero in the long-wavelength limit. Optical phonons arise from out-of-phase motion within the unit cell and therefore retain a finite frequency as the phonon momentum approaches zero, with $3N-3$ optical modes accompanying the three acoustic modes in a unit cell containing N atoms. [14, p. 442]

1.1.3.1 Phonon Interactions in Graphene

In graphene, there are six phonon modes: three acoustic (longitudinal LA, transverse TA, and out-of-plane ZA) and three optical (LO, TO, ZO), due to two atoms in the unit cell, as described above. Optical modes are of higher energy than acoustic modes, this is expected as optical modes require a squeezing and stretching of the atomic bonds, which in graphene are strong covalent σ-bonds in a rigid trigonal pattern.

In monolayer graphene, the LO/TO phonon energy is approximately 200 meV in the long-wavelength limit, and has a minimum energy at the K-point, approximately 160 meV. [22] These high-energy optical phonons may be ignored when the thermal energy is much less than the phonon energy, $k_B T \ll \hbar\omega$, which is true for temperatures much less than 2000 K, as the optical phonon population becomes essentially zero. In addition, an electron at the Fermi surface in graphene (for $n = 10^{12}\,\mathrm{cm}^{-2}$, $\varepsilon_F \approx 110\,\mathrm{meV}$) cannot spontaneously emit an optical phonon because it does not have enough excess energy to drop and still remain in the conduction band. Therefore, optical phonon scattering is ‘frozen out’ below room temperatures. It is only at elevated temperatures (and/or high carrier energies) that optical phonon processes become relevant. The ZO optical phonon branch has a minimum energy of approximately 70 meV at the K-point [22]. However, mirror-reflection symmetry about the atomic plane forbids linear electron-phonon coupling to out-of-plane ZO/ZA modes, resulting in strongly suppressed coupling to in-plane electronic states. [23] In realistic samples, however, ripples, strain, or substrate interactions partially break this symmetry and allow weak linear coupling. This means for many practical purposes, the acoustic LA/TA phonons dominate any electron-phonon interactions in graphene at low energies/temperatures.

At long wavelengths, LA and TA phonons have approximate linear dispersions that tend to zero energy. While TA phonons have a smaller velocity and, therefore, lower energy across a wider range of momenta, compared to LA, their coupling to electrons is weaker. As a result, LA phonon interactions dominate intrinsic electron-phonon scattering. [24]

For phonon energies much less than the electron Fermi energy, $\hbar\omega \ll \varepsilon_F$, consider there is a maximum phonon momentum, $2k_F$, that is able to back-scatter electrons at the Fermi surface (a circle of radius k_F) with an energy equal to a characteristic thermal energy, $k_B T_{BG}$. This limit, $k_B T_{BG} = 2k_F \hbar v_{ph}$, defines the Bloch-Grüneisen temperature, T_{BG}. At temperatures below T_{BG}, only phonons with momenta less than $2k_F$ are sufficiently populated to scatter electrons across the Fermi surface, leading to a strong suppression of electron-phonon scattering. The crossover temperature is approximated for acoustic phonons $T_{BG} \approx 54\sqrt{n}\,\mathrm{K}$, with density mea-

sured in unit of $10^{12}\,\mathrm{cm}^{-2}$ [24]. Therefore, for the typical carrier densities we work with, $n < 10^{12}\,\mathrm{cm}^{-2}$, T_{BG} is below 54 K. The scattering time between electrons and acoustic phonons in this regime is predicted, $\tau(T) \propto T^{-4}$. [25]

At temperatures above T_{BG}, the relevant acoustic phonons satisfy $k_B T \gg \hbar\omega$, and the phonon population is well described by the equipartition (classical) limit. In this regime, the Bose-Einstein distribution yields an approximate phonon occupation number $N_\omega \approx k_B T/\hbar\omega$ for $k_B T \gg \hbar\omega$. Consequently, the electron-phonon scattering rate exhibits a linear temperature dependence, with scattering time $\tau(T) \propto T^{-1}$ for $T > T_{BG}$ due to acoustic phonon scattering.

Using the model of Hwang and Das Sarma [24], one therefore obtains best-case values of $\tau \sim 4-6$ ps at 100 K, decreasing to $\sim 2-3$ ps at 200 K, and $\sim 1-2$ ps by 300 K for carrier densities near $n = 10^{12}\,\mathrm{cm}^{-2}$. These values represent the intrinsic acoustic-phonon scattering times, assuming negligible contributions from impurities and substrate phonons.

This suppression of phonon-mediated scattering as temperature decreases leads to a rapid increase in the electron-phonon scattering time and opens the possibility of other non-phonon scattering mechanisms to dominate transport. At lower temperatures, electron-electron scattering can become the dominant inelastic process; under suitable conditions this may lead to hydrodynamic transport, which we will discuss in Section 1.2.3.

In practice, extrinsic scattering mechanisms such as charged impurities, defects, and substrate phonons contribute to the overall scattering rate. Advances in fabrication techniques, particularly the use of hexagonal boron nitride (hBN) substrates and encapsulation, have enabled experimental access to the intrinsic phonon-limited transport regime in graphene. [26]

Hexagonal boron nitride (hBN) is an ideal substrate and encapsulating layer for graphene as it is: atomically flat, chemically inert, and closely lattice-matched to graphene, which eliminates roughness, minimises charged impurities, and reduces remote substrate phonon scattering compared to SiO_2. [26–28] Consequently, exfoliated graphene on hBN substrates shows measurably higher room temperature mobilities (e.g. $20\,\mathrm{m}^2\,\mathrm{V}^{-1}\,\mathrm{s}^{-1}$), an order of magnitude higher than on SiO_2. [29] This improvement has enabled the observation of viscous transport phenomena, including negative local resistance in hBN-encapsulated graphene. [30]

Conclusion on Graphene-Based Electronic Structures

Graphene's electronic properties originate from its hexagonal lattice symmetry and two-atom unit cell. The band structure, as approximated by the tight-binding model, exhibits a linear dispersion relation near the Dirac points. This relation

results in massless Dirac fermions characterised by a Fermi velocity of approximately $v_F \approx 1.05 \times 10^6\,\mathrm{m\,s^{-1}}$. The density of states and carrier density expressions are derived directly from the band structure.

Electron-phonon coupling gives rise to a temperature dependence of graphene's intrinsic resistivity. Specifically, acoustic phonons dominate the scattering rate, with their thermal population and associated scattering phase space decreasing at lower temperatures, thereby opening up the possibility for transport dominated by electron-electron scattering. Furthermore, the choice of substrate is critical, with hexagonal boron nitride (hBN) identified as an effective dielectric for achieving high carrier mobilities and transport that is intrinsic.

1.2 Transport Regimes in Graphene

Consider that interactions between quasiparticles can come in many forms, such as electron-electron, electron-hole, electron-phonon, and impurity scattering; each depending on the densities of particles, temperature of the system, and external fields. It is how these quasiparticles interact on the microscopic level that, when averaged out over a larger system, gives rise to macroscopic transport features.

On the macroscopic level, keeping only the main features applicable to this research, the transport of electrons and holes in graphene can be broken down into a few main temperature-dependent regimes. The phase diagram, in Figure 1.1, serves to illustrate these regimes.

This chapter will discuss the main features of each type of transport: the diffusive regime (Section 1.2.1) the hydrodynamic regime (Section 1.2.3) and the ballistic regime (see Section 1.2.2). We will also discuss two special cases that essentially interrupt the main transport properties very close to the Dirac point - electron-hole puddles, and Dirac plasma (see Section 1.2.5).

1.2.1 Transport of Quasiparticles in the Diffusive Limit

Charge carrier transport through metals and semiconductors at room temperature is well described as diffusive flow and, by using the Drude model, calculations for electrical properties can be made [31]. Diffusive flow refers to the movement of carriers through a material via a random sequence of scattering events, rather than travelling ballistically (without scattering) over long distances.

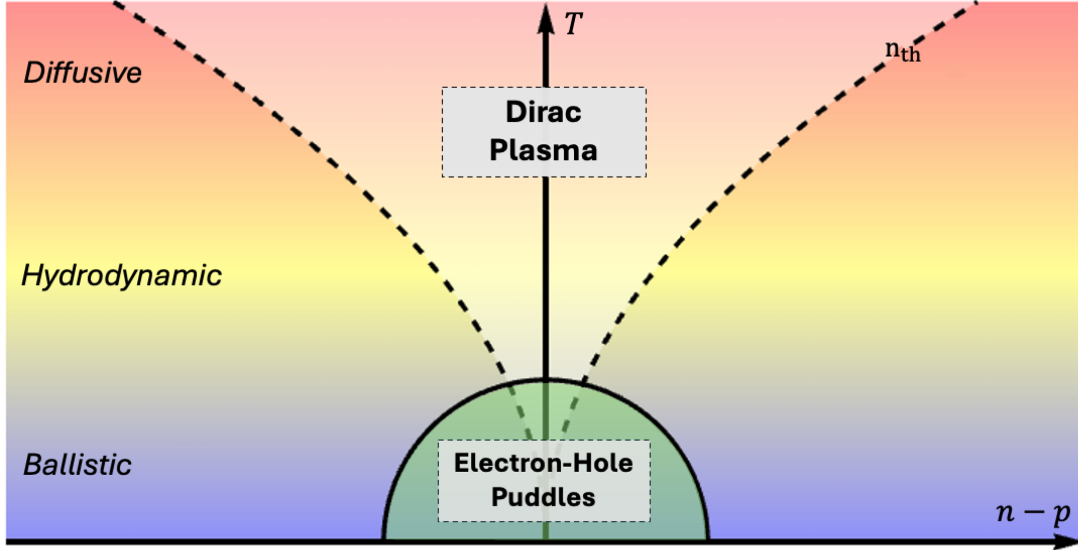

Figure 1.1: Phase diagram of transport regimes in graphene as a function of temperature, T, and net carrier density, $n-p$. The diagram illustrates the crossover between the ballistic, hydrodynamic, and diffusive regimes. Near the neutrality point special density-dependent cases appear: electron-hole puddles at low temperatures; and the Dirac plasma when $|n-p| < n_{th}$, where thermally excited carriers, n_{th}, dominate.

1.2.1.1 The Drude Model

The Drude model is a classical treatment of many independent charged particles whose movement is described by classical equations of motion with an extra frictional force to account for momentum loss due to scattering. The type of scattering is not distinguished in this simplified model; as long as the scattering mechanisms are isotropic, they can be attributed to collisions with impurities, crystal defects, and phonons. In Chapter 2, we will discuss an extension to the Drude model derived here that will include the anisotropic inter-carrier scattering.

In the Drude formulation, charged particles will experience forces in the presence of externally applied electric and magnetic fields, well-described by the Lorentz Force. The microscopic nature of the fields and interactions responsible for carrier dynamics is not treated explicitly in the Drude model. Instead, all such microscopic details are phenomenologically incorporated into a single parameter, the momentum relaxation time τ, which characterises the average rate at which carriers lose momentum due to scattering.

In steady state, the momentum gained from externally applied fields is balanced by the momentum loss due to scattering processes: [17, p. 23]

$$\left[\frac{d\mathbf{p}}{dt}\right]_{\text{field}} + \left[\frac{d\mathbf{p}}{dt}\right]_{\text{scatter}} = 0 \tag{1.15}$$

Using the momentum relaxation-time approximation we obtain:

$$q(\mathbf{E} + \mathbf{v}_d \times \mathbf{B}) - \frac{m\mathbf{v}_d}{\tau} = 0, \tag{1.16}$$

where, m, q, $\mathbf{v}_d$, τ are the carrier mass, charge, drift velocity, and momentum relaxation time, respectively. Here, $\mathbf{E}$ and $\mathbf{B}$ denote the externally applied electric and magnetic fields.

The momentum relaxation time is a phenomenological parameter calculated from observed behaviour. In the Drude model, it can be described as the time over which a carrier will lose the momentum gained from the external field due to scattering (see Eq. (1.15)). Therefore, the average distance travelled between collisions is given by the mean free path length, $l = \nu\tau$, where ν is the group velocity of the quasiparticle (not the drift velocity). Drift velocity, a macroscopic parameter, is the net averaged velocity of an ensemble of carriers, in the presence of externally applied fields, after all collisions are considered. Therefore, drift velocity directly links to current. The relationship between the drift velocity and the applied field is described by the mobility, $\mu_{e,h}$ (note in macroscopic transport context μ is mobility, not chemical potential and the subscripts e and h are included to differentiate between electron and hole mobility), as such Eq. (1.16) under zero magnetic field reduces to

$$\mathbf{v}_d = \mu_{e,h}\mathbf{E}, \tag{1.17}$$

where, the carrier mobility, $\mu_{e,h}$, of a material can be considered as the effectiveness of an applied field, $\mathbf{E}$, at 'pushing' the carriers through the material at a given drift velocity, $\mathbf{v}_d$. The Drude model fundamentally defines $\mu_{e,h} = q\tau/m$ that links the macroscopic drift velocity to the microscopic scattering time τ and mass m.

From Ohm's law:

$$\mathbf{j} = \boldsymbol{\sigma}\mathbf{E},$$

the current density, $\mathbf{j}$, due to an electric field, $\mathbf{E}$, is directly dependent on the conductivity tensor, $\boldsymbol{\sigma}$, of the material. As we have seen, conductivity of a material comes down to microscopic scattering mechanisms. The current density is also the product of the carrier density, N, the carrier charge, q, and the drift velocity of the charges:

$$\mathbf{j} = Nq\mathbf{v}_d.$$

Using these relations with Eq. (1.17), and assuming zero magnetic field finds that:

$$\sigma = \frac{Nq^2\tau}{m}, \tag{1.18}$$

This result from the Drude model reveals that a material's ability to conduct depends

fundamentally on how many carriers are available, how easily they move, and how often they scatter. And it has had wide success in predicting electronic properties in many applications. [32]

1.2.1.2 Validity and Limitations of the Drude Model

The Drude model arises from simple assumptions made about a more complex microscopic system. Alternative models that take a more systematic approach to the problem have also been suggested, particularly the 'semiclassical distribution function in the relaxation-time approximation' (RTA). The linearised Boltzmann solution in the RTA can be found in Ref. [14, pp. 319–320].

This model arises from a generic description of conduction that describes how a nonequilibrium distribution function, $g_n(\mathbf{r}, \mathbf{k}, t)$, giving the occupation probability of semiclassical states, evolves in time. g_n is derived for each electronic band, indexed n, through these assumptions:

1. Electronic motion that occurs between collisions is described by semiclassical equations of motion:
$$\mathbf{v}_n(\mathbf{k}) = \frac{1}{\hbar}\nabla_{\mathbf{k}}\varepsilon_n(\mathbf{k}),$$
$$\hbar\dot{\mathbf{k}} = -e\left[\mathbf{E}(\mathbf{r}, t) + \mathbf{v}_n(\mathbf{k}) \times \mathbf{B}(\mathbf{r}, \mathbf{t})\right].$$
where $\mathbf{r}$ is the real-space position of the electron wavepacket, $\mathbf{k}$ is the crystal momentum, t is time, n is the electronic band index, $\varepsilon_n(\mathbf{k})$ is the energy dispersion of band n, $\mathbf{v}_n(\mathbf{k})$ is the group velocity in band n, $\mathbf{E}(\mathbf{r}, t)$ and $\mathbf{B}(\mathbf{r}, t)$ are the externally applied electric and magnetic fields.

2. Electrons experience collisions in interval dt with probability $dt/\tau_n(\mathbf{r}, \mathbf{k})$, where τ represents the collision time as it depends on band index, position, and wavevector of the electron.

3. The distribution of charges emerging from collisions does not depend on the structure of $g_n(\mathbf{r}, \mathbf{k}, t)$ prior to the collision. This assumption breaks down for momentum-conserving electron-electron collisions and anisotropic scattering.

4. Electrons in a region about $\mathbf{r}$ have the equilibrium distribution as described by the Fermi function at temperature $T(\mathbf{r})$.

Because of the generic nature of the assumptions, the Boltzmann transport equation can offer insight into many situations where these assumptions are true. Such situations where this description will become invalid include: field quantisation of the electronic states, strong carrier-carrier coupling, and non-fermion carriers.

Some extra assumptions can be made in specific cases to simplify the definition of conduction. In the application of the Drude model in this instance, the Drude conductivity (see Eq. (1.18)) can be obtained from the semiclassical distribution function given the following assumptions:

1. The scattering time parameter, τ, depends only on the energy, ε.
2. The temperature of the system is uniform and much less than the Fermi temperature. So as to assume $T = 0$ ($\varepsilon_F \gg k_B T$).
3. The band is isotropic near the Fermi surface, with $\mathbf{v} = \mathbf{v}(\varepsilon)$ and $\tau = \tau(\varepsilon)$; the Drude form then holds using the appropriate Fermi surface effective mass.

In the case of back-gate doped graphene at energies $\varepsilon_F \gg k_B T$, such that flow is well described by a single-carrier transport, and scattering mechanisms are isotropic and momentum-relaxing, these above assumptions are satisfied, and the Drude model provides a valid description.

It is expected that collisions that conserve total momentum cannot be captured by this simple RTA that assumes a single τ for momentum relaxation. Therefore, in regimes where electron-electron and electron-hole scattering dominate, such as the hydrodynamic and electron-drag regimes discussed in the two major experimental chapters of this thesis, Chapter 2 and 3, the Drude model may break down.

1.2.1.3 Single-Carrier Transport Using Drude Model in Magnetic Field

The Drude model can be extended to include external magnetic fields by including the Lorentz force, $\mathbf{F} = q\left[\mathbf{E} + \mathbf{v}_d \times \mathbf{B}\right]$, where an electric field, $\mathbf{E}$, and a perpendicular magnetic field, $\mathbf{B} = (0, 0, B)$, are applied to a 2D material.

In this case, a conductivity tensor is produced as a magnetic field makes the system's response anisotropic. To derive this conductivity tensor, the current density that flows due to one carrier type is calculated [33, pp. 19–21]:

$$\mathbf{j} = qN\mathbf{v}_d = |q|N\mu_{e,h}\left[\mathbf{E} + \mathbf{v}_d \times \mathbf{B}\right],$$

$$
\begin{aligned}
\mathbf{j} &= |q|N\mu_{e,h}\left[\mathbf{E} + \frac{B}{qN}\begin{pmatrix} j_y \\ -j_x \end{pmatrix}\right], \\
\mathbf{j} - \left[\mu_{e,h}B\frac{|q|}{q}\begin{pmatrix} j_y \\ -j_x \end{pmatrix}\right] &= |q|N\mu_{e,h}\mathbf{E}, \\
\begin{bmatrix} 1 & -\mu_{e,h}B\frac{|q|}{q} \\ \mu_{e,h}B\frac{|q|}{q} & 1 \end{bmatrix}\mathbf{j} &= |q|N\mu_{e,h}\mathbf{E}, \\
\mathbf{j} = \frac{|q|N\mu_{e,h}}{1+\mu_{e,h}^2B^2}\begin{bmatrix} 1 & \mu_{e,h}B\frac{|q|}{q} \\ -\mu_{e,h}B\frac{|q|}{q} & 1 \end{bmatrix}&\mathbf{E},
\end{aligned}
\tag{1.19}
$$

where, the current density, $\mathbf{j}$, of the collection of carriers of charge, q, and density, N, is induced by electric field, $\mathbf{E}$ and perpendicular magnetic field, B, in a material that has carrier mobility, $\mu_{e,h}$.

From the relation of Ohm's law, $\mathbf{j} = \boldsymbol{\sigma}\mathbf{E}$, the conductivity of a material can be determined from Eq. (1.19) and reduces to Eq. (1.18) when $B = 0$:

$$
\boldsymbol{\sigma} = \begin{bmatrix} \sigma_{xx} & \sigma_{xy} \\ -\sigma_{xy} & \sigma_{xx} \end{bmatrix} = \frac{|q|N\mu_{e,h}}{1+\mu_{e,h}^2B^2}\begin{bmatrix} 1 & \mu_{e,h}B\frac{|q|}{q} \\ -\mu_{e,h}B\frac{|q|}{q} & 1 \end{bmatrix} \tag{1.20}
$$

The substitution $\beta = \mu_{e,h}B$ is often used, where β is also the ratio between the longitudinal and transverse components. Experimentally, the resistance of a device is measured rather than the conductivity; importantly, therefore, the inverse of the conductivity tensor is thus:

$$
\boldsymbol{\rho} = \begin{bmatrix} \rho_{xx} & \rho_{xy} \\ -\rho_{xy} & \rho_{xx} \end{bmatrix} = \frac{1}{\sigma_{xx}^2+\sigma_{xy}^2}\begin{bmatrix} \sigma_{xx} & -\sigma_{xy} \\ \sigma_{xy} & \sigma_{xx} \end{bmatrix} = \frac{1}{|q|N\mu_{e,h}}\begin{bmatrix} 1 & -\mu_{e,h}B\frac{|q|}{q} \\ \mu_{e,h}B\frac{|q|}{q} & 1 \end{bmatrix} \tag{1.21}
$$

In this single-carrier Drude model, it can be seen from Eq. (1.21) that the longitudinal resistance, ρ_{xx}, is independent of the applied magnetic field (no magnetoresistance).

The single-carrier Drude model resistivity notably diverges as the carrier density tends to zero, $N \to 0$. In reality, for monolayer graphene at finite temperatures, thermal broadening of the Fermi distribution (see Eq. (1.11)) gives a transition region at the neutrality point where both electrons and holes are present in significant numbers.

Therefore, a two-carrier model is required to accurately describe transport in this regime.

1.2.1.4 Two-Carrier Transport Using Drude Model in Magnetic Field

The total conductivity of the material, assuming there is no interaction between carrier types, is the sum of the conductivities resulting from each carrier type present. In this case, we have two carrier types: electrons of charge, $-e$, carrier density, n, and mobility, μ_e, and holes of charge, e, carrier density, p, and mobility, μ_h. Both carrier types see the same externally applied fields.

The total conductivity, $\boldsymbol{\sigma} = \boldsymbol{\sigma_e} + \boldsymbol{\sigma_h}$, is thus from Eq. (1.20):

$$\boldsymbol{\sigma} = \frac{en\mu_e}{1+\mu_e^2 B^2}\begin{bmatrix} 1 & -\mu_e B \\ \mu_e B & 1 \end{bmatrix} + \frac{ep\mu_h}{1+\mu_h^2 B^2}\begin{bmatrix} 1 & \mu_h B \\ -\mu_h B & 1 \end{bmatrix},$$

$$\sigma_{xx} = e\left(\frac{n\mu_e}{1+\mu_e^2 B^2} + \frac{p\mu_h}{1+\mu_h^2 B^2}\right),$$
$$\sigma_{xy} = -Be\left(\frac{n\mu_e^2}{1+\mu_e^2 B^2} - \frac{p\mu_h^2}{1+\mu_h^2 B^2}\right).$$

The total resistivity of the material is calculated by taking the inverse of this conductivity tensor: [34] [14, p. 240]

$$\begin{aligned} \rho_{xx} &= \frac{1}{e}\frac{(n\mu_e + p\mu_h) + \mu_e\mu_h B^2 (n\mu_h + p\mu_e)}{(n\mu_e + p\mu_h)^2 + \mu_e^2\mu_h^2 B^2 (n-p)^2}, \\ \rho_{xy} &= \frac{B}{e}\frac{(n\mu_e^2 - p\mu_h^2) + \mu_e^2\mu_h^2 B^2 (n-p)}{(n\mu_e + p\mu_h)^2 + \mu_e^2\mu_h^2 B^2 (n-p)^2}, \end{aligned} \tag{1.22}$$

where, the total resistivity tensor, $\boldsymbol{\rho}$, is composed of longitudinal resistivity, ρ_{xx}, and transverse (Hall) resistivity, ρ_{xy}.

The resulting terms, longitudinal resistance and Hall resistance, are important parameters in device characterisation. This relation is used to determine, experimentally in Hall measurements, the carrier density and mobility in a device which give indications of the microscopic physics. To do so, a Hall-bar device is used to conduct four-probe measurements to determine the longitudinal and transverse resistances. Methodology can be found in Section 1.4. As with the single-carrier Drude model (see Eq. (1.21)) the two-carrier model (Eq. (1.22)) assumes simple isotropic scattering mechanisms and does not take into account any inter-carrier scattering between the two carrier systems.

Small magnetic field approximation

In many circumstances, it is appropriate to consider limiting cases that constrain the parameters and make calculations simpler. For example, it can be shown that

by taking a small B approximation, the resistivity tensor can be reduced:

$$\begin{aligned}\rho_{xx} &= \frac{1}{e\left(n\mu_e + p\mu_h\right)},\\ \rho_{xy} &= \frac{B}{e}\frac{\left(n\mu_e^2 - p\mu_h^2\right)}{\left(n\mu_e + p\mu_h\right)^2}.\end{aligned} \tag{1.23}$$

In uncompensated systems, that is $n \neq p$, such as graphene when $\varepsilon_F \gg k_B T$, one carrier will be dominant, $n \gg p$. Under this limit, while also considering that the different carrier mobilities are similar, Eq. (1.22) reduces to the single-carrier Drude model result that can be derived from Eq. (1.21).

We can simplify this model (see Eq. (1.23)) by assuming that in the vicinity of the NP, the mobility of electrons and holes will be approximately the same, $\mu_e \approx \mu_h$:

$$\begin{aligned}\rho_{xx} &= \frac{1}{e\mu_{e,h}\left(n + p\right)},\\ \rho_{xy} &= \frac{B}{e}\frac{\left(n - p\right)}{\left(n + p\right)^2}.\end{aligned} \tag{1.24}$$

Given the success in creating high-quality graphene heterostructures, where the effects of impurities are reduced and inhomogeneity is low, the assumption that electrons and holes have approximately equal mobility near the Dirac point could be reasonably justified, given the symmetry of the two systems.

Further Simplifications

It is also valid to consider the result for compensated systems, $n = p$. Such as investigations of magnetoresistance in Bismuth [35], graphite [36], and graphene at the neutrality point (NP). Similar compensation-driven transport phenomena have also been widely studied in other semimetals, including Weyl and Dirac systems such as NbP [37] and WTe_2 [38], where near-perfect electron-hole compensation gives rise to large magnetoresistance and unconventional Hall responses.

The validity of the Drude model in this compensated regime is questionable, as discussed previously, due to not including inter-carrier interactions. However, in the realms of the Drude model, this assumption, $n = p$, is a valid analytical step:

$$\begin{aligned}\rho_{xx} &= \frac{1}{en}\left(\frac{1 + \mu_e\mu_h B^2}{\mu_e + \mu_h}\right),\\ \rho_{xy} &= \frac{B}{en}\left(\frac{\mu_e - \mu_h}{\mu_e + \mu_h}\right).\end{aligned} \tag{1.25}$$

There is a testable prediction that, at the neutrality point, a non-zero Hall resistance may be observed if the mobilities of electrons and holes are not the same, $\mu_e \neq \mu_h$.

Finally, adding the case when the mobilities of electrons and holes are the same, $\mu_e = \mu_h = \mu_{e,h}$, it can be found that Eq. (1.25) simplifies to the scalar form:

$$\begin{aligned} \rho_{xx}(B) &= \rho_{xx}(0)(1 + \mu_{e,h}^2 B^2), \\ \rho_{xx}(0) &= \sigma_0^{-1} = (2en\mu_{e,h})^{-1}, \end{aligned} \tag{1.26}$$

It's evident that at the neutrality point the Hall resistance goes to zero and the magnetoresistance contribution in longitudinal resistance, $\Delta = \mu_{e,h}^2 B^2$, can be determined through experiment. [39, 40]

1.2.1.5 Scattering Mechanisms and Mean Free Path

In the diffusive regime, the mean free path can be estimated from experimentally measured results of carrier density and mobility using the Drude model to define τ. By recalling the previously stated relations from the single-carrier Drude model, the mean free path length is thus:

$$l = v_g \tau = \frac{v_g m \mu_{e,h}}{q},$$

where, v_g is the group velocity of the carrier, m is the effective mass, $\mu_{e,h}$ is the mobility and q is the carrier charge.

In graphene, assuming a single-carrier system of massless Fermi-Dirac quasiparticles, the effective mass is equal to the cyclotron mass, and the density-dependent mean free path length is:

$$l = v_F \tau = \frac{\mu_{e,h} \hbar \sqrt{n\pi}}{e},$$

where, v_F is the Fermi velocity, n is the carrier density, $\mu_{e,h}$ is the carrier mobility.

The diffusion model, therefore, describes that under fixed density, the mean free path length is proportional to the carrier mobility, $l \propto \mu_{e,h}$. As evidenced in Section 1.1.3, the mobility of carriers in graphene increases as the temperature decreases, due to the reduction in phonon scattering.

As the temperature decreases, l can become comparable or larger than the characteristic size of the device, $l \gtrsim L$. At this point, scattering events are dominated by edge scattering, not the disorder scattering mechanisms that lead to diffusive flow. The system is in the ballistic regime, and we must look past the diffusive model to describe different phenomena that occur.

1.2.2 Quantum Transport of Quasiparticles in the Ballistic Limit

Ballistic transport in graphene occurs when charge carriers move across a device without scattering from impurities, phonons, or notably, other carriers. In this regime, conductance is no longer governed by diffusive flow in the bulk but by other interactions, quantum transmission, boundary, and contact scattering. Therefore, conductance will not grow indefinitely as the disorder/phonon scattering decreases; after all, one might have a naïve expectation that a conductor with no bulk scattering would have zero resistance.

If the carriers' kinetic energy is much larger than the potential energy variation across the device, then without scattering events, their motion is approximately along straight trajectories through the device. This is very different from following the local electric field lines, as would be the case in diffusive flow.

Development of ultra-clean graphene devices, particularly hBN-encapsulated and suspended graphene devices, has enabled electronic mean free paths exceeding 1 μm at room temperature. This has allowed ballistic transport to be observed at high temperatures, including phenomena such as negative four-probe resistance up to 250 K. [41]

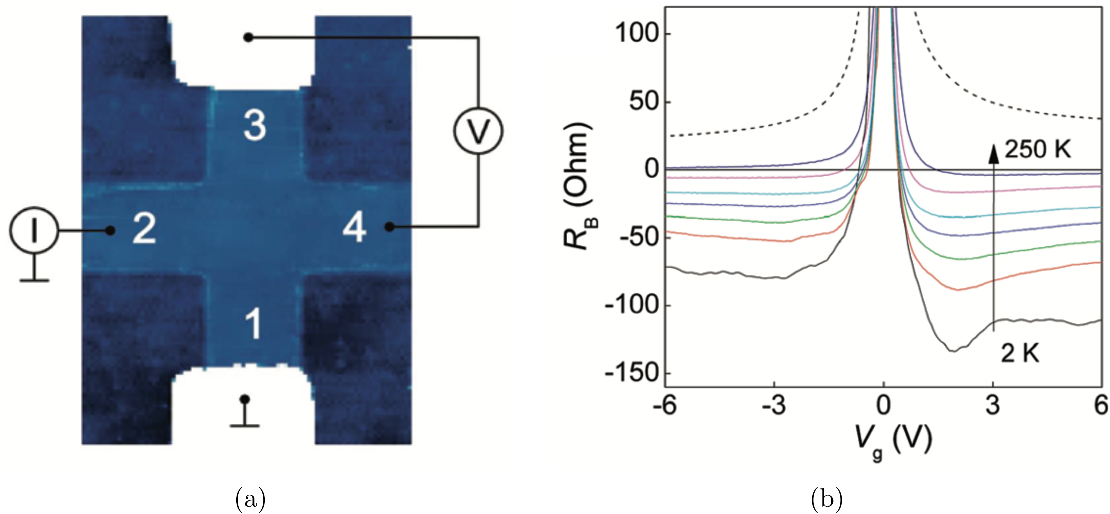

(a) (b)

Figure 1.2: **(a)** AFM image of encapsulated graphene cross. Current is driven between contacts 2 and 1, and the potential is measured between contacts 3 and 4. **(b)** Bend resistance, R_B, as a function of gate voltage at various temperatures. The curves from bottom to top correspond to 2, 50, 80, 110, 140, 200, and 250 K, respectively. Figures reused from Ref. [41] with permission (Copyright © American Chemical Society).

Negative resistance can be both a signature of ballistic and hydrodynamic transport (see Section 1.2.3 for hydrodynamic description). However, in bend geometries,

in which the graphene is patterned into a cross shape where current and voltage probes are directly opposite each other, the effect of the ballistic transport is more pronounced. Using the measurement configuration shown in Figure 1.2(a), bend resistance is defined as the potential difference between contacts 3 and 4 divided by the applied current, $R_B = (\phi_3 - \phi_4)/I$.

Under normal diffusive transport, the bend resistance measured is positive, as the potential distribution is governed by Poisson's equation (via Ohm's law). However, even at 250 K, high-quality graphene shows a negative bend resistance (see Figure 1.2(b)). As the temperature decreases and the mean free path exceeds the device width, a significant fraction of carriers travel directly into the opposite contact rather than diffusing into the adjacent arm. As a result, the transport in this regime is governed by the Landauer-Büttiker formalism [42]: ballistic transmission into the opposite arm increases the carrier flux into the voltage probe, which must adjust its electrochemical potential to satisfy $I_{\text{probe}} = 0$, leading to a sign reversal of the measured bend resistance.

With sufficiently long mean free paths, other ballistic phenomena can be observed, such as transverse magnetic focusing. [43, 44] In this experiment, a weak perpendicular magnetic field causes charge carriers to follow curved trajectories (cyclotron motion) due to the Lorentz force. The current is injected from one contact, and the voltage is measured at a contact located at a known distance across the device. Peaks in the measured voltage occur when the magnetic field curves the path of the carriers to reach the potential contact directly or after a small number of reflections from the device edges. The periodicity and amplitude of these oscillations provide information about the carrier's mean free path, mobility, and the quality of the graphene sample.

In high-quality graphene devices, the transition from diffusive flow to ballistic transport is increasingly dependent on device geometry rather than on impurity and disorder. Devices studied in this thesis are wide enough such that $l \gtrsim L$ is not satisfied at temperatures above 150 K. So, does transport remain diffusive?

When the mean free path due to disorder or phonon scattering is long but still smaller than the device dimensions, collective behavior arising from electron-electron scattering can emerge if the electron-electron mean free path is shorter than the device size. This marks a different transport regime, the hydrodynamic regime, discussed in the next section.

1.2.3 Electronic Transport in the Hydrodynamic Window

While diffusive and ballistic transport can be understood within relatively simple single-particle models, and align well with many experimental observations, they cannot explain all observed behaviours. Such models ignore inter-carrier scattering and, therefore, any collective behaviour that may arise.

The convergence of a broad range of theoretical and experimental techniques and ideas over the last decade has led to rapid advancements in the studies of hydrodynamic electron transport in graphene. [30, 45–53] Hydrodynamics, and the wider field of fluid mechanics, provides a unifying framework for describing a wide range of physical systems, including those that appear solid, such as glaciers [54]. Mathematically speaking, the description of fluid flow can be written down in just a few lines; however, its implications across a wide range of physical systems have motivated an extensive and ongoing body of research aimed at fully understanding fluid behaviour. Whether it is the study of fluid flow inside distant stars [55], the atmosphere that surrounds us [56], or even a glacier in Antarctica, all are described by fluid mechanics. In the following, we consider how this macroscopic language of many-body systems applies to electron transport in graphene.

In graphene, phonon scattering is relatively weak, and disorder scattering can be low in high-quality hBN encapsulated devices. This means that at moderate temperatures, the mean free path due to impurity and phonon scattering is longer than the electron-electron mean free path, but still short enough to avoid the ballistic regime:

$$l_{ee} \ll L \ll l.$$

where, l_{ee} is the electron-electron mean free path, l is the mean free path due to impurity and phonon scattering, and L is the characteristic device size.

This allows the probing of a transport regime where the dominant scattering process is electron-electron scattering, the hydrodynamic regime.

Graphene is not the only material where the equality above can be satisfied; hydrodynamic transport has been observed in a growing number of ultra-clean materials. Early evidence for electronic hydrodynamics came from high-mobility GaAs/AlGaAs two-dimensional electron gases, where transport through narrow channels exhibited Gurzhi-type behavior. A non-monotonic resistivity dependence on electron temperature, tuned by current heating, signaled a crossover from Knudsen transport to Poiseuille-like viscous flow dominated by momentum-conserving electron-electron scattering. [57] Strong hydrodynamic behavior was later demonstrated in ultrapure $PdCoO_2$, where electrical resistance in micron-scale channels depends sensitively on channel width. This size dependence was attributed to

viscous electron flow, allowing the extraction of an electronic viscosity comparable to that of classical fluids. [58] Hydrodynamic electron flow has also been reported in the semimetals WP_2 and WTe_2, enabled by unusually long momentum-relaxation lengths. In WP_2, viscous transport is inferred from size-dependent resistivity and a pronounced low-temperature violation of the Wiedemann-Franz law. [59] In WTe_2, real-space current imaging reveals Poiseuille-like flow with a non-monotonic temperature dependence, with momentum conservation attributed primarily to phonon-mediated interactions. [60] Further, scanning SQUID-on-tip magnetometry of patterned WTe_2 devices has enabled reconstruction of current distributions revealing geometry dependence consistent with hydrodynamic models. [61] Beyond electronic systems, analogous hydrodynamic behavior occurs in phonon transport when momentum-conserving phonon-phonon scattering dominates, enabling collective heat flow. Direct evidence for phonon hydrodynamics comes from observations of second sound, the wave-like propagation of temperature. This phenomenon was first observed at cryogenic temperatures in ultrapure NaF [62] and bismuth [63] using heat-pulse techniques, and more recently in graphite above 100 K via time-resolved transient thermal grating measurements. [64]

The hydrodynamic regime occurs precisely when the collective nature of the many-body dynamics becomes most pronounced. The fluid flow in graphene can be categorised into two groups: a Dirac fluid and a Fermi fluid. When the chemical potential is much less than the thermal energy, such as near the Dirac point, the charged liquid is known as a Dirac Fluid. The charge carriers undergo rapid collisions and behave like a relativistic plasma. [49] In the Dirac fluid, both electron and hole interactions dominate the description of the system; however, away from the Dirac point the fluid can be described as a two-dimensional Fermi fluid consisting of either electrons or holes. [51]

Due to the complexity of hydrodynamic transport in the Dirac fluid, it is much simpler to work in the Fermi regime, where the fluid is more predictable. As mentioned in Sections 1.1.3 and 1.2.1, phonon scattering in graphene rises proportionally with the temperature up until about 250 K, where higher-order phonons start to play a role. Whereas, in the Fermi liquid regime, the scattering rate for carrier-carrier interactions goes with the temperature squared. This means for a temperature range between 150 K and 250 K, the scattering is dominated by carrier-carrier interactions allowing for hydrodynamics.

How do we define Fermi-fluid flow? We need to consider the following forces: electrostatic, shear force, and momentum-relaxing scattering. The Navier-Stokes equation readily supports the first two forces: the external force producing the flow and the shear viscosity as the force between planes of flow. Assuming the linearised approximation, from other works from Tomadin and Polini [65], the simplest thing to

do is to modify the Navier-Stokes to not assume momentum as an exactly conserved quantity. Therefore, a frictional force, $\mathbf{J}/\tau$, is added. This dissipates the fluid-element momentum by a phenomenological transport time, τ, that also simplifies to Ohm's law at zero viscosity. With the addition of the continuity equation, assuming incompressible flow in the linear approximation, then the hydrodynamic equations are:

$$\nabla \cdot \mathbf{J}(\mathbf{r}) = 0, \tag{1.27}$$

$$\frac{ne}{m}\nabla\phi(\mathbf{r}) + \nu\nabla^2\mathbf{J}(\mathbf{r}) = \frac{\mathbf{J}(\mathbf{r})}{\tau}, \tag{1.28}$$

where, $\mathbf{J}(\mathbf{r}) = en\mathbf{v}(\mathbf{r})$ is the linearised current density as a function of the fluid element velocity, $\phi(\mathbf{r})$ is the electrostatic potential as a function of position, n is the carrier density, e is the elementary charge, ν is the kinematic viscosity, τ is a phenomenological transport time describing momentum-relaxing collisions and m is the effective carrier mass given by the 2D massless Dirac fermion cyclotron mass, $m_c = \frac{\hbar k_F}{v_F}$, for monolayer graphene.

1.2.4 Potential Applications for Hydrodynamic Electronic Devices

Hydrodynamic electron transport is not only a striking many-body phenomenon; it may also be useful. The key practical difference between hydrodynamic and single-particle transport is that, in the hydrodynamic window, the electronic system supports viscous and non-linear responses that are either absent or much weaker in conventional diffusive/ballistic devices. Below is outlined several ways where these collective effects may drive practical application.

Plasma-Wave Electronics

A central idea in two-dimensional electronics is that the density of a gated 2DEG is controlled by electrostatic coupling to the gate. Under hydrodynamic conditions, small disturbances in this density may not just relax locally; they propagate along the channel as plasma waves, meaning collective oscillations of the electron density and electric potential (analogous to ripples on a fluid surface). Dyakonov and Shur showed that, with suitable asymmetric source-drain boundary conditions, a field-effect transistor (FET) carrying DC current can support plasma waves that gain energy upon reflecting inside device cavities. This feedback can drive self-sustained oscillations in the terahertz (THz) range, enabling tunable emission of far-infrared/THz radiation. [66] Importantly, the frequency produced by this 'elec-

tronic flute' can be tuned electrostatically via the gate voltage. Moreover, because the oscillation is carried by confined plasma waves in the channel, the resonant cavity is set by the device length and can be much smaller than the corresponding free-space wavelength (unlike conventional electromagnetic resonators and antennas, which typically need dimensions comparable to the wavelength they produce). This makes it natural to consider arrays of such 'electronic flutes' for power combining. [67]

The same hydrodynamic non-linearity that underlies plasma-wave generation may also enable rectification of incident AC/THz signal into a DC voltage. An incident THz field drives plasma oscillations in the channel, and the non-linear terms generate a DC drain-to-source voltage. Beyond direct detection, the same framework enables mixing (with a local oscillator) and frequency multiplication (harmonic generation), including explicit designs for multipliers such as a frequency doubler. [68]

Hydrodynamic Suppression of Contact Resistance

Even a perfectly clean (ballistic) two-terminal device has a finite resistance because only a finite number of transverse quantum modes can carry current; this is the Landauer-Sharvin resistance, which scales mainly with the inverse constriction width. [69] In devices where the available number of modes changes gradually with position (for example, in smooth expansions or in a Corbino disk), the same Landauer-Sharvin contribution can appear as a bulk voltage drop rather than being localised only at the contacts. [69, 70] In the hydrodynamic window, frequent electron-electron collisions continually reshuffle electrons between modes, so electrons that would be reflected when a mode terminates can instead scatter into transmitting modes, suppressing the Landauer-Sharvin drop. For certain smooth expanding geometries, this leads to unusual scaling: at fixed minimal width, theory predicts a hydrodynamic contribution that can scale like $R_{\text{hydro}} \propto \ell_{ee}/(LW)$, so increasing the device length can reduce the total resistance. [69] Consistent with this picture, imaging experiments in high-mobility graphene Corbino devices observe a bulk-distributed Landauer-Sharvin resistance in the ballistic regime and its elimination in the hydrodynamic regime. [70] These ideas motivate using geometry to optimise resistance when electron-electron scattering dominates.

Overall, applications share a common theme: hydrodynamics enriches electronics by introducing collective modes with new parameters and strong geometry dependence. The main practical challenges are to sustain the hierarchy $l_{ee} \ll L \ll l$ under device-relevant conditions and to design geometries/contacts that convert hydrodynamic effects into useful reproducible electrical signals.

1.2.5 Coulomb Drag and Charge Puddles

Coulomb drag is a phenomenon where momentum is transferred between charged carriers due to Coulomb interactions. This phenomenon has been traditionally studied in double-layer structures with a finite separation between layers. This has been investigated in graphene, where layers are separated by a thin layer of hBN [71] and in GaAs double quantum well structures. [72] In our high-quality monolayer graphene, we have a much more extreme case, we have a single-layer system that has zero separation between two oppositely charged systems of particles - electrons and holes (a Dirac plasma). Therefore, in our case, the effect of Coulomb drag becomes particularly pronounced due to the unique properties of its strongly interacting Dirac plasma and weak scattering by phonons over a wide temperature range. The tunability of graphene's carrier density through electrostatic gating allows for the exploration of this region closely, where the electron and hole populations are comparable, leading to significant electron-hole drag effects around the neutrality point.

Another consequence of having a small Fermi energy is the existence of charge puddles at neutrality. Puddles are the result of impurities causing spatial fluctuations in the chemical potential. In general, these fluctuations are much smaller than the Fermi energy and will not affect the carrier density much; however, near the neutrality point, even small potential fluctuations can locally shift the chemical potential above or below the neutrality point. As a result, there are significant fluctuations in carrier density and the charge type, creating regions/puddles of different carriers. The presence of these puddles has been observed through scanning probe techniques [73, 74] such as scanning single-electron transistor technique.

Figure 1.3 shows a spatial map of the local carrier density when the average density is tuned to zero. Electron (red) and hole (blue) regions coexist on submicron length scales, with density fluctuations of order $\Delta n \sim 4 \times 10^{10}\,\mathrm{cm}^{-2}$ in zero magnetic field. [73] These disorder-induced density fluctuations set a residual carrier density scale, which dominates low-temperature transport close to neutrality and limits the observation of intrinsic transport.

1.2.6 Quantum Hall Effect, Landau Levels, and SdH Onset

The appearance of quantised states, known as the Landau levels, due to an applied magnetic field, are to be considered as a potential contribution to the measured resistance. The observation of this quantisation in resistivity is called the Quantum Hall Effect (QHE). Landau levels are quantised energy states arising from the quantised cyclotron motion of charge carriers, and become observable at sufficiently high

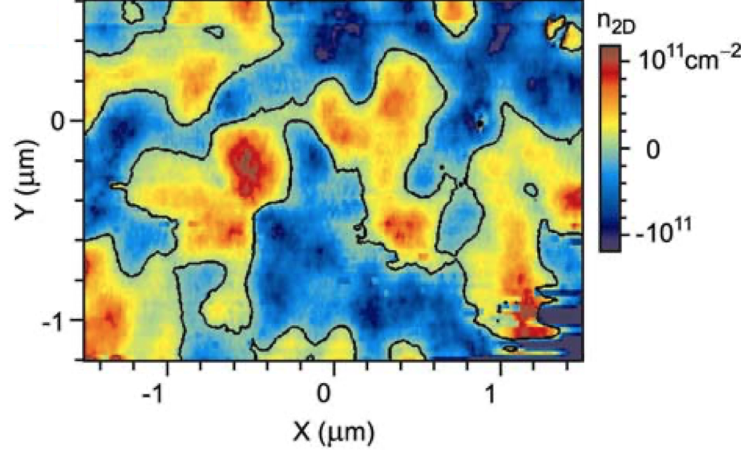

Figure 1.3: Spatial map of local carrier density in graphene at the charge neutrality point, measured using a scanning single-electron transistor. Red and blue regions indicate electron and hole puddles, respectively. The black contour marks zero density. Figure reused from Ref. [73] with permission (Copyright © Springer Nature)

magnetic fields and low temperatures when the Landau gap exceeds the thermal energy, $k_B T$. In graphene, the Landau level spectrum is given by:

$$E_n = \mathrm{sgn}(n)\, v_F \sqrt{2e\hbar B\,|n|},$$

where n is the Landau level index, v_F is the Fermi velocity, e the elementary charge, and $\hbar$ the reduced Planck constant. The largest gap is between the zeroth and first levels,

$$\Delta E = E_1 - E_0 = v_F\sqrt{2e\hbar B}.$$

To ensure that no Landau quantisation is observed, we require

$$\Delta E \ll k_B T \quad \Longrightarrow \quad B \ll \frac{(k_B T)^2}{2e\hbar v_F^2}.$$

Evaluating this upper bound between 100 K and 300 K gives:

$$B(T) \ll \frac{(k_B T)^2}{2e\hbar v_F^2} = \begin{cases} 56\,\mathrm{mT}, & T = 100\,\mathrm{K}, \\ 0.13\,\mathrm{T}, & T = 150\,\mathrm{K}, \\ 0.51\,\mathrm{T}, & T = 300\,\mathrm{K}. \end{cases}$$

In reality, the observability of these effects is typically at higher fields, due to obscuring by disorder and impurities at low temperatures.

For high-mobility hBN-encapsulated graphene samples, onset Shubnikov-de Haas (SdH) oscillations have also been observed at room temperature under moderate magnetic fields. SdH onset occurs when the Landau-level separation becomes comparable to the Landau-level broadening, approximated in the same way as the effects of magnetoresistance, i.e. when the cyclotron frequency $\omega_c = eB/m$ becomes comparable to the scattering rate $1/\tau$, such $\omega_c\tau \sim 1 \rightarrow \mu_{e,h}B \sim 1$. [75]

Given typical room-temp mobility for high-quality devices, $\mu_{e,h} \approx 10\,\mathrm{m^2\,V^{-1}\,s^{-1}}$, the SdH onset field at which the first oscillations can be discerned may be estimated, $B_{\text{onset}} \approx 100\,\mathrm{mT}$. At lower temperatures (5 K), where mobility is higher, this onset shifts to lower fields.

If we operate magnetic fields an order of magnitude below B_{onset} (i.e. below $\sim 1\,\mathrm{mT}$ at $5\,\mathrm{K}$ or below $\sim 10\,\mathrm{mT}$ at room temperature), then both QHE and SdH oscillations can be safely neglected in measurements.

1.3 Fabricating High-Quality Graphene Heterostructures

In this project, devices were made in the National Graphene Institute in Manchester, UK. High-quality fabrication is a key part in the observation of the hydrodynamic regime in graphene, as poor quality fabrication will add impurities, defects, and the substrate choice can cause significant scattering interactions that suppress hydrodynamic transport. This is briefly mentioned in Section 1.1.3, where scattering from substrate phonons can limit carrier mobility.

A heterostructure is a device that combines multiple heterojunctions, *hetero* from the Greek *other/different* and *junction* from the Latin *to join*; heterojunction is simply, in semiconductor physics, the joining of two dissimilar semiconductors.

1.3.1 Using Hexagonal Boron Nitride For Graphene-Based Heterostructures

Hexagonal boron nitride, hBN, is one of few two-dimensional materials that can be fabricated and used to complement graphene in heterostructures. Boron nitride is a crystalline structure made up of boron and nitrogen atoms, and much like carbon, can form into different lattice structures, see Section 1.1.1. Structures include [76]: cubic boron nitride, cBN, wurtzite boron nitride, wBN, and, more usefully, hexagonal boron nitride, hBN. hBN is similar to graphene in structure with a key distinguishing factor, the two non-identical atoms in the unit cell. The

effects of this are minimal on the lattice constant, in fact, the lattice matching is more than 98%, which makes interfacing between hBN and graphene smooth with minimal strain and defects. The monolayer hBN structure, mBN, is approximately a 6 eV direct-gap semiconductor, while bulk hBN is an indirect-gap semiconductor with a band gap of 5.95 eV. [77] This combination of electrical insulation and atomic flatness has made hBN a key part in the fabrication of high-quality graphene-based heterostructures. The similarity of hBN to the graphene hexagonal lattice also gives a qualitatively similar phonon dispersion, see Section 1.1.3, where phonon energies are slightly lower due to the polar and slightly heavier unit cell. Low phonon occupation in hBN is crucial as interfacial phonons between graphene and the substrate can scatter carriers in the graphene layer, limiting mobility. [27]

By encapsulating the monolayer graphene on the top and bottom with hBN, it not only protects the graphene from the environment but also keeps the graphene atomically flat without significantly modifying the band structure.

1.3.2 Graphene Heterostructure Fabrication Process

Hexagonal boron nitride, hBN, encapsulated monolayer graphene heterostructures are now commonly used as an appropriate material system for observations of intrinsic transport in graphene. In our devices, the typical stacking order (from bottom to top) is: 20 nm hBN, monolayer graphene, 20 nm hBN. This heterostructure is placed on a heavily doped conductive silicon wafer with an approximate 300 nm thermally grown SiO_2 layer. The purpose of the silicon dioxide layer is to provide a thick dielectric medium between the silicon back-gate and the monolayer graphene, allowing for the electrostatic tuning of the carrier density in the sheet by a fixed uniform potential on the back-gate.

As a brief outline of the fabrication process, optical imaging is used to identify suitable monolayer graphene and hBN flakes (hBN flake thickness ranges approximately $20 - 100$ nm). Flakes come from the mechanical exfoliation of bulk crystals. Using a dry transfer stamp technique, the heterostructure is assembled by sequentially picking up the top hBN, graphene, and bottom hBN flakes. Standard electron-beam lithography techniques can be used to etch the Hall-bar geometry, and gold one-dimensional edge contacts are evaporated onto the graphene edges. Finally, the device is packaged. [78]

1.4 Experimental Considerations for Characterisation Measurements

As we have discussed in the Section 1.2, transport phenomena on the microscopic scale can vary giving rise to different transport regimes. Macroscopic measurements, such as thermoelectric, magnetic, and optical measurements, may be used to probe different aspects of microscopic physics. Although, in this thesis, we focus on electronic transport regimes that are accessible through electrical measurements of conductivity/resistivity. Electronic transport measurements are experiments that typically revolve around the external application and response of electrical potential.

The combination of the techniques explained below provides a robust and precise method for measuring resistance in devices, even in the presence of sample geometric imperfections and low magnetic field uncertainties.

1.4.1 Device Geometry and Measurement Configuration

In principle, the Hall effect of a conducting medium can be measured in any arbitrary geometry, given a few assumptions. This was shown by Van der Pauw in 1958 [79]. His method requires four contacts be placed around the sample perimeter assuming:

1. The contacts are at the circumference of the sample.
2. The contacts are sufficiently small.
3. The sample is homogeneous in thickness.
4. The surface of the sample is singly connected, i.e. the sample does not have isolated holes.

While this method is very useful, the method can be prone to errors due to finite contact sizes that obscure the first two assumptions. It turns out this technique is not the most efficient method for measuring the Hall effect in a material like graphene. The Hall-bar geometry, shown in Figure 1.4, having arms that are perpendicular to the current flow, allows for the measurement of the full resistivity tensor quickly and accurately.

The Hall-bar geometry, although it is a fundamentally different geometry, satisfies the same assumptions of Van der Pauw but relaxes some of its restrictions. Given the contact terminals are on the ends of the arms, they do not contribute to the same problem of finite-sized contacts near current flow that the Van der Pauw method has. Additionally, the Hall-bar has an ability to measure smaller resistances more

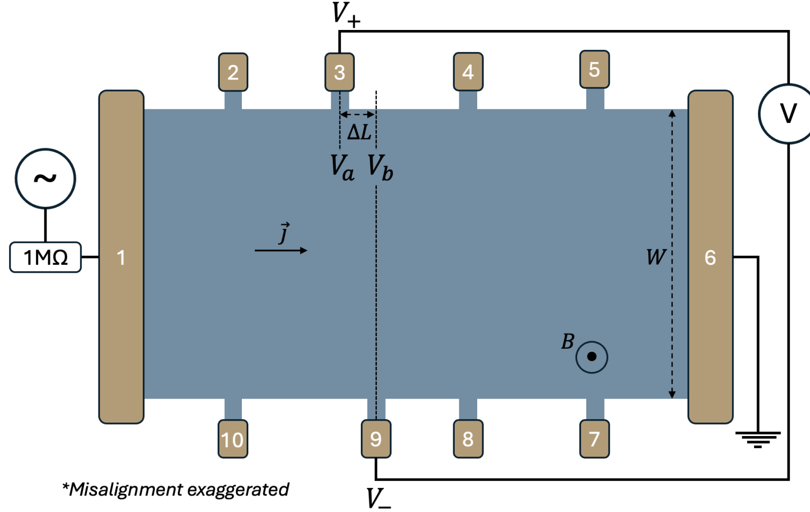

Figure 1.4: Schematic of the Hall-bar device, showing the Hall potential measurement configuration under magnetic field B. An exaggerated misalignment between opposite probes, ΔL, is indicated.

accurately as much more of the applied voltage is dropped where the potential is actually measured, due to the uniform current density.

Consequently, the Hall-bar geometry offers the necessary precision and functionality for comprehensive electronic transport analysis of graphene, but is still not fully immune to the consequences of inhomogeneities that alter the carrier density in the sheet.

Hall-bar geometry is especially suited for probing the resistivity tensor that is described by the Drude model (see Eq. (1.22)) that describes the response of the current density, **j**, to applied electric and magnetic fields. Potential should be measured parallel to the current density in the case of longitudinal resistance and perpendicular in the case of transverse/Hall resistance measurements. Ultimately, this is well-suited to Hall-bar geometry: a constant current flowing along a rectangular sample axis, perpendicular to an applied magnetic field.

1.4.1.1 Geometry Misalignment

When we measure the Hall resistance by measuring the potential difference between contacts 3 and 9 in Figure 1.4, such that $\rho_{xy} = V_+ - V_-/I$, we can find that $\rho_{xy}(+B) \neq -\rho_{xy}(-B)$. This is in disagreement with the expected linear resistivity results from the single-carrier Drude model in small B-fields (see Eqs. (1.21) and (1.23)). This will occur when the measurement axes are misaligned, as exaggerated in Figure 1.4.

When measurement axes are misaligned, the Hall resistance measurements, ρ'_{xy} (prime used to distinguish misaligned measurement from intrinsic resistivity), contain mixed contributions. The measured voltage includes both the desired Hall voltage and an unwanted misalignment voltage, $V_a - V_b$, which is proportional to the longitudinal resistivity. Take the line integral form of Ohm's law:

$$V_a - V_b = -\int_a^b (\boldsymbol{\rho} \cdot \mathbf{j}) \cdot d\mathbf{l},$$

and consider a uniform current density, $\mathbf{j}$, flowing in a Hall-bar as shown in Figure 1.4.

The added contribution to the measured signal can be determined and shown to be proportional to ρ_{xx}:

$$V_a - V_b = -\int_a^b \left[\begin{pmatrix} \rho_{xx} & \rho_{xy} \\ -\rho_{xy} & \rho_{xx} \end{pmatrix} \cdot \begin{pmatrix} I/W \\ 0 \end{pmatrix} \right] \cdot \begin{pmatrix} dl \\ 0 \end{pmatrix} = \frac{I\Delta L}{W} \rho_{xx}$$

where ΔL is horizontal misalignment distance, I is the applied current, and W is the sample width.

The measured Hall resistance, therefore, becomes:

$$\rho'_{xy} = \frac{V_+ - V_-}{I} = \frac{V_b - V_-}{I} + \frac{V_a - V_b}{I} = \rho_{xy} + \frac{\Delta L}{W} \rho_{xx}$$

As can be seen, the misalignment voltage contribution is proportional to the longitudinal resistivity, ρ_{xx}, that is symmetric in magnetic field. As such, the measured Hall resistance in $\pm B$ fields will be:

$$\rho'_{xy}(+B) = \rho_{xy} + \frac{\Delta L}{W} \rho_{xx},$$
$$\rho'_{xy}(-B) = -\rho_{xy} + \frac{\Delta L}{W} \rho_{xx}$$

This dual-measurement protocol enables separation of intrinsic transport properties from geometric artifacts through the distinct parity of ρ_{xy} (odd in B) and ρ_{xx} (even in B) shown by the Drude model (see Eqs. (1.20)–(1.26)). Taking the difference of the two measurements as an average eliminates the misalignment contribution:

$$\rho_{xy} = \frac{\rho'_{xy}(+B) - \rho'_{xy}(-B)}{2} \tag{1.29}$$

The effectiveness of this field-reversal averaging technique relies on the antisymmetric nature of the Hall effect with respect to the magnetic field, while the misalignment voltage remains symmetric. We can therefore take measurements in both

positive and negative fields to extract the true Hall resistance, ρ_{xy}, from the measured Hall resistance, ρ'_{xy}, using Eq. (1.29).

The validity of this procedure depends on the in-plane isotropy of the resistivity tensor. In graphene, the circular Fermi surface, at low energies, ensures isotropic transport. In contrast, anisotropic materials such as WTe_2 [38] have a non-circular Fermi surface, resulting in direction-dependent Fermi velocity that leads to anisotropic transport. Consequently, the resistivity components are not purely antisymmetric in B, which makes Eq. (1.29) inapplicable for anisotropic materials.

1.4.1.2 Onsager-Casimir Reciprocity Relations

The Onsager-Casimir reciprocity relations describe symmetry properties of transport behaviour in systems near thermodynamic equilibrium. [80] A direct result is that transport coefficients in a system transform under time-reversal, and thus relate measurements at magnetic field B to those at $-B$. [42, 81, 82]

We will see that these relations are particularly useful in our low-field measurements where precise field control is difficult. These relations will give rise to a powerful measurement protocol for validating and/or quickly obtaining ρ_{xy} in flipped fields. This technique involves measuring the voltage in at least two complementary configurations. For any conducting media with four-probes, this is achieved by swapping the electrical connections for the current source and the voltmeter (lock-in amplifier).

For example, one transport measurement would source current between two contacts, I_+ and I_-, and measure voltage across the contacts, V_+ and V_-. Then a second reciprocal measurement would take place where the current and voltage probes are switched, such that current is sourced across the contacts that were V_+ and V_-, and vice versa, the voltage is measured across the contacts that were I_+ and I_-. The result is that the two measurements are equal by the symmetry of the Onsager-Casimir relations, and therefore the measured resistivity tensors are related by [42]:

$$\boldsymbol{\rho}_{mn,kl}(B) = \boldsymbol{\rho}_{kl,mn}(-B) \tag{1.30}$$

where the indices of the resistivity tensor are defined as the configuration of voltage and current probes ($\rho_{V,I}$).

To aid in understanding, consider two configurations, A and B, in which each describes the positions of four electrical contacts, two voltage and two current probes. The voltage probes are swapped with current probes in configuration B compared to configuration A. The Onsager relations then require that the transport measurements in configuration A in field $-B$ are equal to transport measurements in

configuration B in field $+B$. This is shown in Figure 1.5.

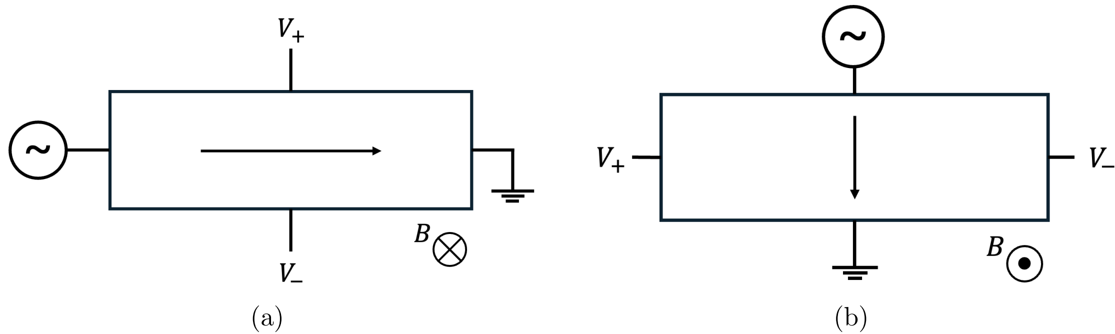

Figure 1.5: Configurations **(a)** and **(b)** are used to measure the Hall resistance under a magnetic field B. Reciprocity requires that transport measurements in **(a)** in field $-B$ are equal to transport measurements in **(b)** in field $+B$.

1.4.2 Experimental Setup for Transport Measurements

In practice, resolving well-defined microvolt-level signals, and reliably switching between reciprocal measurement configurations demand a measurement system with high stability, low noise, and a high degree of automation.

Figure 1.6 provides an overview schematic of the experimental setup used for the transport measurements discussed in this work. The schematic summarises the signal generation, routing, and detection chain, highlighting how AC transport measurements are implemented in practice. All instruments are connected to a control computer via the GPIB/IEEE-488 interface and operated through LabVIEW software, enabling automated measurements and reproducible switching between configurations. A switch matrix routes signals from the instruments to the device under test (DUT) via a breakout box, allowing rapid reconfiguration without manual intervention.

1.4.2.1 Noise and Lock-In Amplifiers

In any transport measurement, noise is an ever-present obstacle. We intend to measure very small AC potentials on order of microvolts or less. Consider a normal amplifier. Every real amplifier has a finite frequency response, meaning it only works well over a certain range of frequencies, usually by design. This is what we call the bandwidth. At low frequencies (below a lower cutoff), capacitors in the circuit intentionally block signals. At high frequencies, gain roll-off arises from a combination of parasitic capacitances, inductive impedances in the circuit, and the finite bandwidth and frequency compensation of active components. So a standard

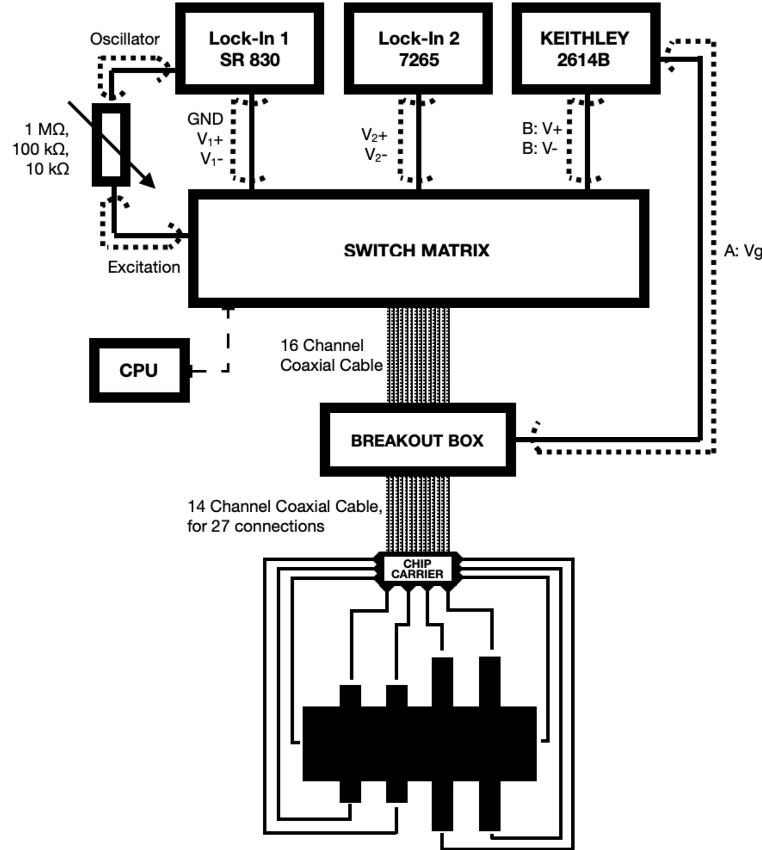

Figure 1.6: Schematic diagram of the transport measurement setup. Shows coaxial connections from the oscillator of SR830 lock-in via current-limiting resistors. Lock-in amplifiers, SR830 and 7265, measure differential voltage. Source measure unit, Keithley 2614B, sets device back-gate voltage and has a second DC source. The CPU-controlled switch matrix does source and instrument selection to the device through a breakout box.

amplifier with a 100 kHz bandwidth, for example, may faithfully amplify signals (both wanted and unwanted noise) in a 100 kHz window.

Noise typically comes from the circuit elements themselves, for example, thermal (Johnson-Nyquist) noise from resistors. This is the random potential fluctuations generated by the thermal agitation of charge carriers in a resistor, with a power spectral density of $\sqrt{4k_BTR}$. If a $100\,\text{k}\Omega$ resistor at room temperature is used to limit current to a device, then it introduces approximately $41\,\text{nV}/\sqrt{\text{Hz}}$ of noise across a wide range of frequencies. When integrated over a $100\,\text{kHz}$ bandwidth, the resistor alone can contribute tens of microvolts of RMS noise, easily masking the microvolt-level transport signals we are trying to measure.

Lock-in amplifiers are designed to pull out these small AC signals buried in noise by locking onto their frequency. By multiplying the incoming signal with a reference signal and filtering the result with a low-pass filter, they strip away everything except the part of the signal oscillating exactly at the reference frequency. This is

a technique called phase-sensitive detection and can reduce the 100 kHz bandwidth of a normal amplifier down to just a few millihertz, depending on the settings.

Referencing the measured input directly to the excitation frequency ensures that the signal kept is the true transport response rather than random noise. The lock-ins can produce the excitation voltage to our circuit and sync to other lock-ins for multi-channel measurements. Any phase shift between the reference and measured signal may be recorded in separate channels, typically called the in-phase (X) and out-of-phase (Y) channels. Equally, they can be recorded as magnitude (R) and phase (θ). Critically, in transport measurements where we are interested in resistive behaviour, we aim to have an entirely in-phase response. Any increase in the out-of-phase channel usually indicates unwanted capacitive effects in the circuit. Therefore, as capacitance increases with frequency, we typically keep an AC frequency range of $30-90$ Hz, to keep the out-of-phase voltage as low as possible while also maintaining some speed to measurements. In other setups with less parasitic capacitance, higher frequencies up to 10 kHz may be used.

The settings of lock-in amplifiers, particularly the time constant, decide how clean but also how fast the measurement is. The time constant sets the cutoff frequency of the low-pass filter applied. The detection bandwidth then is given by the equivalent noise bandwidth (ENBW) of the low-pass filter. Under typical conditions, the ENBW is approximately $1/(10T)$, where T is the time constant, reflecting the use of higher-order (typically 2 to 3-pole, 12-18 dB/oct) low-pass filters in modern lock-in amplifiers, with the exact value depending on the filter order. For comparison, a single-pole (6 dB/oct) low-pass filter has an ENBW of $1/(4T)$. The 12 dB/oct low-pass filter used in this study has an approximate $7T$ settling time for the output to reach 99% of its settled value. The time constant should be much larger than the time period of the reference frequency.

In practice, the choice of time constant sets how quickly you can sweep gate voltage, magnetic field, or other types of scanning while still getting trustworthy data.

Lock-in amplifiers used in our research include Stanford Research Systems (SRS) SR830 and Signal Recovery 7265 DSP lock-in amplifiers.

1.4.2.2 Source Measure Unit

Source Measure Units (SMUs) are valuable pieces of equipment that allow for DC current or voltage sourcing. SMUs typically have separate circuits for different voltage ranges, from millivolts to hundreds of volts, allowing for higher precision in any given range. However, this adds extra caution when changing the voltage range

modes; a small but significant voltage spike may be supplied on output. Therefore, using SMUs requires some careful planning to avoid damage to sensitive devices, such as not switching ranges or turning an SMU on/off whilst there is a direct link to the device under test (DUT).

We use a Keithley 2614B SMU. It is a dual-channel setup with a voltage range up to 200 V. Channel A of the SMU is mainly used as the back-gate voltage source, and it measures leakage current through this gate with a compliance limit of 100 nA. Channel B is used to test 2-probe DC resistances. A constant voltage of 1 mV is set on channel B, and the current is measured with a compliance of 1 µA. This allows for resistances up to 100 kΩ to be measured well, our contact resistances are in the $1 - 10\,\mathrm{k\Omega}$ range and so this is a good method.

A matrix switch is used to route the SMU channel B to different contacts on the device, allowing for multiple 2-probe DC resistance measurements without any manual intervention.

1.4.2.3 Switch Matrix

The switch(ing) matrix, or matrix switch, vastly improves automation and decreases human error. By containing 256 relays/switches, the switch matrix can connect 16 inputs to a multitude of 16 outputs, where the terms inputs and outputs are used arbitrarily, as there is no diodicity. For the Cytec VX/256 switching matrix, relay activation status is displayed via a 16×16 LED front panel, and relays can be controlled by LabVIEW via GPIB/IEEE-488 interface. Latching relays, which do not have to be continuously powered to remain in the 'on' state, are used in this setup.

For transport measurements, the instruments and external power supplies are connected to the 'input' of the switch, up to 16 separate BNC lines. Each 'input' has four internally connected BNC ports, this has little influence on the understanding of the application of the switch matrix in our context. The breakout box, which is the external routing for the DUT, is then connected via coaxial cable to the matrix switch.

On one side of the switch matrix we have the following electrical routing:

1. Lock-in 1: Excitation voltage
2. Ground
3. Lock-in 1: input A (V_1+)
4. Lock-in 1: input B (V_1-)
5. Lock-in 2: input A (V_2+)
6. Lock-in 2: input B (V_2-)
7. SMU channel B ($V+$)
8. SMU channel B ($V-$)

9. Shorted to 10 by $10\,\mathrm{k\Omega}$
10. Shorted to 9 by $10\,\mathrm{k\Omega}$
11. Shorted to 12 by $1\,\mathrm{k\Omega}$
12. Shorted to 11 by $1\,\mathrm{k\Omega}$

On the other side of the switch matrix all the device contacts, up to a maximum of 16, are connected. We can now consider multiple configurations of transport measurements, such as 2-probe DC resistance measurements, 2 and 4-probe AC measurements, and current measurements, without any manual rerouting of cabling. This removes human error and allows for automation of measurements with many different configurations without human intervention.

1.4.2.4 Temperature Dependent Transport

The liquid helium-4 cryostat is an essential tool for low-temperature transport. Allowing for transport measurements in temperature-stable environments in a range of $1.5 - 400\,\mathrm{K}$. This is achieved through a variable temperature insert (VTI) that is an inner chamber that sits within the helium bath. In addition, a superconducting magnet, capable of producing a $\pm 15\,\mathrm{T}$ field perpendicular to the sample space, surrounds the bottom of the VTI. More information about this superconducting magnet will be discussed in Section 1.4.2.5. The structure of the cryostat is given in Figure 1.7.

On the outside of the cryostat are the return lines for boiled-off helium, which go to the liquefier room to be recycled, (see Figure 1.7(l)). We also have adjustment screws for valves controlling the helium going into the inner chamber, (h), and also the exhaust going to the pump, (i). We also have I/O connections to the magnet, VTI heater, thermometer, and switch heater. I/O to the top of the insert probe is for connections with the DUT via the chip carrier and also separate connections to the probe heater and resistance temperature detectors (RTDs) in the insert probe (g). Finally, the insert probe has a pressure valve, allowing for the sample space to be in vacuum or in a different atmosphere, such as helium exchange gas.

Moving inwards, we have a vacuum space for thermal isolation between atmosphere and the liquid helium bath (see Figure 1.7(c)), it is important to spend a long time pumping this chamber down while at room temperature to get the most use out of the helium. All boil-off from the helium bath is waste and costly; therefore, the better maintained the isolation around this layer of the cryostat the better. In the helium bath is the superconducting magnet, which will remain superconducting for as long as it is submerged in the helium (b). This bath is slightly positively pressured compared to the atmosphere, this is due to the helium return line that is positively pressurised to keep the lines helium pure and contaminants low.

Moving through the second smaller vacuum layer, (see Figure 1.7(e)), into the

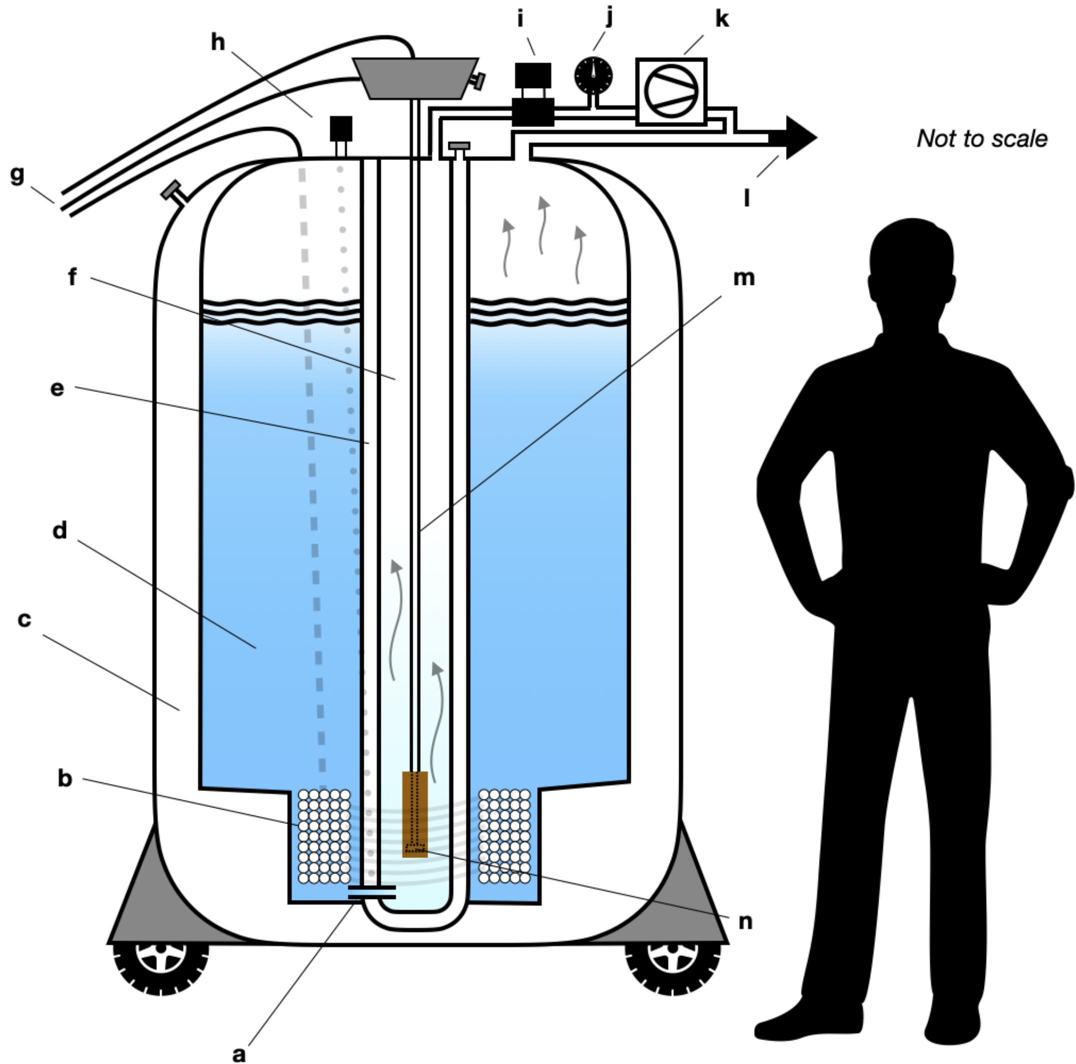

Figure 1.7: Cryostat Simplified Schematic. a) Needle valve. b) Magnet. c) Outer vacuum. d) Liquid helium. e) Inner vacuum. f) Variable Temperature Insert. g) I/O for insert probe (temperature control), DUT to breakout box, and magnet. h) Needle valve adjustment screw. i) Pressure valve. j) Vacuum gauge. k) Vacuum pump. l) Helium return line. m) Insert probe. n) DUT in chip carrier socket.

inner chamber (VTI), (f), is the needle valve that allows for helium flow into the VTI, (a). Helium entering the VTI first flows through the heat exchanger at the base of the VTI, which acts to change the temperature of the Helium entering the VTI space. The temperature achieved is a balance between the helium flow rate and the temperature of the exchanger, which is controlled by VTI heater to high degree of stability (variance less than 0.1 K). The walls of this inner vacuum separate the cold liquid helium from the variable temperature space. At higher temperatures in the VTI, above approximately 150 K, frozen contaminants on the walls of the vacuum chamber become gaseous and act as an exchange gas between the two walls. Therefore, at higher temperatures, it is expected that boil-off of the dewar is higher

and consequently costly.

The VTI outlet is connected to a pressure valve and pump, (see Figure 1.7(i)) and (k) respectively. The pump operates the VTI chamber at a lower pressure than the dewar pressure. Therefore, helium will flow along the pressure gradient through the needle valve and heat exchanger into the VTI, where it evaporates to cool the chamber. The Edwards nXDS 6i dry scroll pump is used with a maximum vacuum capability of 0.020 mbar. This pump features bearing shields separating the bearings from the process gas. This avoids cross-contamination with lubricants and metallic dust, important in the He^4 recycling.

The flow of helium through the VTI is controlled by a balance between the inlet and outlet valves. A helium flow too high has a strong cooling power and can be wasteful if helium sits as a liquid inside the VTI chamber until the temperature controller acts to boil the helium off quicker. A helium flow that is too low will be unstable and could stop unpredictably. In general, the flow rate will change slightly depending on requirements. An Edwards SP25K sealed pressure valve, with a nitrile diaphragm, is used to adjust pressure and flow to the vacuum pump.

Temperatures below the boiling point of helium can be achieved in the VTI by reducing the chamber pressure. This would mean that the flow rate through the needle valve is low and the temperature can drop to as low as 1.5 K. To go to lower temperatures, a continuous flow is not sufficient. By pulling in liquid helium into the VTI quickly and with not too much pumping, the VTI will start filling wih helium. Then by closing the needle valve and maximising the pumping to the VTI the pressure can be dropped enough such that the lowest temperature is approx 1.3 K. This is known as a 'single shot' mode, as the low temperature lasts a few minutes before the helium in the VTI has fully evaporated, and the process has to start again. An Edwards APG100-XM Active linear Pirani vacuum gauge is used as a useful digital gauge with a measuring range of atmosphere down to 0.01 mbar.

The VTI temperature is controlled by Oxford Instruments ITC, a PID temperature controller. A PID (Proportional-Integral-Derivative) controller regulates temperature by continuously adjusting the heater power based on the proportional error, its time integral, and its time derivative, allowing efficient stabilisation at a setpoint. The PID stabilises the temperature of the VTI thermometer but does not accurately represent the temperature of the DUT, (see Figure 1.7(n)), inside the insert probe (m) unless sufficient time has passed to reach equilibrium. Therefore, a secondary PID Arduino-controlled heater on the insert probe is a valuable addition to allow for quicker temperature stabilisation and more accurate DUT temperatures.

The DUT is mounted within a brass sample stage located at the end of the insert probe. This brass casing defines the sample space and has a thermal mass of

approximately 150 g, providing significant thermal stability. All electrical leads to the DUT are coiled and thermally anchored around this brass stage before reaching the chip carrier. This anchoring ensures that the wiring is thermalised to the probe temperature, minimising parasitic heat conduction from room temperature and improving temperature stability at the DUT.

Faster temperature stabilisation of the sample space was achieved by using an Arduino programmed to act as a persistent PID device that monitors the resistance of two temperature-sensitive resistors (RTDs). Two RTDs are used, one for the high temperature range (PT1000) and one for the low temperature range (RuO). A PCB addition was designed for the Arduino that has two instrumental amplifiers which accurately measure 4-probe potential difference across the RTDs, one amplifier per RTD. The Arduino produces a constant DC current of 10 mA across resistors. This is large enough to have precision in measurement with a good signal-to-noise. In order to accurately control the temperature, the output of the PID is connected to a heater: a repurposed strain gauge, which functions as a resistive heater by dissipating electrical power as heat when a current is applied. This heater is mounted with the RTDs close to the chip carrier mount. The arduino runs countinously and independently once a temperature setpoint is given, monitoring temperature changes very quickly and can bring the chip carrier temperature to a new setpoint much quicker. The measured temperature via our added RTDs better represents the temperature of the DUT compared to the cryostat heat exchanger, due to the large thermal mass of the insert probe. Therefore, temperature sweep data can now be as efficient as possible, starting measurements as soon as the chip carrier temperature is stable as the VTI temperature catches up.

This setup enables us to perform accurate temperature-dependent transport measurements across a wide range of temperatures. The 160 litre dewar allows for approximately two weeks of experimentation between refills. Before the first filling, while at room temperature, the outer vacuum layer is pumped overnight. This is essential for good thermal isolation once cooled down. For the initial filling, the dewar must first be partially filled with liquid nitrogen to reduce thermal shock, particularly to the brittle wires in the magnet. Carefully, the liquid nitrogen is blown out by helium gas; this is especially important so that when liquid helium is filled, it does not freeze any leftover nitrogen in the needle valve.

1.4.2.5 Magnetic Field Dependent Transport

Many transport measurements of interest require simultaneous control of temperature and magnetic field. Magnetic field dependence is achieved using a superconducting solenoid magnet integrated into the cryogenic system.

The Oxford Instruments superconducting magnet, S15/52/13, uses superconductive wire, Nb_3Sn, to make coaxial solenoid windings. The magnet can produce a guaranteed maximum central field of 15 T at 4.2 K and provide persistent field operation. The current draw for full field is 102 A and the coils have an inductance of 41.2 H. The energy stored in maximum field is therefore around 0.21 MJ using $E = \frac{1}{2}LI^2$.

As the coils are made with a material that is superconductive at cold temperatures, the current that flows in the coil will be maintained and the magnetic field 'locked'. The field will decay slowly with time due to interactions with residual resistance in joints and energy is lost. Each end of the solenoid is terminated together, completing a superconductive loop. To change the current flowing in the loop, a heater is attached to the section of the loop. The result is that when the switch heater is on, the small section of the loop becomes non-superconducting and has a resistance of a few ohms. Current leads can then be used to create a flow around the loop/coil. When the magnet is energised to the desired level the switch heater can be turned off and the resistive section of the loop becomes superconducting, allowing the current to flow around the loop via the path of least resistance rather than through the current leads. The power supply can then be ramped down, and the magnetic field persists. The Oxford Instruments MercuryIPS intelligent power supply interfaces with the magnet and includes safeguards to prevent unwanted quenching. The iPS system is then communicated with via LabVIEW along with the rest of the lab instruments.

Quenching

In a scenario where high currents are flowing in the loop and any part of the loop becomes resistive, such as turning on the switch heater when the current leads are not connected, quenching could occur. The word 'quenching' is to literally eliminate/extinguish something. Here, the term is used when the magnetic field is suddenly and uncontrollably eliminated. In the case where the switch heater is switched on when the current leads are not connected, then the ohmic heating generated by the current flowing in this resistive section of the loop will raise the temperature rapidly. This propagates around the entire coil until the magnet is no longer superconducting and the energy stored by the field has dissipated as heat into the helium bath. This sudden release of stored energy is often triggered by very small releases of energy, such as minor movements in the coil. Large quantities of helium can fill a Lab in the event of a quench that is uncontained. The latent heat of boiling liquid helium-4 is approximately 21 kJ kg^{-1}; therefore, at full-field energies, 10 kg of helium could be boiled off into a small room. Our lab is approximately 100 m^3 and helium expands to about 6 m^3 kg^{-1}, therefore over half the room, 60 %, could

be filled in a quenching event. Good safety measures and ventilation are required. These risks are mitigated through oxygen deficiency monitoring, forced laboratory ventilation, pressure-relief, controlled ramp rates, and integrated quench-protection and interlock systems.

Summary of Experimental Transport Methods

Bringing this section together, the experimental setup enables precise measurement of macroscopic transport phenomena, primarily electrical resistivity. The accurate measurement of the longitudinal and Hall resistivity components is achieved by using lock-in amplifiers, applying corrections via field-reversal averaging, aided by the Onsager-Casimir reciprocity relations.

The cryogenic system provides a range of temperatures and magnetic fields as high as $\pm 15\,\mathrm{T}$. Measurements made, under correct model assumptions (see Section 1.2.1.1), give us characteristic values such as carrier density, mobility, and mean free path. Deviations from the expected profiles can indicate inhomogeneity and unexplained physics, such as electron-hole drag, which we study in Chapter 2.

1.5 Scanning Gate Microscopy of Nanoscale Devices

Scanning probe microscopy, SPM, is a versatile tool for measuring microscopic features of materials. Different techniques can reveal different aspects of the material under study by scanning a nanometer-scale probe across the surface, revealing electrical, thermal, magnetic, structural, and topological properties throughout the sample, not just on the surface but also in the subsurface.

Examples of different techniques are:

- Atomic Force Microscopy (AFM): [83] Maps the surface topography of a material by measuring the forces between a probe and the sample as the probe scans across it.
- Scanning Gate Microscopy (SGM): [84] Used to visualise charge transport and electrostatic potentials in nanostructures by scanning a voltage-biased tip to locally gate underlying transport.
- Ultrasonic Force Microscopy (UFM): [85] Utilises ultrasonic vibrations applied to the sample to detect subsurface features and elastic responses.
- Scanning Tunneling Microscopy (STM): [86] Detects the quantum tunneling current between a sharp metallic tip and the sample during scanning.

- Magnetic Force Microscopy (MFM): [87] Detects the magnetic interactions between a magnetised probe tip and the sample during scanning.

In this research, we will specifically consider scanning gate microscopy. SGM uses an AFM-style positioning system and a biased conductive tip as a movable local gate during transport measurements.

1.5.1 Basic Principles of Atomic Force Microscopy

In AFM, a small, sharp tip on the tens of nanometre-scale (can be sub-10 nm or over 100 nm but will range in size depending on the use case) is precisely positioned within nanometers to the surface of a sample, and interatomic forces, such as van der Waals and electrostatic forces, cause detectable deflections of a flexible cantilever holding the tip. By monitoring cantilever deflection with a laser and then using a feedback loop to maintain a constant force, one can track surfaces on the atomic scale. AFM requires no conductive sample or tip, opening the door to atomic-scale imaging on a wide range of surfaces. Operational modes of AFM tackle different challenges: contact mode AFM, where the tip maintains a small constant force on the surface; non-contact mode, where the tip oscillates above the surface, sensing attractive forces; and tapping (intermittent contact) mode, to gently scan soft or adhesive surfaces by momentarily touching the surface each oscillation. The relevant modes used in this thesis include contact and tapping modes.

When the tip approaches the surface, within hundreds of nanometers, long-range electrostatic forces can be measured from the sample. As the approach continues to the nanometre scale, Van der Waals, capillary, magnetic, and screened electrostatic forces are felt by the tip. The attractive forces, mainly VdWs, will overcome the cantilever's stiffness, causing the tip to jump to the sample surface by a few nanometers. Of course, the strong short-range repulsive force (Pauli repulsion between overlapping electron orbitals), when the tip makes contact, stops the tip from entering the surface. The force F that causes cantilever deflection from its equilibrium position z is given by Hooke's law, $F = -kz$, where k is the spring constant of the cantilever as long as deflections are small. A reflective coating on the top side of the cantilever allows a laser to reflect off the cantilever via a few mirrors into a split photodiode, converting the laser intensity at 4 quadrants of the photodiode into a measure of the cantilever's deflection and twist. Probes are typically made with silicon or silicon nitride.

Figure 1.8 shows the design of a scanning head, particularly the one used in this research. The laser is adjusted to focus on the back of the cantilever.

In contact-mode AFM, the probe is mounted and can move in three dimensions

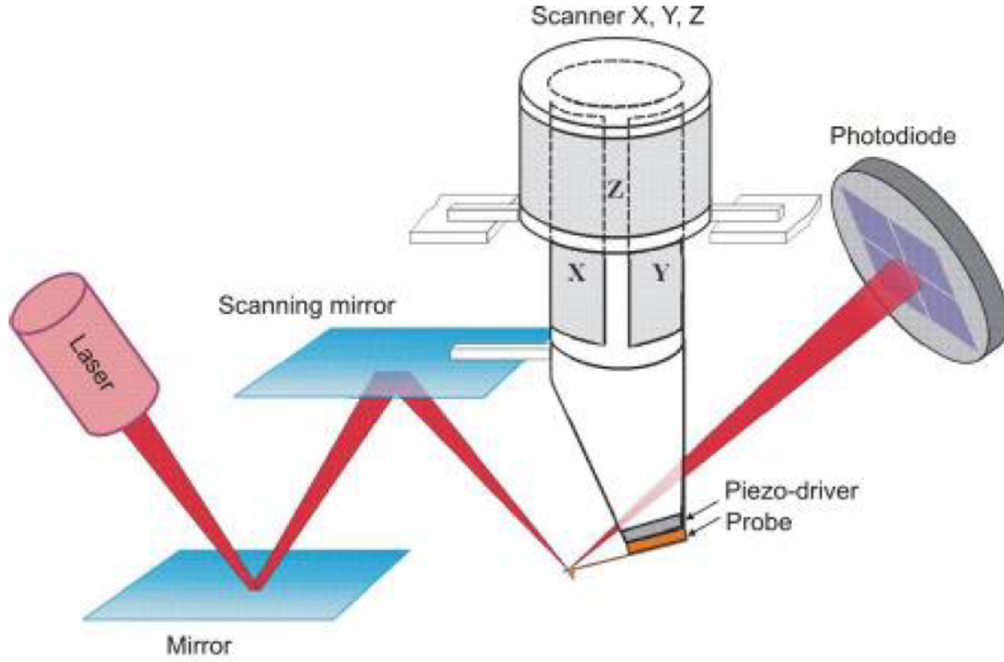

Figure 1.8: A schematic of the scanning head design. [88] The head has a wide range of possible manual adjustments. The probe is mounted via magnets to a piezo-driver, enabling non-contact AFM. And the larger probe assembly is mounted to XYZ piezoelectric translators for scanning.

using piezoelectric transducers offering very fine nanometre-scale translations, while step motors provide very coarse position movement. During scanning measurements, the X and Y piezos scan the sample surface, while the Z piezo, controlled by PID feedback, maintains a predetermined force between the tip and the sample. By recording the Z height at each surface position, we thereby render the sample surface topography to sub-nanometer precision, and moreover, the amount of cantilever twist can also be recorded simultaneously.

Under tapping-mode operation, the cantilever oscillates near its resonant frequency with an amplitude (e.g. 10-100 nm) such that the tip momentarily contacts the surface at the bottom of each swing. Such interactions with the surface reduce the oscillation amplitude, and the instrument uses a fixed oscillation amplitude set-point via feedback to track the surface. Tapping mode alleviates friction, sticking, deposits, and surface damage associated with contact mode.

The method of recording data as a function of XY as the sample is scanned can be extended to as many parameters as possible. During AFM, the device's resistance can be measured simultaneously with topography, thereby yielding a map of resistance as a function of XY. This is crucial in the case of scanning gate microscopy, SGM.

1.5.2 Probing Quantum Carrier Transport Inside Graphene Using Scanning Gate Microscopy

In SGM, a conductive tip is used as a gated voltage source. Therefore, as the tip moves along the sample, the electric field it generates locally modifies the sample's electrical properties. In the case of 2DEGs, the gate electric field locally increases or decreases the carrier density within the 2DEG, thereby directly changing the resistance measured across the device, or, more specifically, the device's potential energy landscape. For SGM to work, the tip must hold a fixed voltage and therefore not come into contact with a conductive sample under test. This requires the probe to be in non-contact scanning mode to ensure no gate leakage through the sample, or to use contact mode, in which the tip and sample are separated by an isolating dielectric layer.

SGM has been adopted by multiple groups to study various phenomena. Notable achievements include imaging of: electron transport from quantum point contacts [84], quantum dots [89], quantum Hall edges [90], ballistic transport in 2DEGs via transverse magnetic focusing [91, 92], and viscous electron fluids in GaAs 2DEGs [93]. The interpretation of such images/maps differs for different types of transport phenomena. In particular, the interpretation of simple diffusive flow in 2DEGs, graphene or otherwise, with typical 4-probe measurement configurations has gone unnoticed. In Chapter 3 of this thesis, we will not only perform such experiments but also shed light on the interpretation of such maps via analytical and numerical modelling, both for diffusive and hydrodynamic flow.

CHAPTER 2

Electron-Hole Drag and Negative Mobility in Graphene's Dirac Plasma

The study of charge-carrier dynamics in graphene has interested condensed matter physicists due to the unique intrinsic properties of this material. Typically, at moderate temperatures, two-dimensional electronic systems are dominated by random isotropic scattering events from impurities and phonons. Such scattering leads to simple diffusive transport well-described by the Drude model, see Section 1.2.1.1. However, as discussed in Section 1.1.3, the in-plane rigidity of the hexagonal graphene lattice leads to a suppression of phonon modes, as they are elevated to higher energies. With a thickness just one atom thick and the ability to be encapsulated in hexagonal boron nitride (hBN), working with graphene has led to high mobility devices with low density of defects. And, as with many two-dimensional electronic systems, the tunability of the transport via a charged electrostatic gate allows for direct exploration of various transport regimes. The unique combination of these properties makes graphene the ideal platform to seek out, what would be typically obscured in conventional 2D materials, scattering mechanisms that go beyond the simple Drude model. Nevertheless, the simple macroscopic probing of the resistivity in graphene has gone without a comprehensive understanding of the underlying microscopic mechanisms. This is especially notable in the Dirac plasma regime of monolayer graphene, where the interplay between electrons and holes enables the investigation of novel transport phenomena that this chapter aims to shed light on. Specifically, conventional phenomenological models like the Drude model, recall Section 1.2.1.1, fail to account for features observed in macroscopic measurements, like resistivity, where added complexity is caused by a strong electron-hole drag regime.

This chapter presents a comprehensive investigation of strong electron-hole interactions within the Dirac plasma of graphene, with emphasis on the implications for hydrodynamic transport. We examine the temperature and density dependence of both longitudinal and Hall resistivities in a high-drag regime, and reveal the responsible mechanism for the experimentally observed apparent negative mobility of minority carriers. From this research, we can establish a robust methodology for extracting microscopic scattering parameters from measured experimental data.

The principal objective may seem somewhat philosophical: to 'understand' how the field effect manifests in graphene's transport, where understanding implies meaningful predictive power. What is science but to develop, test, or even replace theoretical frameworks to get a better grip on the world? As we will see, the present models, see Section 1.2.1.1, are put up to reality and found insufficient to describe the resistivity of graphene in the Dirac plasma regime. This interpretational difficulty in relating measured transport coefficients to underlying microscopic processes is compounded by the fact that experimentally measured transport reflects the combined influence of multiple scattering mechanisms, including substrate disorder, electron-phonon interactions, and sample geometry, whose relative importance depends sensitively on carrier density and temperature.

We will aim to get an understanding that can predict the resistivity of graphene across all densities, temperatures and magnetic fields, with few to no fitting parameters. A very bold objective.

In this chapter, we partially achieve this objective to understand the field effect in this system. We develop a model that accurately predicts measured room-temperature resistivity across a broad range of densities under small magnetic fields. The model uses only two phenomenological parameters, the electron-hole scattering time and the typical momentum relaxation (transport) scattering time. Therefore, we have also developed a method of device characterisation; by simply measuring the longitudinal and Hall resistivities, two microscopic parameters can be extracted.

The chapter is organised as follows. Section 2.1 will describe the methods used to probe electronic transport in graphene, as well as device characterisation. Section 2.2 will present key experimental results, including the observation of negative Hall resistivity and the insufficiency of the standard two-carrier Drude model. Section 2.3 discusses the development of a theoretical model to explain the observed phenomena. And we will finally end with a brief application of inhomogeneity to our model (Section 2.4) and final remarks in Section 2.5.

2.1 Experimental System and Methods

In this section, we discuss our devices, their characterisation, and their suitability for investigating electron-hole drag. We also discuss the measurement techniques used to acquire our data.

2.1.1 Device Fabrication and Structure

The devices used while investigating electron-hole drag were high-quality hBN-encapsulated monolayer graphene Hall bars. Device dimensions were patterned to a size of 30 µm × 15 µm, see Figure 2.1. This geometry was not originally optimised for classical diffusive resistivity measurements but rather fabricated for the study of high-current non-equilibrium magnetotransport, see Ref. [29]. In that work, large-area Hall bars were required to exceed the phonon-limited mean free path and resolve magnetophonon resonances under high drift velocities. The length of the Hall bars is limited by the size of the hBN-graphene-hBN stack. Having wider devices also reduces the onset of ballistic transport, effects of boundary scattering, and charge accumulation at edges. At the temperatures relevant for the electron-hole drag measurements, the mean free path is much smaller than the device dimensions, ensuring diffusive, bulk-dominated transport and an effectively homogeneous current distribution away from the contacts.

A brief outline of the fabrication process can be found in Section 1.3. As with all our devices, they were fabricated at the National Graphene Institute (NGI) in Manchester. More information on fabrication details can be found, see ref. [29, 94]

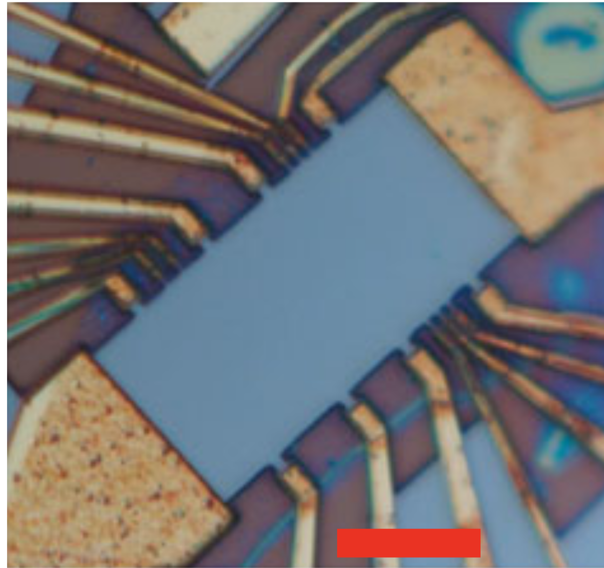

Figure 2.1: Optical image of one of the hBN-encapsulated monolayer graphene Hall-bar devices used in this study. The scale bar is 10 µm.

2.1.2 Measurement Techniques and Protocols

Many of the measurement techniques utilise methods described in Section 1.4. Non-linear quantised effects can be avoided by limiting the magnetic field strength to small values, $|B| \ll 100\,\mathrm{mT}$, see Section 1.2.6 for more details.

2.1.2.1 Non-linear in Magnetic Field Resistance Response

As discussed in Section 1.2.1.1, a simple two-carrier Drude model predicts non-linear contributions to resistivity under magnetic fields (see Eq. (1.22)). While technically feasible, it is complicated to account for these non-linearities in our model and analysis when adding the strong electron-hole interactions expected from a Dirac plasma regime.

Therefore, for simplicity in achieving our goals, we limit our investigation to small magnetic fields where the two-carrier Drude model predicts a linear response in Hall resistance and no response in longitudinal resistance (see Eq. (1.23)).

To consider the linear regime, we will consider acceptable limits on the magnetic field strength, B, such that any non-linear contributions to the measured resistivity are negligible.

Magnetic Field Contributions in Longitudinal Resistance

The longitudinal resistance, ρ_{xx}, has a dependence on externally applied magnetic fields, magnetoresistance, and the cause is not as immediately obvious as the transverse/Hall case. The standard Drude formulation predicts zero change in longitudinal resistance due to magnetic fields according to Eq. (1.21); however, experimental studies confirm that magnetoresistance is present in many metals but typically saturates in low fields with a magnitude of a few percent. The strength of magnetoresistance will vary from material to material and the mechanism for its existence can be different. [14, pp. 234–239]

In conventional metals, the magnetoresistance saturates as the cyclotron frequency, due to Lorentz force, surpasses the scattering rate ($\frac{qB}{m} \gg \frac{1}{\tau} \rightarrow \mu_{e,h}B \gg 1$). For high-mobility devices like ours, with mobilities at room temperature in the order of $10\,\mathrm{m^2\,V^{-1}\,s^{-1}}$, the magnetoresistance onset, as B increases, would occur at $\mu_{\mathrm{e,h}}\mathrm{B} \sim 1$ when $B = 100\,\mathrm{mT}$.

In monolayer graphene near the Dirac point, studies have revealed strong unsaturated B-dependence in longitudinal resistivity [40]. The high-mobility Dirac plasma "exhibits giant parabolic magnetoresistivity reaching more than 100 per cent in a magnetic field of 0.1 tesla at room temperature." That is to say, there is an ap-

proximate doubling of longitudinal conductivity at the neutrality point in a 0.1 T field at 300 K. This behaviour is a direct consequence of near-perfect electron-hole compensation ($n \simeq p$) combined with high carrier mobility, and is therefore closely analogous to the non-saturating quadratic magnetoresistance observed in compensated semimetals such as WTe_2 [38] and, in the low-field regime, bismuth and graphite [36].

The strong magnetoresistance response due to the high mobility Dirac plasma in our device, while scientifically interesting, presents experimental challenges given our requirement to minimise contributions from extraneous interactions and effects. The relative magnetoresistance is shown to evolve quadratically,

$$\mathrm{MR} = [\rho_{xx}(B) - \rho_{xx}(0)]/\rho_{xx}(0) = \mu_{e,h}^2 B^2,$$

consistent with predictions from the two-carrier Drude model for compensated systems according to Eq. (1.26), despite the Drude model's description of two non-interacting fluids. Xin et al [40]. do show that a microscopic description (from kinetic equations) that incorporates interacting fluids yields the same quadratic dependence.

To satisfy ourselves that we do not have magnetoresistance contributions exceeding 1%, we limit our magnetic field. Given that $\mu_{e,h}^2 B^2 = 1.1$ at $B = 0.1\,\mathrm{T}$, the maximum field is constrained to $B_{max} = 0.1\sqrt{0.01/1.1} \approx 10\,\mathrm{mT}$.

Hall Resistance Non-linearities in Magnetic Field

We know from the Drude description that the Hall Resistance will have a linear response to small magnetic fields (see Eq. (1.23)) which highlights the area of primary interest for study. Yet, at higher fields ($\mu_{e,h}B \gtrsim 1$), although still relatively modest due to such high mobility, the two-carrier Drude description predicts quadratic B terms similar to those observed in longitudinal response (see Eq. (1.22)). Consequently, Hall resistance at high fields and small carrier densities may exhibit various non-linear B-dependent behaviors.

To check for any non-linearities caused by unexpected impurities or defects we performed magnetic field sweeps at multiple carrier densities to detect deviations from a linear response across multiple temperatures, as shown in Figure 2.2.

It is observed that a smooth regime change occurs as we go into higher fields in the order of 100 mT, where the Hall resistance becomes non-linear and also non-monotonic (see $V_g = -0.35\,\mathrm{V}$, solid blue line). The B-field sweeps show that at low temperatures (see Figure 2.2(a)) the Hall resistance exhibits a largely linear response at fields below 10-20 mT. Then, perhaps due to some impurity, a small

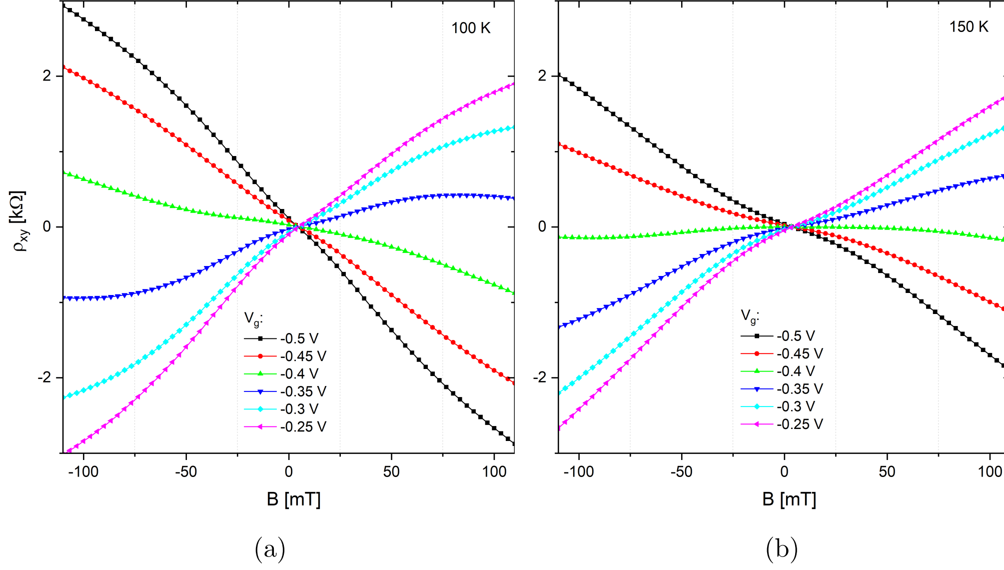

(a) (b)

Figure 2.2: Magnetic field sweeps of Hall resistance at various carrier densities and temperatures. **(a)** 100 K and **(b)** 150 K. The neutrality point is approximately $V_g \simeq -0.40\,\text{V}$. The Hall resistivity magnetic field response appears largely linear in small fields, $|B| \lesssim 20\,\text{mT}$.

non-linearity is seen at around -20 mT when $V_g = -0.35\,\text{V}$ (solid blue line), though this behavior is less pronounced at 150 K (see Figure 2.2(b)). Based on these observations, $|B| \sim 20\,\text{mT}$ marks the upper bound for magnetic field in which Hall resistance is linear in B about $B = 0$. Additional insights emerge from these sweeps: asymmetry between Hall resistance measured in positive versus negative fields is observed, particularly observable at higher carrier densities, likely indicating that there may be some misalignment between Hall contacts used to take the transport measurements. Probe misalignment will cause asymmetry in a magnetic sweep as both ρ_{xx} and ρ_{xy} contribute to measured transverse resistance if the measurement axis is not perpendicular to the current density. This we can correct for, as discussed in Section 1.4.1.

2.1.2.2 High-Field Calibration & Carrier Density Extraction

So far, we have determined that we should limit our field to $B_{\text{max}} = 10\,\text{mT}$ to avoid non-linear contributions to the longitudinal resistance and also quantised effects (see Section 1.2.6). However, accurate Hall-resistance measurements at such low fields are challenging due to accurately determining the magnetic field B. Achieving precise small magnetic fields is challenging due to magnetic hysteresis and remnant flux trapped in the superconducting coils. This can be resolved in other experimental setups by using a magnet and power supply with much better resolving power at

low fields.

Instead, we first perform a high-field calibration at $B = \pm 0.1\,\mathrm{T}$, where the Hall signal is strong and systematic errors in B are no more than 2%.

At elevated net carrier densities, $|n - p| \gg n_{th}$ where n_{th} (see Eq. (1.12)) is the residual carrier density at the neutrality point due to finite temperature, the single-carrier Hall resistivity,

$$\rho_{xy} = \frac{B}{ne},$$

provides a precise mapping between gate voltage and carrier density.

First, we measure Hall resistance, ρ_{xy}, as a function of gate voltage at $B = \pm 0.1\,\mathrm{T}$. Recalling Eq. (1.29), a corrected Hall resistance is extracted from the average of two transverse (Hall) measurements in equal and opposite magnetic fields. Figure 2.3(a) shows the measured Hall resistance of our best device at low temperature (5 K) for $B = \pm 0.1\,\mathrm{T}$, labelled $\rho_{xy,\pm}$ in red and blue, respectively. The black line indicates the average corrected Hall resistance, ρ_{xy}. From the capacitance relation, $C = \frac{Q}{V}$, the net carrier density induced by the gate voltage, V_g, is given by:

$$n - p \;=\; \frac{B}{e\,\rho_{xy}} \;=\; \frac{C}{e}\,(V_g - V_{NP}), \tag{2.1}$$

where C is the areal capacitance to the gate and V_{NP} the charge-neutrality point.

Given the magnetic field is well known, this linear relationship between the carrier density and the gate voltage, by means of a simple linear fit, can be used to extract both the areal capacitance and the offset to the charge-neutrality point, V_{NP}. Such a fit is shown in Figure 2.3(b), yielding $C/e = 5.88 \times 10^{10}\,\mathrm{cm^{-2}\,V^{-1}}$ and $V_{NP} = -0.25\,\mathrm{V}$.

This high-field calibration curve then allows us to use Eq. (2.1) during subsequent low-field measurements ($\leq 10\,\mathrm{mT}$) to accurately infer the magnetic field, B, through measurements of ρ_{xy}.

2.1.2.3 Low-Field Validation Using Sensitive Magnetic Field Probe

With the carrier density calibration established at high fields, our measurement transitions to the low-field regime below 10 mT. This is in the same order as any frozen remnant field in the magnet. In our case, the field of our superconducting magnet is set to zero, and the remnant field is used in our resistivity measurements. No deguassing protocol to reduce this field closer to zero was required. To determine the magnitude of the remnant field, measuring ρ_{xy} as a function of the net carrier density for which we know the relationship of carrier density to the back-gate voltage from the high-field calibration, allows for the determination of $(e\rho_{xy})^{-1}$ vs $n - p$.

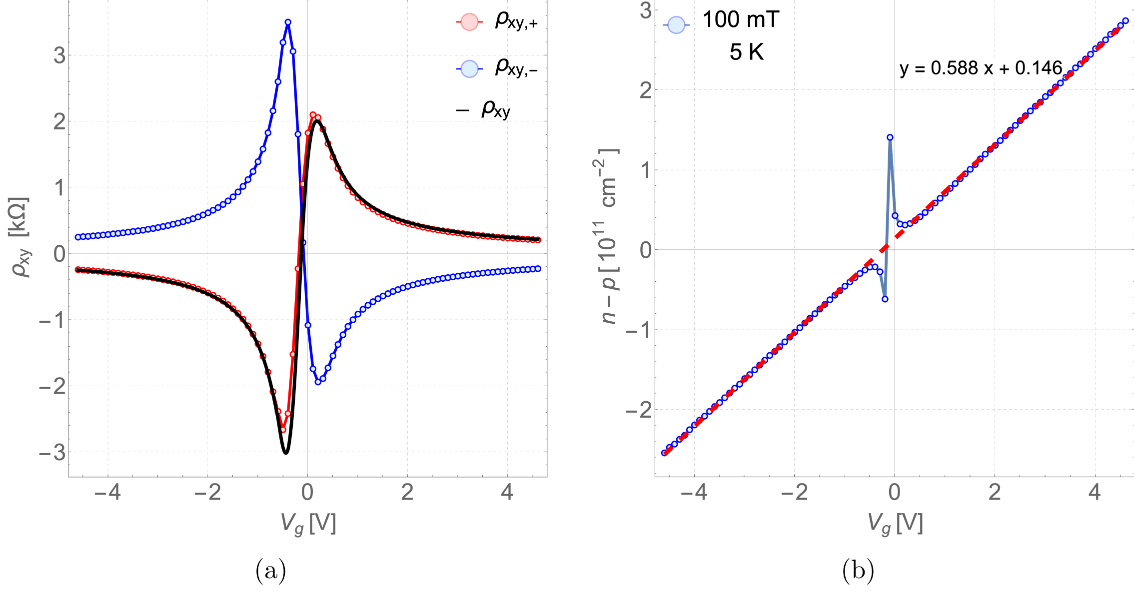

Figure 2.3: **(a)** Measured Hall resistivity, ρ_{xy}, as a function of gate voltage, V_g, at $B = +0.1\,\mathrm{T}$ (red) and $B = -0.1\,\mathrm{T}$ (blue), at 5 K. The black line represents the corrected Hall resistivity ρ_{xy}, obtained as the average of $\rho_{xy,+}$ and $-\rho_{xy,-}$. **(b)** Net carrier density, $n - p$, extracted from the corrected Hall resistivity as a function of V_g. The dashed red line shows a linear fit used to determine the areal capacitance $C/e = 5.88 \times 10^{10}\,\mathrm{cm}^{-2}\,\mathrm{V}^{-1}$ and the neutrality point $V_{NP} = -0.25\,\mathrm{V}$.

The linear relationship between the inverse Hall resistivity and carrier density, seen in Eq. (2.1), gives us the magnetic field, B, as the slope of a linear fit. The results of this measurement are shown in Figure 2.4. However, how was the corrected Hall resistance determined if the magnetic field was unknown?

Using Field Reversal Technique in Low-Field Regime

To correct for geometric artifacts using the field reversal technique Eq. (1.29), the method requires accurately alternating the magnetic field between equal and opposite values (e.g. ± 4 mT perpendicular to the plane). As discussed in Section 2.1.2.2, it is difficult to accurately set the magnetic field to such low values in our setup. For our 15 T magnet, first, the power supply should not be trusted to accurately set the field to 4 mT, and second, the remnant field is on the same order as our target field. To validate any value of magnetic field at these low values, we employed the device itself to be a sensitive magnetic field probe (see Figure 2.4) and determined our field, $B = (4.0 \pm 0.1)\,\mathrm{mT}$.

Then, in order to achieve measurements at $B = -(4.0 \pm 0.1)\,\mathrm{mT}$ we use the Onsager-Casimir reciprocity relations [80] to determine the equivalent Hall resistance for the device in the reciprocal field without having to adjust the actual magnetic field. The details of this method can be found in Section 1.4.1.2.

The validity of the Onsager relation was verified in our device by experimentally checking the Onsager relation at high fields, +0.1 T and -0.1 T. By reversing the magnetic field and swapping current and potential leads, we find that the measured resistances are identical, as predicted by Eq. (1.30).

We can take our transport measurements in a known $B = (4.0 \pm 0.1)\,\mathrm{mT}$ field under configuration A and then switch to configuration B. The Onsager relations allow us to measure the Hall resistance at $B = -(4.0 \pm 0.1)\,\mathrm{mT}$ without having to change the magnetic field, which is particularly useful in our case where low-field precision is difficult to achieve.

Therefore, we can use the reverse-field technique (see Eq. (1.29)) to extract the corrected Hall resistance.

This method was used to determine the Hall resistance at two temperatures, 20 K and 300 K, shown in Figure 2.4(a) by averaging the Hall resistances measured in the two complementary configurations.

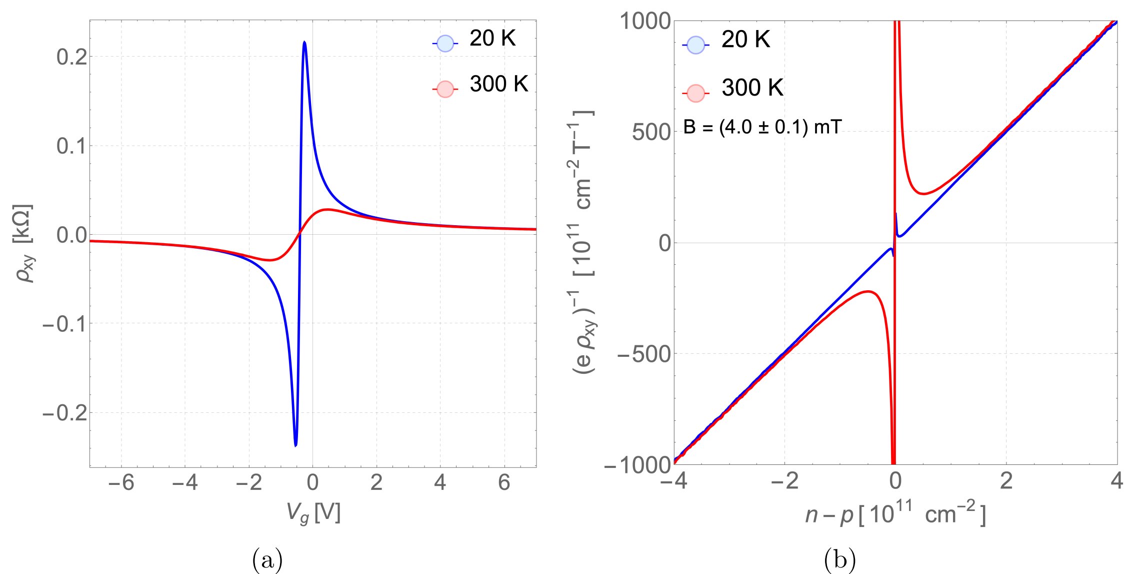

(a) (b)

Figure 2.4: **(a)** Hall resistance, ρ_{xy}, as a function of gate voltage, V_g, at 20 K (blue) and 300 K (red), obtained by averaging measurements in complementary configurations using the Onsager reciprocity relations in a remnant magnetic field. **(b)** Inverse Hall resistance, $(e\rho_{xy})^{-1}$, as a function of net carrier density, $n - p$, at 20 K (blue) and 300 K (red). The slope, $\simeq 250\,\mathrm{T}^{-1}$, gives a remnant magnetic field strength of $B = (4.0 \pm 0.1)\,\mathrm{mT}$.

Using the value of C/e extracted from the high-field calibration (see Figure 2.3(b)) we can convert the gate voltage axis to net carrier density, $n - p$, using Eq. (2.1). Plotting $(e\rho_{xy})^{-1}$ as a function of $n-p$ (see Figure 2.4(b)) the slope is therefore $1/B$, allowing us to determine the remnant magnetic field in our setup. Across the two temperatures, 20 K and 300 K, the slopes were $249\,\mathrm{T}^{-1}$ and $253\,\mathrm{T}^{-1}$, respectively.

This provides a direct and accurate measurement of the perpendicular magnetic field, $B = (4.0 \pm 0.1)\,\mathrm{mT}$, by using the device as a sensitive magnetic field probe. This method is particularly advantageous because it transforms the magnetic field calibration problem into a measurement of transport coefficients, which can be determined with high precision using established electrical measurement techniques. Measurements at multiple temperatures show consistent results.

2.1.2.4 Optimal Choice of AC Excitation

In our experiments we use lock-in amplifiers to produce an AC current through our device and measure the potential at different fixed locations. The choice of AC current excitation parameters, both frequency and amplitude, have important implications on measured resistivity.

As discussed in Section 1.4.2.1, the choice of AC excitation frequency represents a trade-off between measurement speed and noise. Our lock-in AC oscillator frequency was set to 30.3 Hz. This value optimises for measurement accuracy and speed by balancing a few factors: it avoids interference from the 50 Hz mains and its harmonics, it ensures negligible signal phase shift due to the high-impedance capacitance path, and frequency is as high as possible to make measurement times as short as possible. The two main factors are speed and out-of-phase signal. The settling time per measurement point is directly related to the oscillator frequency. Higher frequencies allow for faster measurements, but at the cost of an increased out-of-phase signal. Maintaining the out-of-phase signal below 10% of the in-phase voltage is critical for measurement accuracy and is the generally accepted wisdom. At 30 Hz, this 10% threshold is typically exceeded when contact resistances reach 10-20 kΩ, representing the practical limit for reliable measurements. In our case, the contact resistances are much lower, around 100 Ω to 2 kΩ, ensuring that the out-of-phase signal remains well below this threshold. It is continuously recorded during measurements.

Minimising contact resistances is essential for optimal performance. In our devices, contacts are pseudo one-dimensional; this is important as one-dimensional (edge) contacts offer superior electrical properties compared to conventional two-dimensional interfaces [95]. Most critically, the ground contact maintains low resistance around 100 Ω, which is fundamental for establishing a stable reference potential.

Given the typical values of magnetic field, the estimated order of magnitude of Hall resistance measurements is $\rho_{xy} \sim 10^1 - 10^2\,\Omega$ ($\rho_{xy} \sim \frac{B}{en}$ where $n = n_{th} \rightarrow 5n_{th}$). With Hall resistance approaching zero at high densities and at the neutrality point.

Higher current will give us a larger signal-to-noise ratio, but despite our large 15 µm contact width, we still limit current to avoid excess heating at all temperatures. This is especially true when doing the Onsager configuration, where current flows through the much smaller Hall-bar arms. In fact, we conduct transport measurements at low temperature (5 K) and perform multiple transport sweeps at varying currents, e.g. 100 nA - 1 µA, to check when measured voltage to current becomes non-linear.

Given our lock-in amplifier has an input noise of approximately $300\,\mathrm{nV}/\sqrt{\mathrm{Hz}}$ at an oscillator frequency of 30.3 Hz, a time constant of approximately 300 ms, and an effective bandwidth approximately 0.3 Hz, then our broadband input noise is approximately 170 nV in the best case scenario.

At low currents such as 100 nA, the signal-to-noise ratio (SNR) on a 1 Ω resistance would be limited by this baseline noise, SNR ≈ 0.6 at best. As we increase current, the SNR drastically improves proportionally to the current. For example, at 1 µA, the SNR becomes significantly better and noise is no longer a limiting factor.

As we move to higher currents, we see reduced noise but we start to observe small distortions in the measured resistance. Peaks begin to drift and become larger, likely indicating that the device is heating up and the temperature is no longer well-defined. It is also possible that certain inhomogeneities within the device become apparent at higher currents.

Therefore, we select a current value that is high enough for noise not to be an issue and low enough to avoid excess heating effects. We found that 0.5 µA represents a good compromise, where noise does not exceed acceptable levels and no significant deviations were measured. With 0.5 µA and our measured noise of 170 nV, the corresponding noise-floor is approximately 0.3 Ω, which gives good SNR for experimental observations.

2.1.2.5 Measurement Protocol Overview

In summary, we defined an upper magnetic-field limit of $B_{\mathrm{max}} \approx 10\,\mathrm{mT}$ to suppress non-linear resistivity that arises in high magnetic fields. We determined the relationship between the gate voltage and carrier density. This calibration was performed at high fields, $B = 0.1$ T, free from the uncertainty of low-field conditions. We picked optimal AC current excitation parameters, to maximise signal-to-noise ratio and minimise non-linear excitations and out-of-phase signal contributions. Having verified the validity of the Onsager reciprocity principle in our devices, the longitudinal and Hall resistivities are accurately determined under low-field conditions, 4 mT, using the field-reversal averaging technique (see Eq. (1.29)).

Together, these steps suppress geometric artefacts, eliminate remnant-field ambiguities, and maximise measurement fidelity, enabling reproducible and accurate determination of graphene's intrinsic transport parameters across the full temperature range studied.

2.1.3 Device Quality and Characterisation

At room temperature, with electron n (hole p) carrier densities $n, p \gtrsim 10^{11}\,\mathrm{cm}^{-2}$, our hBN-encapsulated graphene devices exhibit mobility in range $15-18\,\mathrm{m}^2\,\mathrm{V}^{-1}\,\mathrm{s}^{-1}$, consistent with state-of-the-art values. Mobility here is determined by the longitudinal resistivity at high densities, $n \gg n_{th}$, using the single-carrier Drude model (Eq. (1.21)) such $\rho_{xx} = 1/ne\mu_{e,h}$ (for electron gas). Figure 2.5(a) shows the longitudinal sheet resistivity, ρ_{xx}, measured on our best device in zero magnetic field at both 300 K and 5 K as a function of the net carrier density, $n - p$. A black representative line shows the expected single-carrier resistivity Eq. (1.21) for a mobility of $15\,\mathrm{m}^2\,\mathrm{V}^{-1}\,\mathrm{s}^{-1}$ in Figure 2.5(b).

As well as the high mobility, there are a number of other features in the ρ_{xx} data that confirm the device's high quality:

1. **Smooth, symmetric Dirac peak.** At both 300 K and 5 K, ρ_{xx} displays a single, well-defined maximum at the neutrality point, with no discernible asymmetry between the electron and hole sides—suggesting evidence of minimal charge inhomogeneity.

2. **Large low-temperature resistivity enhancement.** The Dirac-peak resistivity at 5 K is roughly three times larger than at 300 K, indicating intrinsic transport down to low temperatures.

3. **Off-peak resistivity drops with cooling.** Away from the neutrality point, ρ_{xx} decreases as temperature is lowered, aligning with reduced phonon scattering and therefore increased carrier mobility. (Note, however, that this temperature dependence alone is not a definitive metric of device quality.)

4. **Dirac-peak narrowing down to a finite width.** The width of the Dirac peak shrinks with decreasing temperature until it saturates at low T; the saturation width is set by disorder-induced carrier-density fluctuations. In our device, the small saturation width indicates very low disorder and permits intrinsic transport at 300 K.

The room temperature peak in resistivity approximately $820\,\Omega$ gives us the shared mobility of electrons and holes at the neutrality point (NP), $\mu_{e,h} = 1/(2n_{th}e\rho_{xx})$ see

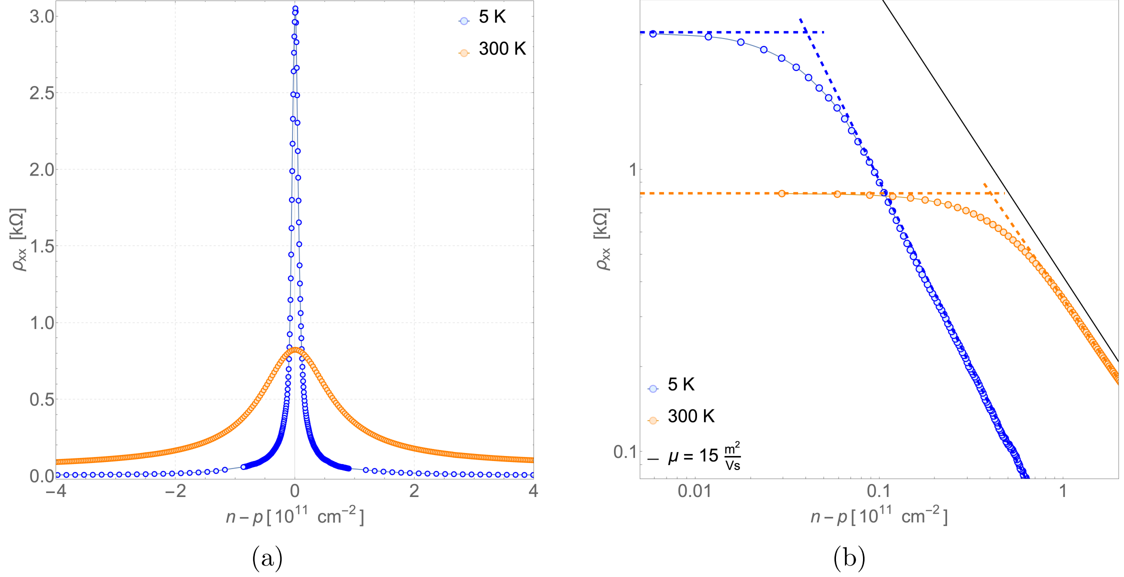

Figure 2.5: Longitudinal resistivity, ρ_{xx}, at room and low temperatures in remnant magnetic field. **(a)** Shows ρ_{xx} as a function of net carrier density, $n-p$, at both 300 K and 5 K. **(b)** ρ_{xx} measured in (a) replotted on a log-log scale. The indicated intersections mark δn, defining the point where resistivity drops, as carrier density becomes proportional to the gate voltage. Solid black line indicates simulated single-carrier resistivity (Eq. (1.21)) at mobility of $15\,\mathrm{m^2\,V^{-1}\,s^{-1}}$.

Eq. (1.26), an approximate value, $\mu_{e,h} = 4.7\,\mathrm{m^2\,V^{-1}\,s^{-1}}$. This is approximately four times lower than the high density mobility of $18\,\mathrm{m^2\,V^{-1}\,s^{-1}}$.

The strength of disorder in the device can be concluded from the maximal narrowing of ρ_{xx} at low T, using a method proposed in Ref. [96] that can be seen by dashed blue lines from Figure 2.5(b) at 5 K. The narrowing given here is the point, δn, at which the high-density 1/n trend intercepts the NP peak. This is the crossover point at which the resistivity goes from being dominated by gate-induced to disorder-induced carrier density.

Disorder in graphene is inevitable, there is no perfectly flat potential landscape. In reality, due to various sources of disorder, such as charged impurities and substrate interface roughness, the potential landscape has random fluctuations in it. This disorder from random potential fluctuations creates localised regions of excess charge called electron-hole puddles. These puddles lead to spatial fluctuations in the local chemical potential with respect to the local Dirac point, resulting in a finite energy window, $\delta\varepsilon_F$, where the effect of gating shifts the Fermi energy window such that it redistributes carriers between electrons and holes rather than altering the absolute number of carriers. As such, the conductivity/resistivity becomes insensitive to the gate voltage near the Dirac point due to disorder, δn. The magnitude of this small energy perturbation due to disorder can be estimated from the residual carrier

density, δn, by using the relation for the Fermi energy in graphene (Eq. (1.14)) replacing n with δn:

$$\delta\varepsilon_F = \hbar v_F \sqrt{\pi \delta n} \tag{2.2}$$

This Fermi energy window is defined by disorder until an expected thermal energy on order of $\delta\varepsilon_F = k_B T$ obscures disorder as thermal carriers become significant and the carrier density near the Dirac point becomes solely thermally induced, $n \to n_{th}$ (see Eq. (1.12)). [96] An approximate relation:

$$\delta\varepsilon = \hbar v_F \sqrt{\pi \delta n} = k_B T \Longrightarrow \delta n = \tfrac{6}{\pi^2} n_{th} \approx 0.6 n_{th}, \tag{2.3}$$

gives a guide towards an expected width of the NP at high temperatures.

From the low-temperature saturation width in Figure 2.5(b), we extract a residual carrier density

$$\delta n \approx (5 \pm 2) \times 10^9\,\mathrm{cm}^{-2} \quad (T = 5\ \mathrm{K}),$$

which exceeds the thermally induced density

$$n_{\mathrm{th}} = \frac{\pi}{6}\left(\frac{k_B T}{\hbar v_F}\right)^2 = 2.2 \times 10^7\,\mathrm{cm}^{-2} \quad (T = 5\ \mathrm{K}),$$

by two orders of magnitude. The strength of the disorder potential can also be estimated using Eq. (2.2), giving $\delta\varepsilon_F \approx 9\,\mathrm{meV}$ (for reference, room temperature $k_B T \approx 26\,\mathrm{meV}$).

This confirms that low-T transport is limited by disorder-induced electron-hole puddles rather than thermal carriers. At 300 K, $n_{\mathrm{th}} = 8 \times 10^{10}\,\mathrm{cm}^{-2}$ and we find

$$\delta n \approx (4 \pm 2) \times 10^{10}\,\mathrm{cm}^{-2} \approx 0.5\, n_{\mathrm{th}},$$

showing that at room temperature transport is intrinsic and not dependent on disorder, consistent with the relation $\delta n \approx 0.6 n_{th}$ for thermal-dominated carrier density.

Graphene on SiO_2 has shown low-temperature saturation, due to puddle-limited δn, is about $7{\times}10^{10}\,\mathrm{cm}^{-2}$ [96]. Whereas, when directly compared with suspended graphene, this drops to roughly $1{\times}10^{10}\,\mathrm{cm}^{-2}$, which is comparable to measurements on hBN-encapsulated monolayer graphene devices [49]. Better results have been reported for suspended bilayer graphene devices where $\delta n \approx 1{\times}10^9\,\mathrm{cm}^{-2}$ [97].

Our disorder-limited residual carrier density, $\delta n \approx 5{\times}10^9\,\mathrm{cm}^{-2}$, is on par with both high-quality hBN-encapsulated and suspended graphene devices, and intrinsic behaviour is expected across our measurement window, 150-300 K.

2.2 Transport Phenomena Near Neutrality Point

We have established the device quality and the measurement protocol, now we can turn our attention to the transport phenomena near the neutrality point (NP). The NP is the point where electron and hole densities are equal, leading to unique inter-carrier interactions that are not available at the single-carrier densities. It is important to understand the behaviour of transport phenomena near the NP because it is where the complex interplay between electron and hole carriers becomes significant, leading to complex macroscopic measurements.

The behaviour of the Hall resistance, ρ_{xy}, near the NP is particularly interesting, but usually overlooked at low temperatures due to the presence of electron-hole puddles. However, as temperature increases, thermal excitations become significant and the transport at the NP becomes intrinsic, warranting a more detailed analysis.

2.2.1 Universal Scaling with Temperature

Before applying the simple two-carrier Drude model (see Eq. (1.24)) let's take a moment to look at the scaling behaviour predicted. In fact, the equations that predict all our experimental measurements of Hall resistance can be scaled, using T^2-scaling, showing that all curves collapse into one dimensionless form.

What is T^2-scaling? Temperature-dependent resistivity comes directly from T-dependent carrier densities, n and p, as given by the T^2 term in the Fermi-Dirac distribution (see Eq. (1.11)). We should be able to reduce all our data to dimensionless equivalents through scaling. This universal scaling will give us a place to generalise, while giving us great predictive power when we reverse the scaling back into the real world.

To find the dimensionless resistivities, ϱ_{xx} and ϱ_{xy}, we take Eq. (1.24) and substitute dimensionless carrier densities, x_e and x_h, for electrons and holes, respectively, scaled from the Fermi-Dirac result in Eq. (1.11):

$$x_{e,h} = \{e, h\} \cdot \left(\frac{k_B T}{\hbar v_F}\right)^{-2} = -\frac{2}{\pi} \operatorname{Li}_2\left(-e^{\pm\eta}\right), \tag{2.4}$$

where, η is the dimensionless chemical potential $\eta = \mu/k_B T$. Experimentally, we control the net carrier density, $n - p$, through the gate voltage. Therefore, in order to plot the resistivities as a function of $n - p$, we need to define x_e and x_h in terms of the dimensionless net carrier density, $x = x_e - x_h$. We can solve the equation $x_e(\eta) - x_h(\eta) = x$ for η numerically for any x; the solution must be numerical as no inverse di-polylogarithm function exists. This gives us $\eta(x)$ as an interpolated

function, from which, $x_e(x)$ and $x_h(x)$ may be defined. Then, we scale the resistivities by the factors that will cancel out all units, giving dimensionless resistivities as functions of x_e and x_h:

$$\begin{aligned} \varrho_{xx} = \rho_{xx} \cdot e\mu_{e,h} \left(\frac{k_B T}{\hbar v_F}\right)^2 &= \frac{1}{(x_e + x_h)}, \\ \varrho_{xy} = \rho_{xy} \cdot \frac{e}{B} \left(\frac{k_B T}{\hbar v_F}\right)^2 &= \frac{x_e - x_h}{(x_e + x_h)^2} \end{aligned} \tag{2.5}$$

The dimensionless longitudinal resistance can be reduced further given the following polylogarithm relation:

$$\begin{aligned} \mathrm{Li}_2\left(-x\right) + \mathrm{Li}_2\left(-\tfrac{1}{x}\right) &= -\tfrac{\pi^2}{6} - \tfrac{1}{2}\log^2 x, \\ \mathrm{Li}_2\left(-e^{\eta}\right) + \mathrm{Li}_2\left(-e^{-\eta}\right) &= -\tfrac{\pi^2}{6} - \tfrac{1}{2}\eta^2, \\ \varrho_{xx} = \frac{1}{(x_e + x_h)} &= \frac{1}{\left(\frac{\pi}{3} + \frac{1}{\pi}\eta^2\right)} \end{aligned} \tag{2.6}$$

It can be seen from this relation that the longitudinal resistance has the form of an inverse quadratic in respect to the chemical potential, $1/(a + cx^2)$.

The scaling of resistivity, seen in Eq. (2.5), predicts that for all temperatures and at the same magnetic field, the measured Hall resistance, $\rho_{xy}(n-p)$, will fall onto the same line when plotted as $\rho_{xy} \cdot T^2$ versus $(n-p)/T^2$. A prediction that can be directly tested experimentally. *Note: this does not apply to the longitudinal resistivity, ρ_{xx}, as it is dependent on mobility, which is temperature dependent.*

Figure 2.6 shows the plots of the dimensionless longituidinal and Hall resistivities (Eq. (2.5)) as a function of dimensionless carrier density. We see that at high densities that $\varrho_{xx} = \varrho_{xy}$, consistent with the single-carrier Drude model (Eq. (1.21)) that is shown in dimensionless form as green dashed lines. Given the complexity of polylogarithm functions, many points of interest do not have simple closed-form solutions and are expressed numerically. The peaks in Hall resistivity occur at $x_e - x_h \approx \pm 1.086$ with a value of $\varrho_{xy} = \pm 0.507$. As predicted from Eq. (2.6), the maximum in longitudinal resistivity occurs at the neutrality point with an exact value of $\varrho_{xx} = 3/\pi$. And the half-width-half-maximum in the longitudinal resistivity is $x_e - x_h \approx 1.90$. The method used previously (see Section 2.1.3) to determine the point where resistivity becomes disorder-dominated, δn, can be applied here to the dimensionless resistivity. This is simply where the high-density $1/(x_e - x_h)$ trend intersects the peak resistivity, giving $x_e - x_h = \pi/3 \approx 1.05$. This value is very similar to the point where the Hall resistivity peaks. These points of interest can be a useful reference when comparing to experimental results.

The ratio of Hall resistance to longitudinal resistance is given by the dimensionless

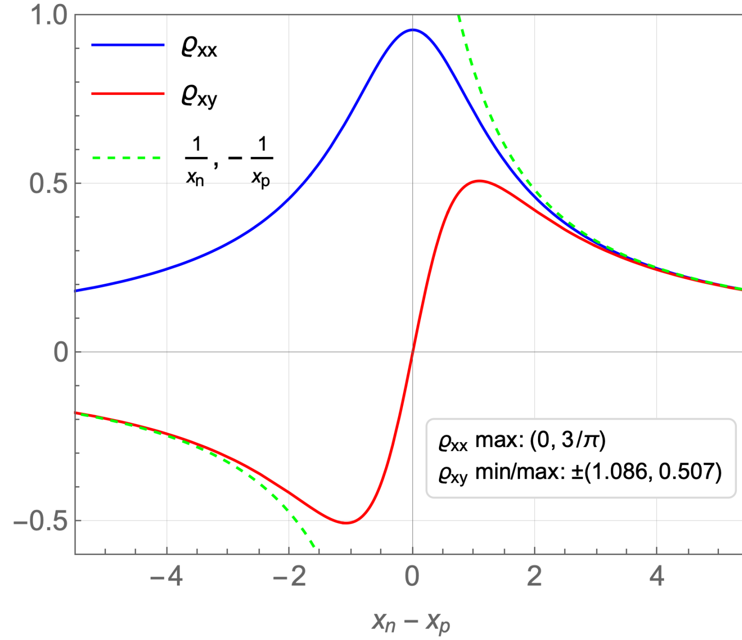

Figure 2.6: Scaled dimensionless resistivity, ϱ_{xx}, and Hall resistivity, ϱ_{xy}, derived from two-carrier Drude model when electron and hole mobilities are equal (see Eq. (2.5)) as a function of dimensionless net carrier density $x_e - x_h$. The single-carrier Drude model result is shown as green dashed lines that diverge near the neutrality point. Eq. (2.5) were evaluated by calculating x_e and x_h as a function of η numerically.

Hall parameter β:

$$\beta = \frac{\rho_{xy}}{\rho_{xx}} = \frac{\varrho_{xy}}{\varrho_{xx}}\mu_{e,h}B = \frac{x_e - x_h}{x_e + x_h}\mu_{e,h}B$$

which is a useful sigmoid-like function that smoothly transitions from $-\mu_{e,h}B$ to $+\mu_{e,h}B$ as the net density changes. We will come back to this parameter in Section 2.4.

To scale these dimensionless resistivities back to the real world, we simply inverse the scaling factors used in Eq. (2.5).

This T^2 scaling begs a simple question: if the amplitude of the resistivity is inversely proportional to T^2 and the carrier density, thus the half-width of the resistivity, is proportional to T^2, what happens at low temperatures? Theoretically, in the model that we have described thus far, as T gets smaller, the peak Hall resistance will just get indefinitely larger and larger, while the half-width approaches zero. So, let's see what happens experimentally.

2.2.2 Hall Resistivity & Predictions of the Drude Model

Using all the methods described in Section 2.1.2, we can now measure the Hall resistivity, ρ_{xy}, as a function of net carrier density $n-p$ and temperature T. This corresponding behavior of Hall resistivity at room temperature is shown in Figure 2.7. The Hall resistivity is measured in a weak magnetic field of $(4.0 \pm 0.1)\,\mathrm{mT}$, which is low enough to ensure linearity in the Hall response, avoiding quantised effects as discussed in Section 1.2.6.

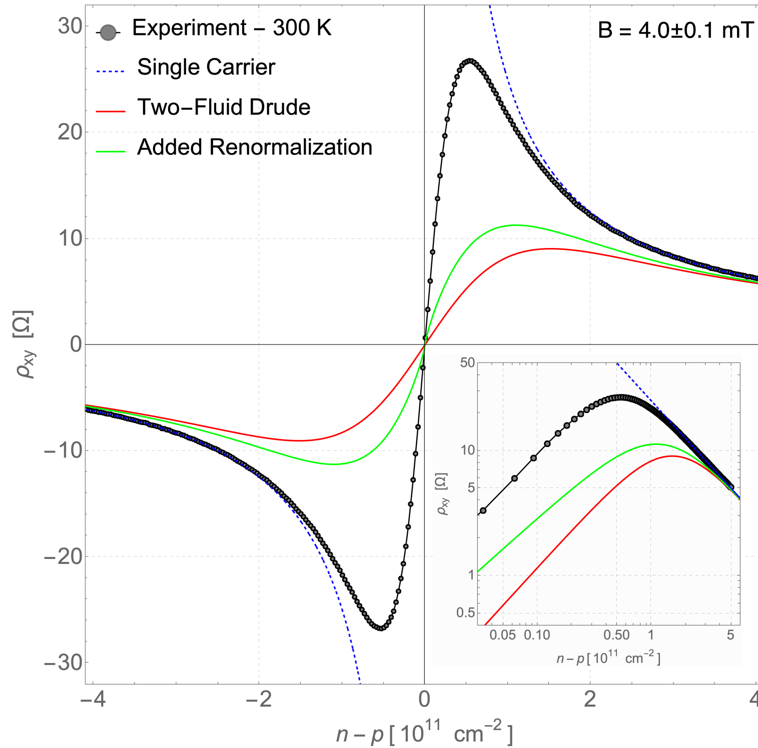

Figure 2.7: Hall resistivity, ρ_{xy}, as a function of net carrier density $n-p$ at 300 K, and perpendicular magnetic field $(4.0 \pm 0.1)\,\mathrm{mT}$. The data is overlaid with theoretical model fits: a single-carrier model (blue dashed line), a two-carrier Drude model (red solid line), also with added Fermi velocity renormalization (green solid line). Inset: log-log plot of same data and models.

Away from the neutrality point, the Hall resistivity ρ_{xy} evolves following the inverse-linear dependence on carrier density n as predicted by the single-carrier Drude model (see Eq. (1.21)) given by the dashed blue line (Figure 2.7). This model diverges as it approaches the NP, where the single-carrier approximation fails with the introduction of oppositely charged carriers. As such, the Hall voltage tends to zero as we approach the NP, where electron and hole densities are equal, $n_e = n_h$, and the net effect of the magnetic field on the transverse voltage is zero. Through the NP, the Hall resistivity ρ_{xy} changes sign, indicating a transition of the majority carrier type between electrons and holes.

A simple two-carrier Drude description of Hall transport measurements is used, see Eq. (1.24), where carrier density is determined from the Fermi-Dirac statistics and the linear dispersion, see Eq. (1.11). The model, which has no fitting parameters, fails to accurately characterise the NP transport and in fact appears to do a little worse than the single carrier description as we approach the NP, shown as a red line in Figure 2.7. The peak of the simulated Hall resistance is smaller and occurs at higher densities compared to what was observed experimentally.

The two-carrier model has a good fit to room temperature data when the Fermi velocity is increased 70% (not shown). However, graphene's Fermi velocity is well characterised, as experiments consistently find v_F of $(1.0 - 1.1) \times 10^6\,\mathrm{m\,s^{-1}}$. [10–12] Methods of measurement include: determining the amplitude of SdH oscillations vs temperature to determine the cyclotron mass, which is directly related to the Fermi velocity (see Eq. (1.7)); mapping the density of states through measurements of quantum capacitance; and by angle-resolved photoemission spectroscopy (ARPES).

Fermi velocity greater than double has been observed in suspended graphene, where dielectric screening is negligible when density is small ($< 10^{11}\,\mathrm{cm^{-2}}$). [98] This divergence from the linear dispersion relation occurs due to renormalisation. Renormalisation, a term from quantum theory, is when a parameter is adjusted to account for an interaction. In this case, our linear dispersion relation defining the Fermi velocity is adjusted to account for electron-electron interactions.

In typical devices on SiO_2 or hBN, screening by the substrate keeps v_F close to its nominal value. Electron-electron interactions will renormalise the Dirac spectrum in encapsulated graphene but only modestly in comparison to suspended devices. For example, detailed quantum-capacitance studies on hBN-encapsulated graphene devices show that v_F grows by $\sim$ 10-20%. [99] These numbers are far below a 70% shift, and also given that renormalisation is masked by thermal broadening at higher temperatures, this alone cannot explain our poor fit. By using a similar logarithmic Fermi velocity fit used by Yu et al. [99], the renormalisation is added to the two-carrier Drude model and still does not account for the poor fit to the data, as shown in green on Figure 2.7.

Recent high-mobility magnetotransport measurements reveal strong interaction phenomena that are largely independent of single-particle v_F but instead arise from many-body scattering through electron-hole Coulomb interactions. [40] Such evidence points away from renormalisation of v_F as the source of discrepancy but towards strong inter-carrier interactions.

Instead of abandoning the Drude framework outright, we should acknowledge that our simple two-carrier Drude model is missing important physics of Dirac plasmas - electron-hole scattering. Before investigating such an interaction source, the

assumption of equal mobility for electrons and holes can be relaxed by making mobility our fitting parameter for data, which we discuss in Section 2.2.3.

T-Dependence of the Hall Resistivity

Recalling the two-carrier Drude model, without disorder (Eq. (1.24)) we can take the difference in density between the maximum and minimum in ρ_{xy} to be our characteristic density, $2\delta n_H$. Given that the dimensionless peak in ϱ_{xy} is at net density 1.086 (see Figure 2.6) a characteristic density of $\delta n_H \approx 1.086(\frac{k_B T}{\hbar v_F})^2 \approx 2.07 n_{th}$ is predicted, which is four times larger than our measured value above 150 K, as seen comparing the model black line and the coloured experimental data in Figure 2.8(b).

As seen previously (see Section 2.1.3) the measured characteristic density below which the longitudinal resistivity only weakly depends on the applied gate voltage, δn, at room temperature is approximately $(4 \pm 2) \times 10^{10}\,\mathrm{cm}^{-2} \approx 0.5\, n_{\mathrm{th}}$, indeed approximately four times smaller than the model prediction. At room temperature, the measured Hall resistivity gives $\delta n_H \approx 5 \times 10^{10}\,\mathrm{cm}^{-2}$. This is consistent with the longitudinal resistivity's characteristic density, δn, and as such, we can see that $\delta n \simeq \delta n_H$ at least at room temperature. The similarity of these two widths follows naturally from carrier compensation, which suppresses both longitudinal and Hall responses: longitudinal resistivity saturates because increasing gate voltage mainly redistributes carriers between electrons and holes; and Hall resistivity is suppressed because opposite charges contribute with opposite sign. The close agreement between δn and δn_H cross-validates longitudinal and Hall measurements, demonstrating that two independent transport coefficients, derived from separate components of the resistivity tensor, are governed by the same underlying microscopic mechanism.

By taking many measurements of ρ_{xy} across a wide range of temperatures, not just room temperature, we can see how these different aspects evolve (see Figure 2.8). The similarity between δn and δn_H holds across our entire temperature range from 5 K up to 300 K and evolves parabolically in temperature as shown in Figure 2.8(b).

The NP width defined by δn and δn_H at high temperatures, above 150 K, have an approximate T^2-dependence consistent with n_{th}. This translates into an approximate linear dependence in energy according to Eq. (2.3). Using Eq. (2.2), the neutrality point width can be expressed in terms of energy as shown in the inset of Figure 2.8(b), that confirms above 150 K the NP width becomes more linear on the order of $k_B T$.

At lower temperatures, below 150 K, the width does not tend toward zero with thermal carriers, but the width begins to saturate towards a density due to disorder that results in fluctuations in charge density (electron-hole puddles). These observations are consistent with the longitudinal resistance and point towards high-quality

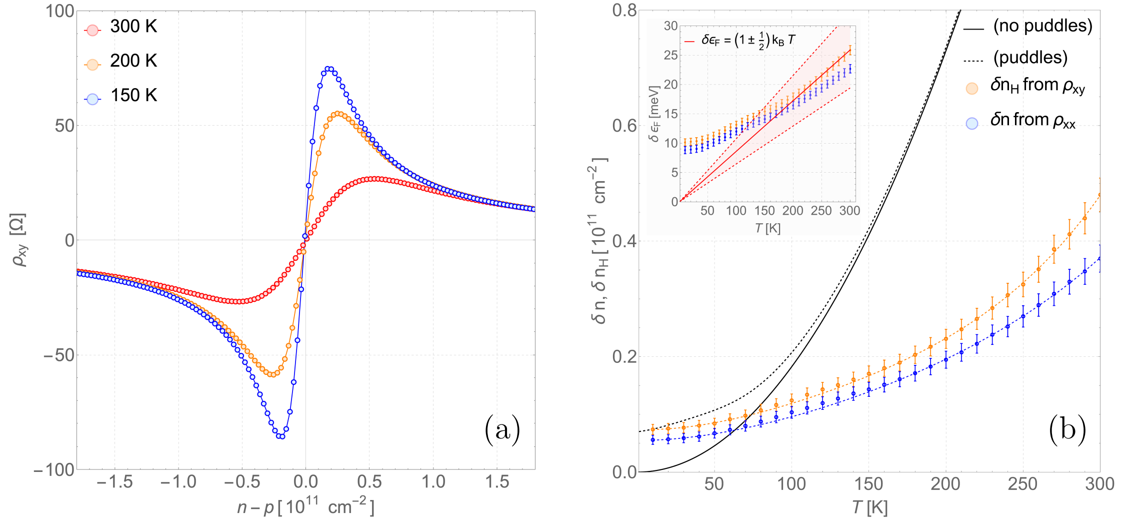

Figure 2.8: (a) Hall resistivity, ρ_{xy}, as a function of net carrier density, $n-p$, at three different temperatures, 150 K, 200 K, and 300 K. (b) δn and δn_H extracted from the Hall and longitudinal resistivities, respectively. Black curves: δn_H expected from the standard Drude model where the dashed line indicates the inclusion of electron-hole puddles. Inset: Equivalent Fermi energy due to δn as defined by Eq. (2.3) where $k_B T$ window is highlighted red.

graphene.

As our temperature window for analysis is safely above 150 K, mainly considering room temperature data, effects of scattering mechanisms due to disorder can be safely set aside.

2.2.3 Drude Model with Unequal and Negative Mobilities

The application of the two-carrier Drude model so far has assumed equal mobility for electrons and holes, $\mu_e = \mu_h = \mu_{e,h}$, in order to create a model with zero fitting parameters, which, as shown in Section 2.2.2, had poor adherence to the experimental data. This assumption was made assuming electrons and holes respond independently to an applied electric field, $\mathbf{E}$, and as such, have the same drift velocity response.

In this section, we will explore how to relax the Drude model to account for unequal mobilities and the possibility of negative mobilities. In this regime, the model no longer has zero fitting parameters, but two in the form of electron and hole mobilities, μ_e and μ_h.

We can work backwards to calculate the electron and hole mobilities necessary to reproduce our data at the correct temperature.

Assuming $n, p \geq 0$, the equations for ρ_{xx} and ρ_{xy}, Eq. (1.23) can be rearranged

to calculate mobility from experimental data. Starting from

$$\rho_{xx} = \frac{1}{e\,(n\mu_e + p\mu_h)}, \quad \rho_{xy} = \frac{B}{e}\,\frac{n\mu_e^2 - p\mu_h^2}{(n\mu_e + p\mu_h)^2},$$

we define the substitutions

$$\alpha \equiv \frac{1}{e\,\rho_{xx}} = n\mu_e + p\mu_h, \qquad \beta \equiv \frac{e\,\rho_{xy}}{B} = \frac{n\mu_e^2 - p\mu_h^2}{\alpha^2}.$$

Hence, the simultaneous equations for the mobilities can be written as:

$$n\mu_e + p\mu_h = \alpha, \quad n\mu_e^2 - p\mu_h^2 = \beta\,\alpha^2.$$

We eliminate μ_h and substitute:

$$n\mu_e^2 - p\Big(\tfrac{\alpha - n\mu_e}{p}\Big)^2 = \beta\,\alpha^2 \implies n(p-n)\,\mu_e^2 + 2\alpha n\,\mu_e - \alpha^2(1+\beta p) = 0.$$

Solving the quadratic for mobility finds

$$\mu_e = \frac{\alpha}{n(p-n)}\Big[-n \pm \sqrt{np\,(1 - \beta(n-p))}\Big].$$

Finally, choosing the sign that ensures $\mu_e \geq 0$ when $n > p$ and substituting α, β back gives

$$\begin{aligned} \mu_e &= \frac{1}{e\,(n-p)\,\rho_{xx}}\left[1 - \sqrt{\frac{p}{n}\left(1 - \frac{e\,\rho_{xy}}{B}\,(n-p)\right)}\right] \\ \mu_h &= -\frac{1}{e\,(n-p)\,\rho_{xx}}\left[1 - \sqrt{\frac{n}{p}\left(1 - \frac{e\,\rho_{xy}}{B}\,(n-p)\right)}\right] \end{aligned} \qquad (2.7)$$

where μ_h is given by symmetry $n \leftrightarrow p,\ \mu_e \leftrightarrow \mu_h$.

Using Eq. (2.7), we can calculate the mobilities from our experimental data, ρ_{xx} and ρ_{xy}, as a function of net carrier density $n-p$. The results for room temperature data is shown in Figure 2.9. The mobility is calculated for both electrons and holes, μ_e and μ_h, separately. The large density dependence of mobility shows the mistake of assuming constant mobility when making predictions using the Drude model. Here are some important observations:

- The most striking feature is that when the net carrier density, $n-p$, is negative (the hole density is greater than the electron density), then the electron mobility continues to decrease and becomes zero at a net carrier density of approximately $|n| \gtrsim n_{th}$. The electron mobility then becomes negative, saturating at an absolute value comparable to the hole mobility at the same carrier density. Vice versa happens for hole mobility when holes become the minor-

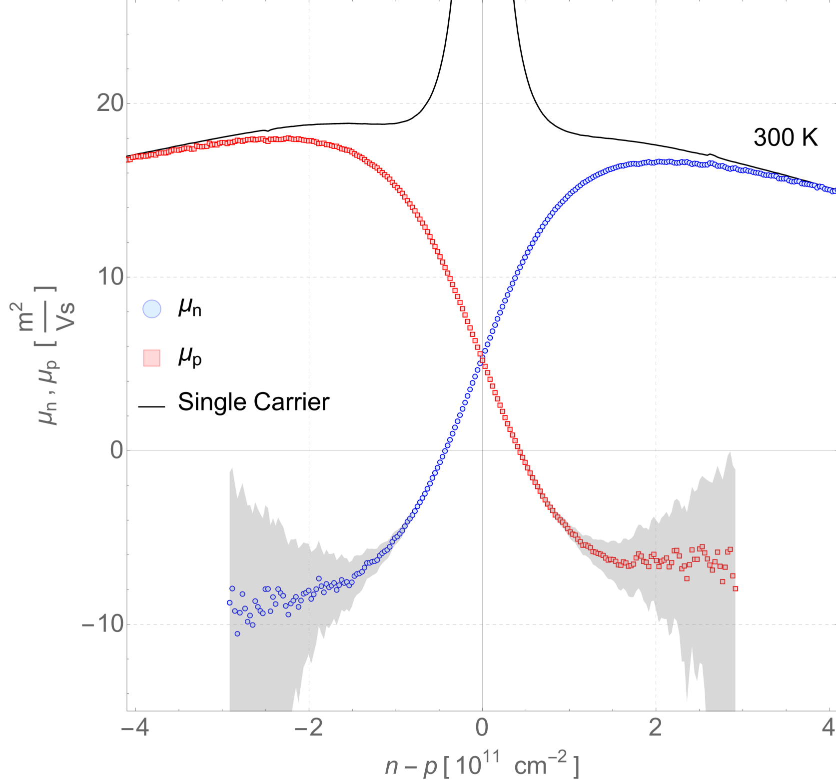

Figure 2.9: Room temperature mobility of electrons (blue circles) and holes (red squares) extracted using two-carrier Drude model, where mobility is the fitting parameter. ρ_{xx} and ρ_{xy} was measured at 300 K in a low magnetic field of 4.0 ± 0.1 mT. The black line is the mobility extracted under the assumption of one type of charge, $1/(e|n-p|\rho_{xx})$. The grey shaded area indicates the error in mobility due to the uncertainty in the Hall resistivity, ρ_{xy}, of $\pm 0.2\,\Omega$.

ity carrier at positive net density. This is a significant finding as it indicates that the minority carriers have a drift velocity in the opposite direction than what is expected from the applied electric field, $\boldsymbol{\nu}_d \approx \mu_{e,h}\mathbf{E}$. This is due to an interaction that drags them to a velocity that compares with the majority carriers.

- When the net carrier density, $n - p$, is positive (the electron density is greater than the hole density), then the electron mobility, μ_e, is positive and has an initial increase with increasing carrier density. There is a maximum mobility, approximately $17\,\mathrm{m}^2/\mathrm{Vs}$, at around $3n_{th}$, before a monotonic decrease in mobility with further increasing of carrier density. A trend that is consistent with other mobility measurements on comparable hBN encapsulated graphene devices [95]. Vice-versa is observed for the hole mobility, μ_h, expected from symmetry.

- The measured neutrality point mobility is approximately $1/(2en_{th}\rho_{xx})$. Con-

sistent with the two-carrier Drude model, when mobilities of electrons and holes are the same (see Eq. (1.26)).

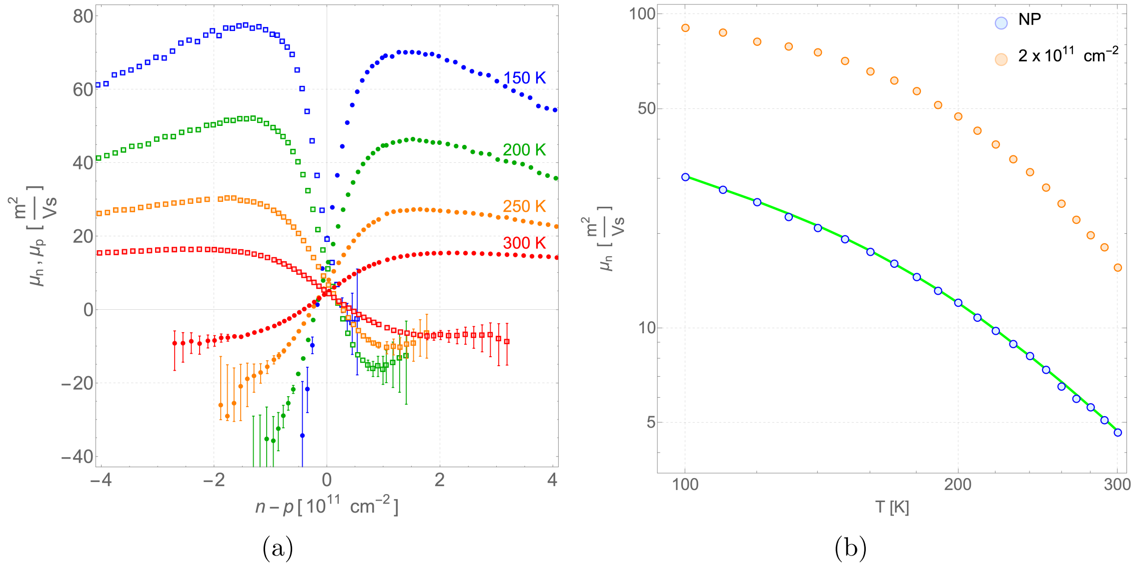

Figure 2.10: **(a)** Temperature-dependent mobility of electrons (solid circles) and holes (hollow squares) measured at various temperatures in a low magnetic field of 4.0 ± 0.1 mT. **(b)** Electron mobility versus temperature extracted from data in (a) at the neutrality point (blue) and at a carrier density of 2×10^{11} cm^{-2} (orange). Mobility derived from the minimum conductivity, $\mu_{e,h} = 1/(2en_{th}\rho_{xx})$, is shown in green.

The reversal in the drift direction of minority carrier was observed consistently across the 150 K to 300 K temperature range in our study (Figure 2.10). To further understand this effect, we analysed the temperature dependence of the extracted mobilities both at the neutrality point, $n = p = n_{th}$ and at finite single carrier densities, $n - p = 2 \times 10^{11}$ cm^{-2}. The results are shown in Figure 2.10(b). Both the neutral density and finite density mobilities show comparable strong monotonic temperature dependences, suggesting no significant change in temperature-dependent scattering mechanisms between single and dual carrier fluids.

As a consistency check, the mobility calculated solely from the minimum conductivity (peak resistivity) assuming density is given by thermal carriers is shown in green in Figure 2.10(b). As shown, the NP mobility calculated from Eq. (2.7) is consistent with the minimum conductivity mobility expected for a compensated two-carrier system with $\mu_e = \mu_h$:

$$\sigma_{min} = \sigma_e + \sigma_h = en\mu_{e,h} + ep\mu_{e,h} = 2(n+p)e\mu_{e,h} \Longrightarrow \mu_{e,h} = 1/(2en_{th}\rho_{xx}).$$

The Drude model definition $\mu_{e,h} = \frac{e\tau_{e,h}}{m_{e,h}}$ (Eqs. (1.16) and (1.17)) uses macroscopic measurements to infer two microscopic fitting parameters $\tau_{e,h}$, which should be

strictly positive. These parameters, under the assumption of two non-interacting fluids, fit our experimental data for negative values, which implies non-physical behavior and therefore the breakdown of model assumptions.

2.2.3.1 Limitations of the Drude Model Near the Neutrality Point

As we saw in Figure 2.7, the two-carrier Drude model poorly describes transport near the neutrality point (NP) when no fitting parameter is used. And, as we saw in Figure 2.9, the mobilities of electrons and holes, when used as fitting parameters to experimental data, return negative values for mobility, which, in the context of a typical Drude description of mobility, requires unphysical negative scattering times.

What is missing from our model to accurately describe the NP transition in Hall resistance? In Section 1.2.1.4, we defined the model result is valid under the assumption that the electron and hole transport processes are independent of each other. This means that they do not interfere with each other's contribution to the total current density, and thus, their conductivities can be linearly superposed. At carrier densities sufficiently far from neutrality, this non-interacting assumption remains valid, as the system tends towards a single-carrier 2DEG.

In reality, this assumption may hold for other semiconductors and semimetals under low-field conditions where scattering with impurities is dominant; however, in high-quality monolayer graphene in the Dirac plasma the contribution of coulomb interactions between the two carrier types looks to be very significant, evidenced also by hydrodynamic transport.

The incorrect application of this non-interacting two-carrier Drude model in a situation of significant inter-carrier interactions then could describe the observed negative mobilities; however, we need a new microscopic description of the transport that takes into account the electron-hole scattering, that does not lead to negative scattering times.

If we consider the scattering of oppositely charged carriers, we find a second indication that the Drude description is flawed. In the standard Drude model scattering is assumed to be isotropic, a reasonable assumption as lattice defects, impurities, and phonon scattering are expected to be equal in all directions. But the addition of charge carrier scattering makes this assumption invalid, as the applied electromagnetic fields cause the momentum of the two fluids to be equal and opposite in the electric field direction but in the same direction in the transverse/Hall direction, leading to anisotropic scattering.

We must therefore create a formulation where the contribution from electron-hole scattering, τ_{eh}, is taken effectively into account. This does not necessarily

mean we must throw out a Drude description of the problem, but rather, modify the microscopic description to account for negative mobility, as we will discuss in the next section.

2.3 Boltzmann Transport Model and Microscopic Theory

The kinetic equation stems directly from Boltzmann's kinetic theory for dilute gases [100, 101], later extended by Lorentz to describe electrons scattering off ions. [102] This theoretical framework forms the basis of the semiclassical Boltzmann transport equation (BTE). [103, pp. 7–11]

The BTE applies to a dilute gas (or gas-like system of particles) where particles follow free linear paths between instantaneous binary collisions, where those collisions obey conservation laws and drive the system toward local equilibrium.

Under these conditions, Boltzmann's equation provides a powerful semiclassical framework for predicting how distributions of particles evolve and how macroscopic transport phenomena emerge from microscopic dynamics.

Compared to the Drude model, the BTE introduces a full distribution function, $f_{\mathbf{k}}(\mathbf{r}, t)$, that evolves in both real and momentum space, providing a more general and flexible framework for describing transport phenomena in materials, including those with multiple scattering mechanisms. BTE can recover the standard Drude model under certain criteria, such as collisions described by a single constant relaxation time and spatial homogeneity. [14, pp. 250–251]

The BTE is given by: [104, pp. 46–47]

$$\partial_t f(\mathbf{v}, \mathbf{r}, t) \; + \; \mathbf{v} \cdot \partial_{\mathbf{r}} f(\mathbf{v}, \mathbf{r}, t) \; + \; \mathbf{F} \cdot \partial_{\mathbf{v}} f(\mathbf{v}, \mathbf{r}, t) \; = \; (\partial_t f)_{\text{coll}} \tag{2.8}$$

where $f(\mathbf{v}, \mathbf{r}, t)$ is the distribution function of particles with velocity $\mathbf{v}$ at position $\mathbf{r}$ and time t. $\mathbf{F}$ is any externally applied force on the particles. The left-hand side describes the free transport of particles, while the right-hand side, $(\partial_t f)_{\text{coll}}$, denotes the change in distribution function due to collisions that drives the particle distribution toward equilibrium.

2.3.1 Kinetic Equation for Coupled Electron-Hole System

Our kinetic equation, that describes the evolution of the electronic probability distribution function (Eq. (1.10)) for an electron-hole fluid, is the Boltzmann equation (Eq. (2.8)) with the Lorentz force included:

$$\partial_t f_{\mathbf{k},\lambda}(\mathbf{r},t) + \boldsymbol{v}_{\mathbf{k},\lambda} \cdot \nabla_{\mathbf{r}} f_{\mathbf{k},\lambda} - e(\mathbf{E} + \boldsymbol{v}_{\mathbf{k},\lambda} \times \mathbf{B}) \cdot \nabla_k f_{\mathbf{k},\lambda} = \mathcal{I}_{ee}[f_{\mathbf{k},\lambda}] + \mathcal{I}_{dis/ph}[f_{\mathbf{k},\lambda}] \quad (2.9)$$

where $f_{\mathbf{k},\lambda}(\mathbf{r},t)$ is the electronic probability density function given by the Fermi-Dirac distribution (Eq. (1.10)) with momentum $\mathbf{k}$ and band index (electrons or holes) λ at position $\mathbf{r}$ and time t. $\boldsymbol{v}_{\mathbf{k},\lambda}$ is the group velocity of an electron in band λ with crystal momentum $\mathbf{k}$, $\boldsymbol{v}_{\mathbf{k},\lambda} = 1/\hbar \nabla_{\mathbf{k}} \varepsilon_{\mathbf{k},\lambda}$, where $\varepsilon_{\mathbf{k},\lambda}$ is the energy of the state with wavevector $\mathbf{k}$ and band index λ. $\mathbf{E}$ and $\mathbf{B}$ are the externally applied electric and magnetic fields, respectively. The terms $\mathcal{I}_{ee}$ and $\mathcal{I}_{dis/ph}$ encapsulate collision terms for electron-electron interactions and disorder/phonon scattering, respectively.

The term $\boldsymbol{v}_{\mathbf{k},\lambda} \cdot \nabla_{\mathbf{r}} f_{\mathbf{k},\lambda}(\mathbf{r},t)$ represents a redistribution of f towards equilibrium wherever spatial gradients exist. Physically, this looks like a diffusion or drift of carriers from regions of higher density toward regions of lower density, driving spatial equilibration.

The term $-e(\mathbf{E} + \boldsymbol{v}_{\mathbf{k},\lambda} \times \mathbf{B}) \cdot \nabla_k f_{\mathbf{k},\lambda}(\mathbf{r},t)$ represents the force exerted by electric, $\mathbf{E}$, and magnetic, $\mathbf{B}$, fields on the charge carriers, with $\boldsymbol{v}_{\mathbf{k},\lambda}$ denoting the carrier's velocity. This term captures the influence of Lorentz force on the carrier's dynamics in the momentum space (∇_k), driving the redistribution of f according to the external field application.

$\mathcal{I}_{ee}$ and $\mathcal{I}_{dis/ph}$ denote effects of different types of collisions. $\mathcal{I}_{ee}[f_{\mathbf{k},\lambda}(\mathbf{r},t)]$ refers to the electron-electron interaction integral, representing the scattering events between charge carriers that can redistribute their momentum and energy. On the other hand, $\mathcal{I}_{dis/ph}[f_{\mathbf{k},\lambda}(\mathbf{r},t)]$ encompasses the combined effects of scattering due to disorder and phonon interactions, accounting for the interactions between charge carriers and imperfections or vibrational modes within the material lattice.

2.3.2 Analytical Modified Drude Equations for Interacting Two-Carrier System

Reducing the kinetic equation (see Eq. (2.9)) into a parameterised Drude-like form that allows us to derive expressions for mobility and Hall resistance while accounting for electron-hole interactions is a non-trivial task. This is not work undertaken by myself but by Dr. Alessandro Principi [105] who collaborated with us on this project. The rest of Section 2.3.2 is summarising this derivation.

More details can be found in the supplementary material of our published work. [106]

Drude-like equations were derived and here are outlined some key assumptions made.

Assumptions Made to Reduce Kinetic Theory to Drude-like Equations

1. The system is in a steady state, $\partial_t f_{\mathbf{k},\lambda}(\mathbf{r},t) = 0$, eliminating explicit time dependence.

2. The system is spatially homogeneous, $\nabla_{\mathbf{r}} f_{\mathbf{k},\lambda}(\mathbf{r},t) = 0$, meaning the distribution function does not depend on position.

3. Electron-hole interactions are assumed to not change the number of electrons in each band but allows momentum transfer between the bands. It is assumed that the momentum lost from one band is gained in the other, ensuring that the total momentum of the system is conserved in these interactions. By contrast, disorder/phonon scattering is treated as a momentum-relaxing process.

4. The distribution functions for electrons and holes are assumed to take specific forms based on Fermi-Dirac statistics and are approximated linearly in the context of small deviations from the Fermi energy, such:

$$f_{\mathbf{k},\lambda} \equiv f^{(0)}(\varepsilon_{\mathbf{k},\lambda}) + (-\partial_{\varepsilon_{\mathbf{k},\lambda}} f^{(0)}(\varepsilon_{\mathbf{k},\lambda}))\mathbf{k} \cdot \mathbf{u}_\lambda$$

   where $f^{(0)}(\varepsilon_{\mathbf{k},\lambda})$ is the equilibrium Fermi-Dirac distribution (Eq. (1.10)), $\varepsilon_{\mathbf{k},\lambda}$ is the energy of the state with wavevector $\mathbf{k}$ and band index λ, and $\mathbf{u}_\lambda$ is the drift velocity of the band.

5. Collision integrals are parameterised using the relaxation time approximation, whereby small deviations from equilibrium are treated within a linearised response framework characterised by a relaxation time. For disorder/phonons, τ is a characteristic time for carrier distribution to relax back to equilibrium. For electron-hole collisions, τ_{eh} is the characteristic time for carrier distribution to relax back to equilibrium towards a common drift velocity, $\mathbf{u}_\lambda$:

$$\mathcal{I}_{dis/ph} \simeq \frac{f_{\mathbf{k},\lambda} - f^{(0)}(\varepsilon_{\mathbf{k},\lambda})}{\tau}, \quad \mathcal{I}_{eh} \simeq \frac{f_{\mathbf{k},\lambda} - (f^{(0)}(\varepsilon_{\mathbf{k},\lambda}) + (-\partial_{\varepsilon_{\mathbf{k},\lambda}} f^{(0)}(\varepsilon_{\mathbf{k},\lambda}))\mathbf{k} \cdot \mathbf{u}_\lambda)}{\tau_{eh}}$$

Boltzmann Drude-like Equations

The result from the kinetic equation (Eq. (2.9)) with the assumptions described above, leads to a Drude-like form. Treating the bands (electrons/holes) separately

gives a set of coupled equations for the drift velocities of electrons and holes, $\mathbf{u}_e$ and $\mathbf{u}_h$, in the presence of an electric field $\mathbf{E}$ and magnetic field $\mathbf{B}$:

$$\begin{aligned} -\frac{e}{m_e}\left(\mathbf{E}+\mathbf{u}_e\times\mathbf{B}\right) &= \frac{\rho_h}{\rho_e+\rho_h}\frac{\mathbf{u}_e-\mathbf{u}_h}{\tau_{eh}}+\frac{\mathbf{u}_e}{\tau} \\ \frac{e}{m_h}\left(\mathbf{E}+\mathbf{u}_h\times\mathbf{B}\right) &= \frac{\rho_e}{\rho_e+\rho_h}\frac{\mathbf{u}_h-\mathbf{u}_e}{\tau_{eh}}+\frac{\mathbf{u}_h}{\tau} \end{aligned} \tag{2.10}$$

where τ is a Drude fitting parameter for the relaxation time due to disorder and impurity scattering, while, τ_{eh} is the relaxation time for electron-hole interactions. $\mathbf{E}$ and $\mathbf{B}$ represent the contribution of externally applied electric and magnetic fields. Finally, $\rho_{e,h}$, $m_{e,h}$ are the mass density and effective mass for electrons/holes respectively, which are analytical expressions defined below (Eqs. (2.12)–(2.13)) that come out of the kinetic theory, see supplementary material of Ref. [106] for more details. As such, the effective mass here is not the cyclotron mass (Eq. (1.6)) that is typically used, recall defining effective mass in Section 1.1.2.1. Mass density is a new quantity not defined previously, it appears as a collection of terms in the kinetic theory that have units of mass per unit area.

These equations of motion retain the familiar structure of the Drude model for each carrier type. On the left-hand side, the Lorentz force drives electrons and holes in response to electric and magnetic fields. On the right-hand side, the term proportional to $1/\tau$ represents the conventional momentum-relaxing 'friction' due to impurity or phonon scattering that always acts in the opposite direction of the drift velocity. The new additional term, scaled by $\rho_h/(\rho_e+\rho_h)$ (or $\rho_e/(\rho_e+\rho_h)$) and proportional to $1/\tau_{eh}$, captures inter-carrier friction or drag arising from electron-hole collisions.

When the electron-hole scattering rate $1/\tau_{eh}$ is sufficiently high (and $1/\tau$ sufficiently low) and the mass density of the opposite carrier type is dominant, then the inter-carrier drag term can overwhelm the applied force term. In this regime, carriers drift opposite to the applied field, producing the experimentally observed negative mobility.

This result is a further generalisation of the standard Drude model that adds a new term to Eq. (1.15), such:

$$\left[\frac{d\mathbf{p}}{dt}\right]_{field}+\left[\frac{d\mathbf{p}}{dt}\right]_{eh-scatter}+\left[\frac{d\mathbf{p}}{dt}\right]_{ph/imp-scatter}=0$$

And when $\tau_{eh}\to\infty$, the electron-hole scattering term vanishes, and we recover the standard Drude model (see Eq. (1.16)).

2.3.2.1 Derived Quantities from Kinetic Theory

To recast the kinetic theory model into a Drude-like form, collections of terms were gathered together such that our transport equation is described in terms for the effective mass, $m_{e/h}$, and mass density, $\rho_{e/h}$. This requires recalling that carrier density, $n_{e,h}$, is given by the integral, over energy, of the Fermi-Dirac distribution, $f(\varepsilon)$, multiplied by the density of states for graphene, $g(\varepsilon)$ (see Eqs. (1.9)–(1.11)). Starting with the Fermi-Dirac distribution $f(\varepsilon, \pm\mu)$ and the graphene density of states $g(\varepsilon)$, we find:

$$n_{e,h} = \int_0^\infty f(\varepsilon, \pm\mu) g(\varepsilon) d\varepsilon = -\frac{2}{\pi}\left(\frac{k_B T}{\hbar v_F}\right)^2 \mathrm{Li}_2\left(-e^{\pm\mu/k_B T}\right) \tag{2.11}$$

$$D_{e,h} = -\frac{v_F^2}{2}\int_0^\infty \frac{d\,f(\varepsilon, \pm\mu)}{d\varepsilon}\, g(\varepsilon)\, d\varepsilon = \pm\frac{v_F^2}{2}\frac{d(n_{e,h})}{d\mu} = -\frac{k_B T}{\pi\hbar^2}\,\mathrm{Li}_1\left(-e^{\pm\mu/(k_B T)}\right)$$

$$m_{e,h} = \frac{n_{e,h}}{D_{e,h}} = \frac{2}{v_F^2}\frac{n_{e,h}}{dn_{e,h}/d\mu} = 2\frac{k_B T}{v_F^2}\frac{\mathrm{Li}_2\left(-e^{\pm\mu/k_B T}\right)}{\mathrm{Li}_1\left(-e^{\pm\mu/k_B T}\right)} \tag{2.12}$$

$$\rho_{e,h} = \frac{3}{2v_F^2}\int_0^\infty \varepsilon f(\varepsilon, \pm\mu) g(\varepsilon) d\varepsilon = \frac{3}{2}\cdot 2\frac{k_B T}{v_F^2}\cdot -\frac{2}{\pi}\left(\frac{k_B T}{\hbar v_F}\right)^2 \mathrm{Li}_3\left(-e^{\pm\mu/k_B T}\right) \tag{2.13}$$

where $n_{e,h}$ is the carrier density, $D_{e,h}$ is a coefficient to calculate mass, $m_{e,h}$ is the effective mass, and $\rho_{e/h}$ is the mass density; where subscript denotes electrons/holes respectively. ε is the carrier energy relative to the Dirac point, μ is the chemical potential, T is the temperature and v_F is the Fermi velocity. Li_n denotes a polylogarithm function of order n.

Given the polylogarithmic limits:

$$\frac{\mathrm{Li}_2\left(-e^x\right)}{\mathrm{Li}_1\left(-e^x\right)} = \begin{cases} 1, & x \ll -1, \\ \frac{\pi^2}{12\ln 2}, & x = 0, \\ \frac{x}{2}, & x \gg 1. \end{cases}$$

then the expression for mass, $m_{e/h}$, predicts a finite effective carrier mass at all energies when $T \neq 0$:

$$m_e = \begin{cases} 2\frac{k_B T}{v_F^2}, & \mu \ll -k_B T, \\ \frac{\pi^2}{6\ln 2}\frac{k_B T}{v_F^2}, & \mu = 0, \\ \frac{\mu}{v_F^2}, & \mu \gg k_B T. \end{cases}$$

As a consistency check, we can see that the effective mass reduces to the temperature

independent cyclotron mass (Eq. (1.7)) in the high-energy/low-temperature limit, $\mu \gg k_B T$.

This effective mass comes out of the kinetic theory and, by means of analogy using Eq. (2.12), described as depending on both the number of carriers (carrier-density, $n_{e,h}$) and how easy it is to add more (compressibility, $\frac{dn}{d\mu}$). When $\frac{dn_{e,h}}{d\mu}$ is high, it means there are lots of energy states available near the Fermi energy. Electrons can easily hop into these states when perturbed, making the system more responsive to external forces (less 'massive'). Figure 2.11 illustrates the smooth crossover between the thermal and high-energy/low-temperature limits and confirms the predicted T^2-scaling of the effective mass.

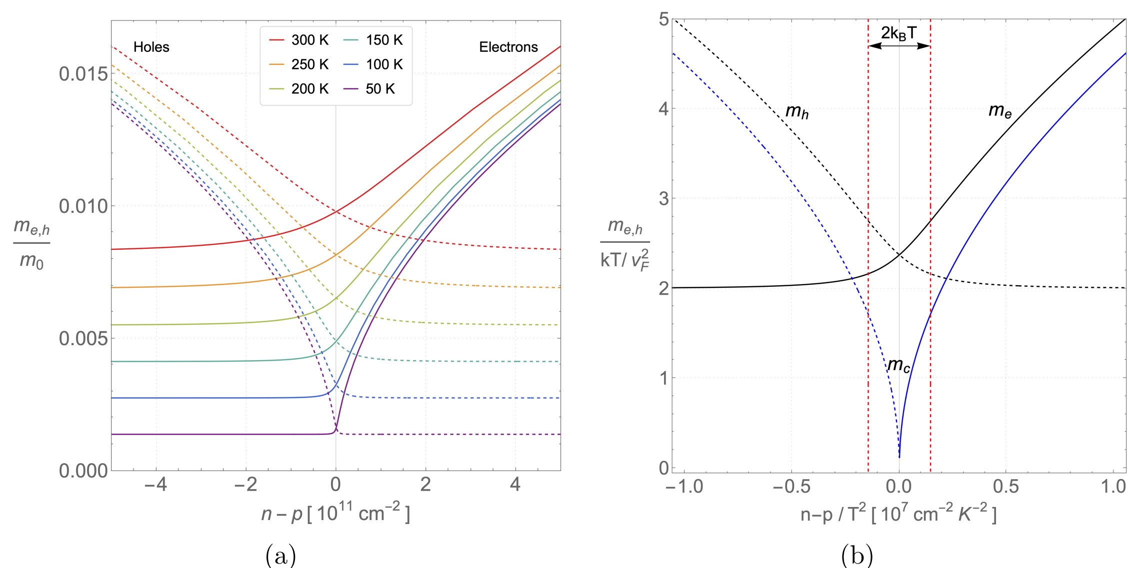

Figure 2.11: Effective Mass (Eq. (2.12)) of electrons (solid) and holes (dashed) as a function of net carrier density. **(a)** Effective mass in units of bare electron mass across temperatures 50-300 K. **(b)** Shows scaling behaviour of the effective mass function. Effective mass in units of $k_B T/v_F^2$ vs T^2-scaled net density. Red dashed lines indicate carrier density where the chemical potential is equal to $\pm k_B T$.

Similarly to the effective mass, the mass density (see Eq. (2.13)) formed here comes out of collecting terms together from the kinetic theory. It is analogous to the average energy density divided by the Fermi velocity squared.

Given the polylogarithmic limits:

$$-\operatorname{Li}_3\left(-e^x\right) = \begin{cases} e^x, & x \ll -1, \\ \frac{3}{4}\zeta(3), & x = 0, \\ \frac{x^3}{6}, & x \gg 1. \end{cases}$$

where zeta function is given by $\zeta(s) = \sum_{n=1}^{\infty} \frac{1}{n^s}$, such $\zeta(3) \approx 1.202$. Then the

expression for mass density, $\rho_{e/h}$:

$$\rho_e = \begin{cases} \frac{3}{2}\cdot 2\frac{k_BT}{v_F^2}\cdot\frac{2}{\pi}\left(\frac{k_BT}{\hbar v_F}\right)^2 e^{\mu/k_BT} \equiv \frac{3}{2}m_e n_e, & \mu \ll -k_BT, \\ \frac{9(k_BT)^3}{2\pi\hbar^2 v_F^4}\zeta(3) \approxeq 2\ln(2)\, m_e n_e, & \mu = 0, \\ \frac{\mu}{v_F^2}\cdot\frac{\mu^2}{\pi\hbar^2 v_F^2} \equiv m_e n_e, & \mu \gg k_BT. \end{cases}$$

We can see that the mass density returns the product of mass and carrier density, in the high-energy/low-temperature limit, $\mu \gg k_BT$.

Figure 2.12 illustrates the smooth evolution of the carrier mass density across the neutrality point and its crossover from thermal to high-energy behaviour, consistent with the limiting cases above of Eq. (2.13).

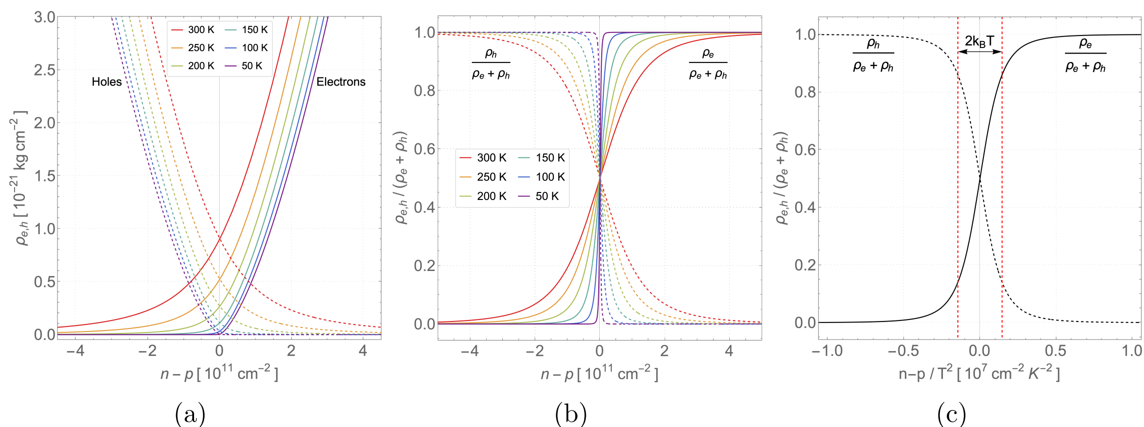

Figure 2.12: Mass Density (Eq. (2.13)) of electrons (solid) and holes (dashed) as a function of net carrier density. **(a)** Mass density across temperatures 50-300 K. **(b)** Shows the ratio of electron/hole density out of the total mass density as a function of net carrier density. **(c)** Shows the T^2 temperature dependence behaviour of (b), where red dashed lines indicate carrier density where the chemical potential is equal to $\pm k_BT$.

2.3.3 Mobility and Hall Response from the Drag-Modified Drude model

In Section 2.3.2, we have shown how the inclusion of inter-carrier scattering in a Boltzmann-based kinetic model leads naturally to drag-modified two-fluid Drude equations of motion for electrons and holes. In this section, we will derive macroscopic transport properties such as mobility and Hall response from these equations.

Zero B-field Mobility

In the absence of a magnetic field ($B = 0$), the drift velocities $\mathbf{u}_e$ and $\mathbf{u}_h$ are

parallel to the applied electric field $\mathbf{E} = E\,\hat{x}$, and the vector equations of motion (see Eq. (2.10)) reduce to the scalar system:

$$
\begin{aligned}
-\frac{e\tau}{m_e}\,E &= \frac{\tau}{\tau_{eh}}\,\frac{\rho_h}{\rho_e+\rho_h}(u_e-u_h)\;+\;u_e,\\
\frac{e\tau}{m_h}\,E &= \frac{\tau}{\tau_{eh}}\,\frac{\rho_e}{\rho_e+\rho_h}(u_h-u_e)\;+\;u_h,
\end{aligned}
\tag{2.14}
$$

It is convenient to define the single carrier mobilities in conventional Drude form and condense the drag-coefficient terms into α:

$$
\mu_{e,0} = \frac{e\,\tau}{m_e},\quad \mu_{h,0} = \frac{e\,\tau}{m_h},\quad \alpha_e = \frac{\tau}{\tau_{eh}}\,\frac{\rho_h}{\rho_e+\rho_h},\quad \alpha_h = \frac{\tau}{\tau_{eh}}\,\frac{\rho_e}{\rho_e+\rho_h},
$$

then in these variables, Eqs. (2.14) become

$$
\begin{pmatrix} -\mu_{e,0}\,E \\ \mu_{h,0}\,E \end{pmatrix} = \begin{pmatrix} 1+\alpha_e & -\alpha_e \\ -\alpha_h & 1+\alpha_h \end{pmatrix} \begin{pmatrix} u_e \\ u_h \end{pmatrix}.
$$

The determinant of the 2×2 coefficient matrix is $\Delta = (1+\alpha_e)(1+\alpha_h) - \alpha_e\alpha_h = 1+\alpha_e+\alpha_h$. Inverting, one finds

$$
\begin{aligned}
u_e &= -\frac{(1+\alpha_h)\,\mu_{e,0} - \alpha_e\,\mu_{h,0}}{1+\alpha_e+\alpha_h}\,E,\\
u_h &= \frac{(1+\alpha_e)\,\mu_{h,0} - \alpha_h\,\mu_{e,0}}{1+\alpha_e+\alpha_h}\,E.
\end{aligned}
\tag{2.15}
$$

We may thus define the effective mobilities $\mu_e = -E/u_e$ and $\mu_h = E/u_h$ in terms of mass density and relaxation times:

$$
\begin{aligned}
\mu_e &= \mu_{e,0} - (\mu_{e,0}+\mu_{h,0})\frac{\rho_h}{\rho_e+\rho_h}\frac{\tau}{\tau+\tau_{eh}},\\
\mu_h &= \mu_{h,0} - (\mu_{e,0}+\mu_{h,0})\frac{\rho_e}{\rho_e+\rho_h}\frac{\tau}{\tau+\tau_{eh}}
\end{aligned}
\tag{2.16}
$$

It is now we clearly see negative mobility that results from electronic drag description when we consider these limits:

Limit $n_h \gg n_e$ (holes are majority carriers), $\tau \gg \tau_{eh}$:

$$
\frac{\rho_h}{\rho_e+\rho_h} \to 1,\quad \frac{\rho_e}{\rho_e+\rho_h} \to 0,\quad \frac{\tau}{\tau+\tau_{eh}} \to 1,
$$

$$
\mu_e \to \mu_{e,0} - (\mu_{e,0}+\mu_{h,0}) = -\mu_{h,0},\qquad \mu_h \to \mu_{h,0}.
$$

Electron mobility is fully dominated by hole drag and has a value equal and opposite to the hole mobility, while hole mobility stays at its conventional value.

Limit $n_e \gg n_h$ (electrons are majority carriers), $\tau \gg \tau_{eh}$:

$$\frac{\rho_h}{\rho_e + \rho_h} \to 0, \qquad \frac{\rho_e}{\rho_e + \rho_h} \to 1, \qquad \frac{\tau}{\tau + \tau_{eh}} \to 1,$$

$$\mu_e \to \mu_{e,0}, \qquad \mu_h \to \mu_{h,0} - (\mu_{e,0} + \mu_{h,0}) = -\mu_{e,0}.$$

Hole mobility is fully dominated by electron drag and has a value equal and opposite to the electron mobility, while electron mobility stays at its conventional value.

Limit $\tau_{eh} \gg \tau$ (no electron-hole scattering, conventional Drude model):

$$\frac{\tau}{\tau + \tau_{eh}} \to 0,$$

$$\mu_e \to \mu_{e,0}, \qquad \mu_h \to \mu_{h,0}.$$

Evaluating in the limit of no electron-electron interaction the mobility returns to the expected conventional value, $\mu_{e,h} = e\tau/m_{e,h}$ where $m_{e,h}$ (Eq. (2.12)) was shown to be positive and finite across all energies, when temperature is also finite. Therefore, mobility is also always positive and finite in the absence of inter-carrier interactions and in the limits with respect to the chemical potential:

$$\mu_e = \begin{cases} e\tau \frac{v_F^2}{2k_BT}, & \mu \ll -k_BT, \\ e\tau \frac{6\ln 2}{\pi^2} \frac{v_F^2}{k_BT}, & \mu = 0, \\ e\tau \frac{v_F^2}{\mu}, & \mu \gg k_BT. \end{cases}$$

We can expect minority carrier mobility to saturate to fixed value proportional to disorder relaxation time and inversely proportional to temperature, when $\tau \to \infty$.

Eq. (2.16) are equally written in terms of effective mass:

$$\begin{aligned} \mu_e &= \frac{e\tau}{m_e}\left[1 - \left(1 + \frac{m_e}{m_h}\right)\left(1 + \frac{\rho_e}{\rho_h}\right)^{-1}\left(1 + \frac{\tau_{eh}}{\tau}\right)^{-1}\right], \\ \mu_h &= \frac{e\tau}{m_h}\left[1 - \left(1 + \frac{m_h}{m_e}\right)\left(1 + \frac{\rho_h}{\rho_e}\right)^{-1}\left(1 + \frac{\tau_{eh}}{\tau}\right)^{-1}\right]. \end{aligned} \tag{2.17}$$

Evaluating the mobility at the neutral point where $m_e = m_h = m_{NP}$ and $\rho_e = \rho_h$ finds:

$$\mu_{NP} = \frac{e\tau}{m_{NP}}\left[1 - \left(1 + \frac{\tau_{eh}}{\tau}\right)^{-1}\right] = \frac{e\tau}{m_{NP}}\left(1 + \frac{\tau}{\tau_{eh}}\right)^{-1} = \frac{e}{m_{NP}}\left(\frac{1}{\tau} + \frac{1}{\tau_{eh}}\right)^{-1}$$

where $m_{NP} = \frac{\pi^2}{6\ln 2}\frac{k_BT}{v_F^2}$ is the effective mass at the neutrality point by evaluating Eq. (2.12) at the zero Fermi energy.

When the scattering rate to phonons and impurities is much greater than the inter-carrier scattering rate, $\frac{1}{\tau} \gg \frac{1}{\tau_{eh}}$, then neutrality point mobility is given by the conventional mobility, $\mu_{NP} = e\tau/m_{NP}$. Conversely, when the inter-carrier scattering rate dominates, $\frac{1}{\tau_{eh}} \gg \frac{1}{\tau}$, the neutrality-point mobility is given by $\mu_{NP} = e\tau_{eh}/m_{NP}$.

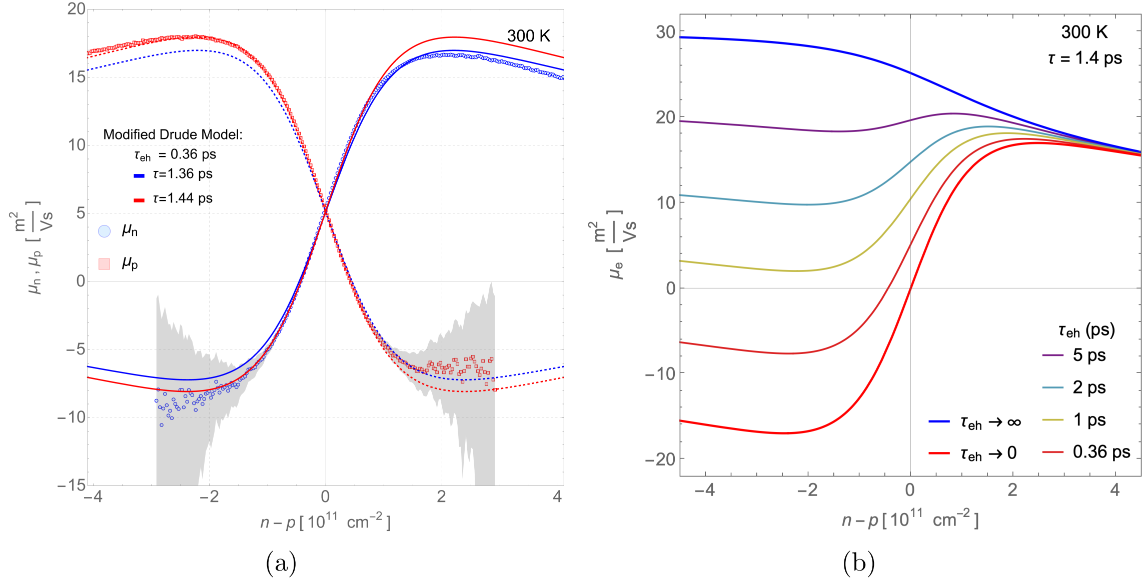

Figure 2.13: Mobility vs net carrier density with constant fitting parameters, τ and τ_{eh}. **(a)** Electron (blue circles) and hole (red squares) mobility measured experimentally at 300 K in small B-field 4.0 ± 0.1 mT (same as Figure 2.9) where grey shaded area is the error in measurement. The blue and red lines are fits to the experimental data for electron (solid) and hole (dashed) mobility under the zero magnetic field solution of the modified Drude model (Eq. (2.16)) where $\tau_{eh} = 0.36$ ps. **(b)** Reference curves for electron mobility under different values of τ_{eh} when $\tau = 1.4$ ps.

Longitudinal and Hall resistivities were combined with the two-carrier Drude model to extract mobility (see Figure 2.9). Figure 2.13, compares the drag-modified Drude model mobility to this experimental data and indicates several important transport characteristics in the studied system. Notably, one might expect density-dependent scattering times (due to the interplay of different scattering mechanisms at room temperature), yet taking constant scattering times τ and τ_{eh}, one finds a good fit for most of the room temperature mobility data.

Although individual microscopic scattering mechanisms can be density dependent, constant τ_{eh} is expected in the near-neutrality regime at fixed temperature because the relevant quasiparticle population is the total carrier density $n+p$, which is set mainly by thermal excitation (and residual density) and, therefore, varies only weakly as the gate tunes the net density $n-p$. Once the system is driven far from neutrality, the minority carrier density rapidly diminishes and the electron-hole drag contributes progressively less to the measured mobility.

As seen in Figure 2.13(a), there is a mild discrepancy between the observed and

modelled mobility, between the hole-dominated region (negative chemical potential / net carrier density) and the electron-dominated region (positive chemical potential / net carrier density). Fitting the hole majority transport is better described by a 1.44 ps relaxation time (red) whereas electron majority transport finds a best fit of approximately 1.36 ps (blue). This slight asymmetry from subtle inhomogeneity in transport highlights the sensitivity to τ of these measurements. In both cases in regions of weaker model agreement, the symmetry of larger-than-expected majority carrier mobility and correspondingly larger-than-expected negative minority mobility suggests that electron-hole drag remains consistently strong.

In Figure 2.13(b) we see also the sensitivity of the mobility to the electron-hole scattering parameter τ_{eh} is significant; as τ_{eh} decreases below approximately four times τ, the mobility behavior becomes non-monotonic, ultimately leading to negative mobility when $\tau_{eh} < 1$ ps. This behavior solidifies the expectation that negative mobility is a direct indication of hydrodynamic flow, as τ_{eh} is significantly smaller than τ. Finally, considering the strong electron-hole scattering limit, as $\tau_{eh} \to 0$, mobility exhibits symmetry around the neutrality point, confirming that minority carriers become fully dragged by the majority carriers, there is no bi-directional flow.

2.3.3.1 Low-Field Mobility and Hall Resistance

Thus far, we have shown that using two constant relaxation scattering times in a drag-modified two-fluid Drude model is adequate to reproduce measured experimental mobility for a two-fluid system. However, laboratory measurements invariably probe resistivity, both longitudinal ρ_{xx} and transverse (Hall, ρ_{xy}), in a finite magnetic field. By extending this model to derive an expression for the Hall resistance, we gain a direct, measurable link to our two microscopic parameters τ (the phonon and disorder scattering time) and τ_{eh} (the inter-carrier scattering time).

Recall that, under the small-field approximation, both the single-carrier model (see Eq. (1.21)) and the non-interacting two-carrier model (Eq. (1.23)) predict a longitudinal resistivity independent of B and a transverse (Hall) resistivity linear in B, as is observed experimentally.

Let us consider the resistivity response that emerges when a weak magnetic field is applied in our drag-modified Drude model. Treating the magnetic field B as a small perturbation about our $B = 0$ solution, we will linearise the coupled drift-velocity equations to first order in B. As we have seen, linearisation is justified experimentally under small magnetic fields and will simplify our equations.

Following linearisation, we will deduce the resistivity tensor describing transport

measurements in a drag-modified Drude system.

Linearised Equations of Motion around B=0

We start with the equations of motion for electrons and holes (see Eq. (2.10)) these are coupled equations for the drift velocities of electrons and holes, $\mathbf{u}_e$ and $\mathbf{u}_h$, in the presence of an electric field $\mathbf{E}$ and magnetic field $\mathbf{B}$ given by:

$$\begin{aligned} -\mu_{e,0}(\mathbf{E} + \mathbf{u}_e \times \mathbf{B}) &= \alpha_e(\mathbf{u}_e - \mathbf{u}_h) + \mathbf{u}_e, \\ \mu_{h,0}(\mathbf{E} + \mathbf{u}_h \times \mathbf{B}) &= \alpha_h(\mathbf{u}_h - \mathbf{u}_e) + \mathbf{u}_h, \end{aligned} \tag{2.18}$$

$$\begin{aligned} \mu_{e,0} = \frac{e\tau}{m_e}, &\quad \mu_{h,0} = \frac{e\tau}{m_h}, \\ \alpha_e = \frac{\rho_h}{\rho_e + \rho_h}\frac{\tau}{\tau_{eh}}, &\quad \alpha_h = \frac{\rho_e}{\rho_e + \rho_h}\frac{\tau}{\tau_{eh}} \end{aligned} \tag{2.19}$$

where it is convenient to introduce conventional mobility parameters $\mu_{e,0}$ and $\mu_{h,0}$ for electrons and holes, respectively, and dimensionless drag coefficients α_e and α_h that control the electron-hole drag. $\rho_{e,h}$, $m_{e,h}$ are the carrier mass densities and effective masses (derived in the previous section Eq. (2.12)–(2.13)), τ is the momentum-relaxation time due to disorder/impurities, and τ_{eh} characterises the inter-carrier (electron-hole) scattering time.

Given a small perturbing magnetic field $\mathbf{B}$, we assume correspondingly small changes in the electric field, $\delta\mathbf{E}$, and drift velocity, $\delta\mathbf{u}_{e,h}$ that are proportional to $\mathbf{B}$. Therefore, substituting

$$\mathbf{u}_{e,h} \to \mathbf{u}_{e,h} + \delta\mathbf{u}_{e,h}, \quad \mathbf{E} \to \mathbf{E} + \delta\mathbf{E}$$

into one of the drag-modified Drude equations Eq. (2.18)(the second follows identically):

$$-\mu_{e,0}(\mathbf{E} + \delta\mathbf{E} + \mathbf{u}_e \times \mathbf{B} + \delta\mathbf{u}_e \times \mathbf{B}) = \alpha_e(\mathbf{u}_e - \mathbf{u}_h) + \mathbf{u}_e + \alpha_e(\delta\mathbf{u}_e - \delta\mathbf{u}_h) + \delta\mathbf{u}_e$$

We now drop all terms that vanish at $B = 0$ and any second-order term like $\delta\mathbf{u}_e \times \mathbf{B}$ (as $\delta\mathbf{u}_e \propto \mathbf{B}$):

$$-\mu_{e,0}(\cancel{\mathbf{E}} + \delta\mathbf{E} + \mathbf{u}_e \times \mathbf{B} + \cancelto{0}{\delta\mathbf{u}_e \times \mathbf{B}}) = \cancel{\alpha_e(\mathbf{u}_e - \mathbf{u}_h) + \mathbf{u}_e} + \alpha_e(\delta\mathbf{u}_e - \delta\mathbf{u}_h) + \delta\mathbf{u}_e$$

Finally, using zero field mobilities $\mathbf{u}_{e,h} = \mp\mu_{e,h}\mathbf{E}$ evaluated at $B = 0$ (Eqs. (2.15)–(2.16)) yields the linearised pair of equations:

$$\begin{aligned} -\mu_{e,0}(\delta\mathbf{E} - \mu_e\mathbf{E} \times \mathbf{B}) &= \alpha_e(\delta\mathbf{u}_e - \delta\mathbf{u}_h) + \delta\mathbf{u}_e \\ \mu_{h,0}(\delta\mathbf{E} + \mu_h\mathbf{E} \times \mathbf{B}) &= \alpha_h(\delta\mathbf{u}_h - \delta\mathbf{u}_e) + \delta\mathbf{u}_h \end{aligned}$$

Solutions to Linearised Equations

Given our new linearised equations of motion, we can solve for how small changes in magnetic field create small changes in drift velocity and changes in the electric field.

First, take the extra condition of unchanged current. Measurements are always held at constant current. As such, any perturbation in the magnetic field must not change the overall current,

$$\delta\mathbf{j} = -en_e\delta\mathbf{u}_e + en_h\delta\mathbf{u}_h = 0,$$

resulting in a system of 6 linear equations (as each equation is two-dimensional):

$$\begin{aligned}
(1+\alpha_e)\delta\mathbf{u}_e \quad &+(-\alpha_e)\delta\mathbf{u}_h \quad &+(\mu_{e,0})\delta\mathbf{E} \quad &= \quad \mu_{e,0}\mu_e\mathbf{E}\times\mathbf{B},\\
(-\alpha_h)\delta\mathbf{u}_e \quad &+(1+\alpha_h)\delta\mathbf{u}_h \quad &+(-\mu_{h,0})\delta\mathbf{E} \quad &= \quad \mu_{h,0}\mu_h\mathbf{E}\times\mathbf{B},\\
(-en_e)\delta\mathbf{u}_e \quad &+(en_h)\delta\mathbf{u}_h \quad &+0\cdot\delta\mathbf{E} \quad &= \quad 0.
\end{aligned}$$

Imposing the constraints of a magnetic field perpendicular to the plane, $\mathbf{B} = B\hat{\mathbf{z}}$, and an electric field directed along the x-axis, $\mathbf{E} = E\hat{\mathbf{x}}$, yields the complete set of linear equations to be solved:

$$\begin{bmatrix}
(1+\alpha_e) & -\alpha_e & \mu_{e,0} & 0 & 0 & 0\\
0 & 0 & 0 & (1+\alpha_e) & -\alpha_e & \mu_{e,0}\\
-\alpha_h & (1+\alpha_h) & -\mu_{h,0} & 0 & 0 & 0\\
0 & 0 & 0 & -\alpha_h & (1+\alpha_h) & -\mu_{h,0}\\
-en_e & en_h & 0 & 0 & 0 & 0\\
0 & 0 & 0 & -en_e & en_h & 0
\end{bmatrix}
\begin{bmatrix}
\delta u_{e,x}\\ \delta u_{h,x}\\ \delta E_x\\ \delta u_{e,y}\\ \delta u_{h,y}\\ \delta E_y
\end{bmatrix}
=
\begin{bmatrix}
0\\ -\mu_{e,0}\mu_e EB\\ 0\\ -\mu_{h,0}\mu_h EB\\ 0\\ 0
\end{bmatrix}$$

Solving the set of 6 linear equations by computational analysis gives us the values of the drift velocity and electric field due to a small change in magnetic field. Here, in order to deduce the resistivity tensor of the system, $\boldsymbol{\rho}$, the change in electric field, $\delta\mathbf{E}$, is given:

$$\begin{aligned}
\delta E_x &= 0,\\
\delta E_y &= -EB\,\frac{(n_e+(n_e-n_h)\alpha_h)\,\mu_{e,0}\mu_e-(n_h+(n_h-n_e)\alpha_e)\,\mu_{h,0}\mu_h}{(n_e+(n_e-n_h)\alpha_h)\,\mu_{e,0}+(n_h+(n_h-n_e)\alpha_e)\,\mu_{h,0}}
\end{aligned}$$

where the carrier mobility in zero field, $\mu_{e,h}$, is given by Eq. (2.16) and other parameters, $\mu_{e,h,0}$ and $\alpha_{e,h}$, defined in Eq. (2.19). The linearised solution shows that, to first order, a perpendicular magnetic field produces only a perpendicular electric field response (linear in B) and leaves the longitudinal electric field unchanged. This is non-obvious when the condition of zero current is easily met whenever $n_e\delta\mathbf{u}_e = n_h\delta\mathbf{u}_h$

and two-carrier transport with interactions is non-trivial. It might be expected that $\delta\mathbf{E}$ has a finite x-component when the two-fluid system is uncompensated ($n_e \neq n_h$). Despite this, the system has a strictly perpendicular electric field response to a small B-field regardless of net density, a result that is similar to the single carrier case where $\delta\mathbf{E} = \pm\mu_{e,h}EB\hat{\mathbf{y}}$ is simply the Lorentz force, $q(\mathbf{v}\times\mathbf{B})$.

2.3.3.2 Resistivity Determination

By Ohm's law, the relationship between the electric field, $\mathbf{E}$, and current density, $\mathbf{J}$, in a material is given by the resistivity, $\boldsymbol{\rho}$:

$$\mathbf{E} = \boldsymbol{\rho}\mathbf{J},$$

where in our system under small B-field perturbation:

$$\mathbf{E} \rightarrow \mathbf{E} + \delta\mathbf{E} = E\hat{\mathbf{x}} + \delta E_y\hat{\mathbf{y}}, \quad \mathbf{J} \rightarrow \mathbf{J} + \delta\mathbf{J} = j\hat{\mathbf{x}}, \quad j = e(n_e\mu_e + n_h\mu_h)E,$$

one solves for the 2x2 resistivity tensor:

$$\begin{bmatrix} E \\ \delta E_y \end{bmatrix} = \begin{bmatrix} \rho_{xx} & \rho_{xy} \\ -\rho_{xy} & \rho_{xx} \end{bmatrix} \begin{bmatrix} j \\ 0 \end{bmatrix}$$

such the longitudinal, ρ_{xx}, and transverse/Hall resistivity, ρ_{xy}, is given:

$$\begin{aligned} \rho_{xx} &= \frac{E}{j} = \frac{1}{e(n_e\mu_e + n_h\mu_h)} \\ \rho_{xy} &= -\frac{\delta E_y}{j} = \frac{B}{e}\frac{(n_e + (n_e - n_h)\alpha_h)\,\mu_{e,0}\mu_e - (n_h + (n_h - n_e)\alpha_e)\,\mu_{h,0}\mu_h}{[(n_e + (n_e - n_h)\alpha_h)\,\mu_{e,0} + (n_h + (n_h - n_e)\alpha_e)\,\mu_{h,0}]\,\big(n_e\mu_e + n_h\mu_h\big)} \end{aligned} \tag{2.20}$$

where E is the applied electric field in the longitudinal (x) direction, δE_y is the transverse (Hall) electric field induced by the small magnetic field B, and j is the magnitude of the total current density. The quantities $n_{e,h}$ are the carrier densities for electrons and holes (Eq. (2.11)) while μ_e and μ_h are the effective mobilities of electrons and holes accounting for drag (see Eq. (2.17)). The conventional Drude mobilities, without drag, are denoted by $\mu_{e,0} = e\tau/m_e$ and $\mu_{h,0} = e\tau/m_h$, where, τ is the momentum-relaxation time due to phonons and disorder, and $m_{e,h}$, is the effective masses of electrons and holes (see Eq. (2.12)). The parameters $\alpha_e = \frac{\tau}{\tau_{eh}}\frac{\rho_h}{\rho_e+\rho_h}$ and $\alpha_h = \frac{\tau}{\tau_{eh}}\frac{\rho_e}{\rho_e+\rho_h}$ quantify the strength of inter-carrier (electron-hole) drag, with τ_{eh} the inter-carrier scattering time and $\rho_{e,h}$ the carrier mass densities (see Eq. (2.13)).

As expected, the resistivity B-dependence is strictly linear in the transverse (Hall) direction.

As a consistency check, consider the limit of zero inter-carrier scattering:

Limit $\tau_{eh} \gg \tau$:

$$\alpha_e \to 0, \quad \alpha_h \to 0, \quad \mu_e \to \mu_{e,0}, \quad \mu_h \to \mu_{h,0},$$

$$\rho_{xx} = \frac{1}{e(n_e\mu_{e,0} + n_h\mu_{h,0})}$$

$$\rho_{xy} = \frac{B}{e}\frac{n_e\mu_{e,0}^2 - n_h\mu_{h,0}^2}{(n_e\mu_{e,0} + n_h\mu_{h,0})^2}$$

Under the limit of no inter-carrier interactions, our drag-modified Drude model reduces to the standard two-carrier Drude model description of resistivity (see Eq. (1.23)).

Through Eq. (2.20), we have connected the microscopic scattering parameters of the drag-modified Drude model to macroscopic transport that can be measured in the lab. This equation allows us to extract τ and τ_{eh} from measured ρ_{xx} and ρ_{xy}, where the ratio $\frac{\tau}{\tau_{eh}}$ indicates the strength of hydrodynamic flow in the two-fluid system.

2.3.3.3 Scaling Behaviour & Dimensionless Substitutions

Just as in Section 2.2.1, it is beneficial to examine the scaling behavior of our drag-modified Drude model by introducing dimensionless parameters. This approach allows us to clearly identify the parameters available for fitting to the experimental data.

Similar to the dimensionless result produced in the simple two-carrier Drude model (see Eq. (2.4)) we define dimensionless carrier density, $N(\pm x) = x_e(\pm x)$, and a dimensionless chemical potential, η, defined as the function given by solving for $x = N(x) - N(-x)$ across the domain $\eta(x)$:

$$N(\pm x) = n_{e,h} \cdot \left(\frac{k_B T}{\hbar v_F}\right)^{-2} = -\frac{2}{\pi}\,\mathrm{Li}_2\left(-e^{\pm\eta(x)}\right) \tag{2.21}$$

where $\eta(x)$ is defined as the inverse function to:

$$x(\eta) = N(\eta) - N(-\eta) = -\frac{2}{\pi}\left[\mathrm{Li}_2(-e^{\eta}) - \mathrm{Li}_2(-e^{-\eta})\right].$$

Extending further than we did in Section 2.2.1, we also define dimensionless results for effective mass, $m_{e,h}$ and our fractional mass density, $\frac{\rho_h}{\rho_e+\rho_h}$, using the

definitions from the kinetic theory (Eqs. (2.11)–(2.13)):

$$\begin{aligned} M(\pm x) &= \frac{2k_BT}{v_F^2}\frac{1}{m_{e,h}} = -\frac{\ln\left(1+e^{\pm\eta(x)}\right)}{\mathrm{Li}_2\left(-e^{\pm\eta(x)}\right)}, \\ R(\pm x) &= \frac{\rho_{h,e}}{\rho_e+\rho_h} = \frac{\mathrm{Li}_3\left(-e^{\mp\eta(x)}\right)}{\mathrm{Li}_3\left(-e^{\eta(x)}\right)+\mathrm{Li}_3\left(-e^{-\eta(x)}\right)} \end{aligned} \tag{2.22}$$

where from now on the following notations are used for convenience:

$$N_\pm = N(\pm x), \quad M_\pm = M(\pm x), \quad R_\pm = R(\pm x), \quad t = \tfrac{\tau}{\tau+\tau_{eh}}$$

Finding Dimensionless Drag-Modified Resistivity

Given the dimensionless substitutions above, we can rewrite the resistivities (Eq. (2.20)) in a dimensionless form. We aim to express resistivity in a compact and symmetric way, convenient for understanding the physical dynamics.

Recall our zero field drag-modified mobility (Eq. (2.16)):

$$\begin{aligned} \mu_e &= \mu_{e,0} - (\mu_{e,0}+\mu_{h,0})\frac{\rho_h}{\rho_e+\rho_h}\frac{\tau}{\tau+\tau_{eh}}, \\ \mu_h &= \mu_{h,0} - (\mu_{e,0}+\mu_{h,0})\frac{\rho_e}{\rho_e+\rho_h}\frac{\tau}{\tau+\tau_{eh}}, \end{aligned}$$

and substitute dimensionless forms from Eq. (2.21)–(2.22) and define a dimensionless mobility parameter, W_+:

$$\begin{aligned} \mu_e &= \frac{e\tau v_F^2}{2k_BT}\left[M_+ - (M_+ + M_-)\,R_+t\right] = \frac{e\tau v_F^2}{2k_BT}W_+ \\ \mu_h &= \frac{e\tau v_F^2}{2k_BT}\left[M_- - (M_+ + M_-)\,R_-t\right] = \frac{e\tau v_F^2}{2k_BT}W_- \end{aligned}$$

where the dimensionless mobility parameter is defined as:

$$W_\pm = M_\pm - t(M_+ + M_-)R_\pm,$$

Therefore resistivities (Eq. (2.20)) can be rewritten:

$$\rho_{xx}^{-1} = e(n_e\mu_e + n_h\mu_h) = \frac{e^2\tau v_F^2}{2k_BT}\left(\frac{k_BT}{\hbar v_F}\right)^2(N_+W_+ + N_-W_-),$$

and a dimensionless resistivity defined:

$$\varrho_{xx} = \rho_{xx}\cdot\frac{e^2\tau k_BT}{2\hbar^2} = \frac{1}{N_+W_+ + N_-W_-} \tag{2.23}$$

Similiarly, substituting a dimensionless result A in Hall resistivity (Eq. (2.20)) finds:

$$\varrho_{xy} = \rho_{xy} \cdot \frac{e}{B}\left(\frac{k_B T}{\hbar v_F}\right)^2 = \frac{A_+M_+W_+ - A_-M_-W_-}{(A_+M_+ + A_-M_-)(N_+W_+ + N_-W_-)}, \tag{2.24}$$

where the dimensionless parameter, A, is defined as:

$$A_\pm = N_\pm \pm (t^{-1} - 1)^{-1}(N_+ - N_-)R_\mp = N_\pm \pm \alpha_\mp \cdot x(\eta),$$

where $\alpha_\pm = \alpha_{e,h} = \frac{\rho_{h,e}}{\rho_e + \rho_h}\frac{\tau}{\tau_{eh}}$ are the dimensionless drag coefficients defined in Eq. (2.19).

The analysis demonstrates that resistivity can be expressed in a dimensionless form that depends solely on the parameter t, defined as the ratio of the momentum relaxation scattering time to the inter-carrier scattering time. This parameter is related to the scattering times by the relation $\frac{\tau}{\tau_{eh}} = (t^{-1} - 1)^{-1}$, such that t is constrained, $0 \leq t \leq 1$. The remaining parameters N, M, and R, are defined by graphene's Fermi-Dirac electronic spectrum via kinetic theory.

So, t, when bound between 0 and 1, uniquely determines resistivity, creating a direct one-to-one mapping between resistivity and t (or equivalently $\frac{\tau}{\tau_{eh}}$), as shown in Figure 2.14, which shows dimensionless resistivity continuously varying with t and dimensionless net carrier density, $x = N(x) - N(-x)$.

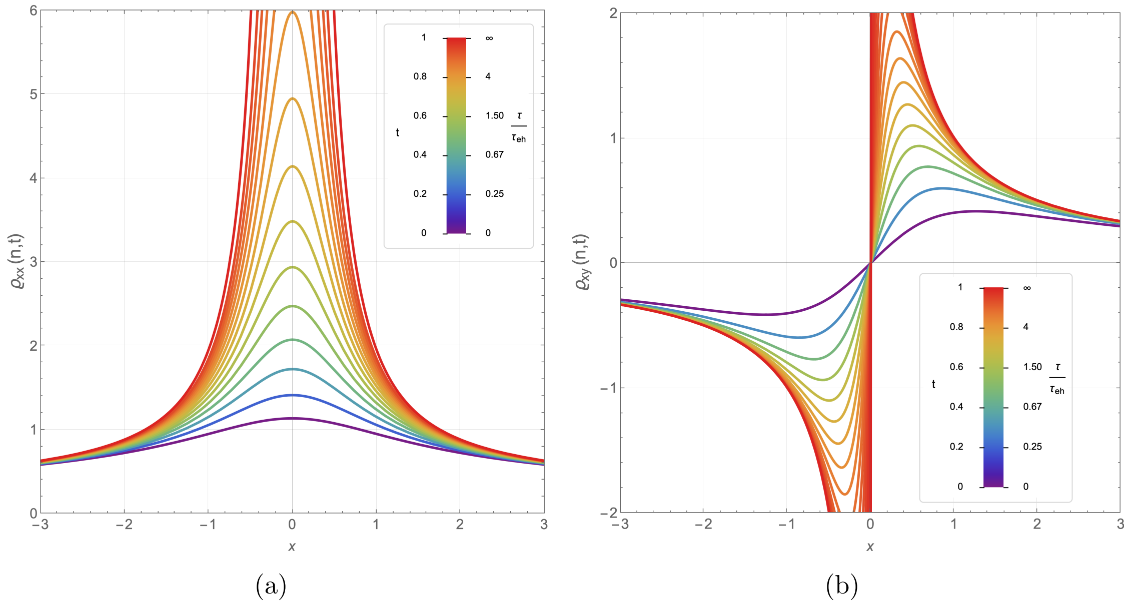

Figure 2.14: **(a)** Dimensionless Longitudinal, $\varrho_{xx}(x,t)$, and **(b)** Hall, $\varrho_{xy}(x,t)$, components of the dimensionless resistivity, calculated from Eq. (2.23) and (2.24). Both are shown as functions of the dimensionless net carrier density, x, and the ratio of microscopic scattering times, $t = (1 + \tau_{eh}/\tau)^{-1}$.

Figure 2.14(a) shows us that as $\frac{\tau}{\tau_{eh}} \to \infty$, when inter-carrier scattering is dom-

inant, the dimensionless longitudinal resistance diverges to infinity at the Dirac point. By quickly evaluating $\varrho_{xx}(0,t)$ (see Eq. (2.23)) at the Dirac point where $N_+ = N_- = N$, $M_+ = M_- = M$ and $R_+ = R_- = 0.5$ one finds:

$$\varrho_{xx}(0,t) = \frac{1}{2MN(1-t)}$$

which at $t = 1$ indeed diverges in this dimensionless form. Restoring physical units by reinserting the scaling prefactor (scaled by τ) used to define ϱ_{xx}, we obtain:

$$\frac{2\hbar^2}{e^2\tau k_B T}\frac{1}{2MN(1-t)} = \frac{m}{2ne^2\tau(1-t)} = \frac{m}{2ne^2}\cdot(\frac{1}{\tau}+\frac{1}{\tau_{eh}}) \equiv \frac{1}{2ne\mu_{eq}} \tag{2.25}$$

where $\mu_{eq} = \frac{e\tau_{eq}}{m}$. The peak in longitudinal resistance does not necessarily diverge when $\tau \to \infty$, it is determined by the sum of the combined scattering rates of the system, $\frac{1}{\tau_{eq}} = \frac{1}{\tau}+\frac{1}{\tau_{eh}}$, and reduces, when $\tau \ll \tau_{eh}$, to the small B-field non-interacting two-carrier Drude model (see Eq. (1.26)) as expected. Divergence then occurs when the scattering rate of any scattering mode approaches infinity. Considering each scattering type we can see why resistance would increase. In a momentum-relaxing disorder, infinite scattering with disorder will take all the momentum out of the fluid system, and no flow occurs. For momentum-conserving inter-carrier scattering, in the case of full interaction between the two fluids, the two fluids essentially become one fluid where dynamics are given by the net density, as shown if we evaluate ϱ_{xx} at $t = 1$:

$$\begin{aligned} \varrho_{xx}|_{t=1} &= \frac{1}{(N_+ - N_-)(M_+R_- - M_-R_+)}, \\ \therefore \rho_{xx} &= \frac{1}{e(n_e - n_h)(\mu_e(1-R) - \mu_h R)} \equiv \frac{1}{en\mu_{e,h}} \end{aligned}$$

likewise the two-fluid looks like a single fluid in the limit of complete coupling between electrons and holes, $t = 1$:

$$\begin{aligned} \varrho_{xy}|_{t=1} &= \frac{1}{(N_+ - N_-)}, \\ \therefore \rho_{xy} &= \frac{B}{e(n_e - n_h)} \equiv \frac{B}{en} \end{aligned} \tag{2.26}$$

In Figure 2.14(b) we see a similar divergence at the Dirac point that was seen in the dimensionless longitudinal resistance. However, in this case, divergence will also be seen in the real Hall resistivity as the scaling has no scattering time (mobility) dependence, as evidenced in Eq. (2.26).

As each value of resistance has a unique correspondence to x and t, particularly apparent in Figure 2.14, this enables direct extraction of microscopic drag parameters from transport data in graphene-based two-fluid systems by inversing Eq. (2.23)

and (2.24) to find t as a function of resistivity, $t(x, \varrho)$.

2.3.4 Fitting Drag-Modified Drude Model to Experimental Data

In the simplest case we can use constant density-independent values for τ and τ_{eh}. This is similar to what was done with fitting zero-field mobility earlier, see Figure 2.13.

How can we determine the values of our scattering times? First, let's consider a single measurement sweep of longitudinal resistance vs carrier density. Recall that in the high density limit, say $n_e \gg n_h$, the Drude two-carrier model reduces to the single carrier form (Eq. (1.21)):

$$\rho_{xx} = \frac{m_e}{e^2 n_e \tau}$$

this is also true in our drag-modified model (as drag is negligible). Hence, in the high-density limit, the disorder scattering time can be simply determined from the longitudinal resistance. From Eq. (2.25), the peak in longitudinal resistance gives us information about the total scattering rate of the system. Then, simply by measuring longitudinal resistance at two points, high density and peak, we can extract an approximate value for both scattering times, τ and τ_{eh}.

Given that Hall resistance is completely a function of t, that is to say that every measurement of ρ_{xy} uniquely defines the ratio $\frac{\tau}{\tau_{eh}}$ (see Eq. (2.24)) we can use two measurements of longitudinal resistance to give us two microscopic scattering times that can be used to predict two independently measured curves, longitudinal and Hall, across the entire density range, as shown in Figure 2.15, assuming constant scattering times.

Much like the zero-field mobility fitting, the assumption of constant scattering times fits remarkably well to the room temperature data. In this data (Figure 2.15(a)) the Hall resistance is used to determine the ratio of the scattering times (approximately 3.88), and longitudinal resistance gives a value of disorder scattering time, $\tau = 1.40\,\mathrm{ps}$, consistent with the fitting of mobility, and, therefore, a value of inter-carrier scattering time is also given, $\tau_{eh} = 0.36\,\mathrm{ps}$.

Moving towards low temperatures we see that this assumption of constant scattering times starts to break down (see Figure 2.15(b)). Around 150 K, we see that the model starts to diverge from the data, where we still have a good fit above this temperature. This divergence at around 150 K is consistent with the observations previously made in Figure 2.8 where 150 K marks the crossover between thermally

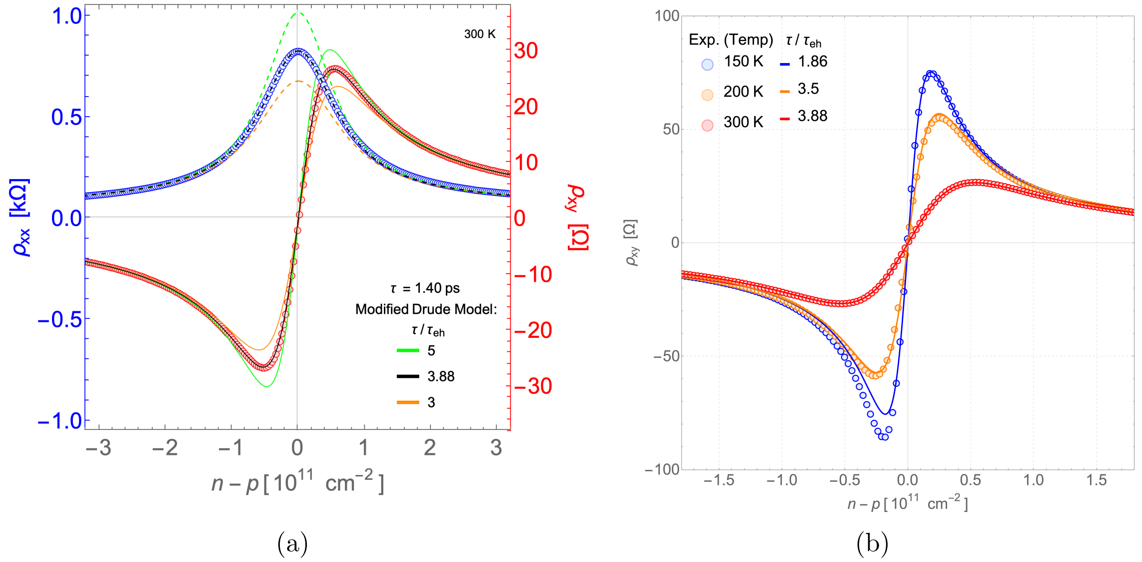

Figure 2.15: Comparison of experimental data to the drag-modified Drude model under density-independent scattering times. **(a)** Experimental Longitudinal and Hall resistivity as a function of net carrier density measured at 300 K and 4.0 mT, modeled using $\tau = 1.40\,\text{ps}$ and varying ratios of τ/τ_{eh}, 5 (green), 3.88 (black), and 3 (orange). **(b)** Hall resistivity at varying temperatures with corresponding best fit for the ratio τ/τ_{eh}.

intrinsic transport and disorder-affected transport. So, as we approach these lower temperatures, it is right to expect that the scattering times might indeed have a density dependence that is not observed at room temperature.

The drag-modified Drude model we have developed is flexible enough to allow us to solve the model and allow the extraction of t and therefore τ and τ_{eh} as functions of carrier density, x, at each temperature. This is done by inverting the dimensionless resistivity equations (Eqs. (2.23) and (2.24)) to extract t as a function of resistivity, $t(x, \varrho)$, and then using a numerical fitting routine to find the best fit for the model.

As expected, the extracted disorder/phonon scattering time, $\tau(n)$, is relatively constant at room temperature (see Figure 2.16(a)) consistent with results in Figure 2.15. The scattering time τ starts to increase with decreasing temperature, this is expected from decreasing phonon occupation. Note, however, the increase in the scattering time is not necessarily monotonic when considering the scattering rate at the Dirac point. At this point, the scattering time τ initially increases with decreasing temperature, presumably due to decreased acoustic phonon scattering, but as we approach 150 K, the scattering time starts to decrease again. This increase in the disorder/phonon scattering rate at lower temperatures must not be due to the phonon scattering rate, which would have an opposite effect, but must be due to increased scattering from disorder, likely charged impurities. This might

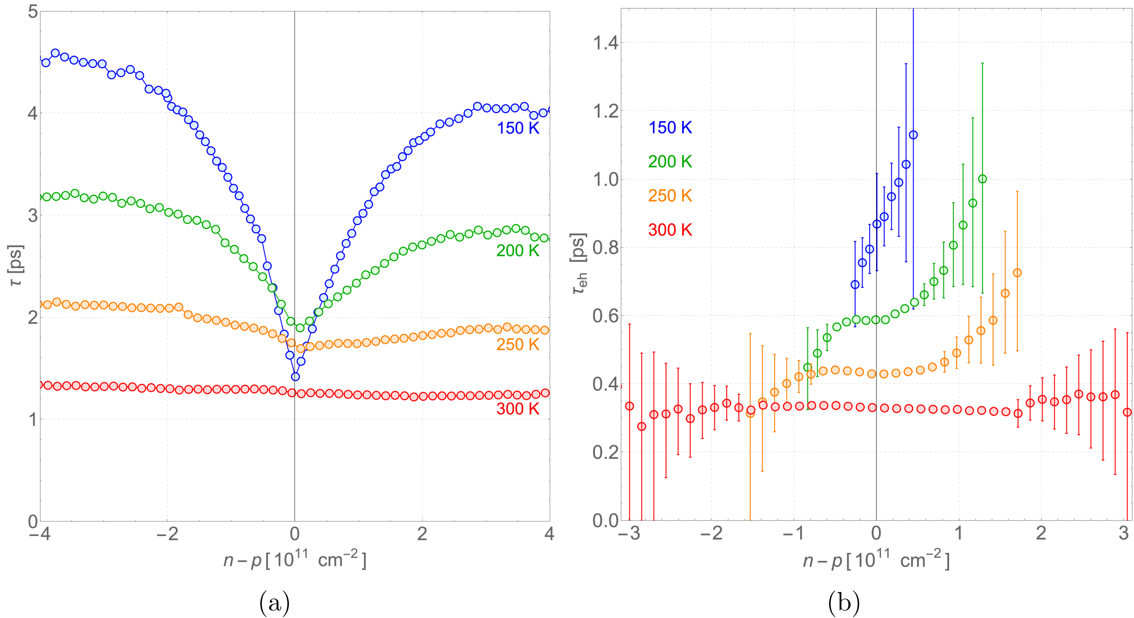

Figure 2.16: Extracted scattering times by solving the drag-modified Drude model to experimental data at different temperatures. **(a)** Disorder/phonon scattering time vs net carrier density, $\tau(n-p)$ **(b)** Inter-carrier scattering time, $\tau_{eh}(n-p)$, is extracted similarly.

occur due to decreased screening of those charged impurities, as the thermal carrier density decreases with decreasing temperature. This is further evidenced by the appearance of a $\sqrt{n}$ scattering time density-dependence at lower temperatures, a dependence which is characteristic of scattering that is responsive to screening. $\sqrt{n}$-dependence on microscopic scattering time explains linear conductivity (constant mobility) observed in the high density (single carrier) limit when temperatures are low. A constant scattering time gives us $\sqrt{n}$-dependence on conductivity and inverse $\sqrt{n}$-dependence on mobility in the same limit.

The inter-carrier scattering time, $\tau_{eh}(n)$ (see Figure 2.16(b)) shows a similar picture of scattering times independence on carrier density. Although, that is not strictly true. The expectation, due to eh-symmetry, is that τ_{eh} should be symmetric about the neutrality point, and we see that this is not the case, particularly towards lower temperatures, where it seems more anti-symmetric. The asymmetry is inconsistent with an intrinsic density dependence of the inter-carrier scattering time and instead points to a small offset of the experimental neutrality point. This is most naturally attributed to remnant doping. Therefore, in the absence of remnant doping, τ_{eh} is very likely independent of carrier density in the vicinity of the neutrality point.

The inter-carrier scattering time is less sensitive to small doping at room temperature, which allowed us to get a good high-temperature fit of resistivity using constant scattering times in this specific regime. The scattering time τ_{eh} shows

approximately a $T^{-4/3}$-dependence.

We also see much larger errors in the measurements of τ_{eh} at higher densities, which are simply due to the fact that the influence of τ_{eh} on the resistivity exponentially decays with increasing density, considering $\frac{d\varrho_{xy}(x,t)}{dt} \to \mathcal{O}(e^{-x})$, which comes as ϱ_{xy} approaches $1/x$ dependence. Points with sufficiently wide error bars were excluded from Figure 2.16(b), as they were not representative of the system.

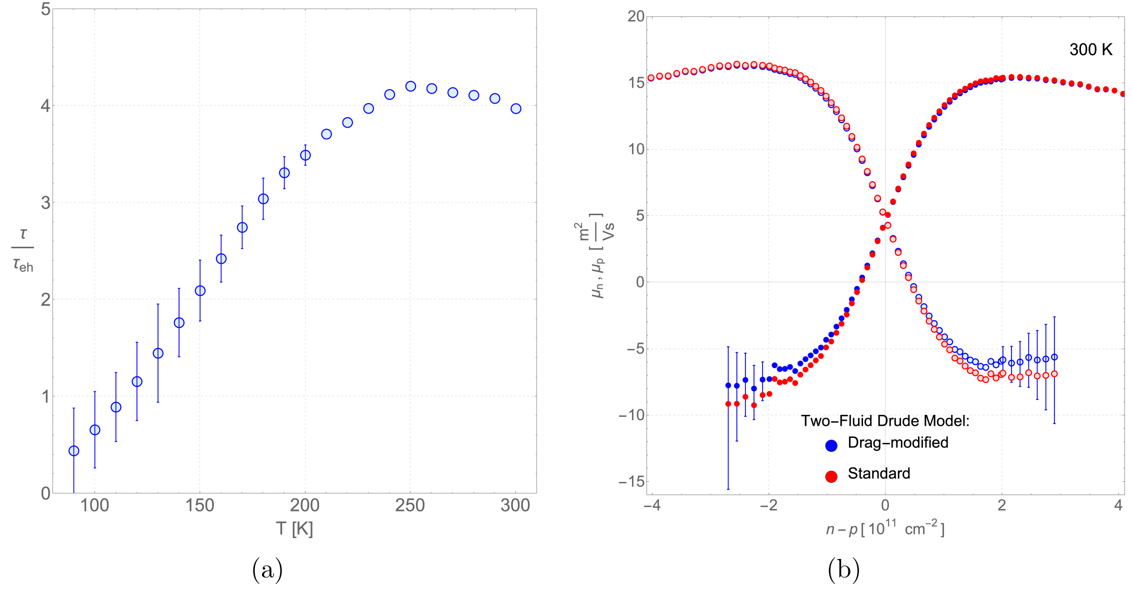

Figure 2.17: Extracting **(a)** the temperature-dependent ratio of inter-carrier scattering time to disorder/phonon scattering time, τ_{eh}/τ and **(b)** the room temperature mobility extracted from experimental data via the standard two-carrier Drude model (red) vs the drag-modified two-fluid Drude model (blue).

Recalling that the Hall resistivity is a function of the ratio of scattering times, $\frac{\tau}{\tau_{eh}}$, we can extract this ratio as a function of temperature (see Figure 2.17(a)) straight from a fit of the Hall resistance measurement. This has the added benefit of minimising error in the numerical analysis, as the Hall resistivity is very sensitive to the absolute value of the ratio $\frac{\tau}{\tau_{eh}}$, particularly near the peak, as seen in Figure 2.15. The ratio of the two scattering times is approximately $\frac{\tau}{\tau_{eh}} = 4$ at room temperature, starting to decrease with decreasing temperature at around 250 K. In fact, there is a slight peak in the ratio at around 250 K, which is consistent with the observation of stronger hydrodynamic effects in monolayer graphene at this temperature (see Section 1.2.3). Hydrodynamic effects are expected when the inter-carrier scattering rate is greater than the momentum-relaxing scattering time, $\tau/\tau_{eh} \gg 1$. A regime occurring because transport is dominated by elastic momentum-conserving collisions between carriers, leading to a collective nature of the many-body dynamics described by Navier-Stokes equations. Any effects of hydrodynamics are expected to decrease at higher temperatures as the acoustic phonon scattering rate increases. With a

ratio of $\tau/\tau_{eh} \approx 4$ at room temperature, we can expect that hydrodynamic effects are observable but not particularly strong near the Dirac point in our system, as the ratio is not much greater than 1. Where, at lower temperatures, as charge impurities start to dominate scattering, the ratio decreases to around 1, and the observation of any significant hydrodynamic transport becomes increasingly difficult. This relation between the ratio of scattering times is a direct indication of the strength of the hydrodynamic nature of the Dirac plasma that can be determined by a single measurement of the peak Hall resistivity.

Finally, we can compare the mobility from our drag-modified model (that falls out of Boltzmann kinetic equation) to the mobility extracted from the standard two-carrier Drude model (that is just a macroscopic description of the superposition of two types of carriers). Calculating the mobility in drag-modified model combines both the longitudinal and Hall resistance measurements to determine the microscopic parameters, τ and τ_{eh} (Figure 2.16), which then can then be used to calculate mobility via Eq. (2.17). The standard two-carrier Drude model combines the longitudinal and Hall resistivities directly to extract the mobility, assuming two equal oppositely charged carriers with well-defined densities (see Eq. (1.17)).

Figure 2.17(b) shows that the room temperature mobility extracted from the drag-modified model (blue) is comparable to the mobility extracted from the standard two-carrier model (red), showing the same characteristic negative mobility expected for dragged minority carriers. As seen previously (see Figure 2.13) the mobility of minority carriers is equal and opposite to the mobility of majority carriers in the limit of inter-carrier scatter dominated transport. The effect of drag then decreases as τ/τ_{eh} gets smaller, and, consequently, the drift velocity of minority carriers is less affected by drag, as seen by the twice as small mobility of minority carriers to majority carriers in Figure 2.17(b).

The surprisingly good agreement between the models, deviations no greater than 20%, shows that there is a microscopic explanation to the measured negative mobility given by the standard two-carrier Drude model, and that despite a less defined Fermi surface, at finite temperatures and mixed carrier interactions, the Drude model of transport is still applicable in this case of significant electron-hole scattering.

2.4 Charge Inhomogeneity: Electron-Hole Puddles

In the context of electronic transport, 'inhomogeneity' will typically refer to any factor that causes a spatial variation in the charge density, that ultimately leads to a measurable deviation in macroscopic measurements. As inhomogeneities can significantly affect the Fermi energy and charge distribution, there can be substantial changes in the electronic transport characteristics, in our context, of longitudinal and Hall resistance measurements.

Inhomogeneity in monolayer graphene can arise from various factors, including:

- **Non-uniform doping**: This includes contributions from metal contacts, surface contaminants, or just poor material choice for substrate. For example, a charged impurity (a spurious ion) beneath the graphene layer can lead to a local fluctuation in charge density.

- **Scanning Probe Microscopy**: As discussed in Section 1.5.2, the external action of scanning a charged probe near to the graphene sheet will result in localised variations in the charge density and therefore deviations in measured resistance. This is foundational in our research to probe current flow within the sheet.

- **Structural variations**: Topological variations, such as ripples, surface roughness, discontinuities, and the interfacial interaction to substrates, all also contribute to electronic inhomogeneity. These structural imperfections will directly alter the electronic spectrum and dispersion relation.

Understanding how inhomogeneity affects our measurements is crucial for accurately interpreting if transport properties are intrinsic and for confirming our theoretical models. We will need to modify our model to better understand how inhomogeneity might change our conclusions.

As seen so far, characterisation of our graphene samples (see Section 2.1.3) has shown them to be of high-quality, showing little deviations from our drag-modified Drude model under small magnetic fields and high temperatures.

The characteristic width of the neutral point region determined by the longitudinal half-width, δn, or the net density at the Hall peak, δn_H, was shown to saturate at low temperatures (see Figure 2.8). However, these characteristic widths as predicted by the standard two-carrier and drag-modified two-fluid Drude models are both proportional to T^2 (recall dimensionless scaling). Therefore, models predict diverging

resistivities with vanishing width of the neutrality region as temperature tends to zero, far from the observed experimental saturation at low temperatures. At these lower temperatures, does the presence of inhomogeneity, particularly electron-hole puddles, account for the saturating characteristic width, δn_H, and can we efficiently modify our models to account for this?

2.4.1 Model for Inhomogeneous Conductivity

Determining the macroscopic response to inhomogeneity is a non-trivial task. So we consider the simplest existing model that permits an analytical solution - a spatially fluctuating system of two discrete phases. [107–109] This convenient simplification can be used to add electron-hole puddles into our model. The two-phase method of reciprocal media focuses on determining the macroscopic electrical properties of a two-dimensional, inhomogeneous conducting medium composed of two types of regions (phases) with arbitrary shapes and dimensions. They provide an exact solution under specific conditions.

Assumptions Made in Two-Phase Inhomogeneity Model

- The medium is spatially inhomogeneous, where local conductivity takes one of two values corresponding to regions (phases) with arbitrary shapes and dimensions. The overall dimensions of the system are much larger than the characteristic dimensions of the individual regions.
- An exact solution is achievable for a two-dimensional medium with a 1:1 mixture of both phases, assuming they are under geometrically equivalent conditions on average.

We assume that each phase exhibits standard Drude Hall response in a perpendicular magnetic field:

$$\sigma_{xx} = \frac{\sigma_0}{1+\beta^2}, \tag{2.27}$$

where σ_{xx} is the longitudinal conductivity, σ_0 denotes the zero-field conductivity of a given phase and β is the Hall parameter that is proportional to the magnetic field, $\beta \propto B$. Note, β can also be calculated from the conductivity/resistivity tensors when magnetic field is applied perpendicular to current, $\beta = \frac{\sigma_{xy}}{\sigma_{xx}} = \frac{\rho_{xy}}{\rho_{xx}}$, see Eq. (1.20) and (1.21).

Following the assumptions of Dykhne [107,108], an effective conductivity is given for the inhomogeneous medium based on the conductivity of each of the two phases, σ_1 and σ_2, and corresponding Hall parameters, β_1 and β_2, of each phase. These two

phases are combined into a statistically isotropic effective medium characterised by effective parameters, σ^* and β^*:

$$\sigma_0^* = \sqrt{\frac{\sigma_1\sigma_2}{1+\left(\frac{\sigma_1\beta_2-\sigma_2\beta_1}{\sigma_1+\sigma_2}\right)^2}}, \quad \beta^* = \sigma_0^*\frac{\beta_1+\beta_2}{\sigma_1+\sigma_2}. \tag{2.28}$$

The effective conductivity tensor, that characterises this new medium, is given by the substitutions $\sigma_0 \to \sigma_0^*$ and $\beta \to \beta^*$ in the standard conductivity (see Eq. (2.27)).

Application to Two-Dimensional Electron-Hole Puddles in Graphene

We can apply the two-phase model to our drag-modified two-fluid Drude model by considering the two phases to be areas, at low temperature and density, where there are puddles of electrons and holes due to spatial inhomogeneities. The fluctuation on the two phases is given as plus or minus some fixed, small, temperature-independent residual value δn_r on the net density $n - p$ (subscript r distinguishes from the half-width in longitudinal resistance δn). As such, the density of the phases at the neutrality point is $\pm\delta n_r$. In dimensionless units, net carrier density is $x = (n-p)\left(\frac{\hbar v_F}{k_B T}\right)^2$ and the residual density is given as $\delta x = \delta n_r\left(\frac{\hbar v_F}{k_B T}\right)^2$. By algebraic manipulation and assumptions of small B-fields then the effective resistivity tensor that includes simple inhomogeneity (see Eq. (2.28)) is given in dimensionless resistivity form:

$$\begin{aligned} \varrho_{xx}^* &= \frac{1}{\sigma_0^*} = \sqrt{\varrho_{xx_1}\varrho_{xx_2}\left[1+\left(\frac{\varrho_{xy_2}-\varrho_{xy_1}}{\varrho_{xx_1}+\varrho_{xx_2}}\right)^2\right]}, \quad \propto (\mu_{e,h}B)^2 \Rightarrow 0 \\ \varrho_{xy}^* &= \beta^*\varrho_{xx}^* = \frac{\beta^*}{\sigma_0^*} = \frac{\beta_1+\beta_2}{\sigma_1+\sigma_2} = \frac{\varrho_{xy_1}\varrho_{xx_2}+\varrho_{xy_2}\varrho_{xx_1}}{\varrho_{xx_1}+\varrho_{xx_2}} \end{aligned} \tag{2.29}$$

where ϱ_{xx_1} and ϱ_{xx_2} are the longitudinal resistivities of the two phases, ϱ_{xy_1} and ϱ_{xy_2} are the Hall resistivities of the two phases given by the drag-modified two-fluid Drude model (Eqs. (2.23) and (2.24)):

$$\begin{aligned} \varrho_{xx_1} &= \varrho_{xx}(x+\delta x, t), \quad \varrho_{xx_2} = \varrho_{xx}(x-\delta x, t), \\ \varrho_{xy_1} &= \varrho_{xy}(x+\delta x, t), \quad \varrho_{xy_2} = \varrho_{xy}(x-\delta x, t). \end{aligned}$$

where x and δx are the dimensionless net and puddle density, respectively and t is the drag-model scattering strength.

The new effective resistivities (Eq. (2.29)) give new transport results in the presence of small inhomogeneities. The addition of the residual density, δx, adds a

temperature-dependent factor into the dimensionless form, since $\delta x \propto \delta n_r T^{-2}$. As the temperature is lowered this residual density eventually dominates over the thermally induced carrier density, so transport near neutrality in dimensionless units has strong T^{-2}-dependence at low temperatures. Consequently, the characteristic width of the Hall response in real density units saturates at low temperature, and will create a temperature-independent (low-temperature saturation) peak in the measured Hall resistance.

The effects of inhomogeneity on the longitudinal and Hall resistivities are shown in Figure 2.18, where a scattering ratio defined in terms of t is $t = 0.2$.

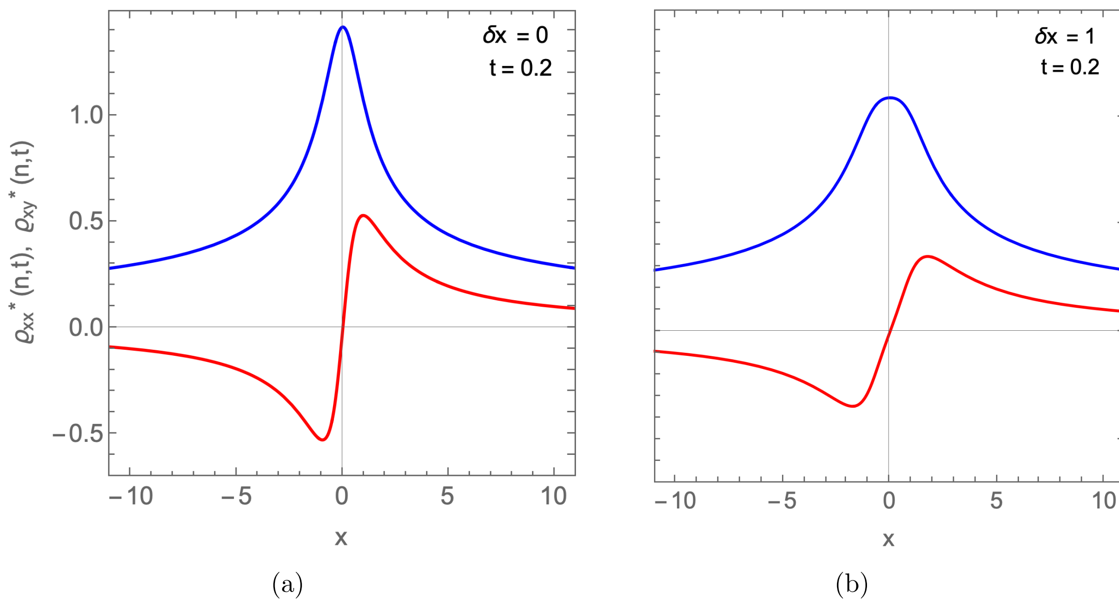

Figure 2.18: Dimensionless longitudinal, ϱ^*_{xx} (blue), and Hall, ϱ^*_{xy} (red), resistivities in the presence of inhomogeneity, δx. **a** No inhomogeneity, $\delta x = 0$. **b** Temperature-dependent term for inhomogeneity added, $\delta x = 1$, shows a smearing and widening of peaks in resistance.

The addition of inhomogeneity, δx, leads to a decreased amplitude and widening of the peaks in both longitudinal and Hall resistivities. To clearly see whether the effects of inhomogeneity cause temperature-independent saturation of the peak, we can plot the position of dimensionless Hall peak resistivity, as a function of the dimensionless puddle density, δx (see Figure 2.19).

From Figure 2.19, we observe the dependence of the peak position in the dimensionless Hall resistivity against the dimensionless puddle density δx. Different representative curves are shown for different electron-hole scattering strengths, t.

At high inhomogeneity strengths ($\delta x \gtrsim 1$), expected at low temperatures, the position of the peak is approximately proportional to and similar in magnitude to δx, rendering the peak position in real units temperature independent and similar

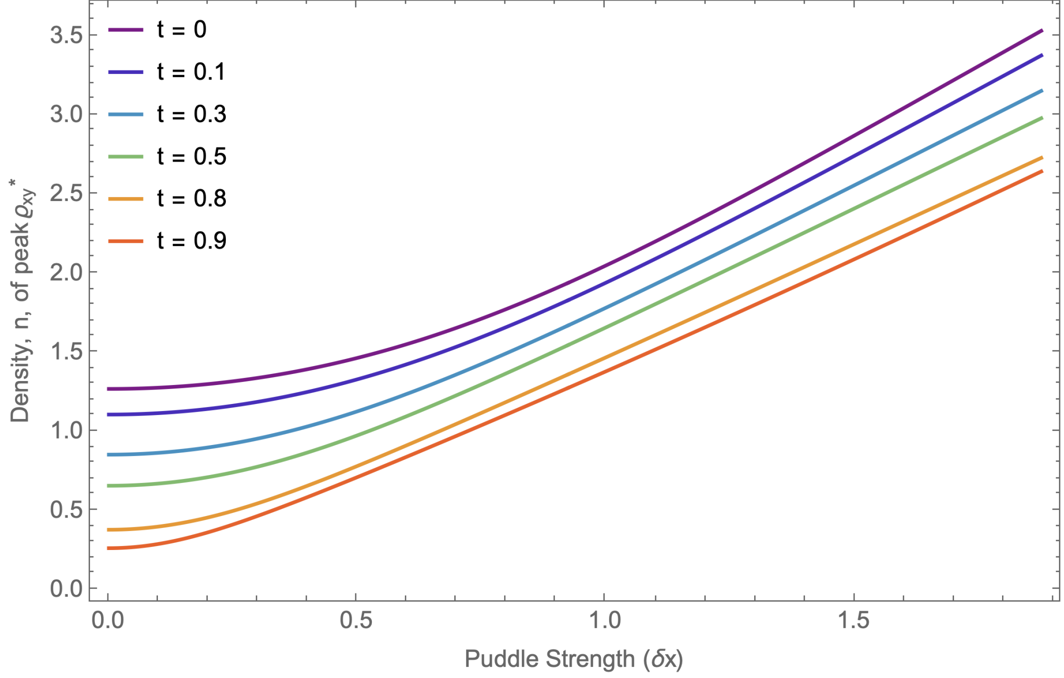

Figure 2.19: The peak in dimensionless Hall resistivity, ϱ^*_{xy}, as a function of the dimensionless puddle density strength, δx and the scattering strength t. The peak position is approximately proportional to δx at high inhomogeneity, i.e. when $\delta x \gtrsim 1$. At low inhomogeneity, i.e. when $\delta x \ll 1$, the peak position is approximately constant, matching the expected value for the homogeneous case.

to the residual density, as:

$$\delta n_H \simeq \left(\frac{k_B T}{\hbar v_F}\right)^2 \cdot \delta x = \left(\frac{k_B T}{\hbar v_F}\right)^2 \cdot \left(\frac{\hbar v_F}{k_B T}\right)^2 \delta n_r \quad \rightarrow \quad \delta n_H \simeq \delta n_r$$

This supports the idea that the density δn_H, at which the peak in the Hall resistance measurements saturates, is a good approximation to the residual density of puddles in the system. (See Section 2.1.3, where we find $\delta n \approx (5 \pm 2) \times 10^9, \mathrm{cm}^{-2}$ at $5\,\mathrm{K}$ from longitudinal data; Figure 2.8 shows that the Hall resistance predicts a similar value.) We can see that even this simple model of two puddle types, with densities set equal to the measured saturation width, can accurately predict the saturation at low temperatures in our measurements.

As a consistency check, we also observe that for small inhomogeneities or at high temperatures, when $\delta x \ll 1$, the peak position becomes independent of puddle strength as expected for a homogeneous device. This implies that the actual density in real units at the peak is proportional to T^2, as anticipated.

2.5 Final Remarks on Drag-Modified Transport in Graphene

In summary, we have presented a comprehensive investigation of the observed negative mobility in the Dirac plasma of high-quality monolayer graphene devices, introducing a robust experimental protocol and a powerful tool for microscopic characterisation via a drag-modified Drude model. All experiments were conducted under ideal conditions for probing intrinsic, non-quantised transport; employing low currents, elevated temperatures, and minimal magnetic fields.

This work demonstrates that negative mobility in graphene can be understood by accounting for electron-hole interactions, which induce substantial drag effects beyond the reach of classical models based solely on isotropic momentum-relaxing processes, such as phonon and impurity scattering. Instead, we have established that a drag-modified Drude model, derived from the Boltzmann kinetic equation, provides a more truthful description by capturing the momentum-conserving nature of electron-hole scattering. Notably, this model converges to the standard two-carrier Drude model when inter-carrier scattering is negligible.

By parameterising the distinct momentum-relaxing (phonon/disorder scattering) and momentum-conserving (inter-carrier scattering) scattering mechanisms through two microscopic timescales, τ and τ_{eh}, respectively, we could extract these quantities directly from experimental data. This approach yielded a remarkable agreement across independent longitudinal and Hall resistivity measurements, even under the assumption of constant scattering times. The extracted timescales remained approximately density-independent in the high-temperature intrinsic regime, while τ exhibited a density-dependent crossover at lower temperatures, consistent with a shift toward disorder-dominated transport.

While the current study provides a strong foundation for understanding mixed two-fluid dynamics and drag phenomena in clean graphene, future work could explore the effects on non-local hydrodynamic transport near the Dirac point, the effects of stronger magnetic fields, or extend these methodologies to multi-layer graphene devices.

Ultimately, these findings illuminate simple methods of characterisation and understanding of hydrodynamic transport in graphene that could offer insights relevant to a wider class of quantum materials exhibiting collective mixed two-fluid electronic dynamics.

Work undertaken in this chapter was published in *Nature Communications*. [106]

CHAPTER 3

Probing Electronic Transport via Scanning Gate Microscopy

Graphene, a two-dimensional honeycomb lattice of carbon atoms, has updated our understanding of transport due to its unique electronic properties. Collective fluid-like motion, hydrodynamics, of the electron gas has been conjectured to explain various observed transport phenomena. [30, 110] This chapter focuses on employing scanning gate microscopy (SGM) to probe such transport phenomena in hBN-encapsulated graphene devices, with an emphasis on unveiling signatures of hydrodynamic flow. The hydrodynamic description of electron transport emerges when the mean free path for electron-electron scattering, l_{ee}, is much shorter than the momentum-relaxing mean free path due to impurities or phonons, l and device dimensions, L. [111] In this limit, $l_{ee} \ll l, L$, the electron system can be modelled as a fluid governed by hydrodynamic equations.

Hydrodynamic electronic transport has been observed in a few material systems, with ultra-clean graphene being a prime candidate. hBN-encapsulated graphene, due to its high mobility, is particularly well-suited to study intrinsic transport. Indicators of hydrodynamic transport have been observed at intermediate temperatures (between ballistic and diffusive regimes), typically 150-250 K, where electron-electron collisions dominate over other scattering mechanisms.

Observations that hydrodynamic transport can explain in graphene include: the Gurzhi effect, a reduction in resistivity with decreasing channel width due to viscous drag [30]; the breakdown of the Wiedemann-Franz law near the Dirac point, revealed by an enhanced Lorenz number [49]; and negative non-local resistance, where current injection induces negative potential measured non-locally. [30]. These measurements provide indirect evidence of hydrodynamic flow, but direct spatial imaging of current flow patterns would offer more definitive evidence. Some studies have attempted to image the current flow in graphene: using SGM in the ballistic regime by taking advantage of transverse magnetic focusing [91, 92], using scanning magnetometry to observe hydrodynamic flow of the Dirac fluid [112] or more recently in special geometries to observe vortices. [113] However, the direct imaging of vortices using SGM in standard Hall-bar geometries in graphene monolayers, until now, has remained unseen.

In hBN-encapsulated graphene, where mobilities are highest and disorder is minimised, SGM could reveal elusive features such as bulk vorticity/whirlpool formation. Our hypothesis is that SGM will exhibit distinctive temperature-dependent patterns transitioning from diffusive flow at room temperature to hydrodynamic responses at low temperatures (160 K).

Through this work, we aim to make advances in the imaging of two-dimensional quantum gases/fluids, and provide insights into the analysis of such images.

Outline of Chapter This chapter will flow as follows. In the first section, we will cover how we aim to perform SGM on hBN-encapsulated graphene devices, including an initial test campaign (Section 3.1.2) followed by characterisation of study devices and resulting SGM maps in Section 3.1.3.

Next, we will develop a simplified theoretical model to understand how SGM perturbs diffusive transport in Section 3.2, before moving on to numerical simulations of hydrodynamic transport under SGM perturbations in Section 3.3. From modelling and simulations, we quantify hydrodynamic viscosity and will finally conclude with a summary of findings and future outlooks in Section 3.4.

3.1 Scanning Gate Microscopy Methodology

Section 1.5 describes the general principles of scanning probe microscopy (SPM) and the specific implementation of scanning gate microscopy (SGM). Here, we detail the experimental setup used to perform SGM on hBN-encapsulated graphene devices, including sample preparation, cryogenic cooling, and electrical measurement configurations.

3.1.1 SGM Experimental Setup

3.1.1.1 Chip Carrier Preparation

For sample preparation, clean devices are bonded to chip carriers using crystalline salol (phenyl salicylate), a solid at room temperature that melts at 42°C, allowing easy clean mounting and removal. The main intention of using salol is to provide good acoustic transmission of ultrasonic sound waves from the piezoelectric transducer the device is mounted on; experiments that utilise this are not presented in this thesis. Conductive silver paint along the device edge ensures good electrical contact to the device gate. Once secured in place, 25 µm gold wires were attached to the device bonding pads via a two-part conductive epoxy; this was essential for

precision compared to low viscosity silver paint. After the epoxy has dried, which can take a few hours, the gold wires are physically pressed into the chip carrier contact pads and then silver paint is applied on top to ensure a secure electrical connection. This process is done careful of the fact that neither the gold wires nor the epoxy should obstruct access to the device by a scanning probe. A small surface-mountable PT1000 temperature-sensitive resistor (RTD) is also attached to the chip carrier in a 4-probe configuration, allowing for accurate temperature measurements of the sample space. The completed chip carrier configuration is shown in Figure 3.1 (right).

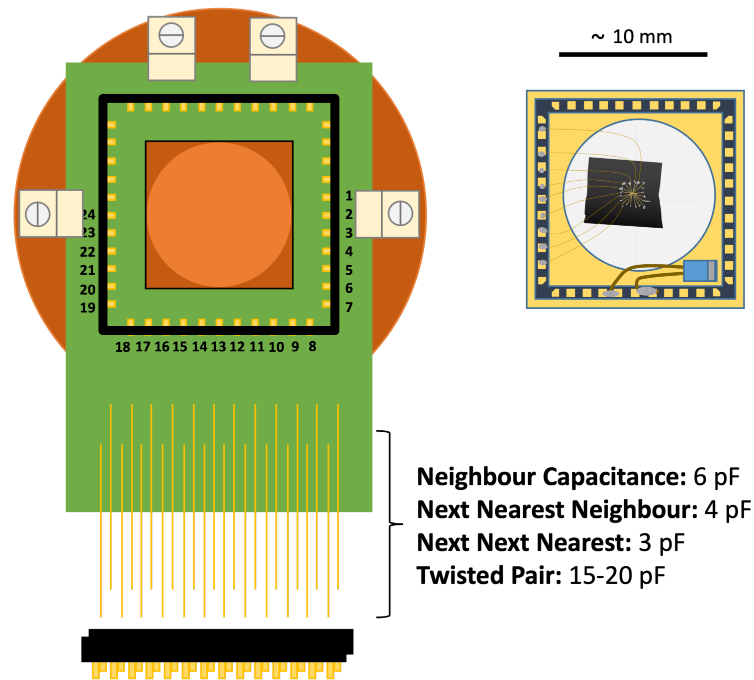

Figure 3.1: Chip carrier PCB, with socket, is securely clamped to the copper sample stage (left). The PCB has a hole in the centre of the socket where the copper sample stage can extend up through the PCB and make thermal contact with the chip carrier. The measured capacitance between contact wires on the socket are given. The device is mounted to a 44-terminal leadless chip carrier (right). The chip carrier has a blue PT1000 RTD mounted.

3.1.1.2 Sample Stage and Cooling

A not-to-scale schematic for the high-vacuum (HV) scanning-probe microscope assembly is shown in Figure 3.2. The chamber is designed to allow for easy access to the sample stage and the scanning head, while also providing a controlled environment for low-temperature measurements.

The sample stage is a solid copper block with a centre protrusion that extends through the centre of the PCB chip carrier socket. This allows for direct carrier-

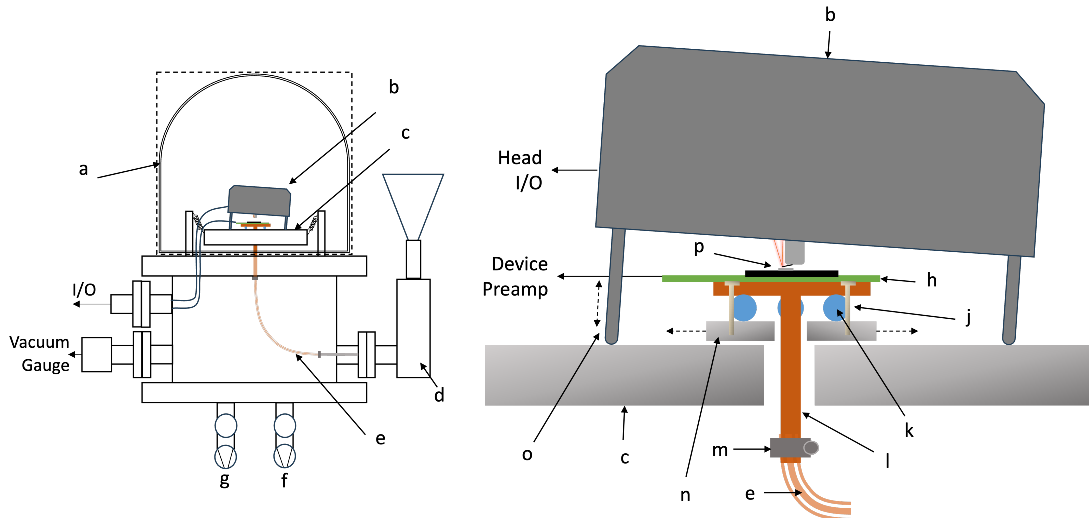

Figure 3.2: High-vacuum (HV) scanning-probe microscope assembly. Cross-sectional schematic of the HV chamber (left), identifying a) glass dome HV enclosure, b) microscope head, c) AFM base suspended on springs, d) liquid-nitrogen reservoir, e) flexible copper braid for thermal linkage, f) turbomolecular pump, and g) ion pump. Close-up of the AFM base (right) showing h) chip-carrier sample board and socket, j) plastic mounting screws, k) 10 mm glass spheres, l) copper sample platform, m) jubilee clip securing the thermal braid, n) step-motor driven XY positioning platform for the sample stage, o) step-motor driven Z adjustment of microscope-head height, and p) measurement area containing the device under test and the scanning probe.

to-copper contact where added cryogenic vacuum grease (e.g. Apiezon N) improves thermal coupling. Modifications were made to the PCB that holds the chip carrier socket, to make a hole in the centre of the socket. The copper stage is then isolated from the room-temperature AFM positioning platform by three 10 mm glass spheres, the assembly is clamped to the platform with plastic screws. The AFM positioning platform is part of the larger AFM base that has integrated step motors for coarse positioning of the sample stage. Coarse positioning uses two stepper motors (5 µm steps over 5 mm range) moving the stage relative to the base and scanning head. The AFM base is then suspended on springs to isolate it from vibrations, as shown in Figure 3.3.

Extra considerations are required for low-temperature measurements. In our setup, the AFM system is isolated inside a sealed glass dome, allowing for high vacuum (HV) environments. It is crucial to remove water vapour from the air such that, when cooling down, ice does not form on the chip surface and hinder AFM measurements. The entire stage is enclosed in the dome and is first pumped by an EXT75DX CF63 turbomolecular pump (multi-stage axial-flow turbine). Below 10^{-6} Torr, the vacuum pumped is switched to an ion pump (e.g., Varian StarCell)

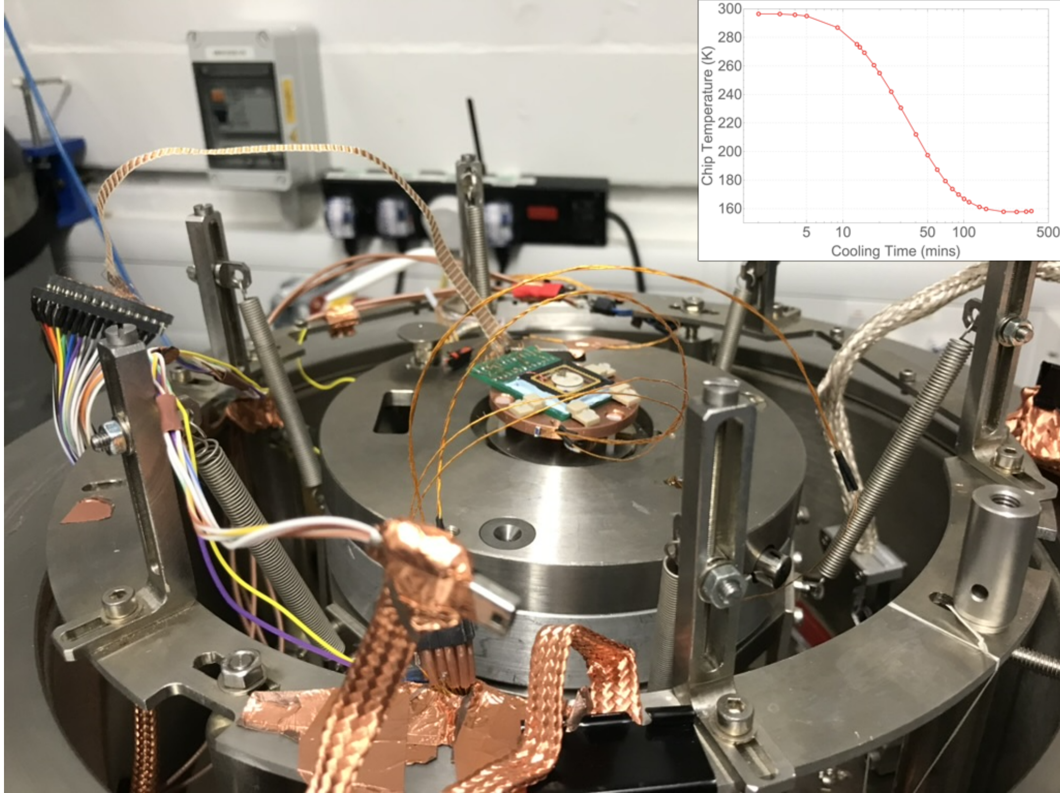

Figure 3.3: The metal AFM base without the scanning head is suspended on springs with the copper sample stage and chip with device is installed in the centre. Inset: the cooling time from room temperature to 160 K for the copper sample stage as measured from the chip carrier.

to reach and maintain pressures $\lesssim 10^{-7}$ Torr.

The cooling mechanism uses a liquid nitrogen bath with access external to the dome but thermally connected to the inside chamber via a metal rod. The copper sample stage has a long rod section that extends down through the suspended AFM base and connects to the liquid nitrogen reservoir via two flexible copper braids. Copper braids are used as a flexible mode of thermal exchange that allows for isolation of the sprung AFM base from external vibrations. This design was upgraded from an older version where braids were soldered together; soldered joints have good electrical properties but are not optimal for thermal exchange, so strong mechanical joints were used in the redesign by using multiple jubilee clips.

In operation, the chip carrier temperature in this configuration reaches 160 K in 2.5 hours using liquid nitrogen, see inset of Figure 3.3. Getting closer to liquid nitrogen temperatures would require more direct cooling.

3.1.1.3 SGM Probe and Scanning Head

For scanning gate microscopy, the tip maintains a constant gate voltage using an external source-measure unit (SMU), routing is via a coaxial cable from the SMU to a SR555 preamplifier that measures current through the line ($\pm 1\,\mu$A input range, converting current to voltage) and then up to the chamber where a standard isolated wire is used up to the scanning head and down to the probe carrier. The probe carrier is attached to the scanning head, which is shown in Figure 3.4 (upper-left). The probe carrier is a small metallic semi-circular plate that can be attached to the scanning head by small magnets. A probe is bonded to the carrier by standard cyanoacrylate adhesive and electrical connections are made to the probe via a small surface-mounted resistor, typically $1\,\mathrm{M\Omega}$ (see Figure 3.4 (lower-left)). The tip voltage is typically set no more than 1 V, depending on the device and the desired electrostatic effect and so to protect both the tip and the device from sudden spikes in current, the $1\,\mathrm{M\Omega}$ resistor is included.

For contact mode, the probe used was a diamond-coated silicon tip with cantilever dimensions $3\times225\times27.6\,\mu$m, with a force constant $6.2\,\mathrm{N\,m^{-1}}$ (CDT-FMR-20, NanoWorld). The top side is coated in 30 nm aluminum for enhancing laser detection by increasing reflectance $\times2.5$, and the tip has a conductive diamond boron doped coating protruding $10\,\mu$m from the cantilever with a tip radius 100-200 nm. The quoted resistivity of the tip is 0.003-0.005 $\Omega\,$cm and the doped single crystal silicon is 0.01-0.025 $\Omega\,$cm.

This tip is durable and ideal for electrostatic applications like SGM on encapsulated graphene devices.

For tapping mode, a silicon tip with cantilever dimensions $4\times125\times30\,\mu$m, with a force constant $80\,\mathrm{N\,m^{-1}}$ (CDT-NCHR-10, NanoWorld) is used. The top side is coated in aluminum for detection, and the tip has a conductive diamond coating protruding $10\,\mu$m from the cantilever with a tip radius 100-200 nm. This probe is very similar to the one used for contact mode, but with a shorter cantilever it has a higher force constant and higher resonant frequency, making it more suitable for tapping mode. The higher force constant allows for more robust scanning in tapping mode, where the tip is oscillated at a frequency of approximately 400 kHz. Faster oscillations enable quicker scanning and better tracking of surface features, improving imaging speed and resolution.

The scanning head houses an optical camera, the laser and photodiode, Z stepmotor and XYZ piezos controlling probe position. It connects to a signal access module interfacing with computer and instruments through an I/O port in the side of the HV chamber. A breakout box handles device I/O, with a BNC coax port

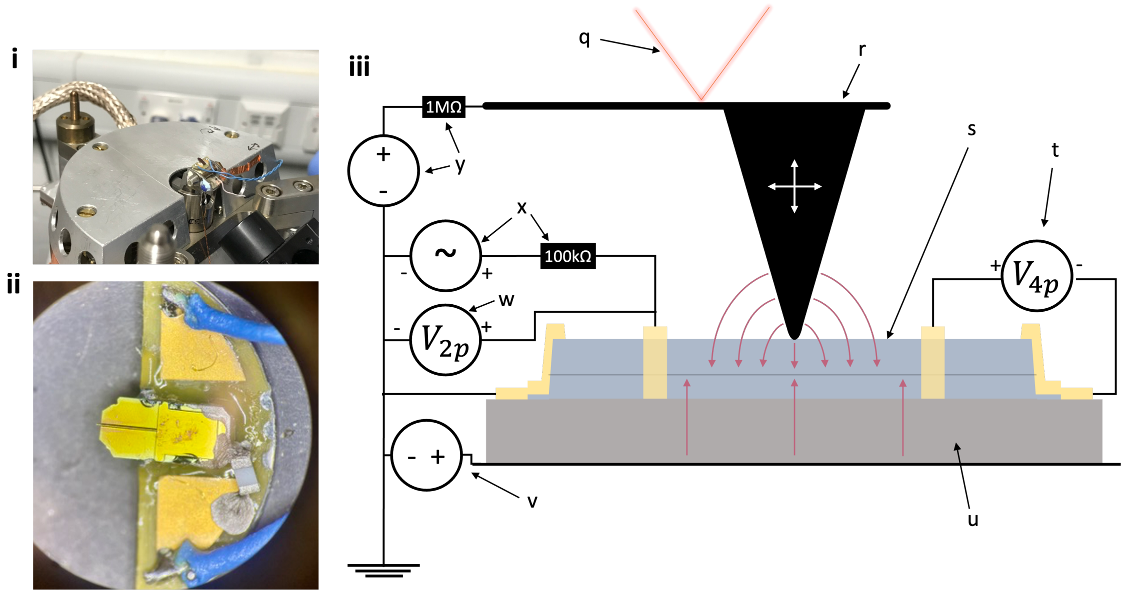

Figure 3.4: Scanning gate microscopy with four-terminal transport measurement circuit. Photograph of the underside of the microscope head (upper-left). Optical image of a scanning probe bonded to metallic carrier with small 1 MΩ surface-mounted resistor integrated (lower-left). Schematic of the measurement configuration (right) showing q) focused laser beam used for optical deflection/read-out of the cantilever, r) scanning-probe tip mounted on a XYZ piezo scanner, s) device under test (DUT) with defined gold contacts (yellow), t) lock-in amplifier providing four-probe (sense) voltage measurement (goes via preamplifier), u) insulating substrate supporting the DUT, v) gate electrode biased by a source-measure unit (SMU) that sets the DC back-gate potential, w) lock-in amplifier providing two-probe voltage measurement (goes via preamplifier) x) AC current drive supplied by an oscillator through a 100 kΩ series (current-limiting) resistor, and y) controllable tip (source) bias delivered through a 1 MΩ protection resistor. The effect on the device's resistivity due to the tip gate and radius is estimated in Section 3.2.1.

for each contact as well as individual ground switches for each contact. Including ground switches allows for easy isolation of separate devices on the same chip carrier.

The scanning head has three adjustable legs: two manual, and a computer-controlled leg for the tip-to-sample approach. The approach/landing process, in contact mode scanning, uses the motorised leg, with PID feedback on, to lower the scanning head down to the surface of the sample. This can be an automatic or manual process. The process starts with the Z-piezo at full extension towards the surface, and then the height of the scanning head assembly (via the front step motor) is lowered until the probe contacts the surface, and a deflection of the cantilever is measured. The whole assembly continues to be lowered until the cantilever deflection hits a set point for the measured force, at which point the PID feedback starts to retract the Z-piezo height to balance out the continuing to lower scanning head assembly until the Z-piezo is in the middle of its range, ready for scanning.

In high vacuum because of a low-damping environment, when the PID feedback is initially enabled, positive feedback can cause runaway oscillations due to the change in dynamics that would require different PID parameters to stabilise. In this situation, the approach is performed manually which requires adjusting the scanning head height using the Z step motor until 'snap-in'. Snap-in is when the tip jumps to the surface, causing negative deflection. Once the tip is in stable contact with the surface then normal feedback can be enabled. Scanning XYZ piezos have ranges of $100 \times 100 \times 10\,\mu m$ with a power supply that can handle less than 0.1 nm steps. Therefore, scan precision will depend on probe choice and environmental variables. Updates made to our Nanoscope software enabled us to scan in any XY direction, allowing scan paths to be precisely aligned with the device geometry and avoiding unnecessary scanning over device edges.

3.1.1.4 Measurements and Capacitance

Current source and potential measurements are done via SR830 lock-in amplifiers for superior signal-to-noise ratio by isolating the reference frequency. The current source is in reality the AC oscillator source of one lock-in, capable of $0.004 - 5\,V_{rms}$, that is limited to below $50\,\mu A$ via a $100\,k\Omega$ resistor in series with the oscillator source. The actual current is then measured via the same lock-in amplifier, at the oscillator frequency, by measuring the potential drop across the current-limiting resistor. Three lock-in amplifiers are used in tandem, synced to the same frequency: one for the AC current source and to measure current, one to measure the 2-probe voltage, and one for the 4-probe voltage. Lock-in layout with respect to the other instruments and the HV chamber can be seen in Figure 3.5.

Figure 3.4 (right) shows an example of a measurement configuration. The 4-probe voltage is measured between two contacts on one end of the device, while the current and corresponding 2-probe voltage is measured across the other end of the device. This configuration aims to give the best chance to observe hydrodynamic transport.

The speed of the SGM scan is significantly limited by the settling time per measurement of the lock-in amplifiers. This is determined by the oscillator frequency, which is constrained by the total capacitance in the circuit. The majority of the capacitance typically comes from the device, the measurement instruments, and the cabling connecting them. To minimise capacitance, one effective approach is to reduce the total length of cabling in the system. This can be achieved by incorporating instrumentation amplifiers, such as the AD8220, positioned close to the device. Two AD8220 instrumentation amplifiers are used to amplify the differential signals before they are transmitted to the lock-in amplifiers. Specifically, one AD8220, configured with a gain of 1, amplifies the differential signal for the 2-probe measurement, while

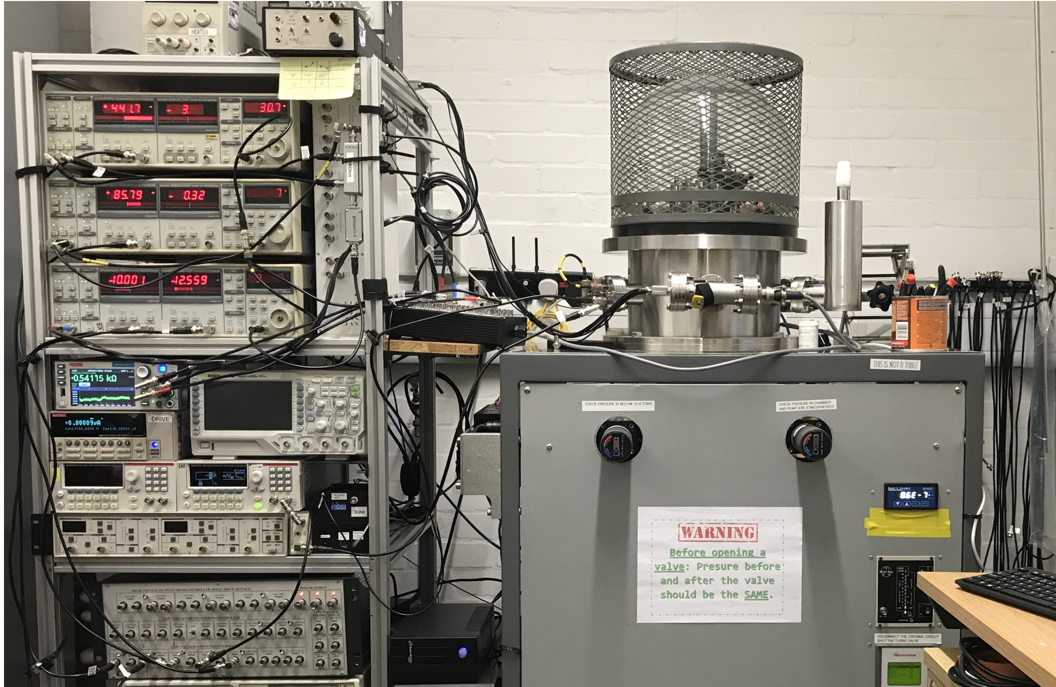

Figure 3.5: Photograph of the HV chamber (right) and measuring instruments (left). Three SR830 lock-in amplifiers are stacked to measure different potentials. Source meters below supply the device back-gate and tip-gate voltages and monitor the chip-carrier RTD for temperature readout.

another, set with a gain of 100, amplifies the 4-probe measurement. This configuration reduces the impact of parasitic capacitance and inductance from long cables, thereby minimising phase shifts and out-of-phase voltage components in the 4-probe measurement, particularly at higher frequencies, while also improving the signal-to-noise ratio. Power supply for the AD8220s is received from the DC output of one of the SR830 lock-in amplifiers at $\pm 10\,\text{V}$ via the DUT breakout box. The AD8220s are mounted to a PCB, schematic in Figure 3.6, designed to intercept the measured signals inside the HV-chamber and can easily be connected/disconnected, when the chamber is not under vacuum. It is inserted in the routing between the I/O of the inner vacuum chamber and the PCB holding the chip carrier socket. In this specific application, we didn't allow for 'hot swapping' of connections, the contacts to be measured were planned in advance, and all other contacts are left electrically floating.

The fine wires that connect the PCB to the I/O socket of the HV chamber have capacitance between them, as shown in Figure 3.1. The wires are packaged as twisted pairs and the capacitance between a single wire and its twisted pair is approximately $15 - 20\,\text{pF}$. Whereas, the nearest neighbour, next nearest and next next nearest neighbour capacitances are 6, 4 and $3\,\text{pF}$ respectively. Therefore, by not using twisted pairs, some capacitance was avoided.

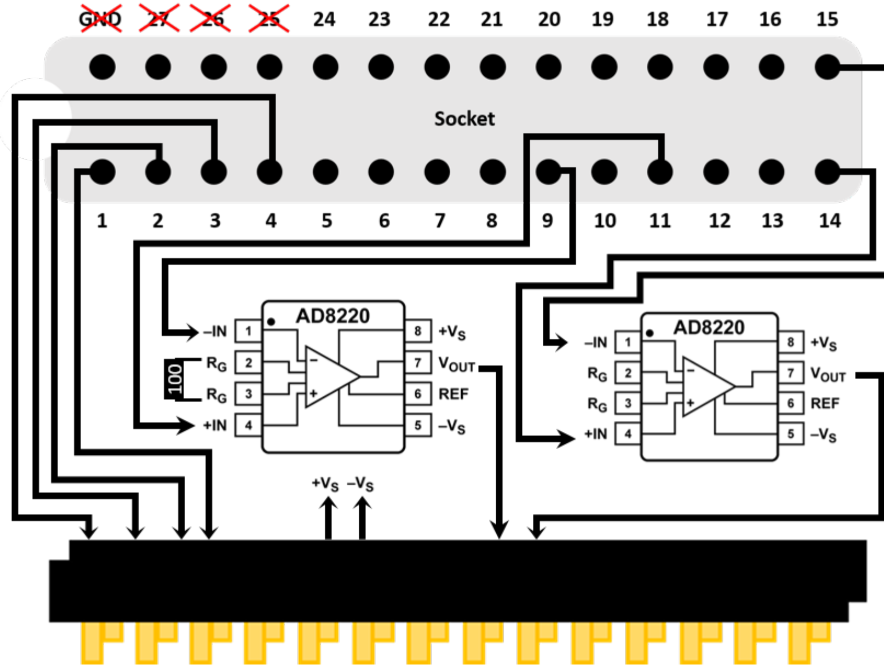

Figure 3.6: Pre-Amplifier PCB stage that intercepts signals from the AFM PCB. 4-Probe voltage is measured across contacts 11 and 9, amplified with a gain of 100. 2-Probe is measured across 14 and 15, with a gain of 1. Contacts 1-4 are pass-through for RTD temperature measurement. Voltage supply for amplifiers, $\pm V_s$, is also carried from breakout box. The stage is mounted inside the HV-chamber.

Capacitance is ultimately dominated by the DUT, and so scanning speeds and ultimate scanning time depend on the device measured.

3.1.2 Preliminary Experiment on Scanning Gate Microscopy

To begin investigations into scanning gate microscopy (SGM) for probing intrinsic transport in graphene, an older device, GHA051016, fabricated in October 2016, was selected as a 'test bench'. This device consists of hBN-encapsulated monolayer graphene on a SiO_2 substrate, consistent with the design of all devices in this research. Although aged and having lost functionality in many contacts due to damage over time, it had previously been characterised as exhibiting non-local negative resistance, indicative of hydrodynamic electron flow. With only three contacts retaining sufficiently low resistance, $\sim 10\,\mathrm{k}\Omega$, SGM experiments were limited to 2-probe and 3-probe resistance measurements. The experimental setup, including details on the scanning system, transport measurements, and environmental control, is described in the preceding Section 3.1.1 and applies uniformly across all devices studied here. An atomic force microscopy (AFM) topography image of the device is shown in

Figure 3.7, revealing the Hall-bar geometry and surface features prior to and after successive SGM scans.

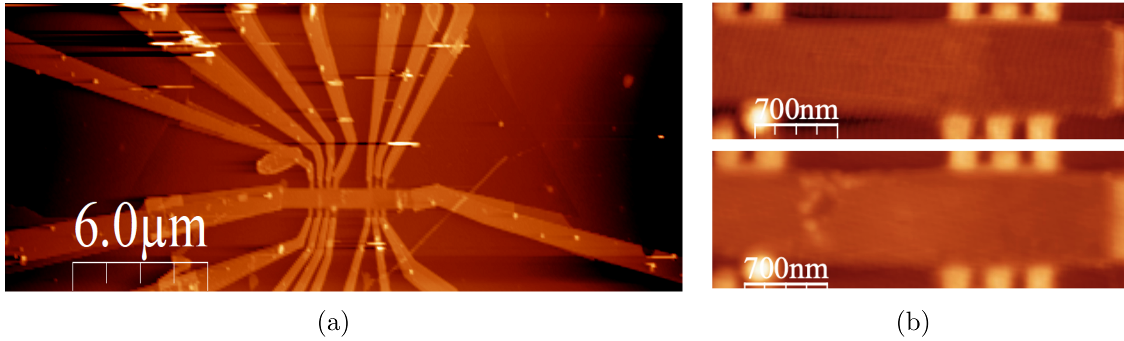

(a) (b)

Figure 3.7: **(a)** 30 µm wide AFM topography of the preliminary device. **(b)** AFM indicates surface damage after successive AFM scans.

Initial SGM scans demonstrated the feasibility of obtaining measurable signals with low noise levels, validating the setup for future testing. A notable observation was the high out-of-phase (OOP) signal component, which approached approximately 1/6 of the in-phase signal in 2-probe measurements and up to 2/3 in 3-probe configurations. This elevated OOP response is directly related to the high contact resistances of this device, and was particularly something to be addressed when performing future 4-probe configurations. The scanning speed and image resolution is directly linked to the OOP signal, so this prompted us to alter the design to integrate instrumentation amplifiers to decrease circuit capacitance. Modifications to add instrumentation amplifiers were implemented for subsequent devices to allow for higher frequency measurements, and therefore, faster scanning. Upgrades to the sample stage for achieving lower temperatures (previously limited to a minimum of -70°C) were done immediately after initial measurements.

At room temperature the 2-probe resistance, that is dominated by contact resistance, was significantly influenced by the tip voltage by approximately 1% ($\sim 200\,\Omega$), with scan patterns showing two bright spots at the current contacts, aligning well with expectation that the tip changes the 2-probe resistance of the device more effectively in areas of higher current density. This is shown in Figure 3.8.

Scans were taken at a rate of 4 ms per point and $5\,\mu\text{m}\,\text{s}^{-1}$, covering a $3.5 \times 1.2\,\mu\text{m}$ region with a 20 nm step size. Lock-in amplifier time constant was four times smaller than the time per point at 1 ms, sufficient for the signal to settle. To optimise image contrast, matrix sweeps of tip and gate voltages were performed, revealing that larger gate voltages combined with small, opposite-polarity tip voltages yielded data exhibiting the most pronounced changes as the tip traversed the device (higher contrast in the image). At low temperatures, similar results were observed as well as for 3-probe measurements. This initial test serves as evidence for SGM's capability

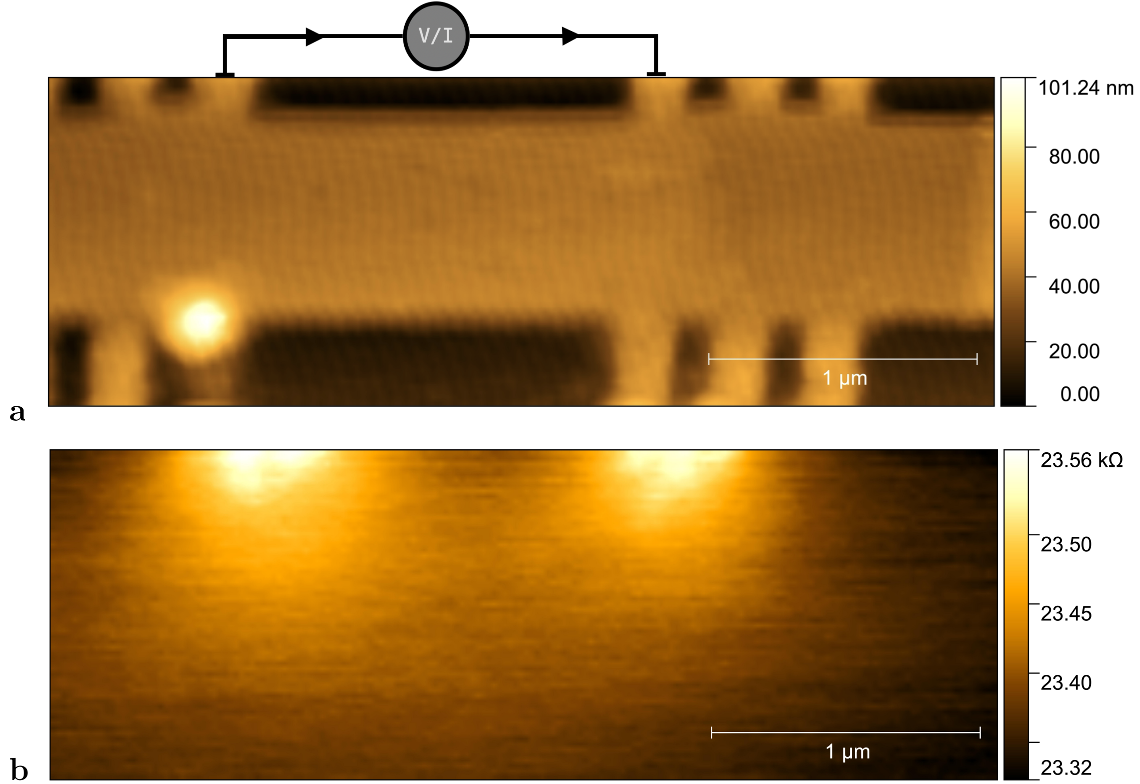

Figure 3.8: 3.5 × 1.2 µm scan of device at 4 ms/pt with 20 nm step size, equiv. 165 × 60 resolution **(a)** Topography measured. **(b)** The 2-probe resistance measured as a function of tip position. Where gate and tip voltages were $V_g = 5\,\text{V}$ and $V_{tip} = 0\,\text{V}$, respectively. Source current of 25 µA was used at 10.678 kHz.

to visualise flow signatures in these devices.

Several practical insights emerged from these tests, informing refinements for future work. Comparative AFM topography 'before and after' scans revealed progressive surface damage, see Figure 3.7(b), indicating the need to minimise scan iterations, and tapping mode SPM is suggested to reduce mechanical wear. Spikes in leakage current were detected along device edges, this is because the graphene monolayer is not protected from the tip gate along the edge, particularly under higher tip voltages. Therefore, we also suggest that scan areas could be confined to the device's main body to avoid edge-related leakage. The initial scanning system was restricted to horizontal or vertical directions, lacking arbitrary xy-plane orientation; this was addressed through a system upgrade to enable flexible scanning paths in subsequent devices. Additionally, resistance measurements exhibited drift and occasional large jumps that were uncorrelated with leakage events or topographical anomalies. We offer an explanation that contact-mode scanning induces surface charge redistribution, such as static charges or mobile charged impurities. While the underlying mechanism of this switching behavior remains not completely understood, post-processing techniques, that flatten drifts and normalise jumps, work

effectively to suppress the switching artefacts while enhancing the image contrast attributable to repeatable tip-induced perturbations.

Overall, these preliminary results established SGM as a viable tool for hydrodynamic studies, while identifying key limitations and optimizations for advancing to newer, fully operational devices.

3.1.3 Probing 4-Probe Non-local Resistance Using Scanning Gate Microscopy

Moving on to functional devices where the 4-probe resistance can be measured, we aim to use the scanning gate to locally modify the resistivity of the graphene sheet under the tip to create an image/map of resistance vs tip position. The configuration for current probes and voltage probes is a 4-probe non-local configuration that is designed to provide the best signal for observing the hydrodynamic flow of a Fermi fluid indicated by a sign reversal of the measured 4-probe non-local resistance. Non-local refers to the separation of the voltage measurement and the current flow path.

3.1.3.1 Device Geometry

In this study, we use two high-quality hBN-encapsulated monolayer graphene devices. Two Hall-bar devices were etched into a single hBN-G-hBN heterostructure approximately 40 nm tall on top a 300 nm SiO_2 substrate; the bottom and top layers of hBN are approximately 20 nm thick. Once the heterostructure was etched down to expose the monolayer graphene, gold was deposited to the edge of the device arms. Approximately 25 nm, in thickness, of gold was deposited, creating one-dimensional edge electrical contact to the graphene sheet.

The Hall-bar geometry has a central 2×6 µm main body with 400 nm wide arms with varying lengths. The differing arm lengths were for a different experiment for ballistic-transport measurements. In our hydrodynamic/non-local configuration we keep the longer arms as the current injection leads and the shorter arms as voltage probes, since this makes the potential probes less invasive while the longer current leads better define the drive boundary conditions. Swapping contacts would mainly increase the series lead resistance approximately in proportion to the arm-length and increase out-of-phase signal. Topography of the two devices can be viewed in Figure 3.9.

Contact mode AFM topography (see Figure 3.9(b)) showed the top surface of the devices were flat with a variation of approximately 5 nm (approximately 10 layers of hBN). A smooth surface is ideal for quicker scans, but more importantly, it allows for a consistent tip to graphene separation distance for scanning gate microscopy.

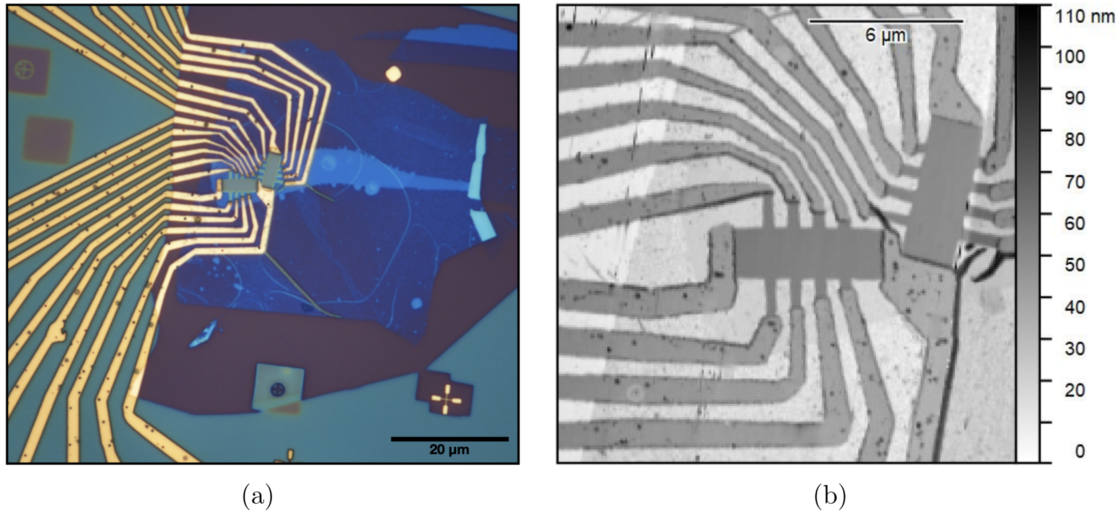

(a) (b)

Figure 3.9: Optical **(a)** and Atomic Force Microscopy **(b)** images of a pair of hBN-encapsulated monolayer graphene devices. Two devices with identical Hall-bar geometries were etched into the same hBN-G-hBN heterostructure. Gold one-dimensional edge contacts provide electrical contact to the device arms.

3.1.3.2 Device Suitablity

Prior to the scanning gate study, it was relevant to see that these devices were actually high-quality to show intrinsic hydrodynamic transport.

The characterisation of the devices used in this study came in a few ways. Here we present the characterisation of the first device used in the study and will not include the second device for brevity; however, the second device, fashioned from the same heterostructure, showed qualitatively similar characteristics to the first.

The resistivity was measured using standard lock-in amplifier techniques, as described previously (see Section 1.4.2). The measured longitudinal conductivity is shown as a function of the deduced net carrier density and of the device temperature (see Figure 3.10(a)). The device shows good symmetry around the neutrality point down to low temperatures, retaining a smooth density dependence down to 100 K. This indicates low residual doping and no large-scale charge inhomogenities. Below 50 K, both periodic and aperiodic density-dependent fluctuations become visible in the conductivity. The periodic oscillations are consistent with Fabry-Pérot interference, while the smaller aperiodic features are characteristic of universal conductance fluctuations (UCF). Fabry-Pérot interference [114] arises in the quasi-ballistic regime from partial reflections between interfaces that form cavities. The observed oscillation period corresponds well to a sub-micron cavity length, making it likely that reflections at the arm-body transitions (arm width is 400 nm) are responsible for the periodic oscillations. The smaller aperiodic fluctuations arise from UCF, which occur when electrons can traverse multiple elastic scattering paths with the

quasiparticle phase remaining coherent over the device dimensions. [115] As the gate voltage tunes the Fermi energy, the relative phases of these paths change, leading to sample-specific modulations of the conductance. At higher temperatures, increased inelastic scattering reduces the phase-coherence length and suppresses quasi-ballistic transport. Consequently, both the Fabry-Pérot interference and UCF are averaged out, resulting in smoother conductivity curves. Mobility is the primary indication of the level of disorder present and, as shown in the inset of Figure 3.10(a), the mobility of the device at 270 K was approximately $20\,\mathrm{m^2\,V^{-1}\,s^{-1}}$, on par with clean devices we have studied previously.

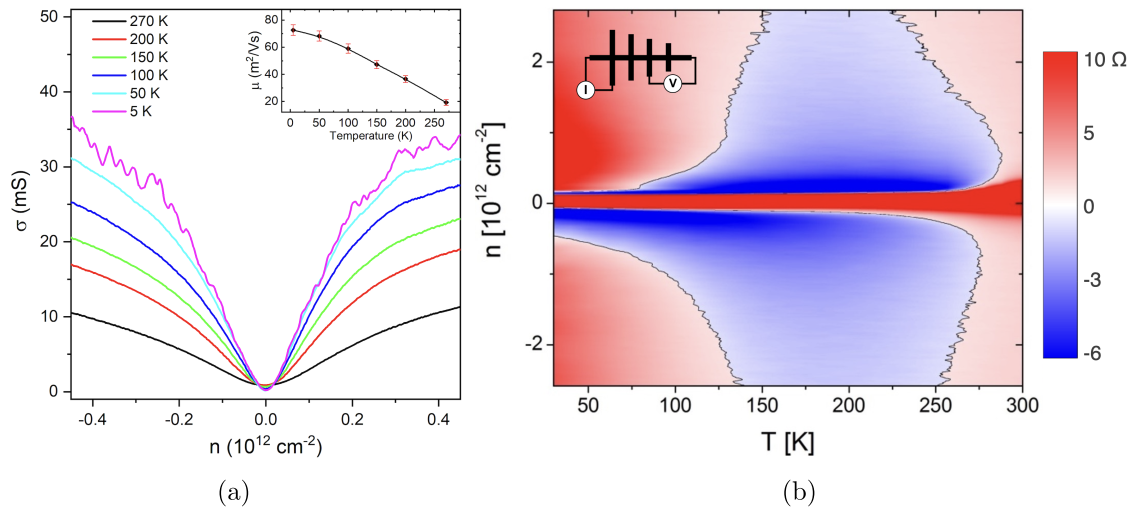

Figure 3.10: **(a)** Longitudinal conductivity as a function of carrier density, n. Inset: Mobility as a function of temperature at density $0.2 \times 10^{12}\,\mathrm{cm^{-2}}$. **(b)** 4-probe non-local resistance, $R_{4p}(n, T)$, measured as a function of net density and temperature. Blue areas indicate regions of negative resistance indicative of hydrodynamic flow. A schematic of the non-local measurement configuration is shown in the upper-left, where I shows current contacts and V shows voltage contacts.

The longitudinal conductivity shows a square-root carrier density dependence at room temperature, quantifiably comparable to longitudinal resistivity measured in the research of electron-hole drag (see Figure 2.5(a)). As shown in that research, disorder/phonon scattering times appeared independent of density, n, at room temperature, and so conductivity was proportional to $\sqrt{n}$, an observation we see in this device at room temperature too. In those previous devices, scattering time of disorder evolved into a $\sqrt{n}$-dependence at low temperatures causing conductivity linear in density, attributed to lower screening of charged-impurities at lower temperatures (see Figure 2.16(a)).

The room temperature mobilities in the devices used in this study are only slightly lower than that of the device studied in the electron-hole drag research, deviating about two times at low temperatures. Deviation at low temperatures, such as linear

conductivity is also suppressed. This is not because the device is cleaner, as evidenced by decreased mobility at room temperature, but because the width of the device in this study is 2 µm compared to the larger 15 µm width of the devices in the electron-hole drag study. In this research, at low temperatures, the mobility becomes limited as the mean free path exceeds the device dimensions and transport becomes ballistic.

The mean free path of the electrons with carrier density $0.2 \times 10^{12}\,\text{cm}^{-2}$ at 270 K is approximately 1.0 µm. This mean free path approximately doubles to 2 µm at 150 K, comparable to the device width. These simple estimates suggest that the onset of ballistic transport at around 150 K will be the limiting factor in the observation of hydrodynamic transport in these devices.

To check for hydrodynamic behaviour, 4-probe non-local resistance was measured both as a function of temperature, T, and of net carrier density, n. The map of $R_{4p}(n, T)$ is given in Figure 3.10(b). From this map, a significant temperature window appears below 275 K where the measured non-local resistance is negative. Focusing on temperatures above 150 K where we are confident that intrinsic transport is not affected by electron-hole puddles or ballistic transport, the largest negative resistance appears close to the Dirac point at around 160-170 K. At room temperature, the non-local resistance further from the Dirac point is approximately 1-2 Ω that transitions to a negative, but similar in magnitude, resistivity in the temperature range 150-250 K.

What is the ideal carrier density for hydrodynamic study of the Fermi fluid? Recalling from the study of electron-hole drag, the width of the Dirac point is proportional to T^2, see Figure 2.12. Therefore, to maintain a Fermi fluid, we should aim for a density greater than 1-2 times the thermal density at room temperature, an approximate $0.2 \times 10^{12}\,\text{cm}^{-2}$ carrier density should be sufficient. Keeping in mind that the neutrality point with respect to the applied back-gate voltage can move on the order of a couple volts ($\sim \pm 0.1 \times 10^{12}\,\text{cm}^{-2}$) between measurements, then an ideal density for scanning gate measurements is in the $0.3 - 0.5 \times 10^{12}\,\text{cm}^{-2}$ range.

Can the effect of a scanning tip gate on the non-local resistance of the order of 1Ω be reliably measured? Let's assume that the tip changes the resistance by 1% (in reality, the effect will be bigger, evidenced in experiment and analytical model). Under a 50 µA current the expected signal is 0.5 µV. Using the preamplifier with gain of 100, gives a required resolution of 50 µV.

What is the expected noise floor for our measurements? When contact resistance is low, these devices for scanning gate experiments operate in the 10 kHz range, allowing for lock-in time constants of order 1 ms. Note, for transport measurements inside the cryostat, where capacitance is higher due to longer cables, frequencies used

are typically 30-90 Hz. The noise floor is determined by the lock-in amplifier's input noise, measured around $30\,\mathrm{nV}/\sqrt{\mathrm{Hz}}$, and the measurement bandwidth (the effective frequency range that contributes to the noise in the system). The equivalent noise bandwidth (ENBW) is inversely related to the time constant, so for a 1 ms time constant and the 12-18 dB/oct low-pass filters used here, the ENBW is approximately $1/(10 \times 1\,\mathrm{ms}) = 100\,\mathrm{Hz}$. The total noise is calculated as the input noise multiplied by the square root of the bandwidth: $30\,\mathrm{nV}/\sqrt{\mathrm{Hz}} \times \sqrt{100\,\mathrm{Hz}} \approx 300\,\mathrm{nV}$. This means that if the scanning tip modifies the device's resistance by just 1%, the resulting signal should be about 100 times larger than the lock-in amplifier's noise floor. In other words, a simple estimate suggests that any change in resistance caused by the scanning tip should be detectable. However, if the preamplifier is removed, a 1% change in the device's nominal resistance (resistance value with no scanning tip present) might be too small to distinguish from the noise.

What voltage on the tip gate will produce the strongest change in resistance? By simple approximation, the largest change in resistance occurs when the chemical potential on the graphene sheet directly under the tip is moved to the Dirac point (neutrality point) where resistance is highest. This can be achieved by simply counteracting the electric field produced by the back-gate with opposite charge on the tip. However, for sufficiently large $|V_{\mathrm{tip}}|$ the tip can push the local density past neutrality while the surrounding sheet remains doped, a p-n junction ring can form and may introduce non-linear contributions, such as thermoelectric signals. [116] In this case, SGM images may qualitatively change because the tip-defined junction modifies transmission (through refraction/scattering) and can produce interference features. [117] We therefore approach neutrality from the same carrier side (no sign change), and can use the following geometric estimate. By simply estimating the distance between the graphene sheet and the back-gate (300 nm) vs the sheet-tip separation distance (20 nm), we can provide an estimate of the tip voltage as a function of the back-gate voltage, $V_{tip} \approx Vg\frac{t_{hBN}}{t_{SiO_2}} \approx 0.07V_g$. This is consistent with the similar relation found on tests with the preliminary device, where images with larger gate voltages combined with small tip voltages yielded data with highest contrast in the image. We can reduce the likelihood of a p-n junction under the tip by checking for a linear response in current and by confirming that the SGM signal varies smoothly and monotonically with $|V_{tip}|$, with no kink/sign-change that would indicate crossing neutrality and the formation of a p-n junction ring.

Is it possible to observe any effects of chemical potential pinning? This refers to the contact-induced doping (and reduced gate tunability) near a metal/graphene interface due to charge transfer. In high-quality encapsulated graphene contacted by metal stacks including gold, the resulting junction/transition typically forms within $\sim 30 - 150\,\mathrm{nm}$ of the contact edge, [118] and edge-contacted encapsulated devices

have shown a junction sharpness of order $d \approx 70\,\mathrm{nm}$. [119] Taking $\ell_{\mathrm{pin}} \lesssim 200\,\mathrm{nm}$ as a conservative bound, any pinning-related feature is at or below our SGM lateral resolution (tip radius $\sim 200\,\mathrm{nm}$), and approaching this close to contacts risks shorting. We therefore do not expect to resolve a distinct pinning signature.

Putting all this together, these devices under a back-gate ranging $\pm$(5-10) V with a tip voltage $\mp$(0.25-1.0) V are expected to give measurable results under scanning gate microscopy under reasonable currents, 50 µA assuming resistance is linear in current.

3.1.3.3 Temperature Gradient Estimates

It is important to establish that we have no significant temperature gradient across the bulk of our device that may change the interpretation of our results.

To estimate heating from the injector contacts, we use a 1D steady-state model for heat flow through the graphene, with distributed cooling into the surrounding hBN that encapsulates the monolayer. As an upper bound, we assume that the gold contacts provide no thermal conduction and, therefore, heat produced by contact resistance may only spread horizontally by means of the graphene sheet. Writing the temperature rise above the background as

$$\theta(x) = T(x) - T_0,$$

the 1D temperature equation is

$$K\frac{d^2\theta}{dx^2} - G\theta = 0,$$

with boundary conditions

$$\lim_{x\to\infty} \theta(x) = 0, \qquad -K\theta'(0) = q_0.$$

Here $K = kt$ is the in-plane sheet thermal conductance of graphene (of thermal conductivity k and thickness t), G is an effective out-of-plane thermal conductance to the surroundings, and q_0 is the injected heat flux at the contact ($x = 0$).

The solution to the second-order differential equation is

$$\theta(x) = \frac{q_0}{\sqrt{KG}} e^{-x/\ell}, \qquad \ell = \sqrt{\frac{K}{G}}.$$

With a drive current of 50 µA and a two-probe resistance of $4\,\mathrm{k\Omega}$, the total elec-

trical power dissipated is

$$P_{\text{tot}} = I^2 R = 10\,\mu\text{W}.$$

Only a small fraction of this power is generated uniformly in the graphene channel ($\sim 0.25\,\mu$W for sheet resistivity of $100\,\Omega$); the remainder is attributed to dissipation in the contact resistances for the current-injection leads.

The narrow current-carrying arm is 400 nm wide, compared to the $2\,\mu$m-wide ground contact. Therefore, the vast majority of the heat dissipated, $P \approx 8\,\mu$W, is injected at the 400 nm-wide contact. This gives a heat flux

$$q_0 = \frac{P}{w} = \frac{8 \times 10^{-6}}{0.4 \times 10^{-6}} \approx 20\,\text{W}\,\text{m}^{-1}.$$

Graphene has a significant in-plane thermal conductivity, $k = 5000\,\text{W}\,\text{m}^{-1}\,\text{K}^{-1}$ [120], which allows heat to efficiently spread into the sheet. Combined with the monolayer thickness $t = 0.34$ nm, and an effective thermal conductance into the surrounding hBN (into both top and bottom hBN flakes) of $G \approx 100\,\text{MW}\,\text{m}^{-2}\,\text{K}^{-1}$ [121], then we obtain

$$K = kt \approx 1.7\,\mu\text{W}\,\text{K}^{-1}, \qquad \ell = \sqrt{\frac{K}{G}} \approx 130\,\text{nm}.$$

The peak temperature rise at the contact edge is therefore

$$\theta(0) = \frac{q_0}{\sqrt{KG}} \approx 1.5\,\text{K}.$$

At the end of the long arm ($L = 1.6\,\mu$m), where the arm connects to the body of the device (note we use the longest arm of the Hall-bar for current injection), the temperature rise is

$$\theta(L) \approx 7\,\mu\text{K}.$$

Similarly, the temperature gradient at the end of the arm is

$$\left.\frac{d\theta}{dx}\right|_{x=L} = -\frac{q_0}{K} e^{-L/\ell} \approx -55\,\text{K}\,\text{m}^{-1}.$$

Within this simple 1D model, where all heat produced at the contacts is dumped into the device, both the temperature rise and temperature gradient decay exponentially away from the contact, characterised by the length $\ell \sim 130$ nm. Since the arm length is much larger than ℓ, essentially all of the heating is confined very close to the 400 nm contact, and the temperature rise at the far end of the arm is negligible. If we also consider the out-of-plane conductivity of hBN, which would reduce the effective vertical thermal conductance by approximately a factor of two, we find the

conclusion is unchanged ($\theta(0) \approx 2\,\mathrm{K}$, $\theta(L) \approx 0.4\,\mathrm{mK}$).

Giving the same treatment to the wider current contact finds a small temperature rise of approximately 0.1 K at the current contact which exponentially decays away over the same length $\ell \sim 130\,\mathrm{nm}$.

Given the sizeable Seebeck coefficient observed in graphene, approximately 50-100 $\mu\mathrm{V\,K^{-1}}$ in our density and temperature range [122], thermoelectric signals arising from contact heating could in principle be measurable. However, all measurements in this study use first-harmonic detection. Since Joule heating scales as I^2, it contributes primarily to the second harmonic, so first-harmonic measurements strongly suppress a direct thermoelectric signal. In addition, the non-local measurement geometry places the voltage probes many micrometres from the injector, while the modeled temperature rise in the bulk of the device is already negligible. Further, given the characteristic decay length is of similar magnitude to the tip radius, it is unlikely that SGM could probe such features.

Therefore, for the interpretation of our results, we can consider an effectively uniform temperature across the bulk of our device. In practice, the SGM images did not change qualitatively when the excitation current was adjusted to optimise signal-to-noise, and remained linear in current.

3.1.3.4 Scanning Gate Microscopy on Device 1

As discussed above, device 1 showed high-quality characteristics for use in scanning gate microscopy (SGM). Device 1 was scanned first due to looking slightly less inhomogeneous of the two devices; it was the better device. We start with the better device so that if something were to go wrong in the SGM measurements, that causes the tip to crash into both devices, then we will have at least some data on the best device.

SGM measurements on the first device were done in a contact mode with the CDT-FMR-20 probe (**C**onductive **D**iamond coated AFM **T**ip - **F**orce **M**odulation mode - **R**eflex coating). Given the spring constant of $6.2\,\mathrm{N\,m^{-1}}$, then the force on the hBN top surface can be determined. The deflection setpoint (the measured deflection that the Z-piezo is attempting to reach) was set at 17 nm, giving a force of approximately 100 nN. In reality, this is the worst case scenario as the nominal value of deflection when the tip is not in contact drifts under vacuum from zero by +5-10 nm. Therefore, forces do not exceed 100 nN, typically remaining in a range of 50-100 nN. This is on the firmer side of AFM, however, thanks to the hexagonal structure of the hBN, the surface holds up well to the shear forces the tip induces on the surface. Prolonged scanning, particularly in one area, does cause some exfoliation of the surface, see Figure 3.7(b).

The variables measured during SGM, as a function of the tip position (xy), were: topography, 2-probe voltage, 4-probe voltage, and leakage current through the tip. Current was not monitored in the same way explicitly during SGM scans, but can be inferred by 2-probe voltage, $I \simeq (V_{\text{osc}} - V_{2p})/100\,\text{k}\Omega$. When AC supply voltage, V_{osc}, was $5\,\text{V}_{\text{rms}}$ the nominal 2-probe voltage V_{2p}, without scanning tip perturbation, was $(192 \pm 1)\,\text{mV}$ giving current $I_{\text{rms}} \simeq (48.1 \pm 0.1)\,\mu\text{A}$. The maximum change in the 2-probe resistance did not exceed 0.4% of the $100\,\text{k}\Omega$ current-limiting resistor, so current was assumed constant in the process of converting voltage maps to resistance, approximately $(48.0 \pm 0.2)\,\mu\text{A}$ is used. This value of current comes from an averaged measurement of the nominal 2p-resistance (nominal meaning that the tip is away from the device), including a 0.4% error when the tip is maximally affecting 2-probe resistance.

The AC frequency used with this device was 11.591 kHz, sufficient for not exceeding out-of-phase voltage of 10% of the in-phase voltage. Scans in Figure 3.11, were performed simultaneously with a speed of 255 pt/s and therefore completed in 4 minutes and 15 seconds. The time per point was $1/255 = 4\,\text{ms/pt}$ which is sufficient for the measurement by the lock-in amplifier to settle between points when using a 1 ms time constant.

Similar to the preliminary device, the best parameters to produce the highest contrast in the image were found by trying a few combinations. The highest contrast found was with a back-gate of -10 V and a tip-gate +0.5 V. The converted maps using these parameters, showing the 2-probe and 4-probe resistance as a function of tip position over the device at room temperature, are provided in Figure 3.11.

The signal-to-noise ratio was very good for these measurements, and we can extract the noise from these maps when the tip has no measurable impact on resistance. For 2-probe resistance, a $(0.4 \pm 0.1)\,\text{mV}$ peak-to-peak noise is observed equivalent to a few ohms, about 2% of the induced change in resistance due to the tip. Equivalently, 4-probe measurements show a $(0.8 \pm 0.1)\,\mu\text{V}$ peak-to-peak noise, about 5% of tip-induced change in signal.

The results are surprising. Contrary to the naïve expectation that changes in 4-probe resistance are most sensitive in areas of high current density, the experimental map in Figure 3.11(b) reveals instead a characteristic crescent shape that stretches across the device. The crescent is symmetric around the halfway point between positive current and voltage probes and does not fade away with current density as we get further away from the current contacts.

Somewhat counterintuitively, the magnitude of the changes due to the tip are also large. The tip produces approximately 50% changes in the nominal 4-probe resistance both in the positive and negative direction. This is when the approximate

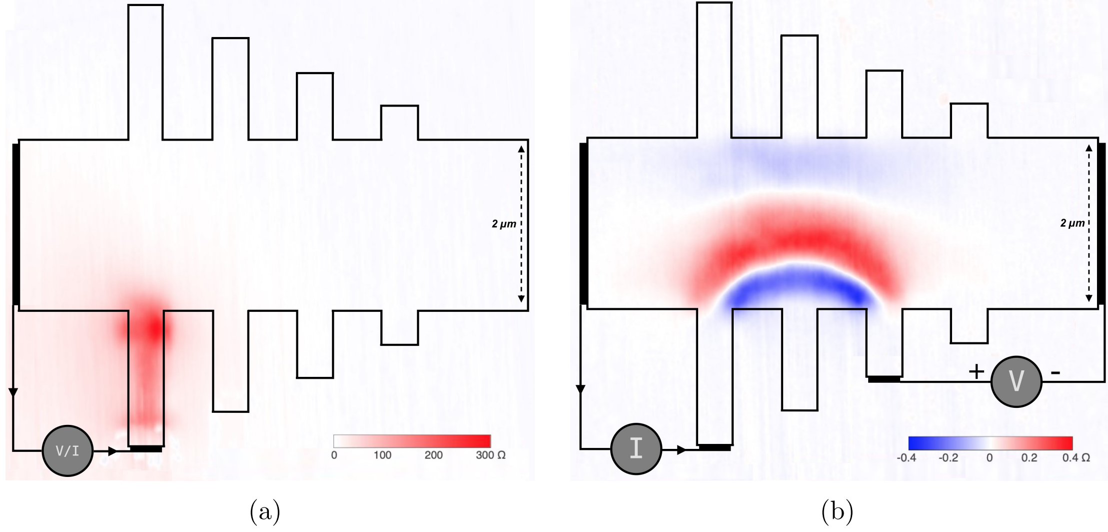

(a)

(b)

Figure 3.11: Resistance change ($\Delta\Omega$) due to a scanning gate tip at room temperature, where the indicated AC current configuration through device, I, is (48.0 ± 0.2) µA at 11.591 kHz. Tip-gate and back-gate voltages were +0.5 V and -10 V respectively. SGM scans an area 6×6 µm at a 255×255 resolution around the 6 µm long device. **(a)** shows 2-probe resistance with nominal value of (3.99 ± 0.02) kΩ and **(b)** shows 4-probe resistance with nominal value (0.75 ± 0.02) Ω

tip diameter is about 100-200 nm which is approximately 10-20 times smaller than the width of the device. While the resolution in the resistance maps seems difficult to judge, some of the map features seem to cut off as the tip scans into the Hall-bar arms, this suggests that the affected area under the tip is constrained to at most 200 nm in diameter.

The map of 2-probe resistance appears more intuitive, see Figure 3.11(a). The largest changes in 2-probe resistance appear to coincide with the expected current density in the device. Current density is highest in the current-carrying Hall-bar arm due to its thinner width, and this is where the strongest signal is observed. Particularly, the tip effect on the 2-probe resistance appears to be at its strongest at the boundary between the arm and the main body. The effect of the tip on 2-probe resistance at this maximum point is approximately 7% of the nominal 2-probe value and only ever increases the resistance.

During scans, tip-to-gold contact would regularly cause leakage current, and on occasion, tip-to-graphene contact on the edges would also occur, causing large discrete jumps in measured resistance, particularly in 2-probe measurements. Here, in all the SGM images provided, the jumps and any drift of the nominal resistance have been subtracted in processing.

Ultimately, the SGM study on this device concluded before a similar experiment at low temperatures could be performed. This was because the device sustained

significant physical damage in a separate AFM study.

At this time, we also tested applying a small AC modulation to the tip bias while driving the device with a DC current, and demodulating the transport response at the tip-modulation frequency. This produced usable SGM images, but from this limited test we could not demonstrate a clear advantage. Introducing an AC tip voltage is expected to introduce additional capacitive coupling, and in tapping-mode operation the time-varying separation could plausibly make the response mixed. Finally, this type of measurement does not yield an absolute resistance map, making quantitative comparison and interpretation across different bias points and scan conditions less direct. For the subsequent measurements on the second device, we therefore retained the standard configuration of an AC current drive through the device.

3.1.3.5 Scanning Gate Microscopy on Second Device

The SGM study proceeded with the second device, which had the identical geometry as the first and similar characteristics. Due to the damage sustained to the chip, this device was left with significant surface damage to one contact and, consequently, also high device capacitance. This required that all measurements be done at lower than ideal frequencies, and the pre-amplifier was not used.

The second device gives us opportunity to show reproducible results on a different device using slightly different techniques to avoid further damage and attempt to reduce the leakage current. The probe used for the second device was CDT-NCHR-10 (**C**onductive **D**iamond coated **T**ip - **N**on-**C**ontact/tapping mode **H**igh resonance frequency - **R**eflex coating) with a spring constant of $80\,\mathrm{N\,m^{-1}}$. The probe was used in tapping mode operation and driven by oscillator frequency of 428.09 kHz with a baseline amplitude of 14 nm. The setpoint amplitude for Z-piezo feedback for constant amplitude scanning was 10 nm, approximately 70% of the 'free' amplitude. These parameters are well-suited for high-resolution tapping mode imaging on flat surfaces where precise control and minimal sample damage are needed.

Scans of 2-probe resistance reveal a qualitatively similar result in this second device compared to the first, see Figure 3.11(a), as such they are not presented here, and our focus turns to 4-probe resistance measurements, see Figure 3.12. A different current and voltage probe configuration is used in the second device; however, with a similar contact separation distance, we expected a similar result.

Scanning parameters are much slower for this device. Factoring in the scanning time available during a single day, and the damage that caused a higher out-of-phase voltage, we compromised to have an increased out-of-phase signal. The 330 Hz oscillator frequency kept out-of-phase from exceeding the in-phase signal. The resulting

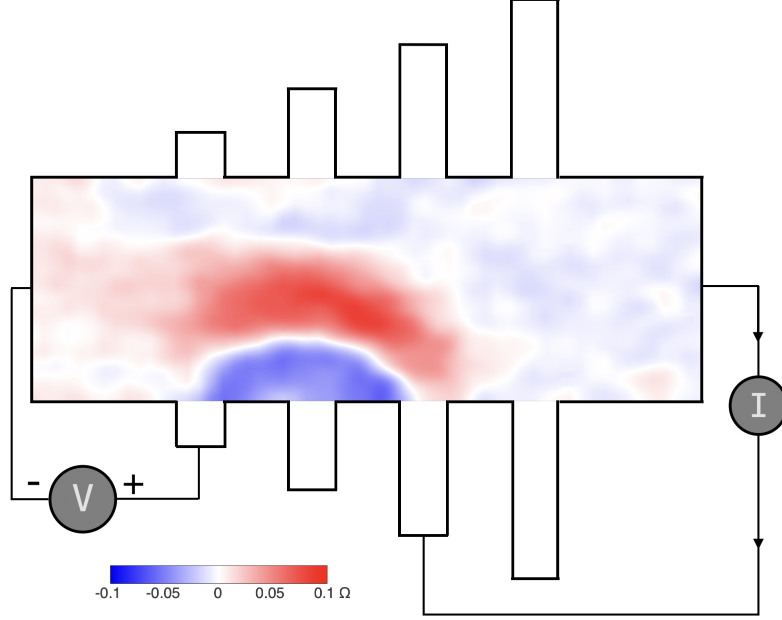

Figure 3.12: 4-probe resistance change due to scanning gate tip where indicated AC current configuration through device, I, is $(44 \pm 0.5)\,\mu$A at 330 Hz. Tip-gate and back-gate voltages were -0.5 V and +10 V respectively. SGM scans an area $6 \times 3.8\,\mu$m at a 404×256 resolution. The 4-probe nominal resistance is $(1.0 \pm 0.1)\,\Omega$.

SGM maps showed that the out-of-phase component of the four-probe resistance exhibited a single 1% change localised at the V_+ probe, with no other spatially resolved features observed. At a time constant, 30 ms, and time per point 80 ms, the SGM scans of this device took 2.5 hrs, drastically longer than the first device. This highlights how important it is to have low capacitance for these types of measurements. The SR830 lock-in amplifiers have a next-smallest time constant setting of 10 ms, which would allow scanning twice as fast at the expense of an increase in the noise floor by roughly a factor of two.

We can see that despite the poorer quality SGM image of this device, a similar crescent is observed. This is in the slightly different 4-probe configuration and also in a switched back-gate polarity; we see a qualitatively similar image probing the Fermi fluid of holes compared to the Fermi fluid of electrons, as expected from symmetry.

The 4-probe resistance has a similar nominal value compared to the first device, $(1.0 \pm 0.1)\,\Omega$, however, the measured change in resistance (as a percentage) was about 2 times smaller compared to the first device. This indicates that the tip in this measurement is likely not fully compensating the back-gate. This was not a surprise as small drifts in the neutrality point of around 3 V can occur over time, and especially with a change in device. Possible reasons for this unintentional doping and drift include [123] changes in ambient humidity, which are largely mitigated by hexagonal boron nitride (hBN) encapsulation, the migration of charged impurities

in the underlying silicon dioxide (SiO_2) during prolonged gate voltage application, and also thermally induced movement of ions. Given it was not as feasible to do many parametric scans, when each scan can take many hours, it is unlikely that the tip voltage used was optimal for maximum resistance change. A few other factors can reduce the effectiveness of the tip: the tip, when operated in tapping mode, had a smaller influence on the resistance when its average separation distance is greater; the tip radius likewise could be smaller on the different probe used. However, these other reasons likely play a negligible role compared to the shifting of the neutrality point. Despite this, the tip changes the 4-probe resistance by up to 20% and exceeds the noise.

Under the same configurations and parameters as above, the room-temperature SGM scan was repeated at low temperature, 160 K. The high vacuum AFM setup takes approximately 2-3 hours to cool, see inset of Figure 3.3, followed by the 2.5 h SGM scan. The maps are compared in Figure 3.13 below.

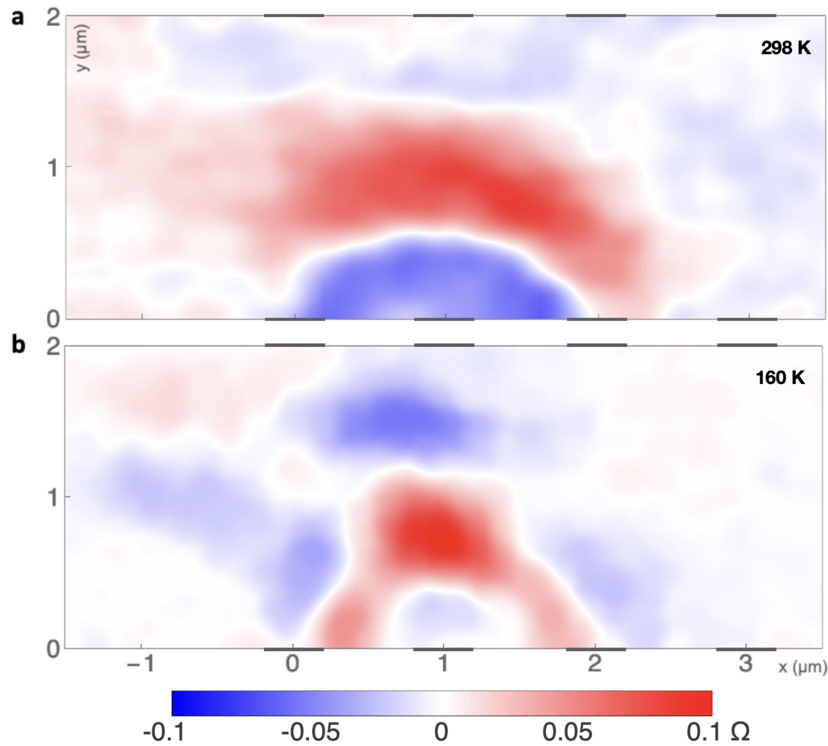

Figure 3.13: 4-probe resistance SGM maps at a back-gate voltage +10 V with tip-gate voltage −0.5 V where current to device is (44 ± 0.5) µA at 330 Hz. **a** room temperature nominal resistance was $(1.0 \pm 0.1)\,\Omega$ (identical to Figure 3.12). **b** For low temperature, 160 K, the nominal resistance was $(-0.33 \pm 0.01)\,\Omega$.

The baseline 4-probe voltage measurement at 160 K was (-14.3 ± 0.1) µV equating to a resistance of $(-0.33 \pm 0.01)\,\Omega$ when current is (44 ± 0.5) µA. This negative non-local resistance is the strong indicator of hydrodynamic flow we expect at low temperatures.

For low temperature 4-probe resistance, a $(0.8 \pm 0.2)\,\mu\text{V}$ peak-to-peak noise is observed, comparable to the noise observed at room temperature and, as the signal is lower in this device compared to the first, the noise is about 30% of the tip-induced signal.

As anticipated, the 4-probe non-local resistance SGM maps (see Figure 3.13) exhibit both qualitative and quantitative differences between measurements conducted at room temperature and those at low temperatures. As described before, the change in sign is directly linked to hydrodynamic flow, and we expect that the tip-induced changes in the sheet resistance at these low temperatures should also distinctly identify hydrodynamic flow. Just like room temperature scans, LT maps show there is a centre-aligned observable symmetric shape, and the magnitude of the tip-induced changes is around $0.1\,\Omega$. As before, the change in resistance does not seem to scale directly with the spatial current density through the device, as naïvely expected. The low-temperature map shows a reversal in the positive and negative regions around the positive current and voltage probes, consistent with the negative non-local resistance. This effectively produces an inversion of the crescent shape colours everywhere except the centre line between the current and voltage probes. This vertical profile, which is a symmetry line in all measured maps, appears not to significantly change with temperature.

We have shown that there is a feasible direct way to probe electronic transport spatially in monolayer graphene using scanning gate microscopy. We also show there is a distinct qualitative change in these measurements as a function of temperature, that has links to hydrodynamic transport. However, without modelling, the nature of what can be learned from such maps is limited.

3.2 Model Solution to Probing Diffusive Transport via SGM

How does the position of a local tip-gate affect the voltage response of a diffusive 2DEG with known resistivity and field effect? In this work, we solve this problem. We consider the influence of an SGM probe on 4-probe and 2-probe resistance measurements, utilizing both analytical and numerical methods. We hope to show and explain the findings from experimental work (see Section 3.1) carried out on high-quality graphene heterostructures in standard Hall-bar geometry. In the experimental work, at room temperature, we considered a well known 2DEG transport regime, the diffusive regime, where the resistivity, ρ, is a local property that obeys Ohm's law, $\rho = \mathbf{E}/\mathbf{j}$, a function of electric field, $\mathbf{E}$, and current density, $\mathbf{j}$. At low temperatures, it has been observed in high-mobility graphene devices that transport

is dominated by a hydrodynamic Fermi fluid, that does not necessarily obey Ohm's Law. [30,124] Consequently, solutions here particularly focus on the room temperature environment to ensure a diffusive flow regime. Applicability to hydrodynamic transport will follow in Section 3.3.

3.2.1 Influence of the SGM probe on a 2DEG

The conductivity of graphene is a smooth function with respect to carrier density, with a minimum at the Dirac point / neutral point (NP). By applying an external electric field from a back-gate of fixed potential, either positive or negative, then the chemical potential can be tuned away from the NP, increasing the conductivity of the graphene device as carrier density rises. [10] Conversely, with the addition of a local top-gate, the carrier density can be locally reduced back towards the NP, and therefore, conductivity decreases in a small local area. This local perturbation in conductivity modifies the current distribution in the device, and the change in electric potential at the device edges can be measured using standard lock-in amplifier techniques. Here, the local top-gate is a movable conductive scanning tip.

The magnitude and area of the local change in conductivity due to the tip are directly linked to a few parameters: the density of states and field-effect strength of the material; and the effective radius, voltage, and work function of the SGM probe.

The effective radius of the perturbed area has significant impact on the measured result. The area must be large enough to produce a detectable change in voltage between potential probes, but also must be sufficiently smaller than the device dimensions to achieve the desired resolution.

3.2.1.1 Effective Size of Perturbed Area Due to Charged Tip

The effect of a charged scanning probe on a 2DEG has been studied previously [125] and requires numerical analysis to determine the size and area of the perturbed carrier density. This change in carrier density, and therefore resistivity, has been shown to be a peak-like function centered at the tip location. In the same work, it is shown that the half-width of the peak, when tip-2DEG separation distances are larger than the tip radius, is found to be approximately equal to the separation distance for a wide range of tip parameters. In our work, however, the tip radius is significantly larger than the tip-graphene separation distance. In this case, the effective perturbation radius is approximately the same as the tip radius. This can be proven using simple approximations, treating graphene as an ideal metal using a mirror charge vs graphene treated as an insulator near a single point charge in free space. These approximations can give us upper and lower bounds on the expected

half-width-half-maximum (HWHM) on the carrier density due to the charged tip. In reality, graphene will sit between these bounds closer to the ideal metal result. In both approximations, it will be presupposed that the dielectric constant of all materials is 1, as such, in the following diagram (see Figure 3.14) the heterostructure is for illustrative purposes, and the analysis is largely down to the separation distance between a point-charge and the plane.

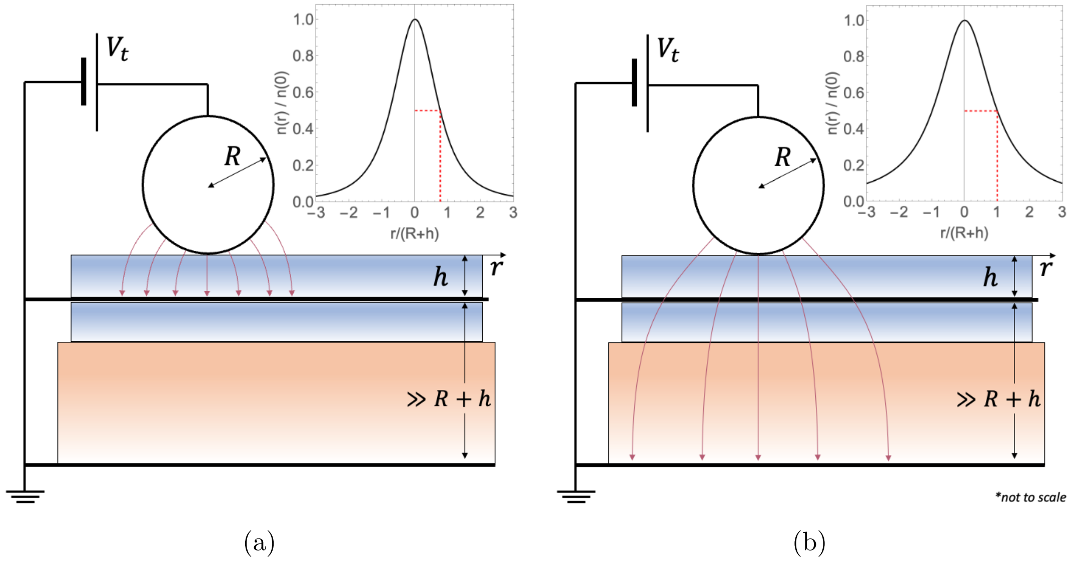

Figure 3.14: Limiting approximations for the area of a charged tip perturbation on a monolayer graphene sheet. **(a)** Ideal conductor model; inset: normalised carrier density $n(r)/n(0)$ vs. $r/(R+h)$, HWHM approx. $0.8(R+h)$. **(b)** Insulating sheet in free space; inset: normalised carrier density, HWHM approx. $R+h$. R: tip radius, h: separation. Distance to back-gate is assumed much greater than $R+h$.

Point Charge Above a Two-Dimensional Ideal Conductor

In the limit of graphene as an ideal metal, the tip is a point potential, V, in free space separated by distance to a conductive sheet equal to the tip radius plus height, $R+h$. The carrier density, n, is estimated using Coulomb's theorem, $E_z = \sigma/\epsilon$, where σ is the surface charge density which is equal to en and E_z is the electric field normal to the surface. The change in carrier density, Δn, of carriers with electronic charge, e, as a function of radial distance from the tip position, r, is approximated using a mirror charge:

$$\Delta n\,(r) = \frac{\epsilon \cdot 2VR(R+h)}{e[(R+h)^2 + r^2]^{3/2}} \quad \Longrightarrow \quad \frac{\Delta n\,(r)}{\Delta n\,(0)} = \left[1 + \left(\frac{r}{R+h}\right)^2\right]^{-3/2} \tag{3.1}$$

where the result can simplify further considering $R \gg h$. The normalised induced carrier density, $\frac{\Delta n(r)}{\Delta n(0)}$, is given in the subset of Figure 3.14(a), where the HWHM of the peak is $r_{hwhm} \approx 0.8R$.

Point Charge in Free Space Above a Two-Dimensional Insulating Sheet

For an insulating plane, considering a charge in free space, the potential spreads radially from the source. We consider a free-space approximation as the distance to the back-gate, and therefore any mirror charge, is far away. The chemical potential induced on the insulating sheet is simply a cross-section of the potential sphere produced from the point charge. Given a point charge, Q, with a separation distance $R+h$ to the plane, the chemical potential, μ, is given:

$$\mu\left(r\right)=-\frac{eQ}{4\pi\epsilon_0}\frac{1}{\sqrt{\left(R+h\right)^2+r^2}},$$

where r is the radial distance in the plane from the point on the plane closest to the charge.

Determination of carrier density in this case must come from graphene's electronic spectrum. Considering the carrier density is proportional to the square of the chemical potential, $n\propto\mu^2$, then the normalised induced carrier density is approximately:

$$\frac{\Delta n\left(r\right)}{\Delta n\left(0\right)}=\left(\frac{\Delta\mu\left(r\right)}{\Delta\mu\left(0\right)}\right)^2=\left[1+\left(\frac{r}{R+h}\right)^2\right]^{-1} \tag{3.2}$$

The normalised carrier density for the insulating plane, without screening, has a longer $1/r^2$ tail (compared to $1/r^3$ for a conductive sheet) that will result in small density variations that extend further. The normalised carrier density is given in the subset of Figure 3.14(b), where the HWHM of the peak is $r_{hwhm}=R$ when $R\gg h$.

Taking The Effective Perturbation Radius Equal to Radius of Tip

In all cases, the effect of the tip acts as the local doping that shifts the carrier density from a uniform homogeneous background to a peak-like distribution with characteristic radius:

$$0.8R\lesssim r_{hwhm}\lesssim R.$$

For simplicity, we take the radius of perturbation in the resistivity of graphene to be approximately equal to the tip radius, approximately 100-200 nm in the experimental work. This assumption is particularly inconsequential in the analytical analysis of SGM maps, as the tip radius becomes a fitting parameter for the experimental result.

3.2.1.2 Target Tip-Gate Magnitude To Induce Largest Change in Current Density

The tip voltage in the experiment is tuned to maximise the observed change in 4-probe resistance measurements and, therefore, increases the contrast of SGM maps. For numerical approximation, consider a conductive plane with uniform conductivity approximately $\sigma_{BG} = 10\,\text{mS}$ (due to back-gate) and a dip in the local conductivity is formed (under a local gate) that can be assumed to be approximately $\sigma_{min} = 1\,\text{mS}$. These numbers correspond to the typical conductivity of a graphene device at room temperature, with back-gate of 10 V and the minimum conductivity at its neutrality point, see Figure 3.10.

The local change in conductivity, $\Delta\sigma(r)$, is therefore approximately 90% at its peak, creating a significant change in resistivity that will strongly perturb the current flow in the device.

The conductivity, $\sigma(r)$, in a graphene sheet can be approximated as a function of the carrier density, $n(r)$, using Eq. (3.1). Given the square-root dependence of carrier density on the conductivity, $\sigma \propto \sqrt{n}$, valid for densities away from the Dirac point, then the change in conductivity, $\Delta\sigma\,(r)$, as a function of radial distance from the tip position is estimated:

$$\frac{\Delta\sigma\,(r)}{\Delta\sigma\,(0)} = \sqrt{\frac{\Delta n\,(r)}{\Delta n\,(0)}} = \left[1 + \left(\frac{r}{R+h}\right)^2\right]^{-3/4} \tag{3.3}$$

Applying the background and minimum conductivity, where $\Delta\sigma(0) = \sigma_{BG} - \sigma_{min}$:

$$\begin{aligned}\sigma(r) &= \sigma_{BG} - \Delta\sigma\,(r) \\ &= \sigma_{BG} - (\sigma_{BG} - \sigma_{min})\left[1 + \left(\frac{r}{R+h}\right)^2\right]^{-3/4}\end{aligned} \tag{3.4}$$

For simplicity, the conductivity (Eq. (3.4)) viewed in Figure 3.15 can be approximated as a Gaussian of width equal to the tip diameter with a magnitude that decreases the conductivity by 90% at its peak. This approximation is used in the analytical and numerical analysis that follows.

A local area of reduced conductivity, σ, distorts the current flow such that the current density, $\mathbf{J}$, is reduced through that local area. Given the continuity equation and Ohm's law:

$$\nabla \cdot \mathbf{J} = 0, \quad \mathbf{J} = \sigma\mathbf{E}, \tag{3.5}$$

a simple result is found, that shows that perturbations in σ are equivalent to the superposition of the unperturbed state (constant uniform conductivity) and addi-

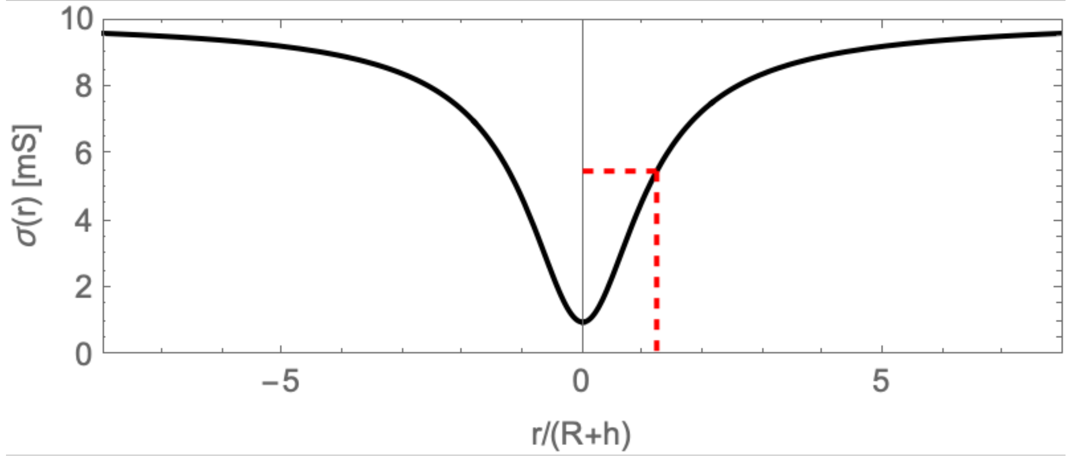

Figure 3.15: Local change in conductivity, $\sigma(r)$, due to charged tip. The change in conductivity has a HWHM indicated by the dashed line, and has minimum conductivity at its center. The conductivity is approximated using Eq. (3.4) with $\sigma_{BG} = 10\,\text{mS}$ and $\sigma_{min} = 1\,\text{mS}$.

tionally a second term that is proportional to both the electric field, $\mathbf{E}$, and the gradient of the perturbed conductivity, $\nabla\sigma/\sigma$: [126,127]

$$\begin{aligned} \nabla \cdot (\sigma \mathbf{E}) &= 0, \\ \nabla \cdot \mathbf{E} + \frac{\nabla\sigma}{\sigma} \cdot \mathbf{E} &= 0, \end{aligned} \tag{3.6}$$

Numerical simulation solving Eq. (3.6), visualised in Figure 3.16, shows that a peak-like change in conductivity coincides with the formation of a current dipole, whose direction and strength is proportional to the unperturbed electric field. This is consistent with the earlier theoretical work on the sensitivity of the van der Pauw method to point-like inhomogeneities that act as electric dipoles. [126]

To deduce a simple analytical result, we can simply recreate a current dipole within our flow. The potential distribution formed from the current dipole can then be used to calculate 4-probe resistance. The maximum effect of the tip on the flow occurs when the current dipole reduces the unperturbed current density, $\mathbf{J}$, to zero at the dipole center.

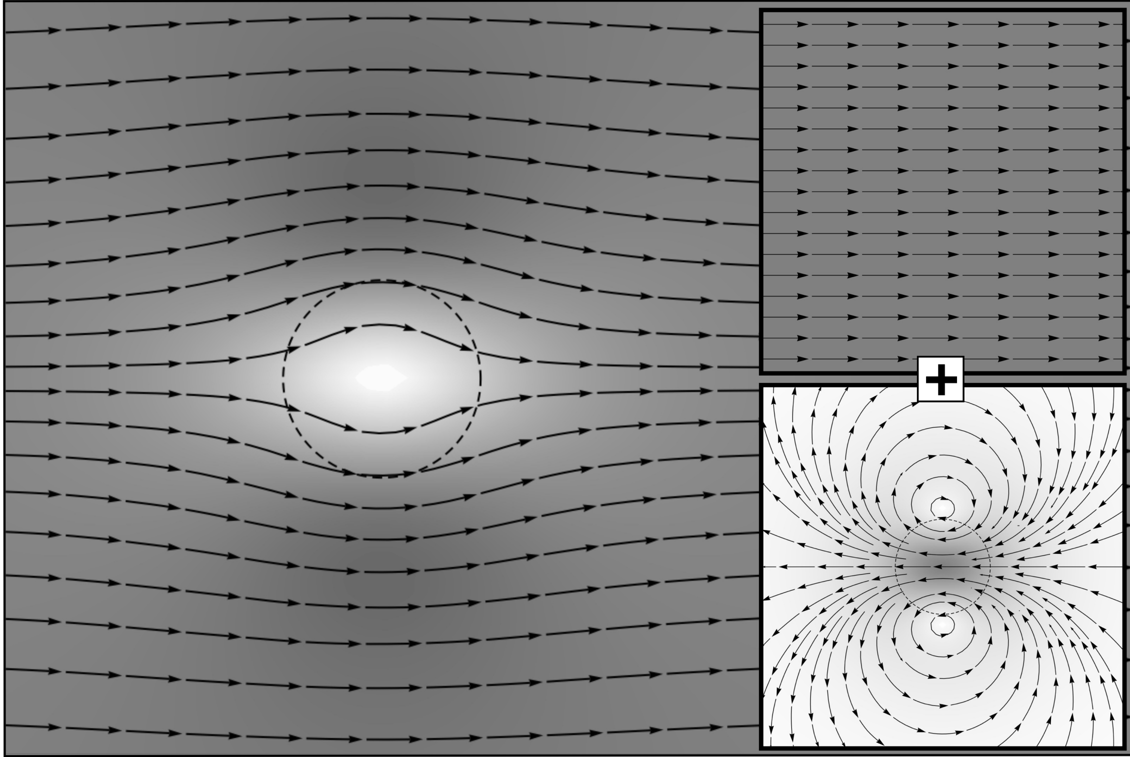

Figure 3.16: Current density response due to reduced conductivity in the two-dimensional plane. The change in conductivity is given by a Gaussian distribution, of FWHM indicated by the dashed circle, and decreases conductance at its center by 90%. The current density is shown to be the sum of the unperturbed current density, upper inset, and the formation of a current dipole, lower inset. The direction and magnitude of current density are given by the streamlines and shades of grey, respectively, where white indicates zero current density.

3.2.1.3 Required Dipole Current to Cancel Uniform Current Density

To model the current dipole, we can combine a current source and a current drain, separated by the tip diameter d, and calculate the current necessary such that the current density at the source/drain midpoint is equal and opposite to $\mathbf{J}$. The current density produced at $\mathbf{r}$ away from a single current source in a 2D-plane is equal to:

$$\mathbf{j}_s = \frac{I \cdot \mathbf{r}}{2\pi r^2}$$

and a dipole is formed when a second source (drain) is added to the plane with flipped polarity, $I \to -I$. Using a source-drain separation equal to the tip diameter, d, with current, I, flowing from source to drain, then the generated current density evaluated at their midpoint is given:

$$J_d = \frac{I}{2\pi \frac{d}{2}} + \frac{-I}{2\pi(-\frac{d}{2})} = \frac{I}{\pi \frac{d}{2}},$$

Therefore, the required current generated by the current dipole to cancel out the uniform current density of the device, J, is $I = \pi\frac{d}{2}J$.

What is the Potential Due to a Current Dipole in 2D?

A current dipole in 2D has a positive current source $+I$ at $\mathbf{r}^{+} = \mathbf{d}/2$ and a negative current source $-I$ at $\mathbf{r}^{-} = -\mathbf{d}/2$, centered at the origin. Where $\mathbf{d} = \mathbf{r}^{+} - \mathbf{r}^{-}$ points from the negative to the positive.

In a 2D medium with resistivity ρ, the potential due to a point current source I at $\mathbf{r}_0$ satisfies $\nabla^2\varphi = -\rho I\delta(\mathbf{r} - \mathbf{r}^{\pm})$. Solving via integration, the potential is:

$$\varphi(\mathbf{r}) = -\frac{\rho I}{2\pi}\ln(|\mathbf{r} - \mathbf{r}^{\pm}|) + C.$$

For a current drain $-I$, the potential is negative.

The total potential is the sum of contributions from the sources at $\mathbf{r}^{+} = \mathbf{d}/2$ and $\mathbf{r}^{-} = -\mathbf{d}/2$:

$$\varphi(\mathbf{r}) = \frac{\rho I}{2\pi}\left[\ln\left(\left|\mathbf{r} + \frac{\mathbf{d}}{2}\right|\right) - \ln\left(\left|\mathbf{r} - \frac{\mathbf{d}}{2}\right|\right)\right].$$

Since $|\mathbf{r}| \gg |\mathbf{d}|$, approximate the distances:

$$\left|\mathbf{r} \pm \tfrac{\mathbf{d}}{2}\right| = |\mathbf{r}|\sqrt{1 \pm \frac{\mathbf{r}\cdot\mathbf{d}}{|\mathbf{r}|^2} + O\left(\tfrac{|\mathbf{d}|^2}{|\mathbf{r}|^2}\right)}.$$

Expanding the square root to first order and taking logarithm approximation, using $\ln(1 \pm x) \approx \pm x$ for small x:

$$\ln\left|\mathbf{r} \pm \tfrac{\mathbf{d}}{2}\right| \approx \ln|\mathbf{r}| \pm \frac{\mathbf{r}\cdot\mathbf{d}}{2|\mathbf{r}|^2}.$$

Therefore, at large distances, $|\mathbf{r}| \gg d$, the potential, φ, of a current dipole in a two-dimensional material with resistivity ρ is given by:

$$\varphi(\mathbf{r}) \approx \frac{\rho I}{2\pi}\frac{\mathbf{d}\cdot\mathbf{r}}{|\mathbf{r}|^2}.$$

which is analogous to the potential formed from the electric dipole that consists of two infinite line charges, oppositely charged with charge density λ, $\varphi\left(\mathbf{r}\right) \approx \frac{\lambda}{2\pi\epsilon_0}\frac{\mathbf{d}\cdot\mathbf{r}}{r^2}$. Modelling a 2D plane of resistivity ρ, where a dipole brings the current density at it's center to zero, the potential, φ, as a function of position from the dipole, $\mathbf{r}$, is then given:

$$\varphi\left(\mathbf{r}\right) \approx \frac{\rho d^2}{4}\frac{\mathbf{J}\cdot\mathbf{r}}{r^2}, \tag{3.7}$$

3.2.2 Current Density in Infinite Strip With Point-like Current Injector

Computation of the current distribution in realistic Hall-bar geometries generally will require numerical simulations, such as the finite element analysis conducted later in this work. For simplicity in the derivation of an analytical result, we consider an infinite strip geometry with a point-like current injector and voltage probes and then extend this method to consider contacts of finite width.

It is derived simply that the current density from a point current source satisfies the continuity equation where $\mathbf{j} = \frac{I\mathbf{r}}{2\pi r^2} = \frac{I}{2\pi(x^2+y^2)}(x, y)$.

$$\nabla \cdot \mathbf{j} = \frac{\partial j_x}{\partial x} + \frac{\partial j_y}{\partial y} = \frac{I}{2\pi} \cdot \frac{y^2 - x^2}{(x^2+y^2)^2} + \frac{I}{2\pi} \cdot \frac{x^2 - y^2}{(x^2+y^2)^2} = 0.$$

Thus, $\nabla \cdot \mathbf{j} = 0$ for $(x, y) \neq (0, 0)$, satisfying the continuity equation everywhere in the plane except the source. Therefore, it is also true that any sum of point current sources will also satisfy the continuity equation, by the distributive nature of vector operators.

Understanding that any combination of point current sources automatically satisfies the continuity equation is a powerful tool for determining a unique analytical solution to our problem. We can, therefore, use the method of electric images to satisfy boundary conditions. [128, pp. 295–296, 317–318]

Our boundaries in the infinite strip geometry are given by two infinite horizontal boundaries separated by distance W, where the current density normal to the boundary should be zero and the continuity equation is satisfied over all space except at points of current injection.

The problem then is: how many, and in what positions, should the point current sources go to satisfy the boundary conditions? Due to symmetry, the problem can be solved using the method of mirror images, Figure 3.17b. By placing a single point source between two parallel 'mirrors', an infinite set of images are generated. By considering the infinite sum of all these point sources (images), the analytical result acquired satisfies the need for zero current flow across the edges of the domain. It is true then that any current source or drain placed anywhere in the domain, satisfies both the continuity equation and boundary conditions, where current density splits in half towards $\pm\infty$.

When a source is placed on a boundary, the locations of the images from each 'mirror' overlap at the same positions; this simplifies the problem to sources of doubled current, $2I$, placed $2W$ apart. Assuming a point current source is placed on the boundary at $\mathbf{r}_s$, then the current density measured in the domain at $\mathbf{r}$ due to

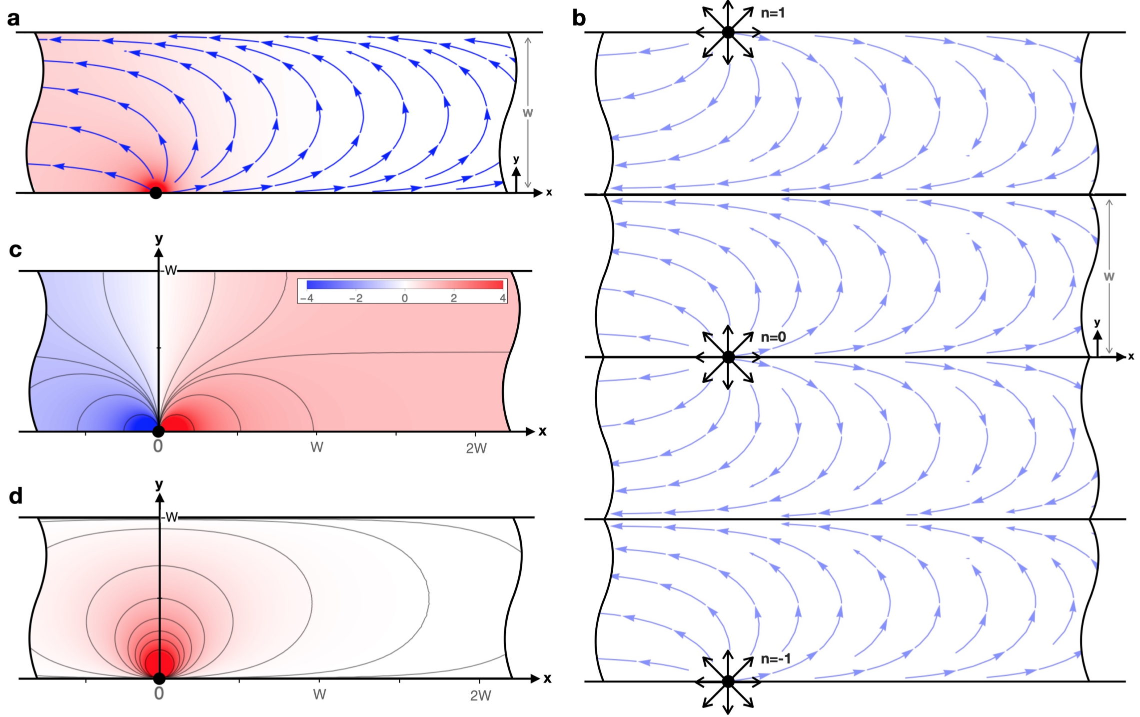

Figure 3.17: **(a)** The solved current distribution in a horizontal infinite strip geometry, of width W, with a point-like current injector. Blue streamlines and colour map in **(a)** indicate the direction and magnitude of the current density $\mathbf{J}(\mathbf{r})$, where white indicates zero current density. A uniform current density is subtracted such that the current density at positive infinity is zero. This is obtained using the method of images, **(b)**, where the infinite sum of current sources positioned at $\{0, 2Wn\}$ return analytical functions $F_1(x, y)$ and $F_2(x, y)$ (Eq. (3.11)) visualised in **(c)** and **(d)** respectively.

an image, indexed by n, is $\mathbf{J}_n(\mathbf{r})$ and is determined by the distance from the image $\mathbf{r}_n$:

$$\mathbf{J}_n(\mathbf{r}) = \frac{I}{\pi}\frac{\mathbf{r}_n}{r_n^2}, \tag{3.8}$$

$$\mathbf{r}_n = \mathbf{r} - \mathbf{r}_s + \{0, 2Wn\} \tag{3.9}$$

The current density, $\mathbf{J}$, of a single point current source/drain, positioned at $\mathbf{r}_s$, is given by the infinite sum of all its images. Note that, for a single source, the current will split equally towards negative infinity and positive infinity, unless a drain is placed somewhere in the domain. The current density in the domain is therefore:

$$\mathbf{J}(\mathbf{r}) = \sum_{n=-\infty}^{\infty} \mathbf{J}_n(\mathbf{r}) = \frac{I}{\pi}\sum_{n=-\infty}^{\infty} \frac{\mathbf{r}_n}{r_n^2}. \tag{3.10}$$

To evaluate this sum, we can represent the vector sum (Eq. (3.9)) in the complex

plane, $z = x + iy$, so the complex form is:

$$\frac{\mathbf{r}}{r^2} \longleftrightarrow \frac{x+iy}{x^2+y^2} = \frac{1}{\overline{z}}$$

Therefore, the following relationship between the distance vector $\mathbf{r}_n$ and the complex number z is:

$$\frac{\mathbf{r}_n}{r_n^2} \longleftrightarrow \frac{1}{\overline{z} - \overline{z_s} - i \cdot 2Wn} = \frac{1}{i2W}\left[\frac{\overline{z} - \overline{z_s}}{i2W} - n\right]^{-1}$$

.

The Mittag-Leffler theorem [129] [130, pp. 187–190] implies the following identity, understood in the sense of a principal value sum:

$$\lim_{N\to\infty} \sum_{n=-N}^{N} (z-n)^{-1} = \pi \cot(\pi z),$$

From this identity, the previous vector sum can be expressed as:

$$\frac{1}{i2W} \sum_{n=-\infty}^{\infty} \left[\frac{\overline{z} - \overline{z_s}}{i2W} - n\right]^{-1} = \frac{1}{i2W} \pi \cot\left(\pi \frac{\overline{z} - \overline{z_s}}{2Wi}\right).$$

Using cotangent identity $\cot(-iz) = i\coth(z)$, therefore finds that the vector sum is equal to:

$$\sum_{n=-\infty}^{\infty} \frac{1}{\overline{z} - \overline{z_s} - i \cdot 2Wn} = \frac{\pi}{2W} \coth\left(\frac{\pi(\overline{z} - \overline{z_s})}{2W}\right).$$

The complex form encodes both the x and y components of the vector sum as the real and imaginary parts, respectively. For simplicity, the current source position, z_s, can be merged into z, and two real-valued functions can be defined by taking the real ($\Re$) and imaginary ($\Im$) components of the hyperbolic cotangent function with respect to the position in the xy-plane parsed as a complex number z:

$$\begin{aligned} F_1(z) &= \Re\left[\coth\left(\frac{\pi\overline{z}}{2W}\right)\right], \\ F_2(z) &= \Im\left[\coth\left(\frac{\pi\overline{z}}{2W}\right)\right], \\ z(x,y) &= (x+iy) \end{aligned} \tag{3.11}$$

the functions $F_1(z)$ and $F_2(z)$ are real-valued functions that depend on position in the xy-plane. They also may be expressed in non-complex form in terms of

hyperbolic and trigonometric functions:

$$F_1(x,y) = \frac{\sinh\left(\frac{\pi x}{W}\right)}{\cosh\left(\frac{\pi x}{W}\right) - \cos\left(\frac{\pi y}{W}\right)},$$
$$F_2(x,y) = \frac{\sin\left(\frac{\pi y}{W}\right)}{\cosh\left(\frac{\pi x}{W}\right) - \cos\left(\frac{\pi y}{W}\right)}.$$

Hence,

$$\sum_{n=-\infty}^{\infty} \frac{\mathbf{r}_n}{r_n^2} = \frac{\pi}{2W} \begin{pmatrix} F_1(x,y) \\ F_2(x,y) \end{pmatrix},$$

where $F_1(z)$ and $F_2(z)$ are written as a coloumn vector. Substituting back into Eq. (3.10) gives the final result for the current density in the infinite strip geometry with a point current source at the origin for complex and vector form, respectively:

$$J(z) = \frac{I}{2W} \coth\left(\frac{\pi \overline{z}}{2W}\right) \Longleftrightarrow \mathbf{J}(\mathbf{r}) = \frac{I}{2W} \begin{pmatrix} F_1(x,y) \\ F_2(x,y) \end{pmatrix}, \tag{3.12}$$

Maps of these functions are given in Figure 3.17 where, for applicability, a uniform current density, $I/2W$, is subtracted such that the current density at positive infinity is zero (equivalent to placing current drain at negative infinity, $F_1 \to -1$ & $F_2 \to 0$).

3.2.3 Impact of a Local Dipole on 4-Probe Resistance

What are the SGM maps actually measuring? Experimental SGM maps (Figure 3.11) are the measurements of potential difference between two voltage probes as a function of the tip position, $\mathbf{r}$, which are then given in units of resistance by dividing by the current through the device, I.

As we have shown in Section 3.2.1, the tip induces a local change in conductivity that can be approximated as a current dipole, whose direction and strength is proportional to the local unperturbed current density. The potential measured at any point in the device due to this dipole is given by Eq. (3.7), where the current density, $\mathbf{J}$, is determined by the position of the current source and drain in the device.

As shown in Section 3.2.2, the current density in an infinite strip geometry with a point-like current source is given by Eq. (3.12). The derivation considers an infinite number of mirror images of the current source.

Considering that a similar consideration should be made for a current dipole in an infinite strip geometry, that it should create infinite images, then the potential, modified from Eq. (3.7), measured at a point on the boundary, $\mathbf{r}_p$, due to a current

dipole positioned at $\mathbf{r}$ in the domain is given by:

$$\varphi\left(\mathbf{r}, \mathbf{r_p}\right) = \frac{\rho d^2}{4} \mathbf{J}\left(\mathbf{r}\right) \cdot 2 \sum_{n=-\infty}^{\infty} \frac{\mathbf{r}_p - \mathbf{r}_n}{|\mathbf{r}_p - \mathbf{r}_n|^2},$$

where $\mathbf{r}_n$ is the nth image of the dipole, ρ is the resistivity of the unperturbed device and d is the tip diameter, used as the separation distance of the two poles of the current dipole. A factor of 2 is included as each dipole mirror image can be paired together when the potential is measured on the boundary, therefore allowing the sum to be simplified to images spaced $2W$ apart, as done previously for a current source on a boundary.

The symmetry of the problem becomes obvious, using the same relations as before (Eqs. (3.8) and (3.10)) the potential difference between Hi/Lo voltage probes, positioned $\mathbf{r}_+$ and $\mathbf{r}_-$ respectively, gives a 4-probe resistance as a function of tip position, $\mathbf{r}$:

$$\begin{aligned} R_{4p}(\mathbf{r}) &= [\varphi\left(\mathbf{r}, \mathbf{r}_+\right) - \varphi\left(\mathbf{r}, \mathbf{r}_-\right)]/I, \\ &= \frac{\rho d^2}{2I} \mathbf{J} \cdot \sum_{n=-\infty}^{\infty} \frac{\mathbf{r}_+ - \mathbf{r}_n}{|\mathbf{r}_+ - \mathbf{r}_n|^2} - \frac{\mathbf{r}_- - \mathbf{r}_n}{|\mathbf{r}_- - \mathbf{r}_n|^2}, \\ &= \frac{\rho \pi d^2}{2I^2} \mathbf{J}(\mathbf{r}) \cdot \widetilde{\mathbf{J}}(\mathbf{r}) \end{aligned} \tag{3.13}$$

where $\widetilde{\mathbf{J}}$ is the current density in the reciprocal configuration, the current density through the device in the case where the voltage probes become the current source and drain nodes. Figure 3.18 shows the current density maps for both configurations, $\mathbf{J}$ and $\widetilde{\mathbf{J}}$, in the infinite strip geometry.

This mathematical relation massively simplifies the computation of the 4-probe resistance map, as it is only necessary to compute the current density in the device for two configurations, the original and reciprocal configuration, and then take their dot product. Moreover, this also concludes that maps of 2-probe resistance are proportional to the square of the map of current density, as $\widetilde{\mathbf{J}} = \mathbf{J}$ in that case.

We show this relation (see Eq. (3.13)) is true for the infinite strip geometry where a multi-terminal configuration has contacts on the boundary; however, as we discovered later, this relation is consistent with previous theoretical work on the sensitivity analysis of Hall effect measurements to local inhomogeneities, where the result appears more general. [131]

The main result of this section is that the change of potential difference in the map of 4-probe measurements, due to a point-like change in resistivity, is proportional to $\mathbf{J} \cdot \widetilde{\mathbf{J}}$, where $\mathbf{J}$ is the current density distribution in the device and $\widetilde{\mathbf{J}}$ is the current

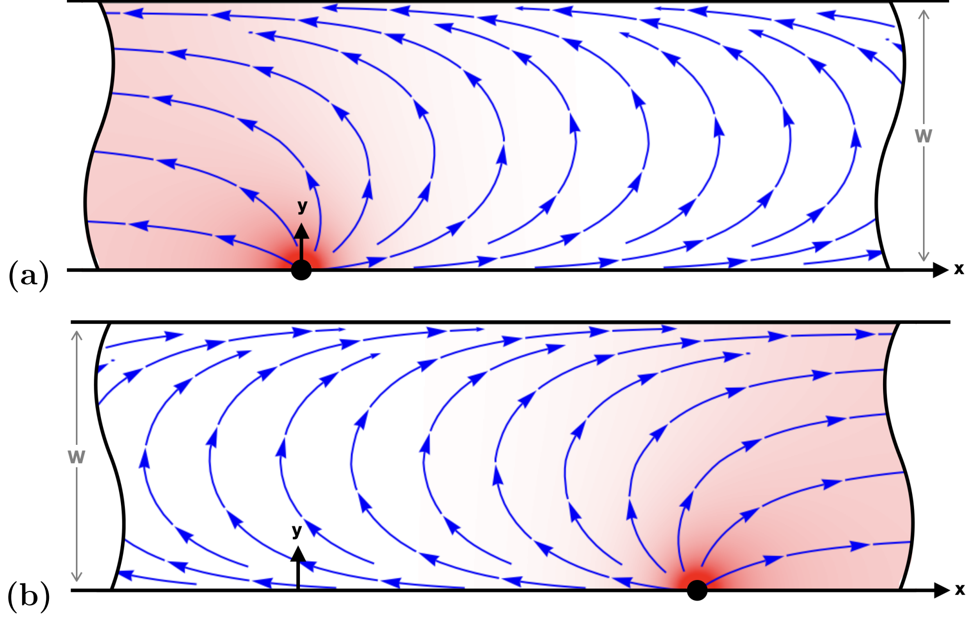

Figure 3.18: Direction and magnitude of current density in the infinite strip geometry, shown as blue streamlines and colour map for two point-sources. **(a)** Current density, $\mathbf{J}$, with point-like current source at $(0, 0)$ and drain at $(-\infty, 0)$. **(b)** Current density, $\widetilde{\mathbf{J}}$, in the reciprocal configuration with point-like current source at $(2, 0)$ and drain at $(+\infty, 0)$.

density distribution in the reciprocal configuration. This is true for any specimen of arbitrary shape with inhomogeneities that are weak enough to be considered a perturbation and dimensionally small enough to be considered point-like. [131] The method has been used previously to interpret multi-terminal SGM maps on graphene Hall-cross devices. [132]

So, Eq. (3.13) can be effectively computed where the positions of terminals are well-defined. Recall functions $F_1(x, y)$ and $F_2(x, y)$ (see Eq. (3.11)). By considering the infinite limits of the infinite strip, $F_1(\pm\infty, y) = \pm 1$, $F_2(\pm\infty, y) = 0$, then the current drain and negative potential probe can be simplified, and the computation simplified further. The configuration used for an analytical prediction for the 4-probe non-local resistance maps for our experimental SGM measurements is given:

1. Current source at $(0, 0)$: $\mathbf{J_s}(x, y) = \dfrac{I}{2W}\begin{pmatrix} F_1(x, y) \\ F_2(x, y) \end{pmatrix}$

2. Current drain at $-\infty$: $\mathbf{J_d}(x + \infty, y) = \dfrac{-I}{2W}\begin{pmatrix} 1 \\ 0 \end{pmatrix}$

3. Positive potential probe at $(2, 0)$: $\widetilde{\mathbf{J}}_{+}(x - 2, y) = \dfrac{I}{2W}\begin{pmatrix} F_1(x-2, y) \\ F_2(x-2, y) \end{pmatrix}$

4. Negative potential probe at $+\infty$: $\widetilde{\mathbf{J}_-}(x-\infty,y) = \frac{-I}{2W}\begin{pmatrix}-1\\0\end{pmatrix}$

Therefore, the 4-probe non-local resistance map in the infinite strip of width W is defined:

$$
\begin{aligned}
R_{4p} &= \frac{\rho\pi d^2}{2I^2}(\mathbf{J_s}+\mathbf{J_d})\cdot(\widetilde{\mathbf{J}_+}+\widetilde{\mathbf{J}_-}) \\
&= \frac{\rho\pi d^2}{8W^2}\begin{pmatrix}F_1(x,y)-1\\F_2(x,y)\end{pmatrix}\cdot\begin{pmatrix}F_1(x-2,y)+1\\F_2(x-2,y)\end{pmatrix}
\end{aligned}
\tag{3.14}
$$

The analytical result is computed with a fit to the experimental result along the midpoint between the positive current and voltage probes, $x=1$:

$$
R_{4p}(x=1,y) = \frac{\rho\pi d^2}{8W^2}\left[F_2(1,y)^2-(F_1(1,y)-1)^2\right],
$$

this was simplified by the identities $F_1(x,y)=-F_1(-x,y)$ and $F_2(x,y)=F_2(-x,y)$. A fit to experimental data finds $\frac{\rho\pi d^2}{8W^2}\approx 1.2\pm0.4\,\Omega$ and, therefore, when the width is $2\,\mu\text{m}$, $\rho d^2\approx(12\pm4)\,\Omega\,\mu\text{m}^2$. Assuming a resistivity of $100\,\Omega$ ($10\,\text{mS}$), this implies a tip radius of approximately 150-200 nm, which is consistent, though on the higher end, with the manufacturer's stated tip radius of 100-200 nm. Comparison of the fit, in both a vertical (x=1) and horizontal (y=1) profile, to the experimental data is shown in Figure 3.19, where tip diameter $d=350\,\text{nm}$ is used.

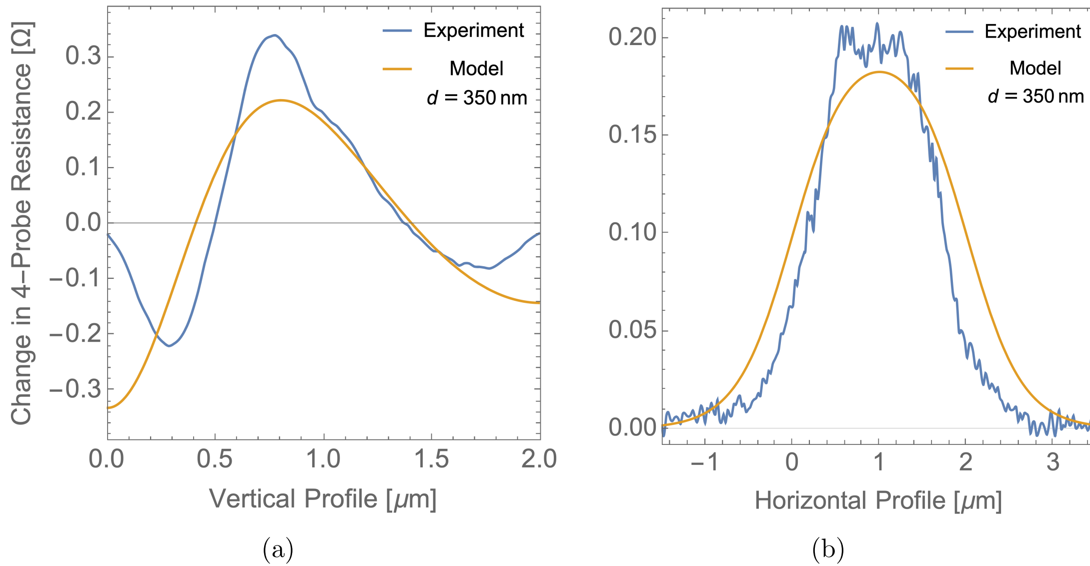

Figure 3.19: **(a)** Vertical profile of 4-probe non-local resistance map at $x=1\,\mu\text{m}$, through the center of the crescent, **(b)** Horizontal profile at $y=1\,\mu\text{m}$. Experimental data is shown in blue and the analytical fit of Eq. (3.14), in orange, where $d=350\,\text{nm}$, $\rho=100\,\Omega$ and $W=2\,\mu\text{m}$.

Note that the fit is not perfect, particularly around the edges of the vertical profile and the width of the peak in the horizontal profile. Some key assumptions made

in the analytical model may explain this: the point-like dipole approximation (by taking the potential of the dipole at distances much greater than the pole separation) and the assumption of diffusive transport throughout the device. Given that the estimated tip diameter is similar in size to the contact width and the resolution in experimental data appears slightly better than this, it could be likely that the fit slightly over-estimates the tip diameter to compensate for these assumptions. Both of these assumptions can be relaxed in numerical finite-element analysis in real geometry.

Full maps of the analytical result (Eq. (3.14)) are shown in Figure 3.20(a), alongside the experimental result, Figure 3.20(c). The analytical result assumes a tip diameter of $d = 350\,\mathrm{nm}$ and resistivity $\rho = 100\,\Omega$. The dimensions of the analytical result are to scale with the experimental result, where the width of the infinite strip is equal to the distance between current source and drain contacts, $W = 2\,\mu\mathrm{m}$. Mathematica was used to compute the analytical results, and representative code can be found in Appendix B.1.

Comparison of the analytical result to the experimental SGM map shows good agreement with the main features observed. A symmetric crescent is clearly observed with three well-defined regions separated by lines of zero resistance change. Lines of zero resistance change are expected where the current density from the current source is perpendicular to the current density in the reciprocal configuration, as $\mathbf{J} \cdot \widetilde{\mathbf{J}} = 0$ in that case. Regions of strong positive and negative resistance change are where current density from the two configurations are parallel and anti-parallel, respectively. In terms of the real current and potential measured due to formation of the dipole, the crescent symmetry is explained: the magnitude of the dipole close to the voltage probe is small due to the small current density at that point; however, the proximity to the voltage probe means that the potential measured at the voltage probe is identical/symmetric to the point mirrored about the center line.

The main discrepancy between the analytical result and the experimental map is the absence of sharp features around the contacts. A simple explanation might be that the analytical result assumes point-like current and voltage probes, whereas in reality, they have a finite width. This is considered in the next section, and shows slight improvement in this area, Figure 3.20(b), using contact widths of 400 nm, but sharp discontinuities are still observed around the contact edges at $y = 0$. Fitting the model over the horizontal line close to the finite contacts, $y = 0.1\,\mu\mathrm{m}$, finds a tip radius approximately 90 nm. It appears that the finite contact width does not fully explain the discrepancy, though it is likely a contributing factor.

Another explanation for the observed discrepancy is that the analytical result assumes a diffusive transport regime throughout the device, which obeys Poisson's

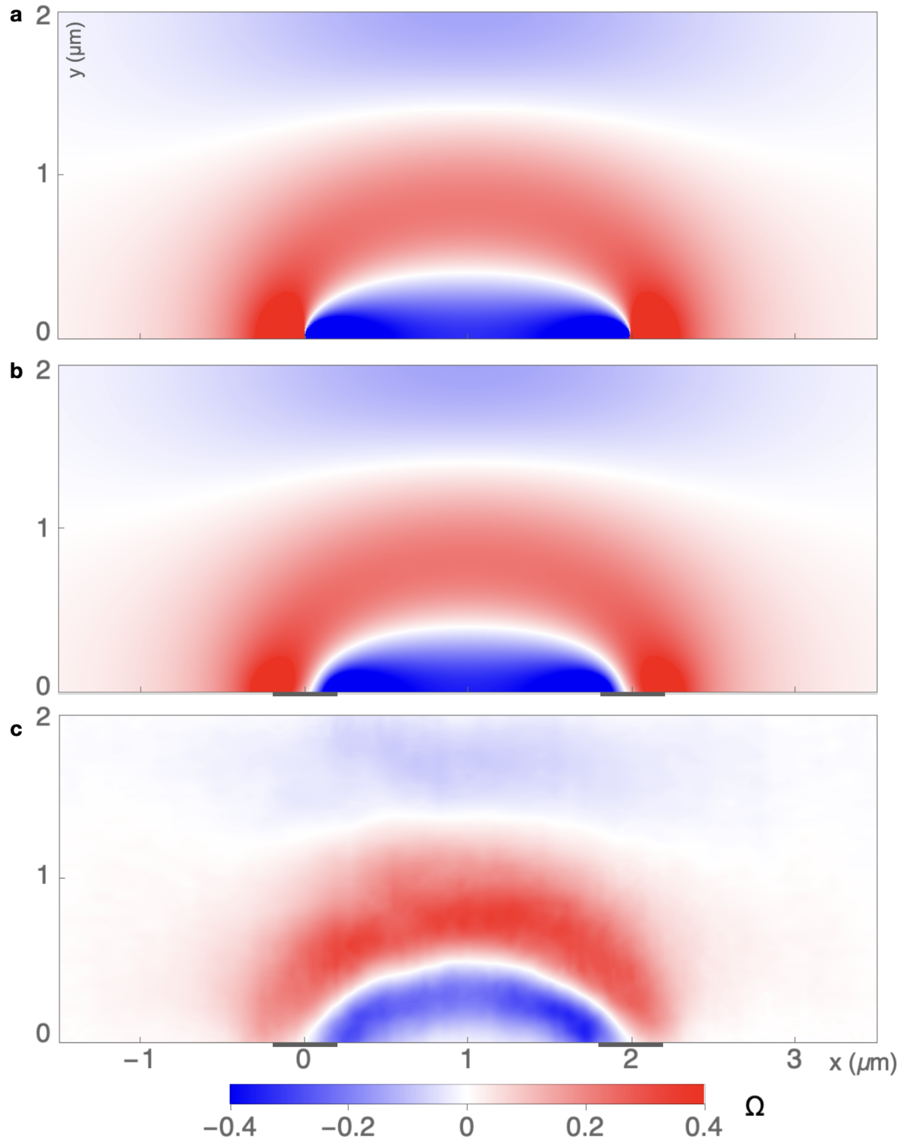

Figure 3.20: 4-Probe non-local resistance maps for SGM measurements given analytical predictions for point-like injection **(a)** and finite-width injection **(b)** of width, $2w = 400\,\text{nm}$. The dimensions are to scale (in µm) with the experimental result **(c)** with identical colour scales. Analytical results assume sheet resistivity $\rho = 100\,\Omega$ and tip radius 175 nm. Experimental data is the same as used in Figure 3.11(b).

equation, whereas in reality, the transport at room temperature in high-quality graphene is slightly hydrodynamic with a finite viscosity. It is possible that a viscous fluid smooths out sharp features in the current distribution, particularly around corners and edges.

Numerical simulations of hydrodynamic transport in the real geometry of the device are considered later in this work (see Section 3.3).

3.2.3.1 Resistance Maps in Infinite Strip With Finite Width Contacts

The analytical result, Figure 3.20(a), assumed point-like current and voltage probes. In Figure 3.20(b), we present an analytical solution considering finite-width contacts for current and voltage probes, where the contact width is assumed to be $2w = 400\,\text{nm}$.

For these new assumptions, we also use the same principles as before, where the current density from a single point current source is given by Eq. (3.8).

For simplicity, the current injectors are assumed to be horizontal, on the boundaries of the infinite strip geometry. To find the current distribution from a single finite-width current source, it is necessary to take the integral of many point current sources across the width of the contact, $2w$, assuming the current density is equal throughout its width:

$$\mathbf{J_n}(\mathbf{r}) = \int_{-w}^{+w} \frac{I}{\pi} \frac{1}{2w} \frac{\mathbf{r_n}}{r_n^2} dx,$$

where $\mathbf{r_n}$ is given by Eq. (3.9). The subscript n again indicates the image index such that the total current density from a single finite-width contact is given by the infinite sum of all its images, $\mathbf{J_n}(\mathbf{r})$, as before:

$$\mathbf{J}\left(\mathbf{r}\right) = \sum_{n=-\infty}^{\infty} \mathbf{J_n}(\mathbf{r}),$$

The current density from a single finite-width contact on the boundary is given in complex form:

$$J\left(z\right) = \frac{I}{\pi} \frac{1}{2w} \left[f(z+w) - f(z-w)\right], \tag{3.15}$$

$$f(z) = \ln\left[\sinh\left(\frac{\pi\overline{z}}{2W}\right)\right],$$

$$z(x,y) = (x+iy)$$

where, W and w are the width of the strip and half of the contact width, respectively. I is the total current through the contact, and z encodes the position in the xy-plane as a complex number.

The vector form of the current density can be expressed in similar terms to the point-like contact case (Eq. (3.12)):

$$J\left(z\right) \Longleftrightarrow \mathbf{J}(\mathbf{r}) = \frac{I}{2W} \begin{pmatrix} F_3\left(x,y\right) \\ F_4\left(x,y\right) \end{pmatrix}.$$

Where functions $F_3(z)$ and $F_4(z)$, analogous to $F_1(z)$ and $F_2(z)$, can be defined by

the real and imaginary components respectively of the current density in its complex form, $J(z) = F_3(z) + iF_4(z)$. For brevity and simplicity, the explicit forms of these functions are not given here, and the 4-probe resistance map can be computed directly from Eq. (3.15).

First, we can perform a consistency check on Eq. (3.15). In the limit of point-like contacts, $w \to 0$, the function, $J(z)$, should simplify to the previous result for point-like contacts (see Eq. (3.12)). Starting from the finite-contact expression (see Eq. (3.15)) we take the limit of point-like contacts, $w \to 0$:

$$\begin{aligned}
\lim_{w\to 0} J(z) &= \frac{I}{\pi} \lim_{w\to 0} \frac{1}{2w} \left[f(z+w) - f(z-w) \right] \\
&= \frac{I}{\pi} \frac{\partial}{\partial \overline{z}} f(z) \\
&= \frac{I}{2W} \coth\left(\frac{\pi \overline{z}}{2W} \right),
\end{aligned}$$

which is the same as Eq. (3.12), confirming consistency.

Substituting Eq. (3.15) in Eq. (3.13) will now determine the 4-probe resistance map for the finite contact width geometry, R'_{4p}. This may be done in the same way as before, considering the vector dot product of the current density in the original and reciprocal configurations. Instead, we can use the complex form where:

$$\mathbf{J} \cdot \widetilde{\mathbf{J}} \Longleftrightarrow \Re\left[J(z)\overline{\widetilde{J}(z)} \right],$$

where $\overline{\widetilde{J}(z)}$ is the complex conjugate of the current density in the reciprocal configuration.

Using a similar contact configuration to the point-like contact case. Where the current source is at $(0,0)$, current drain at $-\infty$, positive voltage probe at $(2,0)$, and negative voltage probe at $+\infty$. The 4-probe resistance map for finite-width contacts is given by:

$$R_{4p} = \frac{\rho \pi d^2}{2I^2} \Re\left[(J_s + J_d)\overline{(\widetilde{J_+} + \widetilde{J_-})} \right]$$

where J_s, J_d, $\widetilde{J_+}$ and $\widetilde{J_-}$ are the source, drain, positive and negative voltage probe current densities respectively, given by Eq. (3.15) with appropriate substitutions for the position of the contacts, as done previously for the point-like contact case.

The resulting map was shown above in Figure 3.20(b). Good alignment with the experimental result is observed, particularly in the main crescent feature. The sharp discontinuities around the edges of the contacts are slightly smoothed out; however, they are still present. By adding new assumptions, namely hydrodynamic transport, it is possible to further investigate the map of 4-probe resistance numerically.

3.3 Numerical Simulation of SGM on Hydrodynamic Transport

The experimental work presented establishes scanning gate microscopy (SGM) as a viable tool for observing the physics of moving charges in two-dimensional electron gases (2DEGs). It is supported by appropriate analytical models that confirm the source of the counterintuitive crescent-shaped SGM signal. However, analysis in the infinite strip presupposed a diffusive, Ohm's law obeying electron gas. This may be true at room temperature (although we will see later that even this is not entirely accurate) where hydrodynamic flow is suppressed by acoustic phonons dominating scatter events, but, as evidenced by Figure 3.13, low temperature non-local 4-probe resistance is negative and SGM maps no longer hold the crescent shape well described by the analytical models above.

As previous studies have shown, a hydrodynamic description of transport predicts the formation of negative potential around current injectors as the viscosity of the fluid increases. [30, 46, 133] Critically, the negative potential, therefore negative measured resistance, does not necessarily have to coincide with the formation of current whirlpools (where current flow switches direction to match the negative potential) due to viscosity aiding in the breaking of Ohm's law. The set of steady-state hydrodynamic equations that govern a two-dimensional electron liquid are given [134, p. 49] [46]:

$$-e\mathbf{E}(\mathbf{r})n(\mathbf{r}) - \nabla P(\mathbf{r}) - mn(\mathbf{r})[\mathbf{v}(\mathbf{r})\cdot\nabla]\mathbf{v}(\mathbf{r}) + \eta\nabla^2\mathbf{v}(\mathbf{r}) - \frac{mn(\mathbf{r})\mathbf{v}(\mathbf{r})}{\tau} = 0,$$
$$\nabla\cdot[n(\mathbf{r})\mathbf{v}(\mathbf{r})] = 0 \quad (3.16)$$

where $\mathbf{v}(\mathbf{r})$ is the velocity field, $n(\mathbf{r})$ the carrier density, $P(\mathbf{r})$ the pressure, η the shear viscosity, τ the momentum relaxation time, m the effective mass and $\mathbf{E}(\mathbf{r})$ the electric field. The electric field is related to the potential via $\mathbf{E}(\mathbf{r}) = -\nabla\phi(\mathbf{r})$.

Building on these experimental and theoretical results, we, through numerical simulations, aim to model the SGM response of the hydrodynamic system and gain insights into the formation of the current whirlpools. The electron system is treated as a viscous fluid, governed by modified Navier-Stokes equations that account for the local carrier density perturbation induced by the scanning tip. Using tools built for computational fluid dynamics (CFD) with spatially varying density is a novel approach in the context of SGM studies of hydrodynamic electron flow.

3.3.1 Linearised Navier-Stokes for Density-Modulated Hydrodynamic Electron Transport

In the hydrodynamic regime, electrons in graphene exhibit viscous flow, analogous to a classical fluid. The steady-state Navier-Stokes equations, adapted for this system, describe the velocity field, $\mathbf{v} = (u, v)$, and potential, ϕ. The modified (modulated carrier density) hydrodynamic equations are determined by simplifying Eq. (3.16) as follows:

1. Express the electric field in terms of the potential, $\mathbf{E}(\mathbf{r}) = -\nabla\phi(\mathbf{r})$.

2. Express the shear viscosity, η, in terms of the kinematic viscosity, ν, as $\eta = mn_0\nu$. where n_0 is the unperturbed carrier density and m is the effective cyclotron mass at that density. Shear viscosity is a measure of a fluid's internal resistance to flow when subjected to shear stress, like how sticky any fluid layer is to another as they slide past each other. The kinematic viscosity includes the fluid's mass density and therefore characterises how a fluid flows. For example, two fluids can have the same shear viscosity (force between layers), but the flow dynamics may significantly change if one fluid is much less dense than the other. In a lower-density fluid, momentum spreads more rapidly because the same viscous forces act on less mass density and, therefore, there is a quicker evolution of the flow.

3. Assume drift velocities, $\mathbf{v}$, small enough that the non-linear convective term $(\mathbf{v} \cdot \nabla)\mathbf{v}$, is negligible compared with viscous and relaxation terms. Formally, this is approximately valid when the Reynolds number $\mathrm{Re} = |\mathbf{v}|W/\nu \ll 1$, where W is a characteristic system size and ν is the kinematic viscosity. In our worst-case scenario, consider the current flowing through a narrow channel, $50\,\mu\mathrm{A}$ through a $0.4\,\mu\mathrm{m}$ wide channel, with an estimated kinematic viscosity of approximately $0.1\,\mathrm{m^2\,s^{-1}}$. This gives $\mathrm{Re} \approx 0.25$, which is large but still below 1. In the bulk, the velocity decreases as the channel widens, so the Reynolds number becomes orders of magnitude smaller. Therefore, the convective term can be safely neglected.

4. Neglect the pressure gradient, $\nabla P(\mathbf{r})$, when the restoring force (∇P is actually in units of force density $\mathrm{N\,m^{-2}}$) is dominated by back-gate electrostatics. The pressure represents the internal energy of the electron gas, which resists compression and provides a restoring force for density variations.

   Evaluating Eq. (3.16) under zero-flow conditions, $\mathbf{v} = 0$, gives:

$$-e\mathbf{E}(\mathbf{r})n(\mathbf{r}) - \nabla P(\mathbf{r}) = 0 \quad \Rightarrow \quad \nabla P(\mathbf{r}) = -en(\mathbf{r})\mathbf{E}_0,$$

where a background electric field, $\mathbf{E}_0$, is formed that balances out the pressure gradient, $\nabla P(\mathbf{r})$, induced by the non-uniform carrier density, $n(\mathbf{r})$, due to external gate electrostatics. Given that these gate-induced density variations are effectively static with respect to the flow dynamics, then we can consider that the driving field, $\mathbf{E}$, under flow conditions, $\mathbf{v} \neq 0$, in Eq. (3.16) is the change from this background field, $\mathbf{E} = \mathbf{E}_{\text{total}} - \mathbf{E}_0$. Assuming that the flow does not induce additional density variations, then the pressure gradient, $\nabla P(\mathbf{r})$, remains unchanged from the zero-flow condition and can be neglected when considering flow dynamics.

Does the flow induce additional density variations? Normally, in a fluid, density variations arise from compressibility effects. If the fluid's internal pressure provides a greater force than the external gate electrostatics, which currently pin the carrier density profile, then the fluid will compress and expand in response to the flow, creating additional density variations, and the pressure gradient may not be neglected. Fortunately, we can compare which forces are larger. [46]

Upon linearisation, small density perturbations δn contribute to this pressure and apply a force density, $F_P = \nabla P$, on the fluid. Assuming small perturbations, $\delta n \ll n_0$, we can Taylor expand the pressure around the unperturbed density, n_0:

$$P(n_0 + \delta n) \approx P(n_0) + \left(\frac{\partial P}{\partial n}\right) \delta n \Longrightarrow F_P = \nabla P \approx \left(\frac{\partial P}{\partial n}\right) \nabla \delta n$$

where $\partial P / \partial n$ is the inverse compressibility of the electron gas. Given the thermodynamic identity $dP = n d\mu$, and from Eq. (2.12),

$$\frac{\partial P}{\partial n} \approx \frac{1}{2} m v_F^2,$$

The electrostatic restoring force (force density) arises from the capacitive coupling between the 2D electron sheet and the gate (assumed at fixed potential). A local carrier density perturbation δn in the 2D sheet induces a local potential perturbation $\delta\phi$ in the plane of the sheet, given by:

$$\delta\phi = -\frac{e}{C}\delta n \Rightarrow \mathbf{E}_g = \frac{e}{C}\nabla\delta n$$

where C is the gate capacitance per unit area. A spatial gradient in δn thus produces an in-plane electric field, $\mathbf{E}_g$, that acts to restore the density to its unperturbed value. The resulting electrostatic force density acting on the

electron fluid is:

$$F_g = (-en)\mathbf{E}_g = -\frac{e^2 n}{C}\nabla\delta n$$

The pressure term, ∇P, can thus be neglected when:

$$\frac{\partial P}{\partial n} \ll \frac{e^2 n}{C} \quad \Rightarrow \quad \frac{1}{2}mv_F^2 \ll \frac{e^2 n}{C}.$$

Given $C = \epsilon/d$ for a back-gate at distance d in a medium of permittivity ϵ, and given a cyclotron mass for densities outside the Dirac point, this condition becomes:

$$C \ll \frac{2e^2\sqrt{n}}{\hbar v_F\sqrt{\pi}} \quad \Rightarrow \quad d \gg \frac{\epsilon\hbar v_F}{e^2\sqrt{n}}$$

$$\therefore d \gg 2\,\text{nm} \quad (\text{for } n \sim 10^{12}\,\text{cm}^{-2},\ \epsilon \sim 4\epsilon_0)$$

Physically, this condition is satisfied when the gate-induced electrostatic stiffness dominates the intrinsic compressibility, which is more than satisfied in our case with a 300 nm silicon dioxide substrate and a 15 nm thick distance to the tip gate. Due to the gate dominance, the intrinsic flow does not create additional variations in density, and in the absence of external perturbations (SGM tip), the density is uniform, $n(\mathbf{r}) = n_0$. Hence, the fluid is incompressible, and the pressure gradient term can be neglected as it gets absorbed into the background electric field.

5. Introduce density modulation due to the SGM tip. The carrier density is expressed as,

$$n(\mathbf{r}) = n_0 g(\mathbf{r}),$$

where n_0 is the uniform unperturbed density and $g(\mathbf{r})$ is a dimensionless spatial profile. We use a Gaussian profile representing the depletion under the tip:

$$g(\mathbf{r}) = 1 - s\exp\left[-\frac{|\mathbf{r}-\mathbf{r}_t|^2}{2\sigma^2}\right], \tag{3.17}$$

with $\mathbf{r}_t$ the tip position, s the perturbation strength (e.g., 0.9 for 90% reduction at $\mathbf{r}_t$), σ the standard deviation of the Gaussian whose HWHM is given by $r_{\text{tip}} = \sigma\sqrt{2\ln(2)}$ where r_{tip} is the effective tip radius (e.g. 150 nm). The continuity equation is modified to $\nabla \cdot [g(\mathbf{r})\mathbf{v}(\mathbf{r})] = 0$, ensuring current conservation in the presence of varying density.

Applying these simplifications step-by-step to Eq. (3.16), we obtain the set of

linearised hydrodynamic equations with spatially varying profile $g(\mathbf{r})$:

$$\begin{aligned} \frac{e}{m}\nabla\phi(\mathbf{r}) + \frac{1}{g(\mathbf{r})}\nu\nabla^2\mathbf{v}(\mathbf{r}) - \frac{\mathbf{v}(\mathbf{r})}{\tau} &= 0, \\ \nabla\cdot[g(\mathbf{r})\mathbf{v}(\mathbf{r})] &= 0, \end{aligned} \tag{3.18}$$

this is a set of three scalar differential equations, where variables $\mathbf{v}(\mathbf{r}) = (v_x, v_y)$ and $\phi(\mathbf{r})$ are the unknowns to be solved for, the velocity field and electrostatic potential, respectively. The other variables are fixed: m is the effective cyclotron mass at carrier density n_0, ν the kinematic viscosity, and τ the momentum relaxation time. The term $g(\mathbf{r})$ represents the local modulation, as a Gaussian, of density due to the SGM tip. An alternate interpretation of the equations is that the kinematic viscosity is effectively modulated such $\nu(\mathbf{r}) = \nu/g(\mathbf{r})$. In this sense, the viscosity is higher under the tip, causing flow to move around the applied perturbation.

Assuming homogenous media, $g(\mathbf{r}) = 1$, the equations reduce to the standard linearised hydrodynamic equations (Eqs. (1.27) and (1.28)) found in Bandurin et al. [30] and Pellegrino et al. [133]. Moreover, a dimensionless parameter D can be defined as:

$$D = \frac{\sqrt{\nu\tau}}{W}, \tag{3.19}$$

where W, ν, and τ are the device width, kinematic viscosity, and momentum relaxation time, respectively. This parameter characterises flow relative to the device's geometry. Scaling W, ν, and/or τ alters the flow profile, but if D remains constant during such scaling, the geometric flow characteristics stay unchanged. In the limit where $D = 0$, i.e. $\nu = 0$, the system simply reduces to the single carrier Drude description of transport (see Eq. (1.17)).

This system is solved numerically using finite element analysis with appropriate boundary conditions, such as no-slip at edges and specified current injection points.

3.3.2 Finite Element Method Implementation

Finite element analysis is discussed in greater detail in Appendix A, but briefly, the method involves discretising (splitting up what is continuous) the geometry into a mesh of small elements (e.g. triangles in 2D) and approximating the solution within each small element using simple linear or polynomial functions. The local solutions are combined into a global solution by enforcing modified (weak form) equations that allow for integrating over the elements to gain a solution over the entire domain. Successive iterations of the solution are performed until convergence is reached. This method can suitably solve complex geometries and boundary conditions that are not easily handled by analytical methods. Including the density modulation, $g(x, y)$, due

to the SGM tip is straightforward in this numerical approach, assuming sufficient mesh refinement at the tip position.

3.3.2.1 Navier-Stokes Implementation in Mathematica

The finite element method (FEM) is implemented using Mathematica's built-in PDE solver to solve the three simultaneous density-modulated hydrodynamic equations (see Eq. (3.18)). The solver calculates numerical solutions for three unknown fields: $u(x, y)$, $v(x, y)$ and $p(x, y)$, where $\mathbf{v} = (u, v)$ is the velocity field and $p(x, y) = \phi(x, y)$ is the electrostatic potential. Eq. (3.18) is expressed in Mathematica syntax:

```
modNavierStokes = {
  el/m*D[p[x,y],x] + nu/g[x,y] Laplacian[u[x,y],{x,y}] - u[x,y]/tau,
  el/m*D[p[x,y],y] + nu/g[x,y] Laplacian[v[x,y],{x,y}] - v[x,y]/tau,
  D[g[x,y] u[x,y],x] + D[g[x,y] v[x,y],y]
} == {0,0,0};
```

where standard Mathematica functions are used, such as `D[f,x]` for the derivative of scalar function f with respect to x, and `Laplacian[f,{x,y}]` for the Laplacian (divergence of the gradient of a scalar function) of function f in the xy-plane. Our own defined function $g(x, y)$ (Eq. (3.17)) is given where the tip position, radius, and strength are parameters:

```
g[x_,y_] := 1 - tipS*Exp[-Log[2]((x-tipX)^2 + (y-tipY)^2)/(tipR^2)];
```

Boundary Conditions

The solution of the equations requires appropriate boundary conditions. No-slip boundary conditions, typical for computational fluid dynamics, are applied at the edges of the device, where the velocity is set to zero, $u = v = 0$. This is done for simplicity, though other boundary conditions, such as free-slip or partial slip, could be considered in future work. Of course, if nothing else is defined, the solution would be trivial, $u = v = p = 0$. Therefore, the current inlet and outlet points are defined on the geometry to drive the flow. The current inlet is defined with a fixed normal inflow velocity, while the outlet is defined with a zero potential condition, allowing the electron fluid to exit freely. The conditions, known as Dirichlet boundary conditions, set a dependent variable, such as velocity or potential, to a fixed value on a defined boundary. While a fixed current could alternatively be imposed via a Neumann (flux) boundary condition on the potential, prescribing the inlet velocity as a Dirichlet condition provides a numerically stable and physically

transparent way to drive the flow. These conditions are applied regardless of the SGM tip's position, setting fixed inlet current allows for the observation of the tip's effect on the potential distribution. Mathematica's built-in `DirichletCondition` function is used to define these conditions. The specific locations of the inlet and outlet are defined by parameters, allowing easy adjustment for different geometries. The expression defining the no-slip Dirichlet condition on all boundaries except the inlet and outlet is given by:

```
DirichletCondition[
    {u[x, y] == 0, v[x, y] == 0},
    !(Inletxi <= x <= Inletxf && y == Inlety) &&
    !(x == Outletx && Outletyi <= y <= Outletyf)
]
```

The inlet and outlet conditions are given by:

```
DirichletCondition[{u[x, y] == 0, v[x, y] == inletVel}, y == Inlety],
DirichletCondition[p[x, y] == 0, x == Outletx]
```

Geometry and Meshing

The geometry of the real devices measured is replicated for the solve domain in Mathematica using built-in region functions. By combining simple rectangle shapes, the geometry is created to scale with the real device. An example geometry is shown in Figure 3.21. The parameters defining the geometry are easily adjusted to model different device sizes and shapes.

Given that the equations, boundary conditions, and geometry have been defined, we can now use finite element analysis to solve the equations over the domain. To do so, we discretise the domain into elements. The number of mesh points (or elements) directly influences computation time. Therefore, for accurate and fast computation time, we strategically define the mesh to be denser in areas that we expect might have steeper/sharper variations in the potential and velocity distributions, and vice versa, a less dense (more coarse) mesh is used elsewhere. To avoid digitisation (artifacts in solution due to low precision/accuracy from poor parameter choice), some simple meshing rules are in place:

1. The default coarse mesh across the domain is given as the quarter width of the contact arms, $w/2$. And the fine mesh size will be one-tenth the tip radius, $t_R/10$.

2. The radius in which the fine mesh applies is $W/4$. Where the mesh size changes linearly from the centre to the edge of the refinement radius.

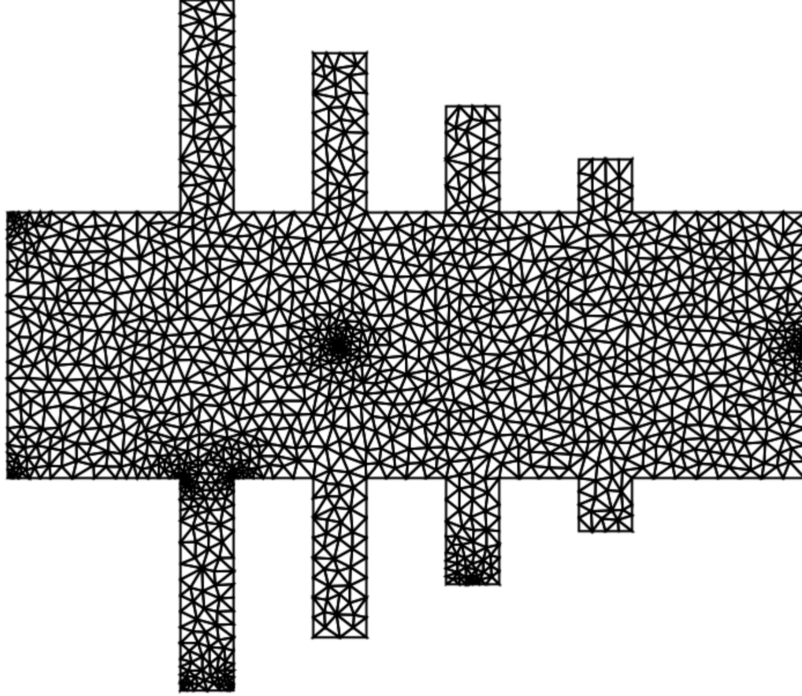

Figure 3.21: The simulated geometry mirrors the real device's dimensions, featuring a 6 µm × 2 µm bulk with 0.4 µm wide edge contacts. The domain is discretised using a trigonal mesh with an average mesh size of 100 nm, refined to 10 nm at critical points, including the corners of current contacts, points where potential is probed and the central tip position.

3. The points to have a refined mesh are the corners of the geometry that see significant current density, points where potential is probed, and the tip position.

These rules are derived from simulation experimentation and may not be optimal for all problems. However, they provide a good starting point for this problem. A mesh refinement analysis was conducted to determine optimal mesh sizes that balance computational accuracy and efficiency for 4-probe resistance calculations. The analysis evaluated various coarse and fine mesh sizes, with results presented in Figure 3.22. Considering two tip locations, in each case the fine mesh size was varied from $2r_{tip}$ to $r_{tip}/12$ for three different coarse mesh sizes: w, $w/2$, and $w/3$. The 4-probe resistance value was calculated for each configuration, where error bars represent the standard deviation measured from 15 different random mesh seeds to account for stochastic variations in mesh generation. The chosen mesh configuration achieves sufficient convergence (within 1% accuracy) while maintaining computational efficiency. Notably, coarse mesh size significantly impacts computation time, as it applies to the entire domain, whereas the fine mesh is localised to critical regions, such as the tip and contact corners. The largest coarse mesh size (w) fails to converge, while the $w/2$ coarse mesh size achieves convergence comparable to $w/3$,

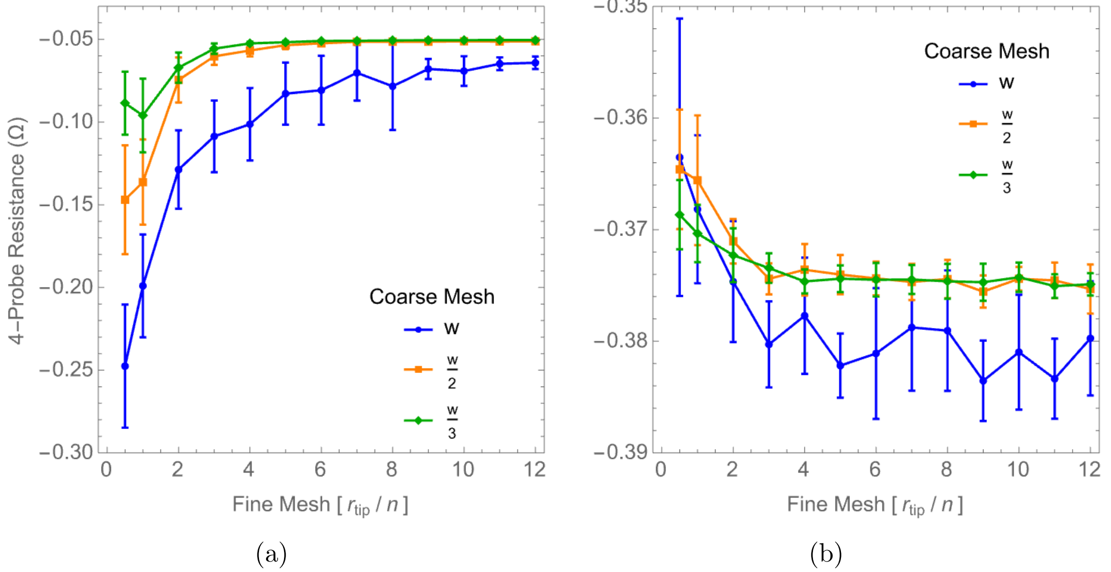

Figure 3.22: Mesh refinement analysis for two tip positions, **(a)** and **(b)**. The 4-probe resistance value is plotted against fine mesh size (r_{tip}/n, where n is the x-axis) for three coarse mesh sizes: w, w/2, and w/3 (where w is half the contact width). Convergence is observed as the mesh is progressively refined. Error bars represent standard deviation from multiple simulations with different random mesh seeds.

saturating at a fine mesh size of $r_{\text{tip}}/7$. Therefore, a coarse mesh size of $w/2$ and a fine mesh size of $r_{\text{tip}}/10$ are deemed sufficient for all tip positions and selected for subsequent simulations based on a balance of accuracy and efficiency.

An example mesh, automatically generated in the solving process, is shown in Figure 3.21, where the refinement points are clearly visible. The tip position is also a refinement point, which moves as the tip scans across the device. The mesh is trigonal, as is typical for 2D FEM problems, and the mesh size varies from coarse in the bulk to fine at the corners of current contacts, points at which potential is measured and also the tip position.

Solver Parameters

When using Mathematica's built-in `NDSolveValue`, we prescribe the interpolation order the function should use when approximating the dependent variables within the finite elements. We set these as quadratic for the velocity fields and linear for the potential field, a common choice for Navier-Stokes problems [135]. For our problem, the orders picked provide a good balance between accuracy, efficiency, and stability.

Solving time is largely dependent on mesh size, as discussed above, and the complexity of the equations. Our equations (see Eq. (3.18)) are linear, which is computationally efficient to solve. Non-linear equations, such as the full Navier-Stokes with convection term, would take significantly longer to solve and require

more attention to stability and solution convergence. For the mesh sizes used here, a single solution of our linearised density-modulated hydrodynamic equations (with tip modulation at a single point in the domain) took approximately 10 ms to solve on a standard desktop computer.

Solutions to Eq. (3.18) are calculated where the parameters are set to match experimental conditions. The effective cyclotron mass, m, is calculated from the carrier density, n_0, using Eq. (1.6). n_0 is set to $5 \times 10^{11}\,\mathrm{cm}^{-2}$ to approximately match the 10 V back-gate voltage used in experiment, although drift in the Dirac point can affect this by 10-20%. From conductivity measurements (see Figure 3.10(a)) the room temperature scattering time is estimated to be $\tau = (0.8 \pm 0.2)\,\mathrm{ps}$ which increases to $\tau = (2.0 \pm 0.1)\,\mathrm{ps}$ at 160 K. The tip modulation strength/depth parameter, s, is set to 0.9, representing a 90% reduction in carrier density directly under the tip. Given the thermal density is $8 \times 10^{10}\,\mathrm{cm}^{-2}$ at room temperature, recall Eq. (1.12), then it is a reasonable assumption for n_0 to drop to n_{th} under the tip.

The tip radius, r_{tip}, can be used as a fitting parameter to fit the amplitude of the change in 4-probe resistance in the simulated SGM maps to the experimental maps. One can recall that the amplitude in potential of the tip-induced current dipole is proportional to $(2r_{tip})^2$ (see Eq. (3.7)). The tip radius is not directly measurable in the experiment and would not be accurately determined by this fitting process as multiple factors can affect the amplitude of the SGM signal, such as the tip height above the surface (tapping mode), the exact tip shape, wear, and the actual density under the tip due to drift of the neutrality point.

And finally, the kinematic viscosity, ν, in conjunction with τ, controls the hydrodynamic nature of the system. This is also a fitting parameter, as it is not directly measurable but can then be estimated by comparing the measured 4-probe resistance maps to the simulated maps across a range of D (see Eq. (3.19)).

3.3.3 Results of Numerical Simulations

Having set up all the parameters, geometry, boundary conditions, and equations, we can now solve the equations numerically to obtain the velocity and potential fields across the domain. We used Mathematica to compute the numerical results; the code reproducing the full SGM maps is available in Appendix B.2.

Setting aside the tip modulation for now, we first examine the velocity field and vorticity of the flow in the absence of the SGM tip.

With no tip modulation, $g(x, y) = 1$, the numerical solution for the velocity field, with a 50 µA current flowing in the same configuration as the experiment, is shown in Figure 3.23. The simulation parameters were for a viscosity of $0.16\,\mathrm{m}^2\,\mathrm{s}^{-1}$ and

scattering time of 2.0 ps, this is equivalent to the flow dynamics given by $D = 0.28$, see Eq. (3.19). The velocity field is shown as arrows overlaid on a colour map of the vorticity, $\nabla \times \mathbf{v}(\mathbf{r})$.

The vorticity indicates areas of high shear forces between the fluid layers that typically leads to rotational flow. In particular, under no-slip conditions the vorticity, as expected, is dominated by the shear at the no-slip boundaries, particularly at the narrow current contact (where current density is high due to the narrow channel).

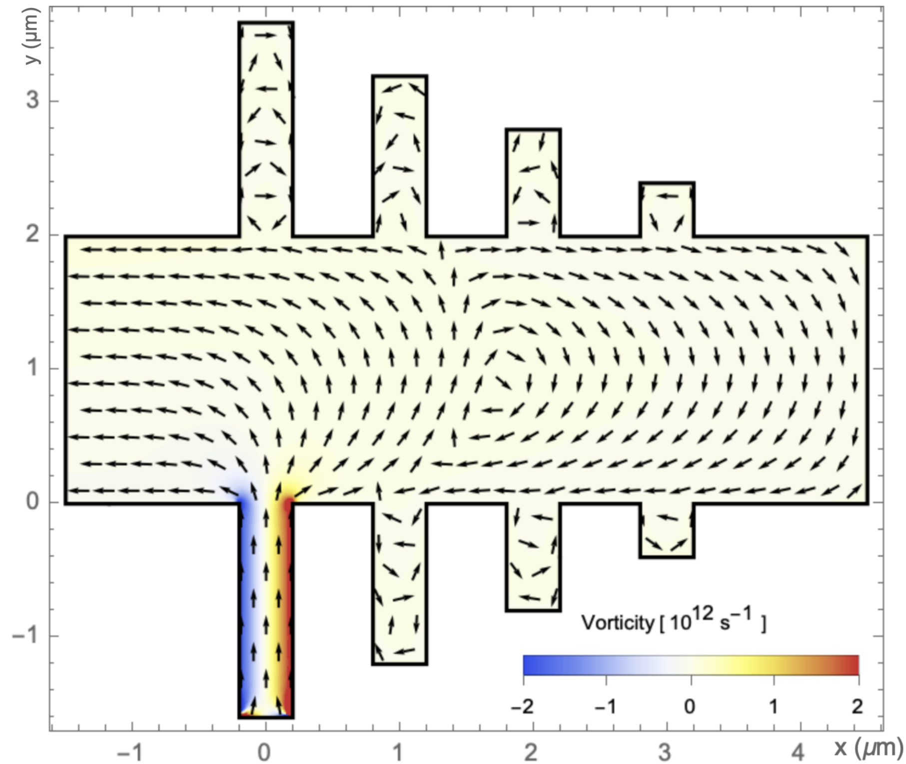

Figure 3.23: The normalised current density (drift velocity) vector field is shown as arrows (of equal size) overlaid on a colour map of the vorticity, $\nabla \times \mathbf{v}(\mathbf{r})$. The vorticity indicates regions of high shear, with positive (red) and negative (blue) values indicating clockwise and counterclockwise rotation, respectively. The formation of a large whirlpool is evident in the right side of the device, where the vorticity at the whirlpool center is evaluated $\approx 0.6 \times 10^9\,\mathrm{s}^{-1}$.

The formation of a large whirlpool is evident in the right side of the device, where the vorticity at the whirlpool center is evaluated $\approx 0.6 \times 10^9\,\mathrm{s}^{-1}$. The formation of this whirlpool is consistent with previous theoretical predictions for hydrodynamic flow in similar geometries and flow configurations. [30, 46, 133]

A visualisation of the current flow, with and without the SGM tip modulation, is shown in Figure 3.24, where the hydrodynamic nature of the fluid is characterised by the parameter $D = 0.28$. The flow lines indicate the direction of current flow, while the colour map indicates the magnitude of the current density. The current density is highest at the narrow current contact, as expected, and decreases as the

current spreads out into the wider region of the device. The large whirlpool is visible with smaller, both physically and in magnitude, vortices also present in corners and contacts.

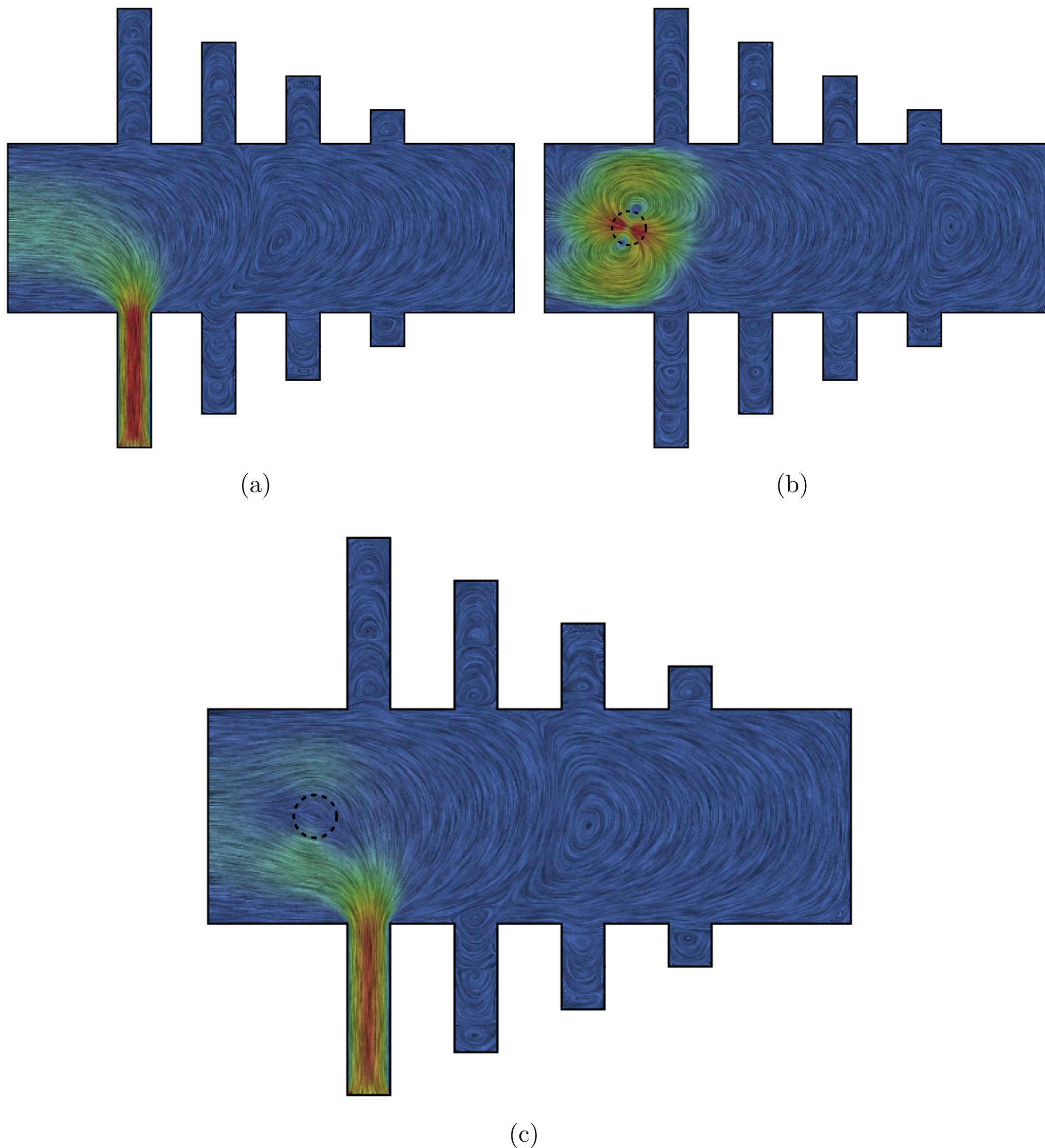

Figure 3.24: **(a)** Flow visualisation without SGM tip for $D = 0.28$. **(b)** Visualisation of the current dipole produced by the SGM tip. **(c)** Flow through the device with tip modulation is the sum of (a) and (b). Areas with high current density are indicated in red, while low current density is indicated in blue. The tip modulation FWHM is indicated by the dashed circle and significantly diverts current around the depleted region.

With the SGM tip (see Figure 3.24(c)) the flow is significantly perturbed around the depleted region under the tip. The current density under the tip is significantly reduced while the current is diverted around the depleted region, causing higher

current density on the sides of the tip position. The position of the whirlpool is also shifted, and its shape is altered by the presence of the tip. Note that the flow with the tip present (Figure 3.24(c)) is simply the sum of the flow without the tip (Figure 3.24(a)) and the dipole-like perturbation caused by the tip (see Figure 3.24(b)). The appearance of the current dipole is consistent with the previous models used in deriving the analytical solution (see Figure 3.16).

3.3.4 Extracting 4-Probe Resistance Maps from the Numerical Solution

The 4-probe resistance is extracted from the numerical solution by evaluating the potential at the voltage probe positions, $\mathbf{r}_+$ and $\mathbf{r}_-$. The potential difference between the positive and negative voltage probes, divided by the known current through the device, gives the 4-probe resistance:

$$R_{4p} = \frac{\phi(\mathbf{r}_+) - \phi(\mathbf{r}_-)}{I}$$

where $\phi(\mathbf{r})$ is the potential field obtained from the numerical solution and I is the current injected at the inlet.

The 4-probe map, $R_{4p}(\mathbf{r}_t)$, where $\mathbf{r}_t$ is the tip position, is generated by scanning the tip across a grid of points covering the area of interest, solving the hydrodynamic equations at each point, and recording the resulting 4-probe resistance. This process is computationally intensive but provides a detailed map of how the SGM tip influences the potential distribution in the hydrodynamic regime. As a simple rule to avoid digitisation artifacts, the step size of the tip scan grid is set to be half the tip radius to provide a more continuous map. Such detail may not be necessary in cases of particularly smooth, continuous fields, where figures presented can use interpolation to smooth the maps between these points.

Maps of the change in 4-probe resistance, $\Delta R_{4p}(\mathbf{r}_t)$, relative to the no-tip case, are shown in Figure 3.25 for various values of the dimensionless parameter $D = \sqrt{\nu\tau}/W$. The tip radius is set to $W/10$ with a 90% carrier density reduction directly under the tip. The geometry shape, current, and potential probes are identical to the experiment (Figure 3.11(b)) where the current inlet and outlet are on the left side of the device and the voltage probes are on the right side. The colour scale is not fixed across all maps, maximising the contrast for each map individually, with red indicating an increase in resistance and blue a decrease in resistance compared to the no-tip case. Streamlines of the current density are overlaid on the maps to illustrate the flow under each value of D.

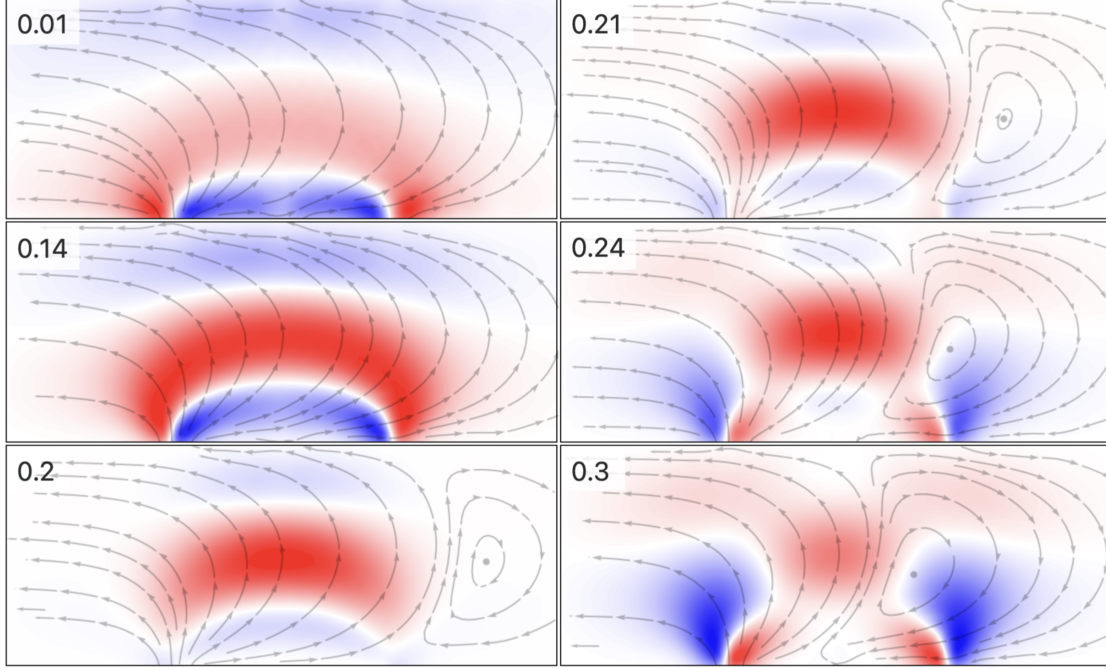

Figure 3.25: Representative maps of the change in 4-probe resistance as a function of tip position, $\Delta R_{4p}(\mathbf{r}_t)$, for various values of D. The effective tip radius is $W/10$, with a 90% carrier density reduction directly under the tip. The geometry proportions are identical to the experiment with the same measurement configuration. The colour scale is not fixed across all maps, maximising the contrast for each map individually, with red indicating an increase in resistance and blue a decrease in resistance compared to the no-tip case. Streamlines of the current density are overlaid on the maps.

The maps in Figure 3.25 show a clear feature evolution as D increases, indicating a transition from diffusive-like to hydrodynamic-like behaviour.

At low D (e.g. $D = 0.01$), the map resembles that of a diffusive system, notably similar to the analytical analysis done previously (see Figure 3.20) as expected. As D increases, the features become more complex. The negative blue region along the bottom edge detaches from the device edge ($D \approx 0.1$), and the positive red region starts to be compressed from the sides ($D \approx 0.2$). At high D (e.g. $D > 0.3$), the map qualitatively stabilises, showing no further significant changes in the features. The flow is distinctly hydrodynamic, evidenced by the formation of whirlpools seen in the current streamlines. The whirlpool center appears strongly correlated to the transition between the red center region and the blue regions to the sides (within a tip radius), with a y-position approximately within 10-15% below the middle of the device. This is consistent across all values of D where a whirlpool that extends the width of the device is present. This appears to be a fundamental feature that when the tip is positioned at the center of the whirlpool, it has zero effect on the 4-probe resistance, as the current flow is not significantly altered by the tip at that position.

While negative non-local resistance does not necessitate whirlpool formation (e.g. negative resistance is observed at $D = 0.18$ without any major whirlpool formed), the presence of whirlpools and the change in the current profile are likely the cause for the observed changes in the scanning gate microscopy (SGM) maps. To reiterate with an example from Figure 3.25, at $D = 0.2$ the 4-probe non-local resistance is negative and a whirlpool has formed to the right of the device. Due to the horizontal position of the whirlpool being significantly offset to the right of the positive voltage probe, then the 4-probe map looks qualitatively similar to the diffusive case, as the current density profile has not significantly changed in the center of the device from the diffusive case. It is only when the whirlpool position becomes similar to or less than the positive potential probe position that the map becomes qualitatively different. Further, the flip between the positive and negative regions in the map near the positive potential probe appears a strong indication of the change in direction of the current flow in that area. Lastly, all maps show symmetry about the midpoint between the positive current and potential probes, much like the analytical diffusive result.

Therefore, we can learn at least two things. One, the positioning of the positive voltage probe closer to the current injection point while creating a stronger signal will, however, come at the cost of the distinction of the SGM map of a diffusive system, making it harder to distinguish hydrodynamic behaviour (i.e. SGM maps become insensitive to D). This is because the whirlpool position starts off to the right of the device and only moves leftwards as D increases. The position of the positive voltage probe should be optimised to be near the expected whirlpool position for the viscosity and scattering time in the system. And two, the relation Eq. (3.13) that relates the measured 4-probe resistance to the dot product of the current densities in the measurement and reciprocal configurations, may hold in the hydrodynamic regime too, despite recalling that it was derived for diffusive systems and point-like current dipoles. Such an assertion would require further theoretical investigation to confirm and, if true, would provide a powerful tool in speed and simplicity in simulating SGM maps and the analysis of experimental data.

Comparing the experimental maps to the series of simulated maps for various values of D allows for the estimation of the viscosity in the system, given the scattering time is known.

Figure 3.26 compares the best experimental maps (see Figures 3.11(b) and 3.13) to the simulated maps (see Figure 3.25). We find that the room temperature map closely resembles the simulated maps for $D = 0.12 \pm 0.03$, corresponding to a kinematic viscosity of $\nu = (0.07 \pm 0.04)\,\mathrm{m^2\,s^{-1}}$ when the momentum relaxation scattering time is $\tau = (0.8 \pm 0.2)\,\mathrm{ps}$. The low-temperature map at 160 K closely resembles the simulated maps for $D = 0.28 \pm 0.03$, corresponding to a kinematic

viscosity of $\nu = (0.16 \pm 0.03)\,\mathrm{m^2\,s^{-1}}$ when the momentum relaxation scattering time is $\tau = (2.0 \pm 0.1)\,\mathrm{ps}$ from device characterisation. These viscosity values are consistent with both previous theoretical predictions [136] and experimental measurements of viscosity in monolayer graphene using the non-local negative resistance. [30, 124] The increase in viscosity at lower temperature is the expected behaviour of electron-electron scattering, which becomes more dominant as phonon scattering decreases.

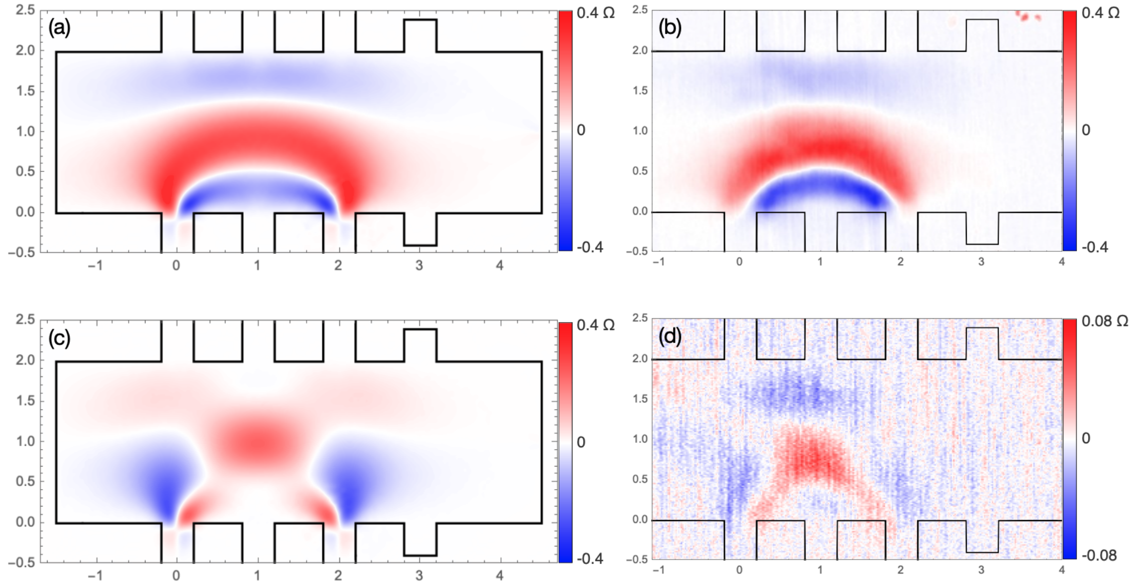

Figure 3.26: Simulated vs Experimental 4-probe non-local resistance SGM maps. Simulated maps have step size of 50 nm (129 × 61) and tip radius of 100 nm. **(a)** Simulated map for $D = 0.12$ ($\nu = 0.07\,\mathrm{m^2\,s^{-1}}$, $\tau = 0.8\,\mathrm{ps}$). **(b)** Experimental map at room temperature, identical data to Figure 3.11(b). **(c)** Simulated map for $D = 0.28$ ($\nu = 0.16\,\mathrm{m^2\,s^{-1}}$, $\tau = 2.0\,\mathrm{ps}$). **(d)** Experimental map at 160 K, using the same scan data from Figure 3.13. The correlation between simulation and experiment strongly suggests hydrodynamic flow is present at both room temperature and 160 K, with viscosity doubling at the lower temperature.

The simulated and experimental maps, particularly at room temperature, are in strong agreement, not only qualitatively but also quantitatively. The predicted nominal 4-probe resistance (the value of resistance without the tip) at room temperature was 0.52 Ω, similar to the measured value of 0.75 Ω, and can be brought into closer agreement by adjusting the viscosity to $0.05\,\mathrm{m^2\,s^{-1}}$. A similar story is true for low-temperature data, where the simulation predicted value of 4-probe resistance was -0.27 Ω while the measured value was -0.33 Ω. The viscosity could be adjusted to $0.19\,\mathrm{m^2\,s^{-1}}$ to bring the values into closer agreement. The tip radius used in the simulation was 100 nm, which is reasonable given the tip geometry. This matches the ±0.4 Ω range of the change in 4-probe resistance seen in the room temperature experiment. For low-temperature data, the range of change in 4-probe resistance was approximately 5 times smaller, likely due to the combination of tapping mode

scanning, insufficient depletion of carrier density or just different tip geometry. The amplitude scales with $(r_{tip})^2$, so a tip radius of 50 nm would give a 4 times smaller signal, which is reasonable.

The single major discrepancy between the simulated and experimental maps is the presence of a large negative region in the top center area of the experimental maps, which is absent in the simulated maps. This feature goes without explanation; inhomogeneity is a possible cause, however, its size and symmetry about the center line indicate that this is likely not the case. Some extra physics may be required to fully explain this feature that are not included in this simplified model, such as the onset of ballistic transport, slip or partial slip boundary conditions, magnetic field effects, or even thermal effects. Further investigation is required to fully understand this feature, as well as more scans on different devices to see if this feature is intrinsic and reproducible. If the SGM map is indeed proportional to the dot product of the current densities in the measurement and reciprocal configurations (see Eq. (3.13)) then this feature may be recovered if the current density in this area is particularly parallel to the device boundary. Ultimately, this discrepancy does not detract from the strong evidence for hydrodynamic flow provided by the rest of the map features and the viscosity values extracted.

3.4 Probing Transport via SGM: Conclusions and Future Work

In our study, we applied scanning gate microscopy (SGM) to probe transport in high-mobility hBN-encapsulated monolayer graphene heterostructures, showing that SGM is a powerful tool for visualising local electron flow, including in regimes where hydrodynamic behavior may emerge. SGM scans provided rich spatial information, indicating strong evidence for hydrodynamic electron flow in intrinsic monolayer graphene at both room temperature and 160 K.

The experimental setup, optimised for high vacuum and low-temperature operation down to 160 K, incorporated thermal management, vibration isolation, and capacitance minimization techniques. Key modifications, such as redesigned thermal interfaces and preamplifiers positioned near the device under test, enabled precise measurements. Both contact and non-contact SGM modes were employed, with the latter minimising mechanical exfoliation at the cost of smaller signal strength. Preliminary experiments on older devices validated the SGM methodology, demonstrating its capability to resolve electrostatic perturbations induced by the scanning probe.

On high-quality functional devices, we report SGM maps of 2-probe and 4-probe resistances in non-local geometries, where current density varies strongly across the device. Experiments were conducted at room temperature and low temperature to probe different transport regimes. Contrary to the naïve expectation that changes in 4-probe resistance are most sensitive in areas of high current density, the maps revealed characteristic crescent shapes stretching between the nearest current and potential probes.

We quantitatively reproduced these results in numerical simulations and provided an analytical solution for diffusive flow in an infinite strip geometry, which matched the main features of the experimental diffusive maps. Numerical fluid flow simulations extended this to hydrodynamic flow; the observed SGM maps aligned well with simulations based on the linearised Navier-Stokes equations adapted for a density-modulated hydrodynamic system, using no-slip boundary conditions and finite-element methods to solve for potential and velocity fields. By comparing simulated and experimental maps, we extracted kinematic viscosity values of $\nu \approx 0.07\,\mathrm{m^2\,s^{-1}}$ at room temperature and $\nu \approx 0.16\,\mathrm{m^2\,s^{-1}}$ at 160 K, consistent with prior theoretical and experimental studies [30, 124, 136]. The increase in viscosity at lower temperatures aligns with theoretical expectations for electron-electron scattering dominance.

These results show SGM's sensitivity to underlying transport mechanisms, providing direct evidence for hydrodynamic electron flow in graphene even at elevated temperatures. We found strong agreement between experiment and simulation, validating the hydrodynamic theory, while discrepancies, such as the unexplained negative regions in the experimental low-temperature map, suggest areas for further study, particularly incorporating different boundary conditions or additional physical effects such as magnetic fields, leading to insights into the magnetohydrodynamic behavior in low-dimensional systems. The onset of ballistic transport effects could have likely played a role in observed discrepancies from model.

Nevertheless, while past studies saw hydrodynamic flow as a reason for observed negative non-local resistance measured at a single point, our SGM maps provide a more comprehensive spatial picture, revealing that hydrodynamic effects predict the overall behavior of the system.

For future work, this approach should be extended to explore various geometries, boundary conditions, different tip or multi-tip perturbations, inhomogeneities, and other two-dimensional electronic systems. The simplified linearised model could be expanded to include non-linear terms and higher bulk velocities, potentially approaching turbulent regimes and higher Reynolds numbers.

More simply, similar SGM experiments on newer devices using the established techniques used in this thesis could provide more temperature-dependent data, map-

ping the transition from diffusive to hydrodynamic to ballistic regimes.

Overall, this work establishes SGM as a versatile probe for visualising current flow and quantifying viscous electron transport, with implications for designing devices that exploit hydrodynamic phenomena in two-dimensional materials.

CHAPTER 4

Last Words

In this thesis we have shown, both in theory and experimentally, that graphene's carriers behave collectively and viscously over a wide range of temperatures, including at room temperature.

When electron-hole scattering dominates near the neutrality point, this hydrodynamic transport behavior can be captured with two simple, experimentally anchored parameters τ and τ_{eh}. A new drag-modified two-fluid Drude model directly links the longitudinal and Hall responses to these microscopic timescales, enabling their extraction from routine transport measurements of resistivity.

This model explains the 'negative mobility' of minority carriers as a natural consequence of strong inter-carrier drag, and at room temperature we find $\tau/\tau_{eh} \approx 4$, a clear indicator of hydrodynamic transport in the Dirac plasma as electron-hole scattering becomes the dominant scattering mechanism.

Complementing this, we showed that scanning gate microscopy, SGM, is a suitable method for imaging intrinsic hydrodynamic transport in graphene. SGM maps allowed us to spatially image a Fermi fluid directly via 4-probe resistance maps. Analytical and numerical simulations provide high confidence in the hydrodynamic description as the main mechanism of the electronic transport observed, indicating a fluid viscosity of $0.16\,\mathrm{m^2\,s^{-1}}$ at $160\,\mathrm{K}$, and a still significant viscosity of $0.07\,\mathrm{m^2\,s^{-1}}$ at room temperature. For comparison, this is an order of magnitude more viscous than molasses!

Our methods clarify SGM maps, provide tools for interpreting when whirlpools appear, and explain how probe placement will affect map sensitivity. More extensions may be made in the future, but do not alter the central picture: hydrodynamic flow in monolayer graphene is both quantifiable and imageable using scanning gate microscopy.

This thesis offers a deeper understanding of electronic transport in graphene, a cohesive toolkit for designing devices to exploit viscous electron transport.

APPENDIX A

Solving Hydrodynamics Using The Finite Element Method

The finite element method, FEM, sometimes referred to as finite element analysis, is a numerical technique for solving partial differential equations, PDEs. FEM originates from the need to solve complex continuous differential equations without having to oversimplify them. Typically, exact solutions to continuous problems can be extremely difficult or even impossible. To overcome the problem, various discretisation methods have been used to approximate the solution, which, in the limit of an increased number of discrete points, tends to the true continuum solution. [137, pp. 1–11] With the increase in computing power, FEM has solidified itself as an extremely useful tool for many disciplines.

Unlike finite difference methods, which approximate derivatives on a structured grid, FEM divides the problem domain into small subregions called elements (often triangles or quadrilaterals in 2D). Within an element, the solution is approximated by simple functions (typically low-order polynomials). A global solution is then built up by assembling these local approximations into a large system of algebraic equations.

Mathematically, if we want to solve a PDE such as:

$$-\nabla \cdot (\epsilon \nabla \phi) = \rho \text{ in } \Omega,$$

with boundary conditions on the domain Ω. Then using FEM, we multiply the equation or set of equations by a test function v, integrate over the domain, and apply integration by parts:

$$\int_\Omega \epsilon \nabla \phi \cdot \nabla v \, d\Omega = \int_\Omega \rho v \, d\Omega.$$

The solution ϕ can then be approximated as a linear combination of polynomial functions c_i:

$$\phi(x) \approx \sum_{i=1}^{N} U_i c_i(x),$$

where U_i are unknown coefficients. This transforms the PDE into a system of coefficients, which can be solved numerically. N is the number of coefficients/basis

functions used, which is proportional to the number of elements in the mesh. For typical computational fluid dynamics problems, polynomial orders used are typically linear in pressure and quadratic in velocity. [135] Higher polynomial orders for c_i come at the cost of computation time and memory, as well as instability-induced artifacts that cause oscillations in the solution, although those higher orders may be necessary for more complex problems.

FEM has several key strengths:

- Geometric flexibility: works on complex 2D or 3D geometries using unstructured meshes.
- Generality: the same framework applies to elliptic, parabolic, and hyperbolic PDEs.
- Coupling: multiple PDEs (e.g., continuity, momentum, electrostatics) can be solved together.
- Accuracy: higher-order basis functions improve precision without requiring very fine meshes.

These features made FEM especially popular in structural mechanics and later in fluid dynamics, where Navier-Stokes equations are non-linear and often apply to unusual geometries.

Although the hydrodynamic equations presented (Eqs. (1.27) and (1.28)) are linear and the Hall-bar geometry can be simplified, there remains an appealing aspect to using FEM. Foremost, the addition of a non-uniform carrier density, induced by a local scanning gate, adds extra complication to the fluid model. Second, using FEM allows for modeling true geometry and greater flexibility for later research or for adding back non-linear terms. And third, FEM is a widely used method with fine-tuned techniques and functions for computational efficiency.

For this reason, we implement the finite element method in our numerical analysis of scanning gate microscopy on 2D electron fluids (see Section 3.3.2).

APPENDIX B

Mathematica Code for SGM Models

B.1 Analytical Model Code

Mathematica code reproducing analytical results is given here with output shown in Figure B.1.

```
(* ----- Parameters ----- *)
current = 50; (* Injector Current *)
rho = 100; (* Sheet Resistivity *)
d = 0.35; (* Tip Diameter *)
w = 0.2; (* Half Contact Width *)
W = 2; (* Strip Width *)

vectorpoints = 14; (* Number of Vectors in Y-direction *)
colourRange = 0.4; (* Colour range for resistance plot *)

(* ----- Plot Ranges ----- *)
minx = -1.5; maxx = 3.5;
miny = 0;    maxy = W;

(* ----- Contact Positions, x+iy, ----- *)
zSourceLo = -10 + 0 I;
zSourceHi = 0 + 0 I;
zProbeHi  = 2 + 0 I;
zProbeLo  = 10 + 0 I;

(* ----- Functions ----- *)
(* Point-like Source *)
JPointComplex[z_] := (current/(2 W)) Coth[(Pi/(2 W)) Conjugate[z]]

(* Finite Width Source *)
f[z_]:=Log[Sinh[(Pi Conjugate[z]/(2 W))]]
JFiniteComplex[z_] := (current/(2 Pi w)) (f[z+w]-f[z-w])

(* ----- Set System Functions ----- *)
SetSystemFunc[JFunc_] := (
  JsourceLo[z_] := JFunc[z - zSourceLo];
  JsourceHi[z_] := JFunc[z - zSourceHi];
  JprobeHi[z_] := JFunc[z - zProbeHi];
  JprobeLo[z_] := JFunc[z - zProbeLo];
  J[z_] := JsourceHi[z] - JsourceLo[z];
  Jonsager[z_] := JprobeHi[z] - JprobeLo[z];

  (* 4-Probe Resistance *)
  R4p[z_] := (Pi rho d^2)/(2 current^2) Re[J[z]Conjugate[Jonsager[z]]];
);

(* ----- Plotting function ----- *)
PlotAll[JFunc_, title_] := Module[{},
  SetSystemFunc[JFunc];
  Grid[{
    {
        Text[Style["Current Density: " <> title, Bold]],
        Text[Style["4-Probe Resistance: " <> title, Bold]],
        Text[Style["4-Probe Profiles: " <> title, Bold]]
    },
    {
```

```
    (* Current Density Plot *)
    ComplexVectorPlot[
        J[z],
        {z, minx + I miny, maxx + I maxy},
        VectorPoints -> {
          Round[vectorpoints*(maxx-minx)/(maxy-miny)], vectorpoints},
        VectorStyle -> Arrowheads[0.025],
        PlotLegends -> Placed[Automatic, Below],
        ImageSize->300,
        PlotRangePadding->None,
        AspectRatio -> Automatic
    ],
    (* 4-Probe Resistance Plot *)
    ComplexContourPlot[
        R4p[z],
        {z, minx + I miny, maxx + I maxy},
        Contours -> 80,
        ContourStyle -> None,
        PlotLegends -> Placed[Automatic, Below],
        ColorFunctionScaling -> False,
        ColorFunction -> (
          Blend[{{-colourRange, Blue}, {0, White}, {colourRange, Red}}, #]
          &),
        ClippingStyle -> Automatic,
        ImageSize->300,
        PlotRangePadding->None,
        AspectRatio -> Automatic
    ],
    Column[{
      (* Horizontal profile (y = W/2) *)
      Plot[
        R4p[x + I W/2],
        {x, minx, maxx},
        Frame -> True,
        Axes -> False,
        PlotLabel -> "Horizontal profile (y = W/2)",
        PlotStyle -> Thick,
        ImageSize->200,
        AspectRatio->0.3
      ],
      (* Vertical profile (x = 0.02) *)
      Plot[
        R4p[0.02 + I y],
        {y, miny, maxy},
        Frame -> True,
        Axes -> False,
        PlotLabel -> "Vertical profile (x = 0.02)",
        PlotStyle -> Thick,
        ImageSize->200,
        AspectRatio->0.3
      ]
    }]
    }
  }]
];
(* ----- Display Point & Finite ----- *)
PlotAll[JPointComplex, "Point-Injector"]
PlotAll[JFiniteComplex, "Finite Width"]
```

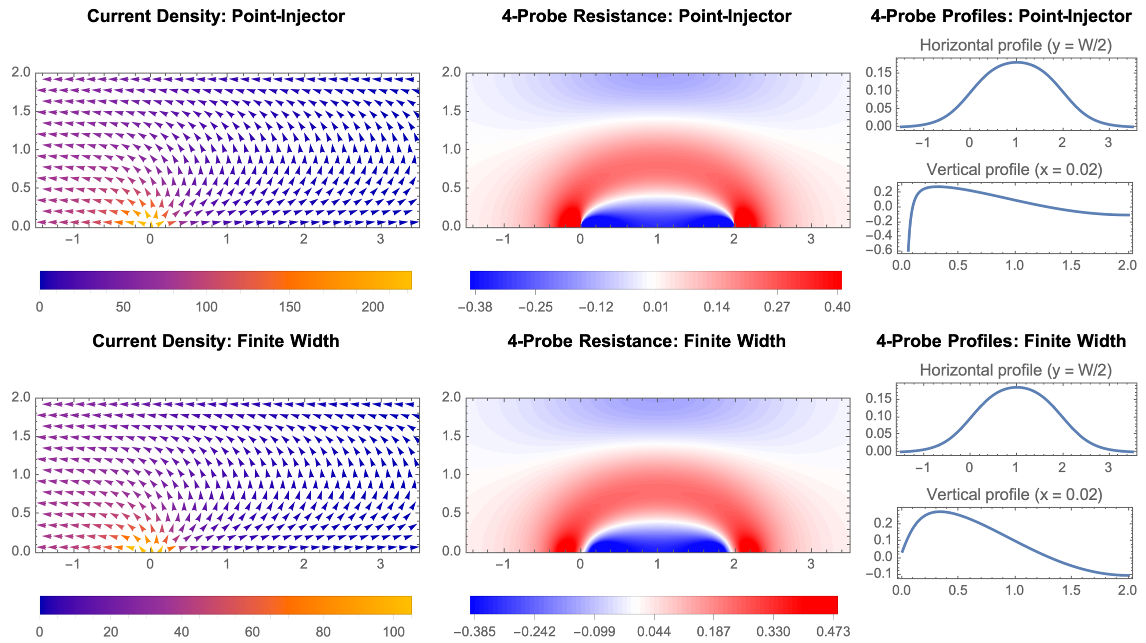

Figure B.1: Output from the analytical code provided above, showing current density plots, 4-probe resistance maps and line profiles for both point-like and finite-width current injectors. Output produced in approximately 3.6 seconds on a standard desktop computer.

B.2 Numerical Finite Element Method Code

Numerical analysis using the finite element method (FEM) requires more extensive code to set up the geometry, mesh, equations, and boundary conditions. Below is Mathematica code reproducing numerical maps similar to those shown in the main text (see Figure 3.26).

```
(* Geometry Params: Length, Width, Arm Half-Width, Arm Length, x-axis Offset *)
{L, W, w, gap, l, offset, refineRadius} =
    {6*^-6, 2*^-6, 0.2*^-6, 1*^-6, 0.4*^-6, -1.5*^-6, 0.5*^-6};

(* Arm Heights *)
{C1x, C1yi, C1yf, C6x, C6yi, C6yf} = {offset, 0, W, L+offset, 0, W};
{C2y, C3y, C4y, C5y} = l Reverse[Range[1, 4]];

(* x-Axis Arm Positions *)
centerL = L/2+offset;
{C2xi, C3xi, C4xi, C5xi} = centerL + {-3*gap, -gap, gap, 3*gap}/2 - w;
{C2xf, C3xf, C4xf, C5xf} = centerL + {-3*gap, -gap, gap, 3*gap}/2 + w;

(* Region Definition *)
domain = RegionUnion[
    Rectangle[{C1x, C1yi}, {C6x, C6yf}],
    Rectangle[{C2xi, -C2y}, {C2xf, W + C2y}],
    Rectangle[{C3xi, -C3y}, {C3xf, W + C3y}],
    Rectangle[{C4xi, -C4y}, {C4xf, W + C4y}],
    Rectangle[{C5xi, -C5y}, {C5xf, W + C5y}]
];
regionElement = Element[{x, y}, domain];
```

```
deviceBoundary = RegionPlot[domain,
    PlotStyle -> None, BoundaryStyle -> Black,AspectRatio -> Automatic];
scaledDomain = RegionResize[domain,
    {{C1x*1*^6, C6x*1*^6}, {-C2y*1*^6, (W + C2y)*1*^6}}];
deviceBoundaryScaled = RegionPlot[scaledDomain,
    PlotStyle -> None, BoundaryStyle -> Black,AspectRatio -> Automatic];

(* Parameters *)
hbar = 1.05*^-34; (* Planck's constant in J*s *)
el = 1.6*^-19; (* Elementary charge in C *)
VF = 1.05*^6; (* Fermi velocity in m/s *)

n0=5*^15; (* Average Carrier density in m^-2 *)
m=hbar*Sqrt[Pi*n0]/VF; (* average mass *)


(* Gaussian Profile For Tip *)
g[x_, y_] :=  (1-tipS*Exp[-Log[2]((x - tipX)^2 + (y - tipY)^2)/(tipR^2)])

(* Modified Navier-Stokes Equations *)
modNS = {
    el/m*D[p[x, y], x] + nu/g[x,y] Laplacian[u[x, y], {x, y}] - u[x, y]/tau,
    el/m*D[p[x, y], y] + nu/g[x,y] Laplacian[v[x, y], {x, y}] - v[x, y]/tau,
    D[ g[x,y] u[x, y], x] + D[ g[x,y] v[x, y], y]
} == {0, 0, 0};

(* Inlet/Outlet and Probe Positions *)
{Inletxi, Inletxf, Inlety} = {C2xi, C2xf, -C2y};
{Outletx, Outletyi, Outletyf} = {C1x, C1yi, C1yf};
{ProbeHix, ProbeHiy} = {(C4xi + C4xf)/2, -C4y};
{ProbeLox, ProbeLoy} = {C6x, (C6yi + C6yf)/2};

(* Boundary Conditions *)
current=50*^-6;
inletVel=-current/(2*w*el*n0); (* Inlet Velocity *)
bcs = {
    (* No-slip Walls *)
    DirichletCondition[{u[x, y] == 0, v[x, y] == 0},
           !(Inletxi<=x<=Inletxf && y==Inlety)
        && !(x==Outletx && Outletyi<=y<=Outletyf)
    ],
    (* Inlet Velocity *)
    DirichletCondition[{u[x, y] == 0, v[x, y] == inletVel}, y == Inlety],
    (* Outlet at Zero Potential*)
    DirichletCondition[p[x, y] == 0, x == Outletx]
};

(* Key points for mesh refinement *)
meshCenters = {
    {C2xi, 0}, {C2xf, 0},
    {C2xi, -C2y}, {C2xf, -C2y},
    {C1x, C1yi}, {C1x, C1yf},
    {C6x, (C6yi+C6yf)/2},
    {(C4xi+C4xf)/2, -C4y},
    {tipX, tipY}
};

(* Solve NS Equations with Modulation Due to Tip *)
(* Solves for viscosity Nu at tip position (tX,tY),
    Gaussian HWHM of tR and depth tS *)
SGMpoint[tX_, tY_, tR_, tS_, Nu_, Tau_, coarseMesh_, fineMesh_] := Module[
    {refinePoints, NS},
    refinePoints = meshCenters /. {tipX -> tX, tipY -> tY};
    NS = modNS /. {tipX -> tX, tipY -> tY, tipS -> tS, tipR -> tR,
        nu -> Nu, tau -> Tau};
    NDSolveValue[
        {NS, bcs},
        {u, v, p},
        regionElement,
        Method -> {
            "FiniteElement",
```

```
            "InterpolationOrder" -> {u -> 2, v -> 2, p -> 1},
            "MeshOptions" -> {
                "MaxCellMeasure" -> coarseMesh^2,
                (* Mesh refined Around Refinement Points *)
                "MeshRefinementFunction" -> Function[{vertices, area},
                    Module[{centroid, x, y, minDist, desiredArea},
                        centroid = Mean[vertices];
                        {x, y} = centroid;
                        minDist = Min[Norm[centroid - #] & /@ refinePoints];
                        desiredArea =
                        (fineMesh)^2
                        +(coarseMesh^2-(fineMesh)^2)*Min[1,minDist/refineRadius];
                        area > desiredArea
                    ]
                ]
            },
            PrecisionGoal -> 6,
            AccuracyGoal -> 6
        }
    ]
];

(* Map SGM over tip positions (parallelised) *)
SGMmap[tS_, tR_, viscosity_, scatTime_, s_, cM_, fM_] := Module[{potentialGrid},
    potentialGrid = ParallelTable[
        sol = SGMpoint[tx, ty, tR, tS, viscosity, scatTime, cM, fM];
        potential = sol[[3]];
        resist2P = potential[(Inletxi + Inletxf)/2, Inlety]/current;
        resist4P =
            (potential[ProbeHix,ProbeHiy]-potential[ProbeLox,ProbeLoy])/current;
        {resist4P, resist2P},
        {ty, s[[2]]}, {tx, s[[1]]},
        Method -> "CoarsestGrained"
    ]
];

(* Contour Plot For Resistivity With Auto Scaling *)
contourPlotResistivity[type_,map_] := Module[
    {resistanceMap,nominal,maxpoint,minpoint,range},
    resistanceMap = map[[All, All, type]];
    nominal=resistanceMap[[1,1]];
    maxpoint=Max[Flatten[resistanceMap]];
    minpoint=Min[Flatten[resistanceMap]];
    range=Max[Abs[maxpoint-nominal],Abs[minpoint-nominal]];

    (* Subtract nominal from value first *)
    resistanceMap = resistanceMap - nominal;
    Show[ListContourPlot[
        resistanceMap,
            InterpolationOrder -> 2,
            DataRange ->
                {{start[[1]]*1*^6, end[[1]]*1*^6},
                 {start[[2]]*1*^6, end[[2]]*1*^6}},
            ColorFunctionScaling->False,
            ColorFunction->(Blend[{{-range,Blue},{0,White},{+range,Red}}, #1] &),
            AspectRatio -> Automatic,
            PlotRange -> All,
            Contours->150,
            ContourStyle->None,
            ClippingStyle -> Automatic,
            ImageSize->400,
            PlotRangePadding->None,
            Frame->True,
            PlotRange->{minpoint,maxpoint}
    ],
    deviceBoundaryScaled
    ]
];

(* Scan Parameters *)
{start, end} = {{C1x, 0}, {C6x, W}}; (* Scan Area *)
tipRADIUS=0.1*^-6;  (* Tip Radius (m) *)
```

```
tipSTRENGTH=0.9; (* Gaussian Depth *)
coarseMeshSize=w/2;
fineMeshSize=tipRADIUS/10;

(* Create grid of tip positions *)
stepSize=150*^-9; (* Step Size of Scan (m) *)
steps = {
    Subdivide[start[[1]], end[[1]], Ceiling[(end[[1]] - start[[1]])/stepSize]],
    Subdivide[start[[2]], end[[2]], Ceiling[(end[[2]] - start[[2]])/stepSize]]
};

(* Create Directory for Output Files *)
fileName="~/Documents/HydrodynamicModelFiles/"<>
DateString[{"YearShort","Month","Day","_","Hour","Minute"}]<>"/";
CreateDirectory[fileName];

(* Compute SGM maps *)
(* Viscosity (m^2/s) and Scattering Times (s) *)
visTau={
    {0.07, 0.8*^-12},
    {0.16, 2*^-12}
};
Table[
    vis=VT[[1]];
    tau=VT[[2]];
    Print["Calculating map for viscosity: "<>ToString[vis]<> " m^2/s"];

    tStart = AbsoluteTime[];
    map=SGMmap[tipSTRENGTH,tipRADIUS,vis,tau,steps,coarseMeshSize,fineMeshSize];
    tCompute = AbsoluteTime[] - tStart;

    Print[ToString[NumberForm[vis]]<>" m^2/s map compute time: "<>
        ToString[tCompute]<>" seconds"];

    (* Export the map to directory *)
    Export[fileName<>"4pSGMmap_nu"<>ToString[NumberForm[vis]]<>".png",
        contourPlotResistivity[1,map]];
    ,{VT, visTau}
];
Save[fileName<>"param.txt",{L,W,tipRADIUS,tipSTRENGTH,coarseMeshSize,
    fineMeshSize,current,n0,m,tau,Dpoints,viscosities}]
```

This code produces two 4-probe maps for viscosities of 0.07 and 0.16 $\mathrm{m^2\,s^{-1}}$ respectively, similar to those shown in Figure 3.26. The code is parallelised to speed up computation time. Each map, with the given parameters, took approximately 60 seconds to compute.

Bibliography

[1] W. B. Jensen. The origin of the term allotrope. *Journal of Chemical Education*, 83(6):838, 2006-06.

[2] L. E. F. F. Torres, S. Roche, and J. C. Charlier. *Introduction to Graphene-Based Nanomaterials*. Cambridge University Press, 2014-01.

[3] A. Streitwieser. *Introduction to organic chemistry*. Macmillan, 3rd edition, 1985.

[4] C. Kittel. *Introduction to solid-state physics*. Wiley, 5th edition, 1976.

[5] A. K. Geim and K. S. Novoselov. The rise of graphene. *Nature Materials*, 6(3):183–191, 2007-03.

[6] L. Shi, P. Rohringer, K. Suenaga, Y. Niimi, J. Kotakoski, J. C. Meyer, H. Peterlik, M. Wanko, S. Cahangirov, A. Rubio, Z. J. Lapin, L. Novotny, P. Ayala, and T. Pichler. Confined linear carbon chains as a route to bulk carbyne. *Nature Materials*, 15(6):634–639, 2016-04.

[7] P. R. Wallace. The band theory of graphite. *Physical Review*, 71(9):622–634, 1947-05.

[8] J. C. Slater and G. F. Koster. Simplified lcao method for the periodic potential problem. *Physical Review*, 94(6):1498–1524, 1954-06.

[9] A. H. Castro Neto, F. Guinea, N. M. R. Peres, K. S. Novoselov, and A. K. Geim. The electronic properties of graphene. *Reviews of Modern Physics*, 81(1):109–162, 2009-01.

[10] K. S. Novoselov, A. K. Geim, S. V. Morozov, D. Jiang, M. I. Katsnelson, I. V. Grigorieva, S. V. Dubonos, and A. A. Firsov. Two-dimensional gas of massless dirac fermions in graphene. *Nature*, 438(7065):197–200, 2005-11.

[11] L. A. Ponomarenko, R. Yang, R. V. Gorbachev, P. Blake, A. S. Mayorov, K. S. Novoselov, M. I. Katsnelson, and A. K. Geim. Density of states and zero landau level probed through capacitance of graphene. *Physical Review Letters*, 105(13):136801, 2010-09.

[12] S. Zhou, G. Gweon, and A. Lanzara. Low energy excitations in graphite: The role of dimensionality and lattice defects. *Annals of Physics*, 321(7):1730–1746, 2006-07.

[13] M. I. Katsnelson, K. S. Novoselov, and A. K. Geim. Chiral tunnelling and the klein paradox in graphene. *Nature Physics*, 2(9):620–625, 2006-08.

[14] N. W. Ashcroft and N. D. Mermin. *Solid State Physics*. New York, South Melbourne, London, Holt, Rinehart and Winston, Brooks/Cole, Thomson Learning, 2012.

[15] V. Ariel and A. Natan. Electron effective mass in graphene. In *2013 International Conference on Electromagnetics in Advanced Applications (ICEAA)*, pp. 696–698, 2013-09.

[16] W. Rindler. *Relativity: Special, General, and Cosmological*. Oxford University Press, 2nd edition, 2006-04.

[17] S. Datta. *Electronic Transport in Mesoscopic Systems (Cambridge Studies in Semiconductor Physics and Microelectronic Engineering)*. Cambridge University Press, 1995.

[18] A. Zannoni and E. Fermi. On the quantization of the monoatomic ideal gas. 1999-12.

[19] P. A. M. Dirac. On the theory of quantum mechanics. *Proceedings of the Royal Society of London. Series A, Containing Pa-*

pers of a Mathematical and Physical Character, 112(762):661–677, 1926-10.

[20] S. Das Sarma, S. Adam, E. H. Hwang, and E. Rossi. Electronic transport in two-dimensional graphene. *Reviews of Modern Physics*, 83(2):407–470, 2011-05.

[21] J. M. Ziman. *Electrons and phonons*. Oxford classic texts in the physical sciences. Clarendon Press, 2007.

[22] N. Mounet and N. Marzari. First-principles determination of the structural, vibrational and thermodynamic properties of diamond, graphite, and derivatives. *Physical Review B*, 71(20):205214, 2005-05.

[23] E. Mariani and F. von Oppen. Flexural phonons in free-standing graphene. *Physical Review Letters*, 100(7):076801, 2008-02.

[24] E. H. Hwang and S. D. Sarma. Acoustic phonon scattering limited carrier mobility in 2d extrinsic graphene. *Physical Review B. 77, 115449 (2008)*, 2007-11.

[25] D. K. Efetov and P. Kim. Controlling electron-phonon interactions in graphene at ultra high carrier densities. *Physical Review Letters. 105, 256805 (2010)*, 2010-09.

[26] E. A. A. Pogna, X. Jia, A. Principi, A. Block, L. Banszerus, J. Zhang, X. Liu, T. Sohier, S. Forti, K. Soundarapandian, B. Terrés, J. D. Mehew, C. Trovatello, C. Coletti, F. H. L. Koppens, M. Bonn, H. I. Wang, N. van Hulst, M. J. Verstraete, H. Peng, Z. Liu, C. Stampfer, G. Cerullo, and K.-J. Tielrooij. Hot-carrier cooling in high-quality graphene is intrinsically limited by optical phonons. *ACS Nano*, 15(7):11285–11295, 2021-06.

[27] Y. G. You, J. H. Ahn, B. H. Park, Y. Kwon, E. E. B. Campbell, and S. H. Jhang. Role of remote interfacial phonons in the resistivity of graphene. *Applied Physics Letters*, 115(4):043104, 2019-07.

[28] S. V. Morozov, K. S. Novoselov, M. I. Katsnelson, F. Schedin, D. C. Elias, J. A. Jaszczak, and A. K. Geim. Giant intrinsic carrier mobilities in graphene and its bilayer. *Physical Review Letters*, 100(1), 2008-01.

[29] M. T. Greenaway, P. Kumaravadivel, J. Wengraf, L. A. Ponomarenko, A. I. Berdyugin, J. Li, J. H. Edgar, R. K. Kumar, A. K. Geim, and L. Eaves. Graphene's non-equilibrium fermions reveal doppler-shifted magnetophonon resonances accompanied by mach supersonic and landau velocity effects. *Nature Communications*, 12(1), 2021-11.

[30] D. A. Bandurin, I. Torre, R. K. Kumar, M. B. Shalom, A. Tomadin, A. Principi, G. H. Auton, E. Khestanova, K. S. Novoselov, I. V. Grigorieva, L. A. Ponomarenko, A. K. Geim, and M. Polini. Negative local resistance caused by viscous electron backflow in graphene. *Science*, 351(6277):1055–1058, 2016-02.

[31] P. Drude. Zur elektronentheorie der metalle. *Annalen der Physik*, 306(3):566–613, 1900-01.

[32] M. A. Ordal, R. J. Bell, R. W. Alexander, L. L. Long, and M. R. Querry. Optical properties of fourteen metals in the infrared and far infrared: Al, co, cu, au, fe, pb, mo, ni, pd, pt, ag, ti, v, and w. *Applied Optics*, 24(24):4493, 1985-12.

[33] S. H. Simon. *The Oxford Solid State Basics*. Oxford, Oxford University Press.

[34] C. Z. Li, J. G. Li, L. X. Wang, L. Zhang, J. M. Zhang, D. Yu, and Z. M. Liao. Two-carrier transport induced hall anomaly and large tunable magnetoresistance in dirac semimetal cd3as2 nanoplates. *ACS Nano 10, 6020 (2016)*, 10, 2016-05.

[35] A. Collaudin, B. Fauqué, Y. Fuseya, W. Kang, and K. Behnia. Angle dependence of the orbital magnetoresistance in bismuth. *Physical Review X*, 5(2):021022, 2015-06.

[36] X. Du, S. W. Tsai, D. L. Maslov, and A. F. Hebard. Metal-insulator-like behavior in semimetallic bismuth and graphite. *Physical Review Letters*, 94(16):166601, 2005-04.

[37] C. Shekhar, A. K. Nayak, Y. Sun, M. Schmidt, M. Nicklas, I. Leermakers, U. Zeitler, Y. Skourski, J. Wosnitza, Z. Liu, Y. Chen, W. Schnelle, H. Borrmann, Y. Grin, C. Felser, and B. Yan. Extremely large magnetoresistance and ultrahigh mobility in the topological weyl semimetal candidate nbp. *Nature Physics*, 11(8):645–649, 2015-06.

[38] M. N. Ali, J. Xiong, S. Flynn, J. Tao, Q. D. Gibson, L. M. Schoop, T. Liang, N. Haldolaarachchige, M. Hirschberger, N. P. Ong, and R. J. Cava. Large, non-saturating magnetoresistance in wte2. *Nature*, 514(7521):205–208, 2014-09.

[39] Y. Zhao, P. Cadden-Zimansky, F. Ghahari, and P. Kim. Magnetoresistance measurements of graphene at the charge neutrality point. *Physical Review Letters*, 108(10):106804, 2012-03.

[40] N. Xin, J. Lourembam, P. Kumaravadivel, A. E. Kazantsev, Z. Wu, C. Mullan, J. Barrier, A. A. Geim, I. V. Grigorieva, A. Mishchenko, A. Principi, V. I. Fal'ko, L. A. Ponomarenko, A. K. Geim, and A. I. Berdyugin. Giant magnetoresistance of dirac plasma in high-mobility graphene. *Nature*, 616(7956):270–274, 2023-04.

[41] A. S. Mayorov, R. V. Gorbachev, S. V. Morozov, L. Britnell, R. Jalil, L. A. Ponomarenko, P. Blake, K. S. Novoselov, K. Watanabe, T. Taniguchi, and A. K. Geim. Micrometer-scale ballistic transport in encapsulated graphene at room temperature. *Nano Letters*, 11(6):2396–2399, 2011-06.

[42] M. Büttiker. Four-terminal phase-coherent conductance. *Physical Review Letters*, 57(14):1761–1764, 1986-10.

[43] T. Taychatanapat, K. Watanabe, T. Taniguchi, and P. Jarillo-Herrero. Electrically tunable transverse magnetic focusing in graphene. *Nature Physics*, 9(4):225–229, 2013-02.

[44] M. Beconcini, S. Valentini, R. K. Kumar, G. H. Auton, A. K. Geim, L. A. Ponomarenko, M. Polini, and F. Taddei. Scaling approach to tight-binding transport in realistic graphene devices: The case of transverse magnetic focusing. *Physical Review B*, 94(11):115441, 2016-09.

[45] M. Müller, J. Schmalian, and L. Fritz. Graphene: A nearly perfect fluid. *Physical Review Letters*, 103(2), 2009-07.

[46] A. Tomadin, G. Vignale, and M. Polini. Corbino disk viscometer for 2d quantum electron liquids. *Physical Review Letters*, 113(23), 2014-12.

[47] I. Torre, A. Tomadin, A. K. Geim, and M. Polini. Nonlocal transport and the hydrodynamic shear viscosity in graphene. *Physical Review B*, 92(16), 2015-10.

[48] L. Levitov and G. Falkovich. Electron viscosity, current vortices and negative nonlocal resistance in graphene. *Nature Physics*, 12(7):672–676, 2015-08.

[49] J. Crossno, J. K. Shi, K. Wang, X. Liu, A. Harzheim, A. Lucas, S. Sachdev, P. Kim, T. Taniguchi, K. Watanabe, T. A. Ohki, and K. C. Fong. Observation of the dirac fluid and the breakdown of the wiedemann-franz law in graphene. *Science*, 351(6277):1058–1061, 2016-03.

[50] B. N. Narozhny, I. V. Gornyi, A. D. Mirlin, and J. Schmalian. Hydrodynamic approach to electronic transport in graphene. *Annalen der Physik*, 529(11), 2017-07.

[51] A. Lucas and K. C. Fong. Hydrodynamics of electrons in graphene. *Journal of Physics: Condensed Matter 30, 053001 (2018)*, 30, 2017-10.

[52] B. N. Narozhny and M. Schütt. Magnetohydrodynamics in graphene: shear and hall viscosities. *Physical Review B*, 100(3):035125, 2019-05.

[53] M. Polini and A. K. Geim. Viscous electron fluids. *Physics Today*, 73(6):28–34, 2020-06.

[54] K. Hutter. Dynamics of glaciers and large ice masses. *Annual Review of Fluid Mechanics*, 14(1):87–130, 1982-01.

[55] F. Kupka and H. J. Muthsam. Modelling of stellar convection. *Living Reviews in Computational Astrophysics*, 3(1), 2017-07.

[56] M. A. LeMone, W. M. Angevine, C. S. Bretherton, F. Chen, J. Dudhia, E. Fedorovich, K. B. Katsaros, D. H. Lenschow, L. Mahrt, E. G. Patton, J. Sun, M. Tjernström, and J. Weil. 100 years of progress in boundary layer meteorology. *Meteorological Monographs*, 59:9.1–9.85, 2019-01.

[57] M. J. M. de Jong and L. W. Molenkamp. Hydrodynamic electron flow in high-mobility wires. *Physical Review B*, 51(19):13389–13402, 1995-05.

[58] P. J. W. Moll, P. Kushwaha, N. Nandi, B. Schmidt, and A. P. Mackenzie. Evidence for hydrodynamic electron flow in pdcoo 2. *Science*, 351(6277):1061–1064, 2016-03.

[59] J. Gooth, F. Menges, N. Kumar, V. Süb, C. Shekhar, Y. Sun, U. Drechsler, R. Zierold, C. Felser, and B. Gotsmann. Thermal and electrical signatures of a hydrodynamic electron fluid in tungsten diphosphide. *Nature Communications*, 9(1), 2018-10.

[60] U. Vool, A. Hamo, G. Varnavides, Y. Wang, T. X. Zhou, N. Kumar, Y. Dovzhenko, Z. Qiu, C. A. C. Garcia, A. T. Pierce, J. Gooth, P. Anikeeva, C. Felser, P. Narang, and A. Yacoby. Imaging phonon-mediated hydrodynamic flow in wte2. *Nature Physics*, 17(11):1216–1220, 2021-09.

[61] A. Aharon-Steinberg, T. Völkl, A. Kaplan, A. K. Pariari, I. Roy, T. Holder, Y. Wolf, A. Y. Meltzer, Y. Myasoedov, M. E. Huber, B. Yan, G. Falkovich, L. S. Levitov, M. Hücker, and E. Zeldov. Direct observation of vortices in an electron fluid. *Nature*, 607(7917):74–80, 2022-07.

[62] H. E. Jackson, C. T. Walker, and T. F. McNelly. Second sound in naf. *Physical Review Letters*, 25(1):26–28, 1970-07.

[63] V. Narayanamurti and R. C. Dynes. Observation of second sound in bismuth. *Physical Review Letters*, 28(22):1461–1465, 1972-05.

[64] S. Huberman, R. A. Duncan, K. Chen, B. Song, V. Chiloyan, Z. Ding, A. A. Maznev, G. Chen, and K. A. Nelson. Observation of second sound in graphite at temperatures above 100 k. *Science*, 364(6438):375–379, 2019-04.

[65] A. Tomadin and M. Polini. Theory of the plasma-wave photoresponse of a gated graphene sheet. *Physical Review B*, 88(20), 2013-11.

[66] M. Dyakonov and M. Shur. Shallow water analogy for a ballistic field effect transistor: New mechanism of plasma wave generation by dc current. *Physical Review Letters*, 71(15):2465–2468, 1993-10.

[67] M. I. Dyakonov and M. S. Shur. Two dimensional electronic flute. *Applied Physics Letters*, 67(8):1137–1139, 1995-08.

[68] M. Dyakonov and M. Shur. Detection, mixing, and frequency multiplication of terahertz radiation by two-dimensional electronic fluid. *IEEE Transactions on Electron Devices*, 43(3):380–387, 1996-03.

[69] A. Stern, T. Scaffidi, O. Reuven, C. Kumar, J. Birkbeck, and S. Ilani. How electron hydrodynamics can eliminate the landauer-sharvin resistance. *Physical Review Letters*, 129(15):157701, 2022-10.

[70] C. Kumar, J. Birkbeck, J. A. Sulpizio, D. Perello, T. Taniguchi, K. Watanabe, O. Reuven, T. Scaffidi, A. Stern, A. K. Geim, and S. Ilani. Imaging hydrodynamic electrons flowing without landauer–sharvin resistance. *Nature*, 609(7926):276–281, 2022-09.

[71] R. V. Gorbachev, A. K. Geim, M. I. Katsnelson, K. S. Novoselov, T. Tudorovskiy, I. V. Grigorieva, A. H. MacDonald, S. V. Morozov, K. Watanabe, T. Taniguchi, and L. A. Ponomarenko. Strong coulomb drag and broken symmetry in double-layer graphene. *Nature Physics*, 8(12):896–901, 2012-10.

[72] T. J. Gramila, J. P. Eisenstein, A. H. MacDonald, L. N. Pfeiffer, and K. W. West. Mutual friction between parallel two-dimensional electron systems. *Physical Review Letters*, 66(9):1216–1219, 1991-03.

[73] J. Martin, N. Akerman, G. Ulbricht, T. Lohmann, J. H. Smet, K. von Klitzing, and A. Yacoby. Observation of electron–hole puddles in graphene using a scanning single-electron transistor. *Nature Physics*, 4(2):144–148, 2007-11.

[74] Y. Zhang, V. W. Brar, C. Girit, A. Zettl, and M. F. Crommie. Origin of spatial charge inhomogeneity in graphene. *Nature Physics*, 5(10):722–726, 2009-08.

[75] A. Isihara and L. Smrcka. Density and magnetic field dependences of the conductivity of two-dimensional electron systems. *Journal of Physics C: Solid State Physics*, 19(34):6777–6789, 1986-12.

[76] C. Cazorla and T. Gould. Polymorphism of bulk boron nitride. *Science Advances*, 5(1), 2019-01.

[77] C. Elias, P. Valvin, T. Pelini, A. Summerfield, C. J. Mellor, T. S. Cheng, L. Eaves, C. T. Foxon, P. H. Beton, S. V. Novikov, B. Gil, and G. Cassabois. Direct bandgap crossover in epitaxial monolayer boron nitride. *Nature Communications*, 10(1), 2019-06.

[78] M. Holwill. *Nanomechanics in van der Waals Heterostructures*. Springer International Publishing, 2019.

[79] L. J. van der Pauw. *A Method Of Measuring Specific Resistivity And Hall Effect Of Discs Of Arbitrary Shape*, Semiconductor Devices: Pioneering Papers. pp. 174–182. World Scientific, 1991-03.

[80] H. B. G. Casimir. On onsager's principle of microscopic reversibility. *Reviews of Modern Physics*, 17(2–3):343–350, 1945-04.

[81] L. Onsager. Reciprocal relations in irreversible processes. i. *Physical Review*, 37(4):405–426, 1931-02.

[82] L. Onsager. Reciprocal relations in irreversible processes. ii. *Physical Review*, 38(12):2265–2279, 1931-12.

[83] G. Binnig, C. F. Quate, and C. Gerber. Atomic force microscope. *Physical Review Letters*, 56(9):930–933, 1986-03.

[84] M. A. Topinka, B. J. LeRoy, S. E. J. Shaw, E. J. Heller, R. M. Westervelt, K. D. Maranowski, and A. C. Gossard. Imaging coherent electron flow from a quantum

point contact. *Science*, 289(5488):2323–2326, 2000-09.

[85] K. Yamanaka, H. Ogiso, and O. Kolosov. Ultrasonic force microscopy for nanometer resolution subsurface imaging. *Applied Physics Letters*, 64(2):178–180, 1994-01.

[86] G. Binnig, H. Rohrer, C. Gerber, and E. Weibel. Surface studies by scanning tunneling microscopy. *Physical Review Letters*, 49(1):57–61, 1982-07.

[87] Y. Martin and H. K. Wickramasinghe. Magnetic imaging by ‘“force microscopy”’ with 1000 Å resolution. *Applied Physics Letters*, 50(20):1455–1457, 1987-05.

[88] NT-MDT. *High Vacuum Scanning Probe Microscope Solver HV-2 Instruction Manual*. NT-MDT, 2008-10.

[89] M. T. Woodside and P. L. McEuen. Scanned probe imaging of single-electron charge states in nanotube quantum dots. *Science*, 296(5570):1098–1101, 2002-05.

[90] N. Paradiso, S. Heun, S. Roddaro, L. Sorba, F. Beltram, G. Biasiol, L. N. Pfeiffer, and K. W. West. Imaging fractional incompressible stripes in integer quantum hall systems. *Physical Review Letters*, 108(24):246801, 2012-06.

[91] S. Morikawa, Z. Dou, S.-W. Wang, C. G. Smith, K. Watanabe, T. Taniguchi, S. Masubuchi, T. Machida, and M. R. Connolly. Imaging ballistic carrier trajectories in graphene using scanning gate microscopy. *Applied Physics Letters*, 107(24):243102, 2015-12.

[92] M. D. Petrović, S. P. Milovanović, and F. M. Peeters. Scanning gate microscopy of magnetic focusing in graphene devices: quantum versus classical simulation. *Nanotechnology*, 28(18):185202, 2017-04.

[93] B. A. Braem, F. M. D. Pellegrino, A. Principi, M. Röösli, C. Gold, S. Hennel, J. V. Koski, M. Berl, W. Dietsche, W. Wegscheider, M. Polini, T. Ihn, and K. Ensslin. Scanning gate microscopy in a viscous electron fluid. *Physical Review B*, 98(24):241304, 2018-12.

[94] P. Kumaravadivel, M. T. Greenaway, D. Perello, A. Berdyugin, J. Birkbeck, J. Wengraf, S. Liu, J. H. Edgar, A. K. Geim, L. Eaves, and R. Krishna Kumar. Strong magnetophonon oscillations in extra-large graphene. *Nature Communications*, 10(1), 2019-07.

[95] L. Wang, I. Meric, P. Y. Huang, Q. Gao, Y. Gao, H. Tran, T. Taniguchi, K. Watanabe, L. M. Campos, D. A. Muller, J. Guo, P. Kim, J. Hone, K. L. Shepard, and C. R. Dean. One-dimensional electrical contact to a two-dimensional material. *Science*, 342(6158):614–617, 2013-10.

[96] X. Du, I. Skachko, A. Barker, and E. Y. Andrei. Approaching ballistic transport in suspended graphene. *Nature Nanotechnology*, 3(8):491–495, 2008-07.

[97] Y. Nam, D.-K. Ki, D. Soler-Delgado, and A. F. Morpurgo. Electron–hole collision limited transport in charge-neutral bilayer graphene. *Nature Physics*, 13(12):1207–1214, 2017-08.

[98] D. C. Elias, R. V. Gorbachev, A. S. Mayorov, S. V. Morozov, A. A. Zhukov, P. Blake, L. A. Ponomarenko, I. V. Grigorieva, K. S. Novoselov, F. Guinea, and A. K. Geim. Dirac cones reshaped by interaction effects in suspended graphene. *Nature Physics*, 7(9):701–704, 2011-07.

[99] G. L. Yu, R. Jalil, B. Belle, A. S. Mayorov, P. Blake, F. Schedin, S. V. Morozov, L. A. Ponomarenko, F. Chiappini, S. Wiedmann, U. Zeitler, M. I. Katsnelson, A. K. Geim, K. S. Novoselov, and D. C. Elias. Interaction phenomena in graphene seen through quantum capacitance. *Proceedings of the National

Academy of Sciences, 110(9):3282–3286, 2013-02.

[100] L. Boltzmann. Weitere studien über das wärmegleichgewicht unter gasmolekülen. *Sitzungsberichte Akademie der Wissenschaften*, p. 275–370, 1872.

[101] L. Boltzmann. *Further Studies on the Thermal Equilibrium of Gas Molecules*, The Kinetic Theory of Gases. pp. 262–349. Imperial College Press, 2003-07.

[102] H. Lorentz. The motion of electrons in metallic bodies i. *Koninklijke Nederlandse Akademie van Wetenschappen*, (7):438–453, 1905.

[103] E. M. Lifshitz, L. P. Pitaevskii, J. B. Sykes, and R. N. Franklin. *Physical Kinetics*, Vol. 10. Elsevier, 1981.

[104] S. Chapman and T. G. Cowling. *The Mathematical theory of non-uniform gases*. Cambridge University Press, 3rd edition, 1970.

[105] A. Principi. Department of Physics and Astronomy, University of Manchester, Manchester, UK. Private collaboration.

[106] L. A. Ponomarenko, A. Principi, A. D. Niblett, W. Wang, R. V. Gorbachev, P. Kumaravadivel, A. I. Berdyugin, A. V. Ermakov, S. Slizovskiy, K. Watanabe, T. Taniguchi, Q. Ge, V. I. Fal'ko, L. Eaves, M. T. Greenaway, and A. K. Geim. Extreme electron–hole drag and negative mobility in the dirac plasma of graphene. *Nature Communications*, 15(1), 2024-11.

[107] A. M. Dykhne. Conductivity of a two-dimensional two-phase system. *Soviet Physics JETP*, 32(1):63–65, 1971-01.

[108] A. M. Dykhne. Anomalous plasma resistance in a strong magnetic field. *Soviet Physics JETP*, 32(2):348–352, 1971-02.

[109] M. B. Isichenko. Percolation, statistical topography, and transport in random media. *Reviews of Modern Physics*, 64(4):961–1043, 1992-10.

[110] U. Briskot, M. Schütt, I. V. Gornyi, M. Titov, B. N. Narozhny, and A. D. Mirlin. Collision-dominated nonlinear hydrodynamics in graphene. *Physical Review B*, 92(11), 2015-09.

[111] R. N. Gurzhi. Hydrodynamic effects in solids at low temperature. *Soviet Physics Uspekhi*, 11(2):255–270, 1968-02.

[112] M. J. H. Ku, T. X. Zhou, Q. Li, Y. J. Shin, J. K. Shi, C. Burch, L. E. Anderson, A. T. Pierce, Y. Xie, A. Hamo, U. Vool, H. Zhang, F. Casola, T. Taniguchi, K. Watanabe, M. M. Fogler, P. Kim, A. Yacoby, and R. L. Walsworth. Imaging viscous flow of the dirac fluid in graphene. *Nature*, 583(7817):537–541, 2020-07.

[113] M. L. Palm, C. Ding, W. S. Huxter, T. Taniguchi, K. Watanabe, and C. L. Degen. Observation of current whirlpools in graphene at room temperature. *Science*, 384(6694):465–469, 2024-04.

[114] A. F. Young and P. Kim. Quantum interference and klein tunnelling in graphene heterojunctions. *Nature Physics*, 5(3):222–226, 2009-02.

[115] P. A. Lee and A. D. Stone. Universal conductance fluctuations in metals. *Physical Review Letters*, 55(15):1622–1625, 1985-10.

[116] E. C. Peters, E. J. H. Lee, M. Burghard, and K. Kern. Gate dependent photocurrents at a graphene p-n junction. *Applied Physics Letters*, 97(19), 2010-11.

[117] B. Brun, N. Moreau, S. Somanchi, V.-H. Nguyen, K. Watanabe, T. Taniguchi, J.-C. Charlier, C. Stampfer, and B. Hackens. Imaging dirac fermions flow through a circular veselago lens. *Physical Review B*, 100(4):041401, 2019-07.

[118] Y. Zhao, M. Kapfer, M. Eisele, K. Watanabe, T. Taniguchi, O. Zilberberg, and B. S. Jessen. Emergent cavity junction around metal-on-graphene contacts. *ACS Nano*, 19(19):18156–18163, 2025-05.

[119] V. E. Calado, S. Goswami, G. Nanda, M. Diez, A. R. Akhmerov, K. Watanabe, T. Taniguchi, T. M. Klapwijk, and L. M. K. Vandersypen. Ballistic josephson junctions in edge-contacted graphene. *Nature Nanotechnology*, 10(9):761–764, 2015-07.

[120] A. A. Balandin, S. Ghosh, W. Bao, I. Calizo, D. Teweldebrhan, F. Miao, and C. N. Lau. Superior thermal conductivity of single-layer graphene. *Nano Letters*, 8(3):902–907, 2008-02.

[121] Y. Liu, Z.-Y. Ong, J. Wu, Y. Zhao, K. Watanabe, T. Taniguchi, D. Chi, G. Zhang, J. T. L. Thong, C.-W. Qiu, and K. Hippalgaonkar. Thermal conductance of the 2d mos2/h-bn and graphene/h-bn interfaces. *Scientific Reports*, 7(1), 2017-03.

[122] Y. M. Zuev, W. Chang, and P. Kim. Thermoelectric and magnetothermoelectric transport measurements of graphene. *Physical Review Letters*, 102(9):096807, 2009-03.

[123] N. Norhakim, T. Gunasilan, Z. R. Kesuma, H. F. Hawari, and Z. A. Burhanudin. Elucidating the time-dependent charge neutrality point modulation of polymer-coated graphene field-effect transistors in an ambient environment. *Nanotechnology*, 35(50):505201, 2024-10.

[124] A. I. Berdyugin, S. G. Xu, F. M. D. Pellegrino, R. Krishna Kumar, A. Principi, I. Torre, M. Ben Shalom, T. Taniguchi, K. Watanabe, I. V. Grigorieva, M. Polini, A. K. Geim, and D. A. Bandurin. Measuring hall viscosity of graphene's electron fluid. *Science*, 364(6436):162–165, 2019-04.

[125] M. Eriksson, R. Beck, M. Topinka, J. Katine, R. Westervelt, K. Campman, and A. Gossard. Effect of a charged scanned probe microscope tip on a subsurface electron gas. *Superlattices and Microstructures*, 20(4):435–440, 1996-12.

[126] D. W. Koon and C. J. Knickerbocker. What do you measure when you measure resistivity? *Review of Scientific Instruments*, 63(1):207–210, 1992-01.

[127] D. W. Koon and C. J. Knickerbocker. What do you measure when you measure the hall effect? *Review of Scientific Instruments*, 64(2):510–513, 1993-02.

[128] J. C. Maxwell. *A Treatise on Electricity and Magnetism*, Vol. 1. Clarendon Press, 3rd edition.

[129] G. Mittag-Leffler. Sur la représentation analytique des fonctions monogènes uniformes: D'une variable indépendante. *Acta Mathematica*, 4(0):1–79, 1884.

[130] L. V. Ahlfors. *Complex analysis*. International series in pure and applied mathematics. McGraw-Hill, 3rd edition, 1979.

[131] D. W. Koon, F. Wang, D. H. Petersen, and O. Hansen. Sensitivity of resistive and hall measurements to local inhomogeneities. *Journal of Applied Physics*, 114(16):163710, 2013-10.

[132] D. M. A. Mackenzie, V. Panchal, H. Corte-León, D. H. Petersen, and O. Kazakova. Qualitative analysis of scanning gate microscopy on epitaxial graphene. *2D Materials*, 6(2):025023, 2019-02.

[133] F. M. D. Pellegrino, I. Torre, A. K. Geim, and M. Polini. Electron hydrodynamics dilemma: whirlpools or no whirlpools. *Physical Review B. 94, 155414 (2016)*, 2016-07.

[134] L. D. Landau and E. M. Lifshitz. *Fluid Mechanics*, Vol. 6. Pergamon Press, 2nd edition, 1987. Aus d. Russ. übers.

[135] P. Huyakorn, C. Taylor, R. Lee, and P. Gresho. A comparison of various mixed-interpolation finite elements in the velocity-pressure formulation of the navier-stokes equations. *Computers and Fluids*, 6(1):25–35, 1978-03.

[136] A. Principi, G. Vignale, M. Carrega, and M. Polini. Bulk and shear viscosities of the two-dimensional electron liquid in a doped graphene sheet. *Physical Review B*, 93(12):125410, 2016-03.

[137] O. C. Zienkiewicz. *The Finite Element Method: Its Basis and Fundamentals*. Butterworth-Heinemann, 2005.